TURBULENT FLOW ANALYSIS AND COHERENT STRUCTURE IDENTIFICATION IN EXPERIMENTAL MODELS WITH COMPLEX GEOMETRIES

A Dissertation

by

NOUSHIN AMINI

Submitted to the Office of Graduate Studies of
Texas A&M University
in partial fulfillment of the requirements for the degree of

DOCTOR OF PHILOSOPHY

December 2011

Major Subject: Mechanical Engineering

Turbulent Flow Analysis and Coherent Structure Identification in Experimental Models

with Complex Geometries

TURBULENT FLOW ANALYSIS AND COHERENT STRUCTURE IDENTIFICATION IN EXPERIMENTAL MODELS WITH COMPLEX GEOMETRIES

A Dissertation

by

NOUSHIN AMINI

Submitted to the Office of Graduate Studies of
Texas A&M University
in partial fulfillment of the requirements for the degree of

DOCTOR OF PHILOSOPHY

Approved by:

Chair of Committee,	Yassin A. Hassan
Committee members,	Kalyan Annamalai
	Hamn-Ching Chen
	William H. Marlow
Head of Department,	Jerald Caton

December 2011

Major Subject: Mechanical Engineering

ABSTRACT

Turbulent Flow Analysis and Coherent Structure Identification in Experimental Models with Complex Geometries. (December 2011)

Noushin Amini, B.S., Amirkabir University of Technology (Tehran Polytechnic);

M.S., Shahid Beheshti University

Chair of Advisory Committee: Dr. Yassin A. Hassan

Turbulent flows and coherent structures emerging within turbulent flow fields have been extensively studied for the past few decades and a wide variety of experimental and numerical techniques have been developed for measurement and analysis of turbulent flows. The complex nature of turbulence requires methods that can accurately estimate its highly chaotic spatial and temporal behavior. Some of the classical cases of turbulent flows with simpler geometries have been well characterized by means of the existing experimental techniques and numerical models. Nevertheless, since most turbulent fields are of complex geometries; there is an increasing interest in the study of turbulent flows through models with more complicated geometries.

In this dissertation, characteristics of turbulent flows through two different facilities with complex geometries are studied applying two different experimental methods. The first study involves the investigation of turbulent impinging jets through a staggered array of rods with or without crossflow. Such flows are crucial in various engineering disciplines. This experiment aimed at modeling the coolant flow behavior and mixing phenomena within the lower plenum of a Very High Temperature Reactor

(VHTR). Dynamic Particle Image Velocimetry (PIV) and Matched Index of Refraction (MIR) techniques were applied to acquire the turbulent velocity fields within the model. Some key flow features that may significantly enhance the flow mixing within the test section or actively affect some of the structural components were identified in the velocity fields. The evolution of coherent structures within the flow field is further investigated using a Snapshot Proper Orthogonal Decomposition (POD) technique. Furthermore, a *comparative POD* method is proposed and successfully implemented for identification of the smaller but highly influential coherent structures which may not be captured in the full-field POD analysis.

The second experimental study portrays the coolant flow through the core of an annular pebble bed VHTR. The complex geometry of the core and the highly turbulent nature of the coolant flow passing through the gaps of fuel pebbles make this case quite challenging. In this experiment, a high frequency Hot Wire Anemometry (HWA) system is applied for velocity measurements and investigation of the *bypass flow* phenomena within the near wall gaps of the core. The velocity profiles within the gaps verify the presence of an area of increased velocity close to the outer reflector wall; however, the characteristics of the coolant flow profile is highly dependent on the gap geometry and to a less extent on the Reynolds number of the flow. The time histories of the velocity are further analyzed using a Power Spectra Density (PSD) technique to acquire information about the energy content and energy transfer between eddies of different sizes at each point within the gaps.

DEDICATION

I would like to dedicate this dissertation to my loving mother, Shahrzad Zandi, and my wonderful father, Mohammad Hassan Amini, who always believed in me and supported my intellectual and emotional growth. Their unconditional love and continuous encouragement have been an invaluable source of inspiration at every step of my life. This dissertation is also dedicated to my grandmother, Masoumeh Shahpasandi Motlagh, whose passion for learning has been an immense motivation for me to pursue my academic goals.

ACKNOWLEDGEMENTS

I would like to express my sincere gratitude to my academic advisor and committee chair, Prof. Yassin A. Hassan, for his vision, leadership, and support. I consider him an exceptional mentor, a great teacher, and an excellent researcher and I wish to follow his example in my future career. I am also grateful to the rest of my advisory committee members, Prof. Kalyan Annamalai, Prof. Hamn-Ching Chen, and Prof. William H. Marlow, for their invaluable feedback, guidance, and insight throughout the course of this research study.

I would like to thank my fellow graduate and undergraduate students in the Laser Diagnostics Multiphase Flow Laboratory at Texas A&M University. Their help during my Ph.D. studies was crucial and is truly appreciated. Moreover, I wish to thank my friends, classmates, and Mechanical Engineering and Nuclear Engineering departments faculty and staff for making my time at Texas A&M University a pleasant experience.

I am immensely indebted to my family for their encouragement and sacrifices throughout my life. At the end, my deepest gratitude goes to my dearest friend, companion, and partner in life, Dr. Amir H. Izadparast, for his love, help, and unwavering support.

TABLE OF CONTENTS

Page

CHAPTER Page

CHAPTER Page

LIST OF FIGURES

Page

Page

Page

Page

Page

Page

Page

Page

LIST OF TABLES

Page

CHAPTER I

INTRODUCTION

I.1. Background

Turbulent flows are commonly found in nature as well as various engineering and technological systems. Atmospheric and ocean currents, air flow over aircraft wings, blood flow through veins, and mixing of fuel and air in engines are examples of turbulent flows commonly found in nature and engineering systems. Turbulence is often referred to as the last great unsolved problem of the classical physics. The discovery of coherent structure within certain turbulent flows by means of experimental fluid mechanics methods has been a step forward towards better understanding the nature of turbulent flows (Holmes *et al.* 1996). Turbulence is normally characterized by 1- its effectiveness in heat, mass, and momentum transport resulting in enhanced mixing of the fluid flow, 2- existence of coherent structures of different length-scales within the turbulent flow, 3- having a chaotic nature (Pope 2000). Through the years, researchers have applied different methods to measure parameters that can help in characterizing the turbulent flows among which velocity is the most important parameter. A wide variety of techniques ranging from methods using a theoretical and/or an empirical relationship between flow velocity and other properties of the flow to estimate flow velocities to

This dissertation follows the style of *Journal of Fluid Mechanics*.

methods that directly measure the flow velocity using flow markers and tracer particles have been invented and implemented (Tavoularis 2005).

Hot Wire Anemometry (HWA) technique was one of the earliest methods used to measure the local flow velocity within turbulent flows. HWA measurement takes advantage of a high sampling frequency which is important in the study of temporal behavior of turbulent flow structures. Different statistical methods have been implemented to further analyze turbulent velocities measured by HWA method. Most of these techniques such as probability density functions, Reynolds decomposition, and power spectra analysis provide information about the temporal behavior of a single point within turbulent flow fields. It has been observed that turbulent flow velocities are time dependent as well as space dependent; however, the spatial evolution of turbulent flows cannot be fully captured by HWA measurements. To address this issue, flow visualization techniques have been utilized to qualitatively study the spatial variations of turbulent flow fields and to identify the coherent structures in turbulent flows (Hussain 1983). The field of turbulence was revolutionized by the introduction of Particle Image Velocimetry (PIV) technique in 1984 (Adrian 1984, Pickering & Halliwell 1984). PIV technique provides turbulent velocity fields with high spatial and temporal resolutions. The high spatial resolution of the PIV acquired velocity fields is absolutely essential in identification of the coherent structures in turbulent flow fields while the high temporal resolution of the measurements helps in characterizing the temporal evolution of these structures. For this reason, PIV technique has been extensively used in the study of turbulent flows. Due to technological advancements in different components used in PIV

systems, i.e. high speed cameras, double-pulsed solid-state lasers, and the vast improvement of computer processing power, PIV technique has progressed significantly within the past two decades (Adrian 2005, Raffel *et al.* 1998). The high-resolution experimentally measured velocity fields have provided reliable benchmarks for numerical models and helped in validation of advanced numerical models e.g. Direct Numerical Simulation (DNS) and Large Eddy Simulation (LES). Moreover, application of robust mathematical models e.g. Galilean decomposition, Reynolds decomposition, Proper Orthogonal Decomposition (POD), etc. in post-processing of PIV velocity fields has helped researchers in better identification of coherent structures within turbulent flow fields (Adrian *et al.* 2000). Application of advanced velocity measurement techniques as well as robust numerical models along with the powerful coherent structure identification techniques have provided a vast knowledge of many of the classical cases of turbulent flows such as free shear flows (e.g. jets, wakes, mixing layers), wall bounded turbulent flows (e.g. channel flows), flow around bluff bodies of different types (e.g. flow around a cylinder, sphere), etc. However, study of turbulent flows in complex geometries is still a challenge for researchers in different engineering disciplines. Two excellent examples of turbulent flows within facilities with complex geometries are jet flows through rod bundles which are of great importance in various engineering applications such as mechanical and nuclear engineering fields and flow through packed bed columns with extensive applications in chemical, petroleum and nuclear engineering.

In this dissertation, turbulent flow through two different experimental facilities with highly complex geometries is investigated. The first experimental study presented in Chapter II, investigated the behavior of impinging jet flows through a channel containing a staggered rod bundle. The experimental facility aims at modeling the coolant flow behavior within the lower plenum of a prismatic core Very High Temperature Reactor (VHTR). Velocity fields within the test section are acquired using a 2D Dynamic PIV system. Coherent structure identification within the instantaneous PIV velocity fields are performed applying a snapshot POD technique (Sirovich 1985) for the whole field and a new adaptive POD method for identification of smaller but key structures existing throughout the velocity field. The second experimental investigation presented in Chapter III, models the coolant flow behavior passing through an annular packed bed core VHTR. The main objective of this experiment is the study and characterization of the *bypass flow* phenomena occurring close to the outer reflector wall of a packed bed reactor. For this purpose, HWA technique is applied to obtain the velocity profiles of the coolant flow within near wall gaps between the spherical packing elements of the test section modeling an annular core packed bed VHTR. In order to further investigate the turbulent behavior of the coolant flow through the gaps close to the outer wall of the packed bed, the high frequency time histories of the local velocities are further analyzed using Power Spectra Density (PSD) analysis.

I.2. Background on Very High Temperature Reactors

The rapidly increasing demand for electrical energy in the United States as well as all over the world requires safe, emission-free, and sustainable energy supplies. The proposed development of Next Generation Nuclear Plants (NGNPs) is in concert with securing nuclear energy as a reliable source of energy. The Very High Temperature Reactors (VHTRs) are the leading candidate for the NGNP program due to their higher efficiency in electricity production, improved fuel cycle, and their capability in production of Hydrogen as a clean and affordable source of energy which is needed in petroleum refining industry, chemical industry, etc. (U.S. Department of Energy 2011).

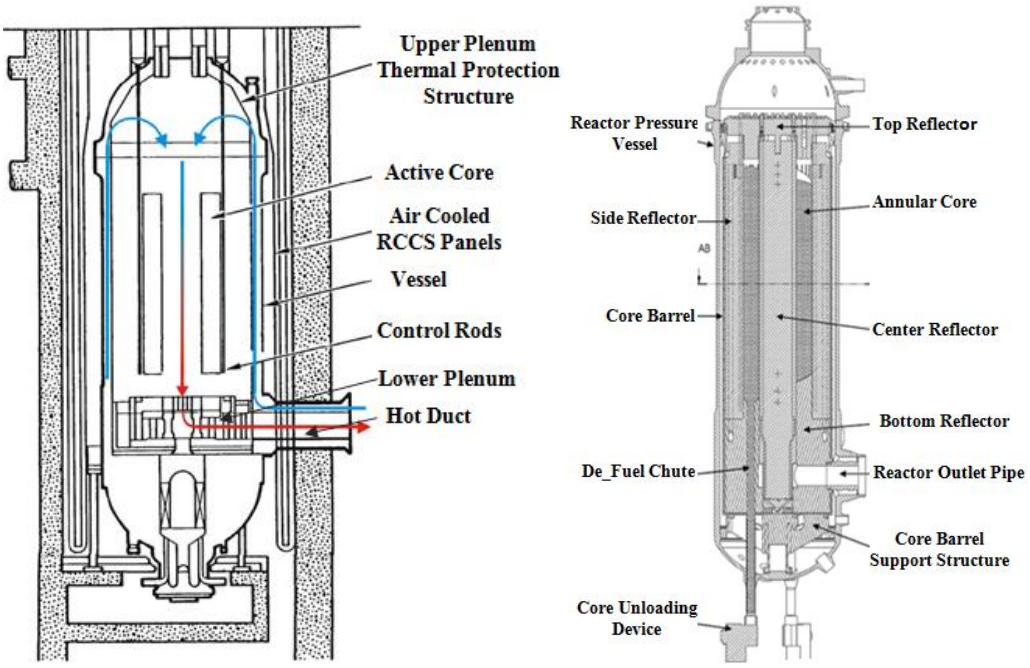

Figure I-1 Schematic of the two VHTR designs (a) prismatic core (Schultz *et al.* 2004), (b) pebble bed core (Dudley *et al.* 2008).

The two main designs proposed for VHTRs are prismatic core helium gas-cooled reactor and pebble bed core helium gas-cooled reactor. Both designs are expected to meet the basic requirements of: a) having inherent safety, b) outlet coolant temperature of 950°C for increased thermal efficiency, c) a total output power consistent with that of the commercial High Temperature Gas Cooled Reactors (HTGRs). The basic technology for prismatic core NGNP is based on the General Atomics Gas Turbine-Modular Helium Reactor (GT-MHR) design which needs to be modified to meet the requirements of the NGNP design (GT-MHR 2011). The South African Pebble Bed Modular Reactor (PBMR) which has an annular core with a solid inner reflector and a modified fuel pebble design is a starting point for development of pebble bed NGNP (Koster *et al.* 2003). The schematic of both core designs of the VHTRs are represented in Figure I-1.

The key design characteristics for both prismatic and pebble bed core VHTRs are the application of helium as coolant, graphite as moderator and using refractory coated fuel particles (TRISO coated fuel particles). In both designs, high power blowers provide helium coolant flow through the core during normal operation. Helium as an inert gas remains single phase through all stages of the reactor operation and while passing through different sections of the reactor and power conversion unit. Graphite has a high heat capacity and structural stability at high temperatures. The TRISO coated fuel particles have the capability of retaining the fission products at higher temperatures than the normal operational temperature. As shown in Figure I-1, helium enters the reactor vessel through a circular pipe or annulus in the bottom of the vessel. This pipe is mounted at a right angled direction to the reactor vessel axis. Helium then makes a 90-

degree turn and goes upward towards the upper plenum. Subsequently, helium flows downward from the upper plenum into the reactor core and then is directed towards the lower plenum. Helium temperature increases about 400-500°C while passing the core. Helium flows from lower plenum into the "hot duct" which is basically a circular pipe mounted at a 90-degree angle with respect to the reactor vessel axis. Finally, helium goes towards the intermediate heat exchanger and the turbine inlet (MacDonald *et al.* 2003, Schultz *et al.* 2004).

I.2.1. Coolant Flow Behavior within the Lower Plenum of a Prismatic Core VHTR

The study of the coolant flow behavior within the core and the lower plenum of a VHTR is essential in the improvement of the current thermal-hydraulic codes and the development of new models predicting the system's behavior under normal operation as well as the accident conditions. The high temperature helium coolant exits the core and enters the lower plenum of the core in form of high temperature circular helium jets. Some of the important phenomena that needs to be studied are the interaction between the high temperature helium jets and the adjacent graphite support rods present in the lower plenum as well as the surrounding walls, distribution of the high temperature helium flows within the lower plenum and the extent of mixing between the helium jets and the lower plenum flows, and also how and with what velocity the high temperature helium jets hit the bottom surface of the lower plenum. One of the main concerns during reactor's normal operation is the issue called "hot streaking" which is caused by poor and non-uniform mixing of the high-temperature jets entering the lower plenum. The

"hot streaks" could move through the lower plenum and the hot duct and further downstream affect the performance of components such as the turbine and the intermediate heat exchanger. The objective of this experimental study is to obtain the velocity fields along the vertical planes within a rod bundle representing the lower plenum structure through which the key flow features are expected to be identified. Some of these main flow structures may be representations of the interaction between the jet flows and the adjacent graphite rods which could affect the degree of mixing within the lower plenum.

I.2.2. Coolant Flow Behavior within the Core of a Pebble Bed VHTR

Characterization of complex coolant flow behavior in gaps between the spherical fuel elements in the core of pebble bed VHTRs is highly important in the design and development of such reactors. It is observed that in gaps close to the outer reflector wall, the velocity increases from zero at the wall to a maximum value after which it begins to decrease. This sudden increase in the velocity is called *bypass flow* and is best explained by the special arrangement of the pebbles close to the wall i.e. increased local porosity in the vicinity of a solid boundary. *Bypass flows* can significantly affect the heat transfer in packed beds which could lead into changes in the core average temperature.

I.3. Dissertation Organization

In the first experimental study presented in Chapter II, velocity fields of jets impinging into a channel containing a staggered rod bundle representing the lower plenum of a prismatic core VHTR are obtained using MIR technique along with a 2D Dynamic PIV technique. Experiments were carried out for various experimental conditions and with single and dual jets injecting into the test facility with or without crossflow. Time-averaged velocity and instantaneous vorticity fields obtained for different cases represent some key flow features within the impingement plane which in turn could affect the degree of mixing within the lower plenum. The time-averaged velocity and instantaneous vorticity fields along with the line-probes of Y-velocity and X-velocity components and other statistics of the flow such as turbulence intensities and Reynolds shear stresses as well as the line-probes of Y-velocity profiles for different planes within the lower plenum model are acquired. These results were published in a paper by (Amini & Hassan 2009) in International Journal of Heat and Mass Transfer. The PIV velocity fields are further analyzed using a Snapshot POD analysis to identify the large-scale coherent structures within the turbulent fields which are normally masked by the presence of the smaller scale coherent structures. Moreover, a *comparative POD* technique is proposed for analysis and reconstruction of the key flow features observed within the flow field that might have lower energies with respect to the whole flow field but could still be influential in enhancement of mixing within the flow field or could affect other components within the flow field. The results for the POD analysis are also

presented in Chapter II. The results of the POD analysis will be submitted to International Journal of Heat and Mass Transfer for review.

The objective of the experimental investigation presented in Chapter III is to study the turbulent flow behavior of the coolant flow and to characterize the bypass flow phenomena within the gaps close to the outer reflector wall of a test facility modeling the core of a pebble bed VHTR. Axial and Radial velocity profiles of the coolant flow within the near wall gaps are acquired utilizing a HWA system coupled with a hot film X-probe. Subsequently, the location and magnitude of the *bypass flow* and the effect of the flowrate and the gap geometry on the characteristics of the *bypass flow* are investigated. Moreover, in order to study the turbulent behavior of the coolant flow, the time histories of the velocity at different points within the gap are further analyzed using a PSD method which provides information about energy content of the large-scale and smaller-scale eddies under different experimental conditions. The results presented in Chapter III will be submitted for publication in near future.

CHAPTER II

EXPERIMENTAL STUDY OF THE COOLANT FLOW BEHAVIOR WITHIN THE LOWER PLENUM OF A PRISMATIC CORE VHTR*

II.1. Background

The proposed development of the Next Generation Nuclear Plants (NGNPs) holds great promise as a viable solution to burgeoning global energy. The NGNP has the opportunity to ensure the sustainability of nuclear energy through its efforts to improve the fuel cycle, reprocessing and fuel treatment. The Very High Temperature Reactors (VHTRs) are the primary reactor design under consideration for the NGNP program because of their higher efficiency in electricity production and their capability in Hydrogen production (U.S. Department of Energy 2011). However, development of the VHTR systems, and other advanced systems, will require the enhancement of current - and development of new - predictive methods utilized to model the phenomena associated with a nuclear power production plant. Particularly, modeling system's thermal hydraulic behavior is essential to the development of predictive methods for performance studies of new reactor designs. Therefore, the study of flow structure

*Part of this chapter is reprinted with permission from "Measurements of jet flows impinging into a channel containing a rod bundle using dynamic PIV" by Amini N. and Hassan Y. A., 2009, International Journal of Heat and Mass Transfer, 52, 5479-5495, Copyright [2009] by Elsevier.

within the core of a VHTR, whether a prismatic block or a pebble-bed core, is of great importance. In the present study, investigations were conducted to study physical phenomena expected in a prismatic core NGNP, especially the flow of high temperature Helium coolant jets exiting the core and entering the lower plenum of the core (core bottom structure). Some of the important phenomena occurring in the lower plenum are how the coolant flow is hitting the lower plenum bottom surface, the interaction between the circular coolant jet flows and the neighboring circular graphite support rods of the lower plenum and the surrounding walls, as well as the distribution and the degree of mixing of the high temperature Helium coolant flows with the lower plenum flows. Experimental characterizations of the flow behavior in this system are an essential element in the efforts to develop models capable of accurately predicting plant's thermal hydraulic behavior. To understand these phenomena and to measure the fluid characteristics in the lower plenum, many experiments have investigated single or dual jets effusing into flat plates or a rod bundles.

One of the early investigations was performed by Donaldson & Snedeker (1971) and Donaldson *et al.* (1971) who presented the mean flow characteristics and the heat transfer rates of a circular convergent nozzle jet impinging on plates of different shapes at different angles. Additionally, the turbulent characteristics and the heat transfer rates of a circular subsonic jet effusing normally to a flat plate were studied. Landreth & Adrian (1990) used Particle Image Velocimetry (PIV) techniques to obtain the instantaneous and average velocity fields of a circular water jet which was connected to a converging nozzle at its end and was impinging vertically on a flat plate. They used the

instantaneous velocity fields to calculate the vorticity and shear stress rate. In another study, Cooper *et al.* (1993) investigated flow from a turbulent jet impinging orthogonally upon a large plane surface. In this experiment both the jet discharge velocities and the jet outlet height above the plate were varied. Such efforts allowed analysis of the mean velocity profile in the vicinity of the plate surface as well as each component of the Reynolds stress exerted on the plate for a variety of flow conditions. In another study, Nishino *et al.* (1996) implemented 2-D and 3-D Particle Tracking Velocimetry (PTV) technique to analyze the turbulence statistics in the stagnation region of a fixed Reynolds number jet which was impinging normally into a flat plate. Sakakibara *et al.* (1997) obtained measurements of simultaneous velocity and temperature profiles in the stagnation region of an impinging plane jet using both digital PIV and Laser-Induced Fluorescence (LIF). Moreover, Mi *et al.* (2001) investigated the effects of jet exit conditions on the passive scalar field by using two types of nozzles at a fixed Reynolds number; a smooth converging nozzle and a long straight pipe. They obtained the jet scalar field and the flow structure of each jet and showed that their experimental results corresponded well to the analytical results. In the investigation done by Alekseenko *et al.* (2007) stereo and 2D PIV techniques helped to study the flow characteristics of a jet impinging on a flat plate with varying swirl rates for a fixed Reynolds number of 8,900. Alekseenko et *al.* (2007) observed that the decay rate of the absolute velocity of the non-swirling jets is less than that of the swirling jets. Abdel-Fattah (2007) numerically and experimentally studied the case of two circular air jets impinging on a flat plate with no cross-flow in two dimensions. He investigated the effects of the Reynolds number,

nozzle to plate spacing, nozzle to nozzle centerline spacing and the jet angle on the creation of a sub-atmospheric region between the two jets.

Aside from experiments concerned only with the behavior of jets impinging on flat plates, flow mixing phenomena, including the velocity fields associated with impinging jets within rod bundles, have frequently been studied experimentally. The flow structure within the rod bundles is of great interest among nuclear reactor engineers because of the special configuration of the fuel rods in a nuclear reactor core. In an investigation performed by Trupp & Azad (1975), the mean velocity and turbulent characteristics of the axial flow within a triangular rod bundle were measured for different Reynolds numbers and different tube spacings. Hooper & Wood (1984) obtained the mean axial velocity, wall shear stress, and all six Reynolds stresses with varied Reynolds numbers for a fixed pitch squared bundle consisting of six rods. Hooper & Rehme (1984) and Rehme (1987) used hot-wire anemometry to measure the turbulence intensities of a rectangular channel. In the former experiment, they used two geometries, one containing four rods and the other one having six rods, while in the latter the bundle consisted of four rods. Renksizbulut & Hadaller (1986) used Laser-Doppler Anemometry (LDA) to obtain the mean velocity and turbulent flow characteristics at a fixed Reynolds number within a square channel of six rods. Additionally, Smith *et al.* (2002) performed thermal hydraulic experiments in a 5×5 rod bundle with a heated rod using a PIV system. Subsequent Computational Fluid Dynamics (CFD) simulations were also performed to develop confidence in the use of CFD as a tool to investigate the flow and temperature distributions in a rod bundle array

with spacer grids. In an effort to examine the lateral flow structure of a square sub-channel geometry, Chang *et al.* (2007) used two dimensional LDA to measure detailed turbulent flow profiles on a 5×5 rod bundle array. Notably, the study of impinging jets is not limited to nuclear industry. There are many other applications of impinging jets such as cooling electronic components or gas turbine blades, annealing of metals and drying of textiles, paper and hard wood. One example of research for different applications of impinging jets was demonstrated in Velasco *et al.*'s (2007) investigation. They carried out a 2D PIV measurement to obtain the gas flow behavior in the space between the breach and neighbor tubes of a shell-and-tube heat exchanger for a range of Reynolds number from 0.8×10^5 to 2.7×10^5. They showed that increasing the gas Reynolds number improves the jet penetration and turbulence intensity level close to the breach. Velasco *et al.* 2007 observed that the presence of the tubes distorts the jet shape.

McEligot & McCreery (2004) and McCreery & Condie (2006) emphasized the need for performing benchmark experiments and investigating the combined effects of the lower plenum flows for the purpose of developing effective models in such systems. They also asserted that the development of CFD codes to model flow in the lower plenum of a conceptual VHTR should be in concert with carrying out the experimental investigations over a wide range of operating conditions. These estimates predicted Reynolds numbers for jets exhausting into the lower plenum to vary from 50,000, at full-power operation, to as low as 5,000, under partial loading conditions. Such large variations in flow parameters require that prediction methods anticipate and consider the mechanisms which control fluid flow behavior under different operating conditions.

For the current investigation, experimental studies of flow behavior in a model representing the lower plenum of a conceptual VHTR were conducted in the Laser Diagnostics Multiphase Flow Laboratory at Texas A&M University. Dynamic PIV technique was used in conjunction with Matched Index of Refraction (MIR) technique to acquire the instantaneous and time-averaged velocity fields of impinging jet flows within a channel containing a rod bundle. Some important flow features are identified in the velocity fields obtained by PIV technique and are discussed in detail. Subsequently, Snapshot Proper Orthogonal Decomposition (POD) method is used to decompose the flow fields into series of orthogonal POD modes, and the energy distribution of each of the POD modes is obtained showing their role in the formation of different flow patterns in the flow field. Snapshots of the flow fields have been reconstructed using the most energetic modes which would suggest that those modes are contribute to the formation of the dominant flow structures. The effect of the jet's Reynolds numbers and the number of impinging jets on the size, shape, and formation of the coherent structures are also studied. These efforts will help in the development of the predictive methods utilized in analysis of the VHTR systems by aiding in the development of experimental databases, and providing benchmark data for CFD codes.

II.2. Experimental Methodology

II.2.1. Experimental Set-up and Flow Configuration

A detailed schematic of the experimental set-up aiming at modeling the flow behavior in the lower plenum of a conceptual VHTR is shown in Figure II-1. The experimental facility consisted of a hydraulic loop equipped with a submergible pump which would drive the water flow into two separate loops each leading to one of the inlet jets of the channel. The separate loops had flowmeters (Blue-White Industries, accuracy ±5%) indicating the flow rates of each loop for determining mean flow velocity in each inlet jet. Both of the inlet jets entered the channel top wall at an angle of 90◦. The channel had a rectangular cross section with the dimensions of L=1016 mm, H=76.2 mm and W=76.2 mm. The channel had a single outlet located at one of its ends. In order to ensure good visual conditions for PIV measurements, the channel was constructed with transparent polycarbonate sheets. To have uniform flow, two flow straighteners are installed close to the two ends of the channel. As it is shown in Figure II-1, the rod bundle consisted of 29 tubes fixed to the upper and lower surfaces of the channel. These tubes possessed a 10.67 mm outer diameter and a 10.16 mm inner diameter and were set as “in-line” in z direction, each row of tube is exactly placed behind the next row, with 19 mm pitch and as “staggered” in x direction, each row of tubes is displaced with regards to the previous row, with 25.4 mm pitch (Figure II-2). The inlet jets were fixed 1 cm from the top wall of the channel. It should be noted that the inlet jets were made of the same tubes as the rod bundle was.

Flow Channel Dimensions:

Length: 1016 mm

Width: 76.2 mm

Height: 76.2 mm

Rod Bundle Characteristics:

29 rods

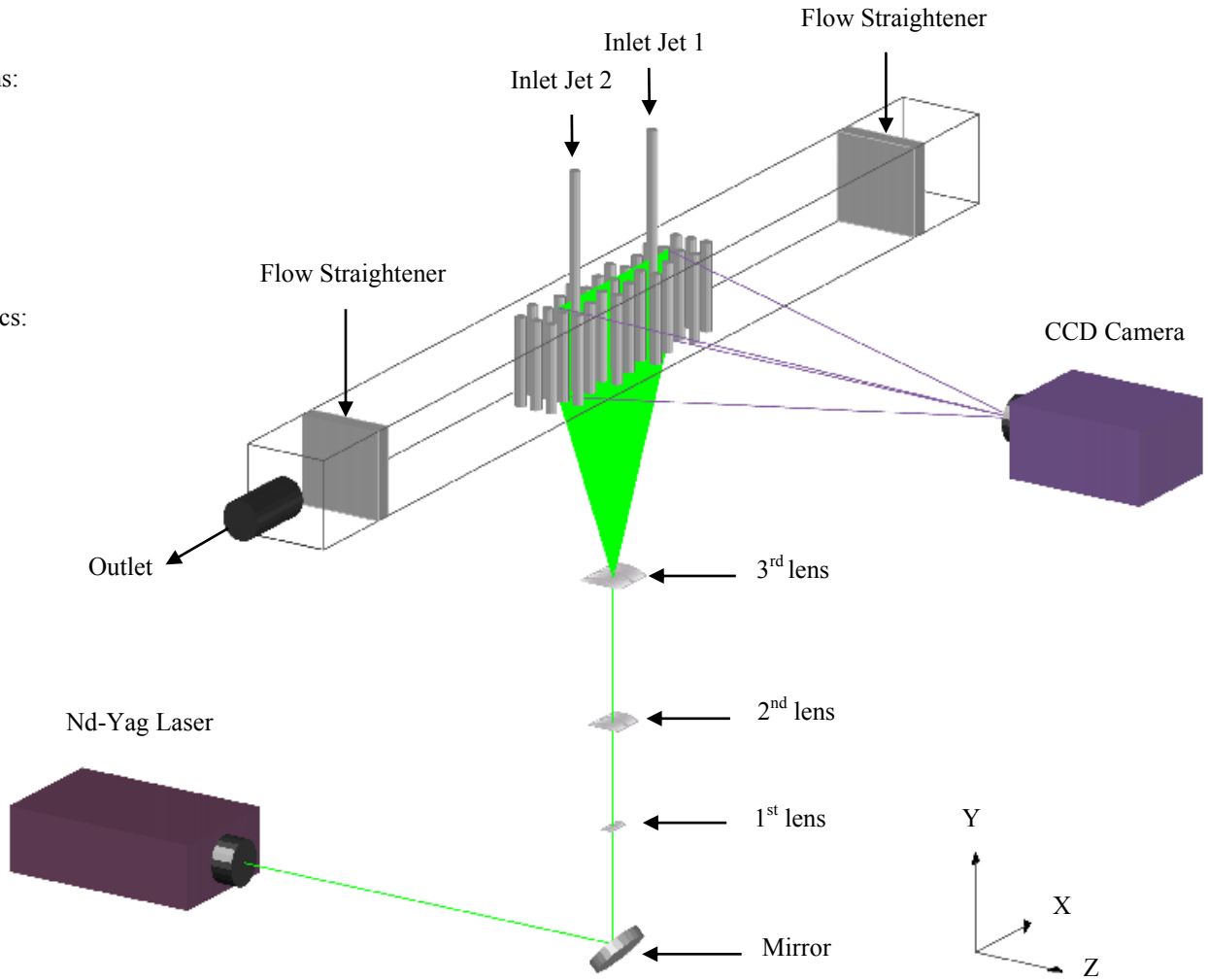

Figure II-1 Schematic of the test section.

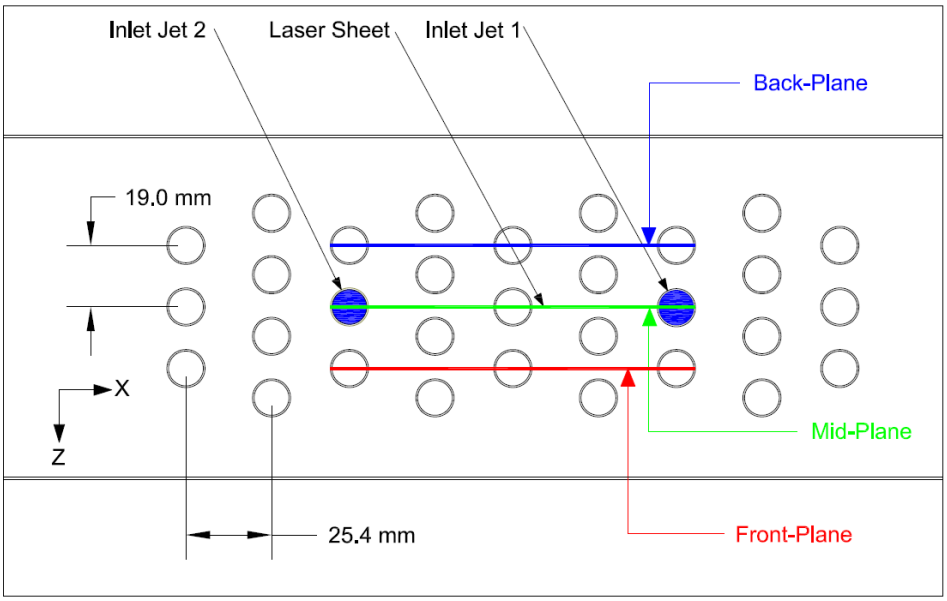

Figure II-2 Schematic of the channel top wall showing the two inlet jets and the measurement planes.

In this study, the Reynolds number is calculated as shown in Eq. II-1, where U_0 is the inlet jet's mean velocity, d is the inlet jet's inner diameter, ρ is water density and μ is water dynamic viscosity both at room temperature.

$$\mathrm{Re}_{jet} = \frac{\rho U_0 d}{\mu} \qquad \text{(II-1)}$$

MIR technique was used in the development of the experimental test facility to allow the more complete investigations of flow behavior to be executed. The material used for the rod bundle tubes and the inlet jets had the same index of refraction as water which was the working fluid in the experiment. Using MIR technique allowed for complete visualization of the flow in the interior regions of the bundle. Since the rods were represented as hollow cylinders, water filled the tubes to avoid optical aberrations.

Such an approach allows complete visualization of the flow without hidden regions obstructed by the presence of the rods. Moreover, a variety of flow conditions were developed in response to cursory investigations suggesting the possibility of large variations in reactor operating conditions. The matrix characterizing the flow conditions used in experimental investigations is presented in Table II-1 to demonstrate the range over which parameters were evaluated during the execution of this investigation. It should be mentioned that the Reynolds number of the crossflow is calculated based on channel inlet velocity and the height of the channel.

			$Re_{jet\ 1}$	$Re_{jet\ 2}$	$Re_{crossflow}$
Single Jet	Jet in the Middle	Jet Up	6,700	-	-
			4,470	-	-
		Jet Down	4,470	-	-
	Jet in the corner		13,400	-	-
			8,980	-	-
			4,470	-	-
Dual Jets			11,160	6,250	-
			13,400	4,470	-
			13,400	6,590	-
Dual Jets with Crossflow			11,160	6,700	1,670

Table II-1 Experimental matrix of variation of parameters, $Re_{jet\ 1}$ is the first jet's Reynolds Number, $Re_{jet\ 2}$ is the second jet's Reynolds number, and $Re_{crossflow}$ is the crossflow's Reynolds Number.

Relevant characteristics of the PIV and MIR systems, which are developed for this experiment, will be discussed separately in the following sections.

II.2.2. Matched Index of Refraction (MIR) Technique

II.2.2.1. Introduction to MIR Technique

Laser diagnostic techniques such as Laser LDA, PIV, Particle Tracking Velocimetry (PTV), and Planar Laser Induced Fluorescence (PLIF) have been widely applied in fluid dynamics studies in various engineering and scientific fields. The main advantage of the optical measurement methods is their capability in measuring the flow characteristics without disturbing the flow. Application of laser diagnostic techniques in the experimental study of the flow fields requires optical transparency of the test section in order for the laser light to pass through the facility and also for the cameras to capture images of flow field. Refraction of the laser light while passing through the experimental set-up walls and the interfaces between different solid and fluid phases is a major issue for all optical diagnostic methods. A solution for this problem especially in the experimental flow studies is obtained by application of Matched Index of Refraction (MIR) technique in which the refractive index of the fluid is matched to that of the test set-up walls or interfaces. For this purpose, it is highly important to accurately determine the refractive index of both the working fluid and the transparent solid material. Other important factors such as physical and chemical properties of the fluid (e.g. density, viscosity, flammability, toxicity, etc.) need to be considered while selecting fluids for refractive index matching applications. Also additional research needs to be done on the

compatibility of the candidate fluid with the solid material to determine the possibility of any chemical reaction between the fluid of interest and the solid material considered for the test section.

Previous research studies have indicated that non-uniformities in the refractive index throughout the test section may result in optical distortions of the measurement volume. Schmidt *et al.* (1984) addressed the significant errors in LDA velocity measurements of a flow field with large temperature gradients perpendicular to the laser beams. Temperature variations within the flow field results in variations of refractive index through the measurement volume affecting the path of the laser beam which in turn introduces errors in the results obtained from LDA measurements. It should also be noted that the issue with refraction of the laser light from the test section walls becomes even more complicated in case of facilities with curved surfaces/walls. An investigation done by Lowe & Kutt (1992) illustrated the complexities caused by refraction of light from the curved surface of cylindrical tubes and the differing refractive index in the medium which might lead into having multiple images or hidden regions in the measurement field. A method to eliminate the refractive index variations within density-stratified liquid flows was proposed by McDougall (1979). This approach included the application of two solutions with nearly identical refractive indices with significantly different densities. This method of matching the refractive indices of the two fluids removed the loss of laser signal ("drop out") through regions that originally had drastically different refractive indices and enabled the application of LDA technique in the study of stratified flows. Budwig (1994) presented a robust method for eliminating

the refraction of the laser light passing through the test section and/or from the solid walls in experimental fluid dynamics studies. This method involved matching the refractive index of the working fluid and the transparent solid walls within the experimental test section. The research study done by Budwig became the basis for application of MIR technique in fluid dynamic experiments. Ever since, matched index of refraction technique has been implemented in conjunction with LDA, PIV, PTV, and PLIF techniques to visualize the flow field and study the flow behavior within experimental facilities with complicated geometries in different areas such as mechanical engineering, nuclear engineering, chemical engineering, biology, etc.

Table II-2 summarizes the choice of transparent solid material and the working fluid in some of the experimental fluid flow research studies in which MIR technique was applied. Additionally, when applicable, the laser imaging technique used in the experiment is also listed in the table.

Solid	n_S	Liquid	n_L	Optical Technique	Application	Reference
Acrylic	1.49	Mixture of Dow Corning 550 fluid and Dow Corning 200 fluid	-	LDA	Velocity measurement in porous media	Johnston *et al.* (1975)
		Mixture of 73% by weight Dow Corning 505 fluid and 27% by weight Union Carbide L42 fluid	1.4905	LDA	Velocity measurement in porous media	Dybbs & Edwards (1984)
		Mixture of 27% L42 organosilicone fluid (Union Carbide Co.) and 73% 550 fluid (Dow Chemical Co.) by weight	-	PIV	Velocity measurement in porous media	Northrup *et al.* (1991, 1993)
		Mixture of 83% Dow Corning 550 and 556 fluid, 83%/17% by weight	1.4885	PTV	Velocity measurement in porous media	Peurrung *et al.* (1995)
		Mixture of 83% Dow Corning 550 and 556 fluid, 83%/17% by weight	1.4885	PTV	Velocity measurement in porous media	Rashidi *et al.* (1996)
		Saturated solution of Amonium Thiconayante in de-ionized water	-	LDA	Study of the abdominal aortic aneurysms	Egelhoff *et al.* (1999)
		P-Cymene	1.49	LDA	Velocity measurement of a liquid flow in presence of dispersed beads	Haam *et al.* (2000)
		P-Cymene	1.49	PTV	Velocity measurement of solid beads dispersed in liquid	Haam & Brodkey (2000)
		Aqueous solution of NaI (62-64% concentration by weight)	1.49-1.5	PIV	Velocity measurement of an axial turbo-pump	Uzol *et al.* (2001)
		Dibutyl phthalate ($C_{16}H_{22}O_4$)	1.490	PIV	Velocity measurement in porous media	Aziz & Wong (2003)
		Mixture of 80% glycerin and 20% water	1.494	-	-	Bailey & Yoda (2003)
		Mixture of Diethyl Phthalate and Ethanol	-	-	Study of blood flow in cardiovascular models	Nguyen *et al.* (2004)
		P-Cymene	1.491	PTV	Velocity measurements in a packed bed	Hassan & Dominguez-Ontiveros (2008)
		P-Cymene	-	PTV	Velocity and pore geometry measurements in a packed bed	Huang *et al.* (2008)

Table II-2 A review list of the solids and liquids chosen for MIR technique in the literature.

Solid	n_S	Liquid	n_L	Optical Technique	Application	Reference
Pyrex	1.47-1.49	Mixture of 48.5% by weight Dow Corning 556 and 51.5% by weight Dow Corning 550	1.474	LDA	Velocity measurement in porous media	Dybbs & Edwards (1984)
		Mixture of 71.4% by weight Sohio MDI-57 oil and 28.6% by weight mineral seal oil	1.474	LDA	Velocity measurement in porous media	Dybbs & Edwards (1984)
		Mixture of Dow Corning 556 fluid and Dow Corning 550 fluid	-	LDA	Velocity measurement in porous media	Yarlagadda & Yoganathan (1989)
		NaI solution 55% by weight	1.474	PIV	Velocity measurements in a 3-D gas-liquid-solid fluidized bed	Chen & Fan (1992)
		Mixture of ESSO MARCOL 82 and PRIMOL 352	-	PIV	Velocity measurement in porous media	Saleh *et al.* (1992)
		NaI solution 54.5% by weight	-	-	-	Narrow *et al.* (2000)
		Mixture of 81.1% Diethyl Phthalate and 18.9% Ethanol by volume	1.474	-	Study of blood flow in cardiovascular models	Miller *et al.* (2006)
Borosilicate	1.471	Mixture of 32.2% Dow Corning 556 and 67.8% Dow Corning 556 by volume fraction	1.4736	PIV	Measurement of the thickness of the transition layer between a porous layer and its overlaying viscous fluid layer	Goharzadeh *et al.* (2005)
Synthetic fused quartz	1.4584	Tetrathylene Glycol	1.459	-	Velocity and porosity measurements in a packed bed	Stephenson & Stewart (1986)
		Tetrahydropyran-2-methanol	1.458	-	Velocity and porosity measurements in a packed bed	Stephenson & Stewart (1986)
		Mixture of cyclooctane and cyclooctene (9 to 1 by volume)	1.4584	-	Velocity and porosity measurements in a packed bed	Stephenson & Stewart (1986)
		Light mineral oil (Penreco Drakeol #5)	-	LDA	Velocity measurement of a transitional boundary layer behind a roughness element	Stoots *et al.* (2003)
		Mixture of 70.3% Diethyl Phthalate and 29.7% Ethanol by volume	1.4585	-	Study of blood flow in cardiovascular models	Miller *et al.* (2006)
Silicone elastomer	1.41	Mixture of 36.3% Diethyl Phthalate and 63.7% Ethanol by volume	1.41	-	Study of blood flow in cardiovascular models	Miller *et al.* (2006)
FEP	1.33	Water	1.33	PIV	Velocity measurements of turbulent jets in a channel containing a rod bundle	Amini & Hassan (2009)

Table II-2 Continued.

II.2.2.2. Refractive Index Theory

Reflection, refraction, and absorption are the main mechanisms controlling the light propagation through interfaces between different media. Refraction happens when light is passing through a non-homogenous medium or when it goes from one medium to another which results in a change in the light direction. The Refractive Index (or Index of Refraction) of a material (n) is defined as (Hecht 2002):

$$n = \frac{c}{v} \tag{II-2}$$

where c is velocity of the electromagnetic wave in free space (vacuum) and v is the electromagnetic wave velocity in the medium. This ratio shows how much the speed of light or other electromagnetic waves is reduced in that material. Since the speed of light in vacuum is the highest speed possible, it is concluded that $n \geq 1$. The refractive index of gases is normally close to one while it is higher for liquids and solids (in the range of 1.3-3.5).

Refractive index is one of the most important optical characteristics of any material; therefore, precise measurement of this parameter is essential in the field of optics and also for applications such as MIR technique. Various methods have been suggested for measuring the refractive index of solids, liquids, and gases ranging from simple refractive index measurements using refractometers to more complicated techniques to measure refractive index of solid materials or human tissue. Different techniques applied to measure the refractive indices of various types of materials and

their improvements over the past two decades have been summarized in a study done by Singh (2002).

In the early studies performed on refractive index (Gladstone & Dale 1863 and Lorentz & Lorenz 1880), index of refraction was introduced as an invariant parameter. However, more recent studies have indicated that the index of refraction is a function of various parameters, e.g. temperature of the medium, pressure of the medium, and wavelength of the incident light. A research study done by Ashton & Guggenheim (1956) led to introduction of a temperature coefficient to the Lorentz & Lorenz equation for refractive index calculations. Subsequently, the temperature dependence of refractive index of various materials was investigated by different researchers. The results of the experimental study done by Beysens & Calmettes (1977) indicated the temperature dependence of 15 different liquids and emphasized the significant deviation of the refractive index from the value obtained by Lorentz & Lorenz equation under temperature variations. Temperature dependence of refractive indices of acrylic and polycarbonate was represented in studies done by Waxler *et al.* (1979) and Cariou *et al.* (1986). The dependency of the refractive index of water on wavelength, temperature, and density was addressed in an experimental investigation by Thormählen *et al.* (1985). Schiebener *et al.* (1990) developed a formulation for calculation of refractive index of water and steam with respect to changes in wavelength, temperature, and density. Schiebener *et al.*'s (1990) formulation was further revised by Harvey *et al.* (1998).

Table II-3 represents a list of refractive indices of some common materials. The solid materials mentioned in this table are the ones that are frequently used to construct

transparent test facilities for optical measurement techniques. Once the solid material for the test section walls is chosen, the search for a fluid with nearly the same refractive index as that of the solid walls begins. As it is seen in Table II-3, a significant difference exists between the refractive indices of the solids and gases while there are some liquids which possess refractive indices close to that of some of the common solid transparent substances.

Gases†	**n†**	**Liquids††**	**n††**	**Solids††**	**n††**
H_2	1.00013	Water	1.33	FEP	1.33
Air	1.00029	Ethanol	1.362	Fused Quartz	1.4584
He	1.00036	Glycerin	1.47	Pyrex Glass	1.47-1.49
CO_2	1.00045	Mineral Oil	1.48	Optical Glasses	1.45-1.96
		P-Cymene	1.49	PMMA (Acrylic)	1.49
		Diethyl Phthalate	1.504	Polycarbonate	1.58

Table II-3 Refractive indices of some common material.

† At a light wavelength of 589 nm; temperature of 273 K, and standard atmospheric pressure (Tavoularis 2005)

†† Ref: Hassan & Dominguez-Ontiveros (2008)

II.2.2.3. MIR Technique and Fluid Flow Experiments

There are many advantages in using water as the working fluid in fluid flow experiments including: 1- it is the most accessible liquid, 2- its physical and chemical characteristics are well known, 3- its optical characteristics and specifically its refractive index have been comprehensively studied, 4- it does not exhibit any significant chemical reaction with none of the above-mentioned transparent solid materials, 5- it does not show any potential health hazards, 6- it is non-flammable, and 7-it is odorless. As observed in Table II-3, FEP (Fluorinated Ethylene Propylene) has a refractive index close to that of water which at first glance makes it an ideal material for construction of a refractive index matched test facility along with water used as the working fluid. However, there are some issues with the application of FEP in experimental facilities such as low stiffness due to which it cannot be used for construction of parts of the test facility which will undergo extensive forces. Acrylic, fused quartz, Pyrex glass, and polycarbonate are more common materials for construction of transparent test sections and do not have the flexibility problem as transparent FEP does; as a result, they can be used in the construction of the entire test section. The refractive index of fused quartz is lower than that of Pyrex glass, acrylic and polycarbonate; therefore, more fluids and solutions can be found that would have nearly the same refractive index as fused quartz. It should be noted that fused quartz is fragile and this needs to be considered while using fused quartz for construction of test facilities. Pyrex glass is not as widely used as the other transparent solid materials due to its relatively high refractive index and being fragile. Acrylic, on the other hand, is shatter-resistant, reasonably priced, and available

in different shapes and sizes. All these characteristics make acrylic one of the most commonly used transparent solid materials in fluid flow experiments where optical transparency is required. However, the refractive index of acrylic is higher than most of other transparent solid materials mentioned in Table II-3 except for polycarbonate. The main restrictive factor on the application of polycarbonate in construction of transparent test sections is its high refractive index which drastically limits the number of fluids that would match its refractive index. Moreover, polycarbonate has low scratch-resistance characteristics which as well limit its application in the construction of the entire experimental facility. A comprehensive investigation on finding the appropriate working fluids and solid transparent materials for MIR facilities used in the fluid dynamic experiments was carried out during the course of this research study and the results are included in Appendix A.

In the design of the test section for this experiment (see Figure II-1), MIR principles were employed to enhance the capability of the experimental investigations to characterize flow behavior inside the rod bundle without having the effect of the rods obstructing the view. The exterior of the flow channel was constructed with transparent polycarbonate sheets to allow both the passage of the illuminating laser sheets and the acquisition of PIV images. Although Polycarbonate does not exhibit the same refractive index as water, since it only comprises the outer surface of the channel, it does not affect imaging inside the channel. Thus, MIR techniques were used in the selection of a material to simulate rods. FEP tubes were selected for the rod material and the inlet jets since this material possessed an index of refraction nearly identical to that of water;

consequently it does not produce any optical distortion. In this experiment, the laser light frequency and the water temperature were kept constant; therefore, it was assumed that the refractive index of water remained constant through the data collection period.

In total, twenty nine tubes made of FEP material were fixed to the upper and lower surfaces of the test section, near the two inlet jets located on the upper surface of the facility, to simulate the presence of a rod bundle in the jet exhaustion area. It is important to note that FEP tubes were filled with water. This measure was necessary to maintain a constant index of refraction throughout the test facility and to reduce the noise due to reflections and refraction at the interior rod interface. The effect of MIR technique can be distinctly observed when visualizing partially submerged tubes as seen in Figure II-3. Such measures allow flow behavior to be assessed throughout the channel volume by significantly reducing undesirable reflection and refraction and, effectively eliminating the blockage of interior regions by rod structures.

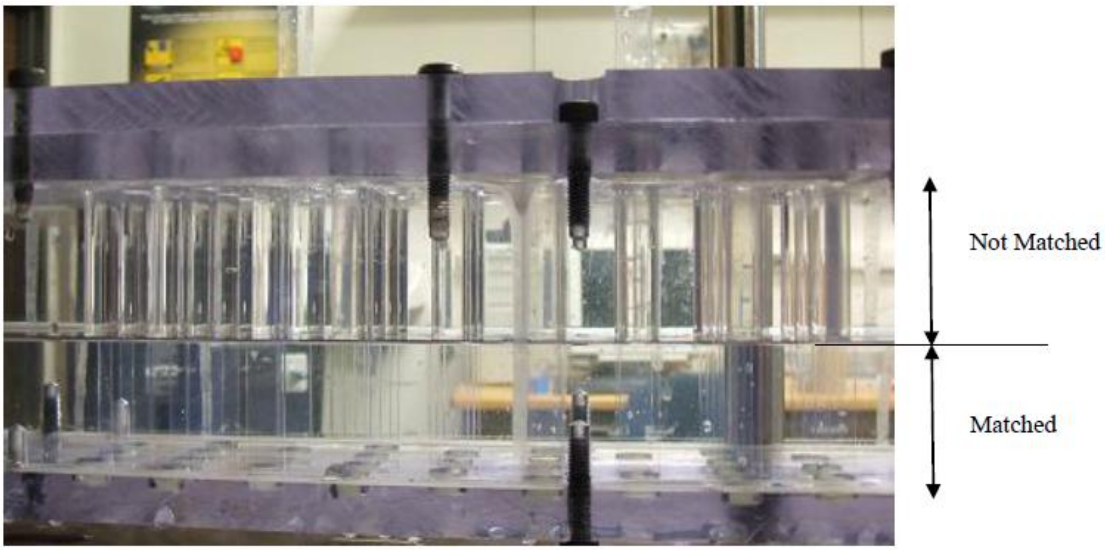

Figure II-3 Picture of the experimental setup illustrating the MIR technique with channel which is half filled.

II.2.3. Particle Image Velocimetry (PIV) Technique

II.2.3.1. Introduction to PIV Technique

PIV is a valuable flow visualization technique to measure the flow velocity since full field velocity measurements can be obtained without disturbing the flow (i.e. the technique is non-intrusive). In PIV, the motion of particles (i.e. – tracers) within a fluid, are tracked to ascertain the motion of the fluid itself. Since it must be assumed that tracers' motion is determined by that of the fluid, tracer particles must faithfully follow the fluid for accurate full-field velocity profiles to be obtained (Raffel *et al.* 1998). In general, these tracer particles may be naturally occurring impurities or, manufactured seeds added to the fluid prior to the experiment. Another superior feature of PIV technique is the ability to measure full-field velocity components. The principles of PIV technique have been explained by Adrian (1991) and Hassan *et al.* (1992), and the development and progression of this technique is described by Adrian (2005).

In PIV, to measure the velocity, two consecutive recorded images are compared at sub-region level through signal processing methods such as cross correlation technique and the particles displacement vectors are obtained subsequently. According to Hassan *et al.* (1992), the binary cross correlation coefficient, $C_{ij,}$ between candidate spot pairs in frames 1 and 2 of Figure II-4 is given by:

$$C_{ij} = \frac{\sum_{y,x=1}^{L} F_1^b \cap F_2^b}{\sqrt{(B_1 \times B_2)}} \qquad \text{(II-3)}$$

where the numerator is the sum of the logical products between the corresponding pixels in the sub-regions of frames 1 and 2 (F_1^b and F_2^b being the binary pixel values in frames 1 and 2, respectively and L being the size of the sub-regions), and B_1 and B_2 show the total number of pixels of binary value 1 in the sub-regions in frames 1 and 2. It should be noted that during the post-processing, the size of the sub-regions was adjusted for each case depending on the Reynolds number and the number of impinging jet.

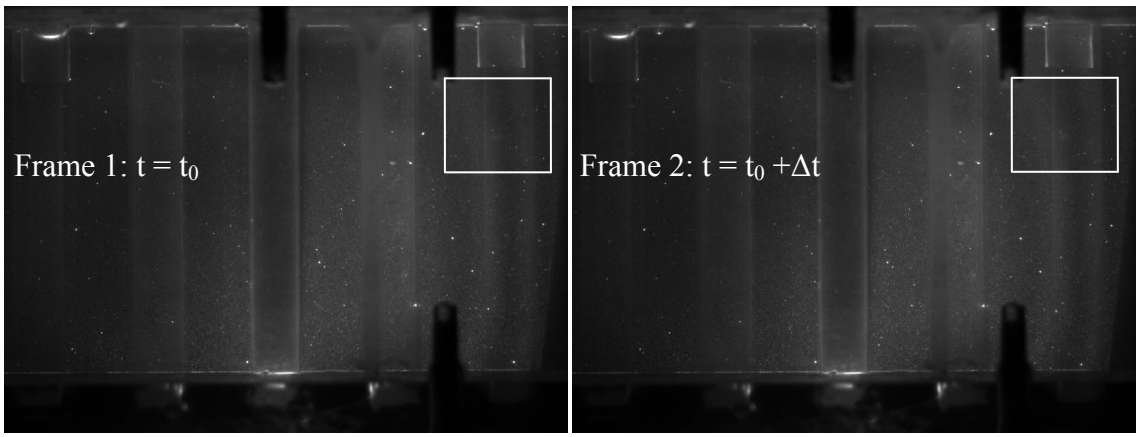

Figure II-4 Two subsequent images illustrating the cross correlation technique.

In this study, a 2-D Particle Image Velocimetry (PIV) technique was used to measure the flow field. In the present investigation, the fluid was seeded with Expancel 091 UD particles with diameters in the range of 6-9μm and specific gravity of 1.05. These tracer particles were specifically chosen because their material density is close to that of water, which assures the tracer particle motion best reflects the actual flow path.

The PIV system consists of several sub-systems including a high power laser which is used as the illumination source and an optical set up consisting of a number of lenses to turn the laser light into a laser sheet. The seeding particles in the fluid scatter

the laser light which is captured by a video acquisition system. In the current experiment, a Nd-Yag laser (New Wave Research, Pegasus PIV, wavelength of 527nm, maximum energy of 20mJ per pulse), served as the illumination source for the PIV system. Illumination from this source was manipulated through the appropriate use of optical instruments (a mirror and three cylindrical lenses) to produce a laser sheet of 1 mm thickness on the channel's bottom wall. This allowed the illumination of planes parallel to the vertical axis. A high speed/high resolution CCD camera (Vision Research, Phantom v7.3, 800×600 pixels, 12 bit) captured images of the illuminated PIV particles at a rate of 1000 frames per second (fps). The camera was oriented perpendicular to the laser sheet direction to acquire video data depicting fluid behavior in the illuminated planes. A system of automatic and manual translation mechanisms were utilized to synchronize the laser plane of illumination with camera focal planes to allow movement of the measuring area within the measuring volume in Z direction. This allowed flow behavior to be evaluated in three different planes parallel to the vertical axis (see Figure II-2).

In this experiment, the CCD camera captured 5,000 images (with a frequency of 1000 fps over a five-second period) for each plane in each case. Then, the acquired data were analyzed through the use of appropriate image processing and PIV analysis techniques. The fore mentioned cross-correlation algorithm was applied to the captured images through the use of a software specifically written for the analysis of the PIV images (Stanislas *et al.* 2008). The results were filtered to remove the erroneous vectors. The final results were imported to TecPlot 360 for visualization and analysis.

II.2.3.2. PIV Error Analysis

Considering the accuracy of PIV, a few different sources contribute to PIV measurement error. First, the experimental set-up and the optical instrument imperfections should be considered such as the flowmeter errors which is ±5% and optical errors due to laser sheet misalignment. The second type of possible error is attributed to the seeding particles, specifically regarding their sizes and how faithfully those particles follow the fluid motion. By choosing seeding particles with a density close to water (specific gravity of 1.05); the particles are expected to follow the fluid motion very well.

Another possible error source is a result of the limited sample size. The mean flow characteristics are calculated by post processing the PIV images. If the number of images or the sample size is not high enough, an error would be caused because of averaging insufficient number of images. In this experiment, 5,000 images have been captured for each set of measurement. To ensure the adequacy of this procedure, the results of averaging 5,000 images were compared to those of 100, 200, …, 500, 1,000, …, 4,500 images of the mid-plane of the test section. Figure II-5 shows the deviation in the average velocity between different sample sizes and the average velocity obtained by averaging 5,000 images for the case of single impinging jet with $Re_{jet\ 1}$=13,400. As seen in the Figure II-5, the smaller the number of the analyzed images, the higher is the difference between the obtained velocity magnitudes from the velocity magnitude calculated by averaging 5,000 images. Figure II-5 represents that the sample size error tends to decrease with increasing the number of images and it goes from 11.8% for 100

images down to 0.45% for 4,500 images. The same trend was observed for all of the other cases; therefore, to have the highest possible accuracy, each test condition was evaluated with 5,000 images.

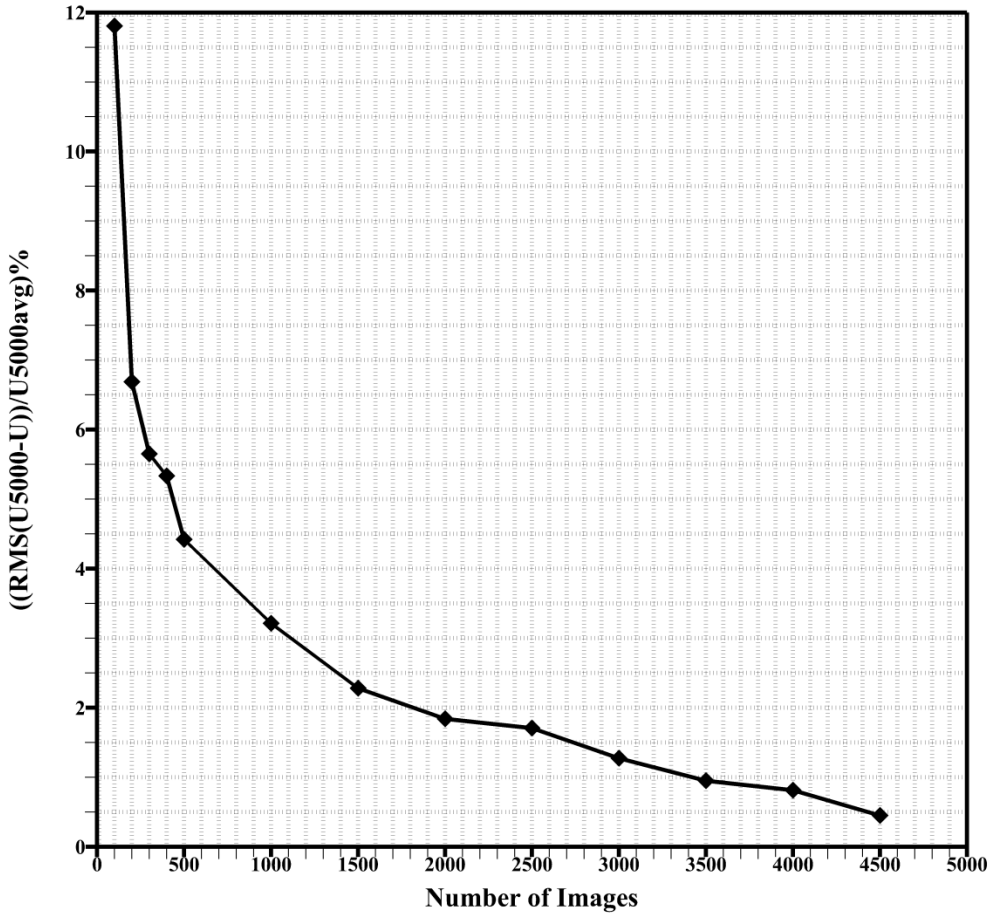

Figure II-5 Effect of sample size on the accuracy of measured velocities when compared to a sample of 5,000 images. Data obtained for the case of single isothermal inlet jet with $Re_{jet\ 1}$=13,400.

An additional source of error arises from the post-processing software's error in analyzing the PIV images. The accuracy of the post-processing software was tested using synthetic images of a 3D shear jet flow obtained from the PIV Standard Image

website (PIV Challenge 2011). The characteristics of the synthetic images used for these tests are shown in Table II-4. The results indicated that the error of the post-processing software is of sub-pixel order which is 0.629 pixel/(time interval) for particles moving with the maximum velocity of 10 pixels/(time interval).

		Unit
Image Size	256×256	$pixel^2$
Area	4×4	cm^2
Laser Thickness	2	mm
Interval	0.005	sec
Maximum Velocity	10	pixel/interval

Table II-4 Characteristics of the synthetic images used for error analysis.

II.2.4. Proper Orthogonal Decomposition (POD) Analysis

II.2.4.1. Introduction to POD Analysis

POD, as an unbiased and powerful technique, has been used to extract the large-scale coherent structures from turbulent flows and to reconstruct lower-order models of the complex flows since 1960's when it was first introduced to turbulent flow concepts by Lumely (1967). Berkooz *et al.* (1993) emphasized the application of POD analysis in the study of all turbulent flows including jet flows. They reviewed the experimental and numerical investigations done on the jet flows and their mixing layers using POD

analysis. In an investigation done by Glauser *et al.* (1987), POD analysis was applied to the velocity data of the near-field of an axisymmetric jet mixing layer obtained by hot wire anemometry. The results show that the primary mode contains 40% of the turbulent kinetic energy of the field which corresponds to a large scale coherent structure in the mixing layer of the jet. The next two modes approximately contain 40% of the energy; therefore, the flow field could be accurately reconstructed using the first three modes. Sullivan & Pollard (1996) used hot wire anemometry technique to obtain data from the near field of a three-dimensional wall jet. The flow field data was further analyzed using POD, Linear Stochastic Estimation (LSE), Gram-Charlier Estimation (GCE), and Wavelet Decomposition (WD) methods. It has been shown that POD helps to extract underlying turbulent structures in the wall jet flow. Citriniti & George (2000) applied POD technique to the ensemble velocity field obtained by hot-wire anemometry from a turbulent round jet nozzle. As a result of using POD analysis, the small-scale structures which obstruct viewing the large-scale turbulent structures get filtered; therefore the evolution of the large-scale structures is presented more clearly. Reconstruction of the velocity field with the first five azimuthal modes shows the existence of counter-rotating streamwise vortex pairs which advect the high velocity from the core and also advect slow moving fluid from the low-speed outer layers of the jet to the core. In a study done by Gordeyev & Thomas (2002), POD technique was applied to the self-similar region of a turbulent planar jet obtained by multiple X-probe arrangements to study the behavior of large-scale flow structures in this region. They suggested that it is possible to

reconstruct a realistic low-dimensional model of the jet using POD technique due to the rapid energy convergence of the POD modes.

One of the first investigations which employed both PIV and POD techniques to study the jet flows was done by Bernero & Fiedler (2000) in which the characteristics of a jet in a counterflow was studied. The analysis was carried out for the cases of low and high velocity ratios and the transition between stable and unstable flow conditions. They concluded that the key features of the flow were better represented using energy POD than that obtained by vorticity POD. In another study by Patte-Rouland *et al.* (2001), PIV and POD techniques were applied to the velocity fields of the recirculation zone of an annular jet having Reynolds numbers of 2048 and 7680. The results of the POD analysis show that the first four modes contain the majority of the energy of the flow field and that each mode has a specific effect on the nature of the flow, location of the stagnation point, and the organization of the recirculation zone of the annular jet.

Maurel *et al.* (2001) studied the application of POD method to analyze the jet/vortex interactions in a square model engine cylinder. The analysis is focused on the central vertical region of the jet flow. It has been shown that the space–time correlation between different flow patterns can be captured experimentally using POD method. Bi *et al.* (2003) used time-resolved PIV and POD methods to study the characteristics of coherent structures forming around a turbulent round jet. POD analysis educes the most energetic flow structures and clearly represents their spatial- temporal evolution in the mixing layer of the jet. In a paper by Kim *et al.* (2007), PIV technique was used to study the characteristics of a confined slot jet impinging on a flat plate. The range of Reynolds

numbers used in this experiment varied from 404 to 1026 which puts the flow in the transient regime. The results confirmed the appearance of vortical structures in the shear layer and also the transition of the flow from steady to unsteady regime when the Reynolds number increases beyond Re=404.

Meyer *et al.* (2007) obtained the velocity fields of a jet in crossflow using Stereoscopic PIV and consequently analyzed the PIV results by snapshot POD method. The experiment was carried out with two different velocity ratios of jet to crossflow velocity, R=3.3 and R=1.3 for a Reynolds number of 2400 defined based on crossflow velocity and the pipe diameter. It has been found for R=3.3 that the first two POD modes have a higher energy than the other modes and the wake vortices are the dominant flow patterns which strongly interact with the jet core. However, for R=1.3 case, the jet shear-layer vortices are much more dominant than the wake vortices. In a study by Merzari & Ninokata (2009), Large Eddy Simulation (LES) was used to simulate the axial turbulent flow (Re=6,400) in a tight triangular lattice rod bundle (P/D=1.05). POD method was applied to study the three-dimensional flow patterns and especially the large-scale periodic oscillations observed in the tightly packed rod bundle configurations. The results show that the velocity profile presents multiple wavelengths (short and large scale wavelength) and also the velocity profile in each gap is different from the others. The results confirm that the coolant flow is more complex in a rod bundle than flow in a channel.

Conventional PIV technique with its high spatial resolution helps in obtaining the 2D velocity field of a turbulent flow which could later be further analyzed applying POD

techniques. However, this technique does not have the high temporal resolution needed for POD to investigate the behavior of high frequency turbulent flow patterns. With the recent development in the camera technology and production of cameras having frame rates in the order of KiloHertz, a new technique called Dynamic PIV (DPIV) has emerged benefiting from improved temporal resolution compared to normal PIV. DPIV solves the low temporal resolution problem of conventional PIV for POD applications.

II.2.4.2. Mathematical Background for POD Analysis

In 1967, Lumley suggested the application of the POD technique to analyze the turbulent flows and to identify large-scale coherent structures in turbulent velocity fields. In POD, the velocity field is decomposed into a finite expansion of orthonormal functions or eigenfunctions (Φ_n) and orthonormal amplitude coefficients a_n :

$$V(x,t_n) = \sum_{n=1}^{N} a_n(t)\,\Phi_n \qquad \text{(II-4)}$$

Sirovich (1985) introduced a time-efficient method to carry out the POD analysis which is called Snapshot method. This method works best for cases in which the spatial resolution of the flow field is much higher than its temporal resolution which is normally the case for PIV data. The Snapshot POD method greatly reduces the computation time of the eigenfunctions; therefore, enables the analysis of the large velocity fields. Each instantaneous PIV velocity field is known as a snapshot of the flow. It should be noted that the POD analysis is often carried out using the fluctuating part of the velocity component (u, v, w) and the mean velocity field which is often called the zeroth POD

would only be added to the POD results when the velocity fields are being reconstructed using the POD modes.

Now if each instantaneous PIV fluctuating velocity field (i.e. snapshot) is represented as:

$$v^{(n)} = v(x, t_n) \tag{II-5}$$

Therefore, the Kernel of the velocity field or the two-point time-averaged correlation function for cases where the number of snapshots (N) is sufficiently high is:

$$K(x, x') = \frac{1}{N} \sum_{n=1}^{N} v^{(n)}(x) v^{(n)}(x') \tag{II-6}$$

The Kernel is degenerate; therefore, it has eigenfunctions of the form:

$$\Psi = \sum_{k=1}^{M} A_k v^{(k)} \tag{II-7}$$

In which the constants A_k need to be estimated. Then the eigenvalue problem would be of the form:

$$CA = \lambda A \tag{II-8}$$

where

$$A = (A_1, ..., A_M) \tag{II-9}$$

The k-th eigenvector A_k corresponds to the eigenvalue λ^k of C. The components of the temporal correlation matrix C_{ij} are given as:

$$C_{mn} = \frac{1}{M} (v^{(m)}, v^{(n)}) \quad ; m, n = 1, ..., M \tag{II-10}$$

C is a symmetrical matrix and therefore all the eigenvalues are real and positive numbers. The eigenvalues are organized in descending order as $\lambda^k \geq \lambda^{k+1}$ so that the first POD eigenvalue has the most energy. The magnitude of these eigenvalues is an indication of the kinetic energy of the modes and the total energy of the system is represented by the sum of all of the eigenvalues.

$$E = \sum_{k=1}^{M} \lambda^k \tag{II-11}$$

The relative energy stored in each mode is shown as

$$E_k = \lambda^k / E \tag{II-12}$$

Now the POD modes (eigenfunctions) can be obtained using the eigenvectors of Eq. II-8:

$$\Phi^i = \frac{\sum_{n=1}^{N} A_n^i V^n}{\left\| \sum_{n=1}^{N} A_n^i V^n \right\|} \tag{II-13}$$

The POD modes can be arranged as:

$$v^n = \sum_{i=1}^{N} a_i^n \Phi^i \tag{II-14}$$

The amplitude coefficients or the POD coefficients are calculated as follows:

$$a^n = \Psi^T v^n \tag{II-15}$$

Finally snapshots of the flow field can be reconstructed as:

$$v^n = \sum_{i=1}^{N} a_i^n \Phi^i \tag{II-16}$$

In POD analysis, the most energetic modes are the principle modes which can be used to represent the most energetic coherent structures, i.e. the large-scale coherent

structures, of the flow field. Therefore, the large-scale structures of the flow field would be captured by the first few POD modes; therefore a snapshot reconstructed by the first few modes would satisfactorily represent the original flow field. On the whole, it can be said that the POD method helps to make a low-dimensional model of the real velocity field which represents most of the characteristics of the coherent structures. POD analysis can be applied to flow fields obtained either experimentally or numerically.

II.2.4.3. POD Sample Size Analysis

The temporal resolution of the POD analysis is determined by the number of snapshots chosen to reconstruct the velocity or the vorticity fields. Therefore, choosing the right number of snapshots enables accurate calculation of the eigenfunctions. Following the change in the energy of the eigenvalues and their convergence with the number of snapshots shows that the sample size needs to be large enough for the statistical data obtained by POD to be valid. Figure II-6 shows the change in the eigenmodes' energies by increasing the number of snapshots for the first ten eigenmodes. As it is seen in Figure II-6, for most of the eigenvalues, there is not much of a difference in the energy of the eigenmodes when the number of snapshots is greater than 1000. Therefore, in this study, to optimize both the temporal resolution and the computing time, 1000 snapshots are used in order to carry out the POD analysis.

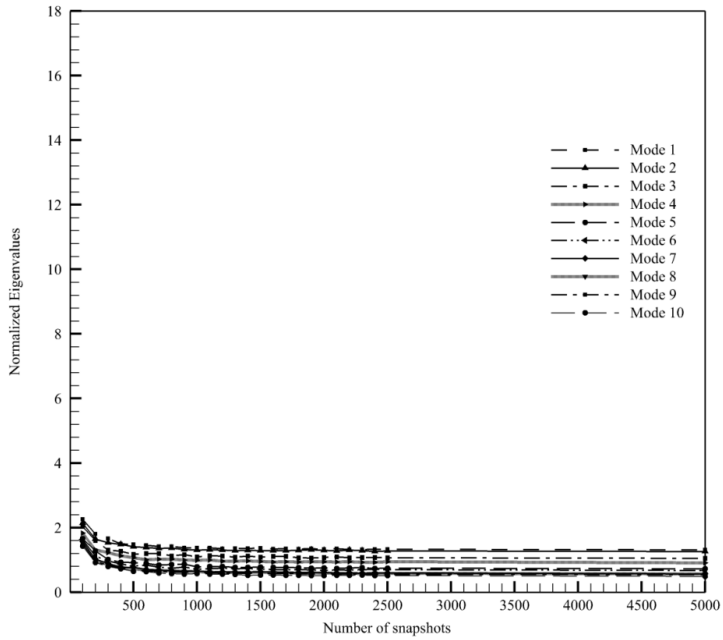

(a)

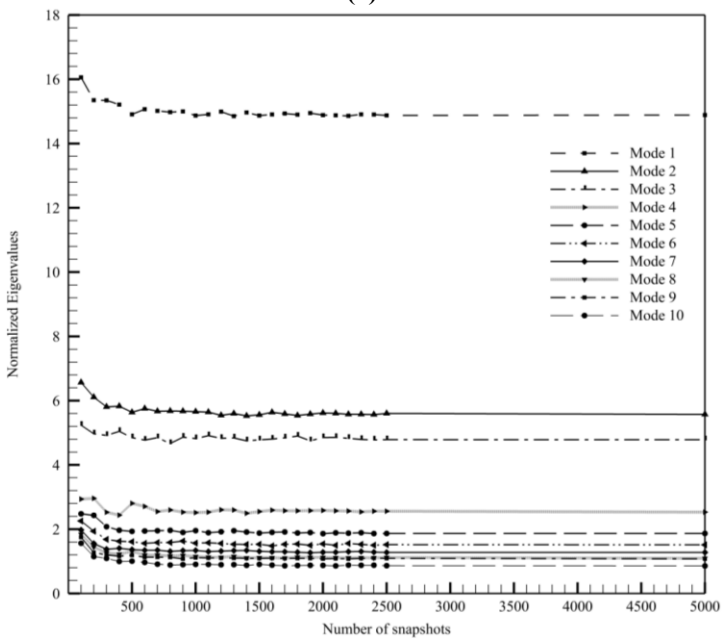

(b)

Figure II-6 Effect of sample size on calculated eigenvalue energy for the first ten eigenvalues (a) single isothermal inlet jet with $Re_{jet\ 1}$ = 4470, (b) single isothermal inlet jet with $Re_{jet\ 1}$ = 13,400, (c) dual isothermal inlet jets with $Re_{jet\ 1}$=11,160 and $Re_{jet\ 2}$= 6,250.

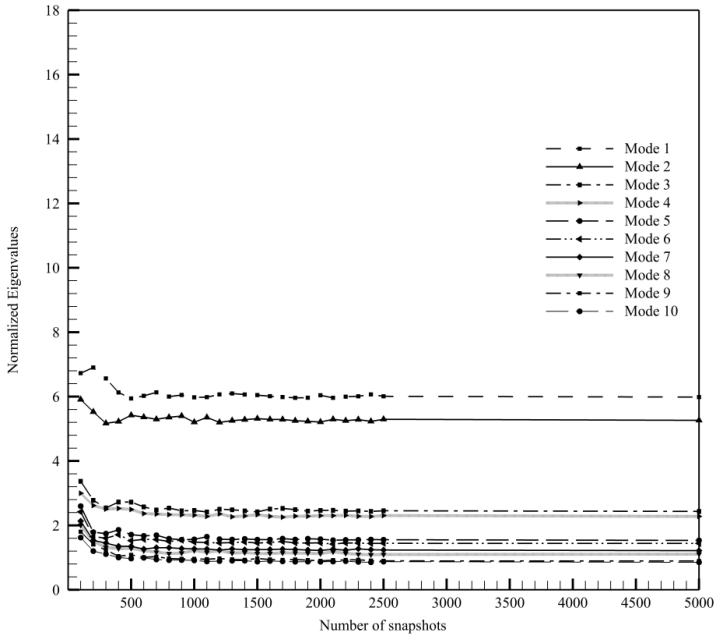

(c)

Figure II-6 Continued.

II.3. Results

As it was mentioned earlier in the Experimental Methodology section, the experiment was performed for several cases with single and dual inlet jets impinging into the channel with various Reynolds numbers as well as cases with dual inlet jets impinging into the channel having crossflow. The results containing instantaneous and time-averaged velocity fields, instantaneous vorticity fields, line-probes of velocity and different velocity statistics at different heights of the channel and different measurement planes, as well as the results of the POD analysis for coherent structure identification within the flow field are presented in the following sections.

II.3.1. Time-Averaged Velocity Fields

The time-averaged velocity fields were obtained for three discrete planes throughout the interrogation domain for each of the test cases mentioned in Table II-1. For better clarification of the differences between various cases, the results representing the time-averaged velocity fields are represented in the following sub-sections.

II.3.1.1. Single Impinging Jet in the Corner of Mid-Plane

In this case, a single inlet jet (Inlet Jet 1) was injecting into the bundle. The time-averaged velocity fields were obtained for three discrete planes throughout the interrogation domain for each of the selected inlet jet Reynolds numbers. Figure II-7 depicts the average velocity fields obtained for a single isothermal inlet jet discharging into the mid-plane for two different Reynolds numbers. The white lines in the figure represent the streamtraces calculated by means of Tecplot 360 which help to identify flow structure. The velocity vectors are shown in black and are overlaid on a contour map which describes the Y-velocity component.

As seen in both Figure II-7 (a) and Figure II-7 (b), a discontinuity is observed in the upper section of the jets' velocity profiles. This can be attributed to undesired laser reflections at these locations. The data obtained for those regions was omitted, since it had no effect on the rest of the results. It is possible to interpolate the data during post-processing and obtain the velocity profile in the excluded regions; however to maintain the integrity of the raw data, no data interpolation, approximation, or smoothing was performed.

Both of the plots in Figure II-7 show a well-defined radial velocity gradient, with the maximum velocity at the jet's core and decreasing velocity in radial direction. In both cases the streamtraces on both sides of the jet are seen to shift toward the jet which indicates the jet entrainment process through its shear layer. Additionally, the higher Reynolds number jet (Figure II-7 (a)), the jet maintains its highest velocity core further into the channel than the lower Reynolds number jet (Figure II-7 (b)).

In both cases a recirculation zone is identified on the right hand side of the center rod; however, the size and the location of these recirculation zones are different from one case to another. In the higher Reynolds case, the recirculation zone appears at a lower height and closer to the center rod and displays a stronger recirculation than the lower Reynolds number jet. In Figure II-7 (a), there are two other recirculation zones observed on the left hand side of the center rod which are not present in Figure II-7 (b). The time-averaged velocity fields for the impinging jets with the same Reynolds numbers are presented in a paper by Amini *et al.* (2008) although it should be mentioned that those velocity fields are obtained by averaging over 500 images. It is seen that for each of the cases, the recirculation zone on the right hand side of the center rod is identified either by averaging over 500 images or by averaging over 5000 images. However, a significant difference is observed in the number and the size of the recirculation zones observed on the left hand side of the center rod as a result of the sample size. When averaging 5,000 images, the two key recirculation zones previously mentioned are present on the left hand side of the center rod, but when the velocity field is obtained by averaging 500 images, three small vortices appear in the same region.

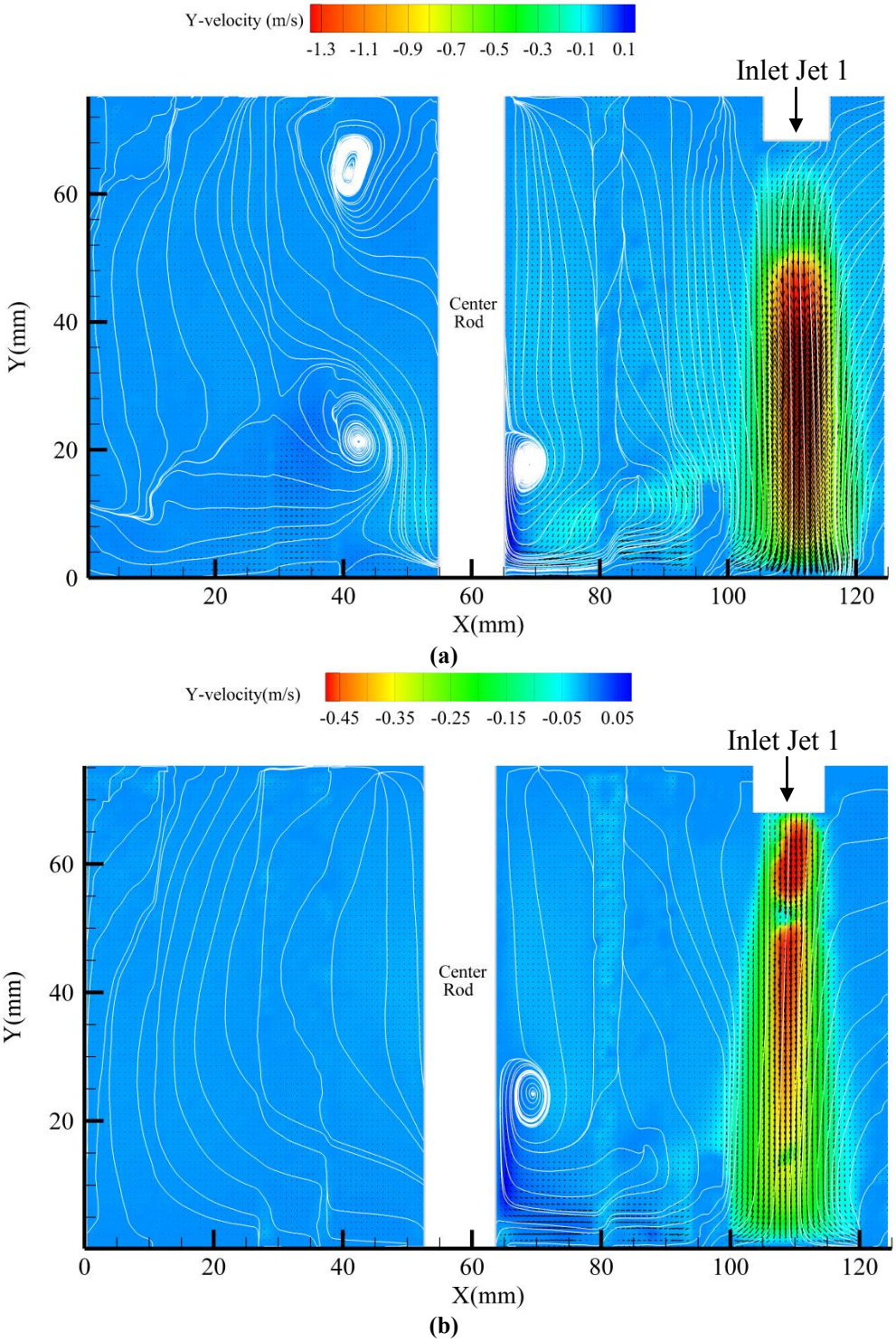

Figure II-7 Time-averaged velocity field, the contour plot of the Y-velocity component and the streamlines along the vertical mid-plane for a single isothermal inlet jet with (a) $Re_{jet\ 1}$=13,400, (b) $Re_{jet\ 1}$=4,470.

II.3.1.2. Single Impinging Jet in the Middle of the Measurement Plane

The flow pattern observed in velocity fields of the single impinging jets presented in the previous section and the asymmetry of the flow field between the impingement side and the other side of the center rod raised a few important questions such as: Is the recirculation zone observed close to the center rod actually created as a result of the jet/rod interaction or it could have happened on the other side of the center rod as well? Would another recirculation happen on the other side of the jet close to the other adjacent rod which is not captured in these images? Is the strength and position where the main recirculation zone is created directly depends on the jet Reynolds number and the distance of the jet from the bottom surface of the channel (the impingement plate)? To find an answer for these questions, a different geometry of the impingement plane is considered in which the jet is located in the middle of the measurement planes with two rods symmetrically places at each side of the jet. For this case, experiments have been carried out with two different Reynolds number of the jet and different jet to impingement plate distance in order to acquire a better understanding of the evolution of jet itself (spreading and decay of the center line velocity) as well as the potential effect of the jet/rod interaction on the formation and characteristics of the main recirculation zone observed close to the adjacent rod (see Figure II-7). It should be mentioned that the velocity fields presented in Figure II-8 are obtained using an in-house Particle Tracking software (Estrada-Perez 2004).The average error of the software for velocity calculation was reported as 0.1 (pixel/Δt) by Estrada-Perez & Hassan (2010). In all three plots of Figure II-8, the white lines represent the streamtraces calculated by

means of Tecplot 360 which help to identify the key flow structure within each velocity field. The velocity vectors are shown in black and are overlaid on a contour map of the Y-velocity component.

It is seen from all three plots of Figure II-8 that the key recirculation zone observed in the vicinity of the adjacent rod to the jet in Figure II-7 is present here close to both rods located at each side of the jet for all cases with different Reynolds numbers of the jet and different distances between the jet exit plane and the impingement plane. This actually supports the idea that the recirculation zone is created as a result of the interaction between the jet flow and the neighboring rod. However, no direct conclusion can be made from these plots regarding the effect of the jet Reynolds number on the size or location of the recirculation zones. Some of the flow features that have been notices in Figure II-7 are also present here and are even more clearly seen because of the symmetry in the flow field as well as the fact that more of the area surrounding the jet is captured in these measurements. For instance, the entrainment of the channel flow by the jet is better represented in these plots since both sides of the jet are equally captured in the flow field. For all cases shown in Figure II-8 (a) and (b) in which jet has a larger distance from the impingement plate, entrainment begins approximately from the top part of the channel and the streamtraces on both sides of the jet are drawn towards the jet. However, in Figure II-8 (c) the streamtraces, especially on the left-hand side of the jet, are not as drastically shifted towards the jet compared to the two previous cases.

One of the interesting flow patterns that is clearly seen in the plots of Figure II-8 is the flow structure created at each side of the jet as a result of the interaction between

two phenomena that are simultaneously present at each side of the jet -jet entrainment which is pulling the streamtraces towards the jet and the recirculation zone close to the neighboring rod which is in turn attracting the streamtraces towards itslef-. This interesting flow feature which is created due to the separation of the streamtraces close to the bottom surface of the channel is present in both sides of the jet for all cases and is called *"Separation Region"* hereafter.

A comparison between Figure II-8 (a) and Figure II-8 (b) indicates that the jet maintains its high velocity core region up to a further distance into the channel in case of the higher Reynolds number jet (Figure II-8 (a)). Furthermore, in case of jets with identical Reynolds numbers and different jet to impingement plate distance (Figure II-8 (b) and (c)), it is observed that the jet flow in Figure II-8 (a) loses its high velocity at the core region as it travels further downstream on the channel and has a relatively lower velocity while hitting the channel bottom surface (this phenomenon is called decay of the center line velocity of the jet); however, in case of the jet flow in Figure II-8 (c) where the jet to impingement plate distance is much shorter, the jet flow maintains its high velocity at the core region nearly until it reaches the channel bottom plate and interact with the bottom plate of the channel with a much higher velocity and momentum compared to the jet in Figure II-8 (b). Therefore, the jet to impingement plate distance is one of the most important criteria that needs to be considered in the design process in order to avoid structural damage to the nuclear graphite comprising the bottom surface of the lower plenum of a VHTR or any other impingement plate in other facilities including impinging jets.

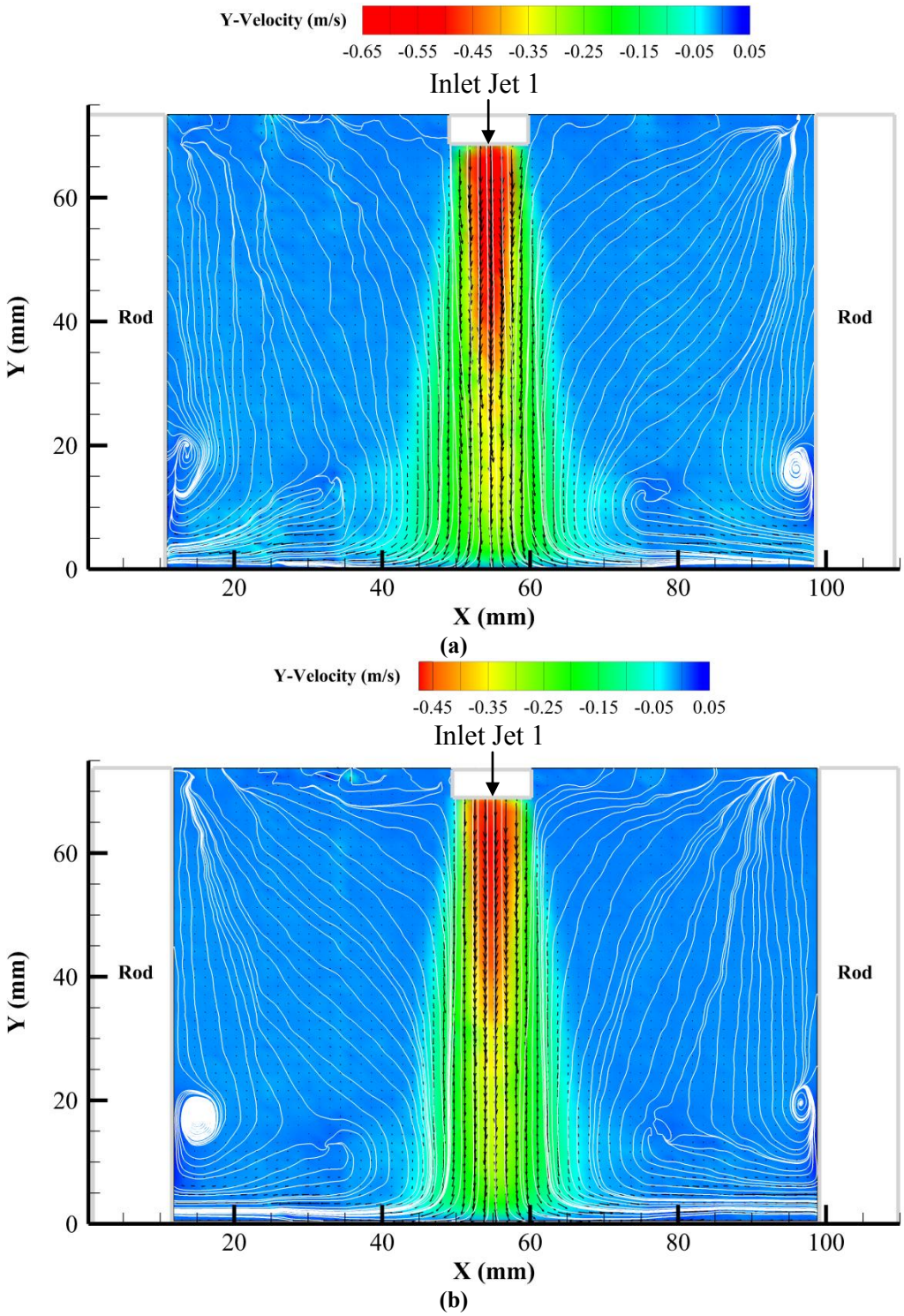

Figure II-8 Time-averaged velocity field, the contour plot of the Y-velocity component and the streamlines along the vertical mid-plane for a single isothermal inlet jet for (a) jet up with $Re_{jet\ 1}$=6,700, (b) jet up with $Re_{jet\ 1}$=4,470, (c) jet down with $Re_{jet\ 1}$=4,470.

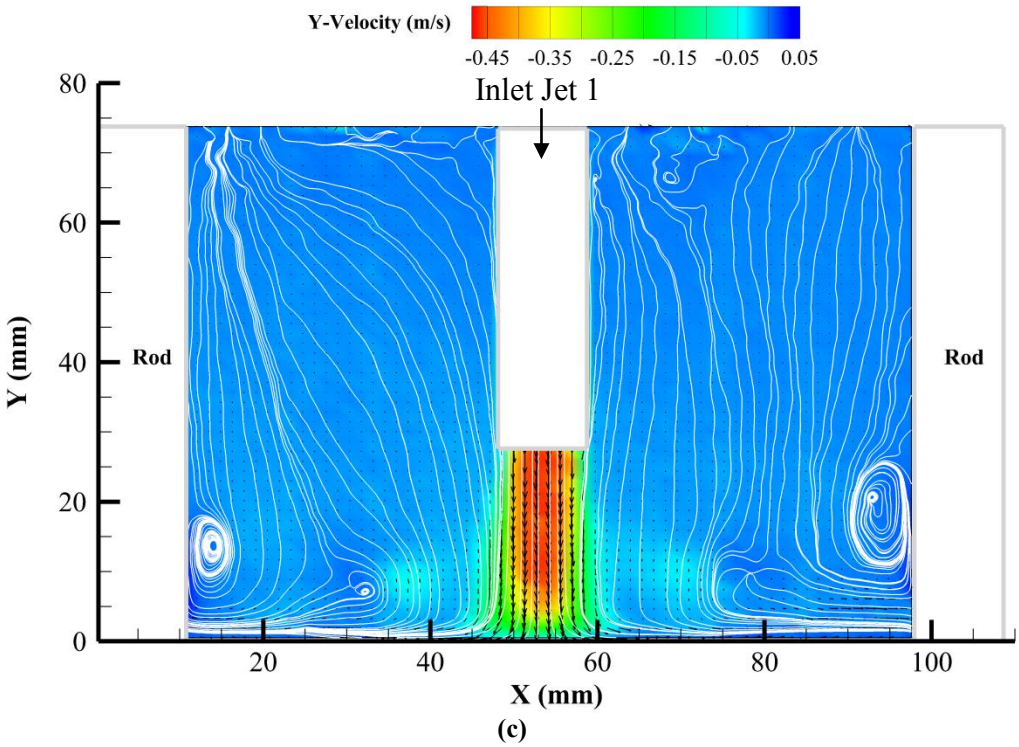

(c)

Figure II-8 Continued.

Another flow pattern that is distinguished in all plots of Figure II-8, is the flow structure created by the sidewise and slightly upward distribution of the jet flow after hitting the bottom surface of the channel. This flow feature is observed on both sides of jet in the two-dimensional PIV velocity fields and is more pronounced in the case of the higher Reynolds number jet (Figure II-8 (a)) and the lower Reynolds jet with smaller jet to impingement plate distance (Figure II-8 (c)). Moreover, for all the three jet flows represented in Figure II-8, the radial distribution of the jet flow as it travels further down into the channel follows the same pattern observed for the jet flows in Figure II-7 meaning that at each vertical distance from the jet exit plane, the jet's core has the highest velocity and as the jet spreads out the velocity decreases in the radial direction.

II.3.1.3. Dual Impinging Jets within the Mid-Plane

In this case, both inlet jets (Inlet Jet 1 and Inlet Jet 2) impinged into the channel, each with a different Reynolds number. As in the case of the single jets, the time-averaged velocity fields were developed for three different planes within the interrogation volume for each of the inlet jet conditions. Figure II-9 depicts the time-averaged velocity field for one test case, with white streamtraces showing the important features of the flow. Again, the black arrows represent the velocity vectors which are overlaid on a contour map of the Y-velocity component.

Contrary to the discontinuity observed in Figure II-7, Figure II-9 shows that both inlet jets velocity profiles were completely captured using the PIV technique. It should also be asserted that in this case the time-averaged velocity field has been presented without any data interpolation, approximation or smoothing.

For both of the jets in Figure II-9, a well-defined velocity gradient is observed in each of them, showing a maximum velocity at the jet's core and decreasing in the horizontal direction. It can also be observed that the streamtraces on left hand side of the higher Reynolds number jet and the streamtraces on right hand side of the lower Reynolds number jet are shifted towards the jets while the streamtraces on the left hand side of the lower Reynolds number jet are shifted towards the left hand side of the picture where the channel outlet is located. The camera lens was not able to capture information to the right of the higher Reynolds number jet and thus the streamtraces could not be identified in that region. However, if the streamtraces in this section follow the same pattern as the streamtraces of the single jet case, they are expected to be pulled

towards the jet. Furthermore, as it is presented in Figure II-9, the higher Reynolds number jet maintains its highest velocity core up to a higher depth of the channel from the inlet jet exit than the lower Reynolds number jet. Most of the above mentioned observations reflect the remarks made about the single jet cases.

Two recirculation zones of different sizes are detected on either side of the center rod; however, the locations of these recirculation zones differ from one jet to the other. The recirculation zone on the right hand side of the center rod appears slightly higher and farther from the center rod and is stronger when compared to the left hand side recirculation zone. These observations resemble those of the single jet excepting a few key differences. A brief evaluation of both Figure II-9 and Figure II-7 indicates that the size of the recirculation zones on the adjacent rod of an impinging jet is directly related to the Reynolds number of the jet. However, no such statement could be made about the dependence of the location of the recirculation zone on the Reynolds number of the jet. As mentioned before, in Figure II-7 the recirculation zone of the single impinging jet with a higher Reynolds number occurs at a lower height and closer to the adjacent rod than the lower Reynolds number case, while in Figure II-9 the recirculation zone adjacent to the higher Reynolds number jet appears at a higher height and farther from the adjacent rod compared to the lower Reynolds number jet. The discrepancy in the location of the recirculation zones between the cases of a single jet and the case of the dual impinging jets may be a result of the interaction between the two jets. In that case, additional dual jet flows must be studied to verify any corresponding relationship.

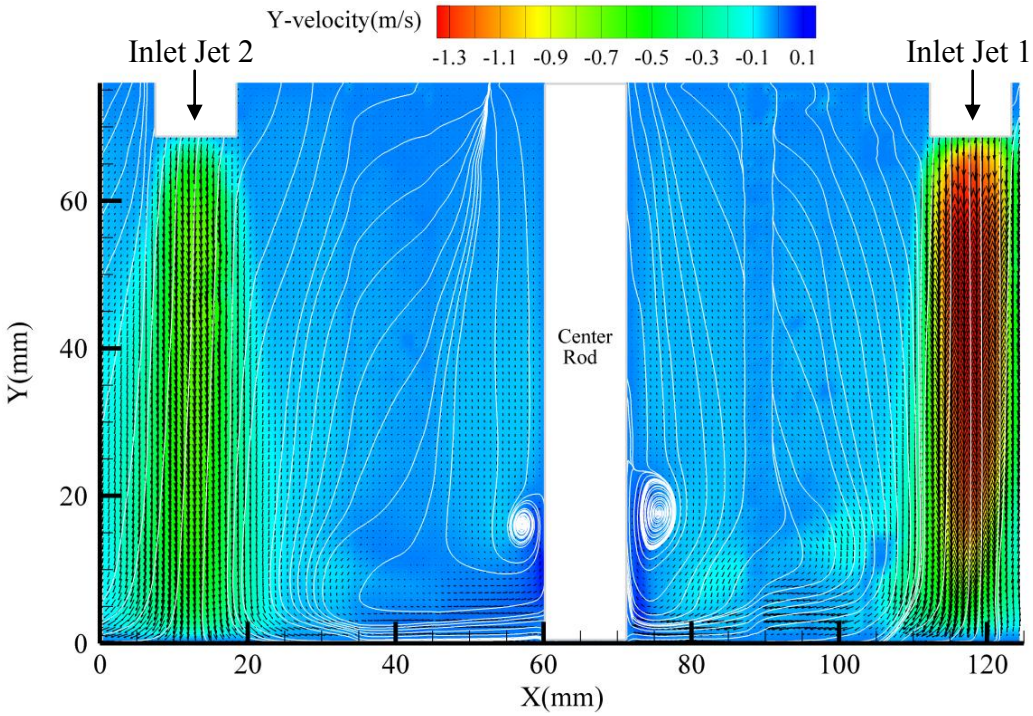

Figure II-9 Time-averaged velocity field, the contour plot of the Y-velocity component and the streamlines along the vertical mid-plane for two isothermal inlet jets with different Reynolds numbers $Re_{jet\ 1}$=11,160 and $Re_{jet\ 2}$=6,250.

II.3.1.4. Dual Impinging Jets with Crossflow within the Mid-Plane

Figure II-10 represents the time-averaged velocity fields for the case of dual jets injecting into the channel having crossflow. This case is rather important since the crossflow here represents the crossflow exerted on the coolant jet flows in the lower plenum of a VHTR. The crossflow in the lower plenum of a VHTR is formed by the coolant flows injecting into the lower plenum from the jets located before a certain jet as the coolant flow eventually converges to a single outlet. Therefore, each jet encounters a different crossflow velocity depending on its location with respect to the outlet of the plenum. In this case, the idea was using a very general test case with twin jets having different Reynolds numbers injecting into a channel containing a rod bundle with crossflow passing through it. It is worth mentioning that the Reynolds number of the crossflow is calculated based on water dynamic viscosity, crossflow velocity, and the height of the channel. The time-averaged velocity field for this case is represented in Figure II-10. It should be mentioned that the crossflow velocity field presented in Figure II-10 is obtained using an in-house Particle Tracking software developed by Estrada-Perez (2004) which has an average error of 0.1 (pixel/Δt) for velocity calculations (Estrada-Perez & Hassan 2010). The Reynolds numbers of the jets are chosen to be close to those of the jets in the dual impinging jets case represented in Figure II-9 in order to better see and more easily compare the influence of the crossflow on the jets evolution with respect to the case without crossflow (Figure II-9). In this figure, the white lines represent the streamtraces calculated by means of Tecplot 360 which help to identify the

key flow structure within the velocity field. The velocity vectors are shown in black and are overlaid on a contour map of the Y-velocity component.

The streamtraces on the far left side of the velocity field in Figure II-10 clearly represent the crossflow in the channel in the left to right direction. However, as soon as it approaches the higher Reynolds jet (Inlet Jet 1), entertainment in the shear layer of the jet changes the horizontal direction of the crossflow to some extent, specifically in the lower parts of the channel and the jet. The interaction of the jet with crossflow on the other hand affects the jet evolution while going downstream in the channel in different ways which become more clear if the jet in crossflow is compared to the higher Reynolds jet in Figure II-9 where there was no crossflow. It should be noted that the Reynolds number of the higher Reynolds jet in both Figure II-9 and Figure II-10 are the same which provides the basis for a better comparison of the behavior of the jets. First, the jet in crossflow loses its high velocity core much faster than the jet without crossflow. Secondly, in the crossflow case the velocity profile of the jet is more spread out especially in the crosflow direction. The jet in crossflow is more spread out on its right-hand side compared to the jet with no crossflow which is quite symmetrical on both sides. The trail of the higher Reynolds number jet in cossflow is seen in the flow field approximately until it reaches the recirculation zone in the vicinity of the center rod on the higher Reynolds jet. It seems like the effect of the crossflow is so dominant on the jet that it has pushed the jet in its own direction in a way that no effect of jet entrainment is seen on the right-hand side of the jet and that part of the jet is inclined in the direction of the crossflow. Therefore, the *"Separation Region"* that was previously observed due

to the interaction between the jet entrainment process and the recirculation zone is not seen here. A comparison between the directions of the streamtraces at the right-hand side of the higher Reynolds number jet in Figure II-9 and Figure II-10 further clarifies this point. Moreover, it looks like the presence of the crossflow and the addition interaction of the crossflow with the center rod (in addition to jet/rod interaction) creates an even larger recirculation zone close to the center rod. It should be noted that at this point no general conclusion can be made with regards to the effect of the crossflow on the size and location of the recirculation zone created close to the center rod. Further, investigation and analysis with different combinations of jet to crossflow velocities is needed for such conclusions to be made.

The effect of the crossflow on the lower Reynolds number jet and the flow field on the right hand side of the center rod is even more drastic. Figure II-10 shows that even with the presence of the crossflow, the key recirculation zone still exists on the right hand side of the center rod and that even the dominant effect of the crossflow was not capable of eliminating this flow feature. The lower Reynolds jet especially from Y= 60 mm downwards is strongly pushed to the right (in the direction of the crossflow). This becomes more noticeable while comparing the evolution of this jet compared with the approximately axisymmetric evolution of the lower Reynolds jet in vertical direction in Figure II-9. Unfortunately, the area on the right-hand side of the lower Reynolds jet is not fully covered by the camera view; therefore, no further observation can be made for the behavior of the jet on that side. The phenomenon that is particularly significant in this part of the flow field is the existence of a large recirculation area close to the bottom

surface of the channel between the main recirculation zone on the right-hand side of the center rod and the lower Reynolds number jet. In the previous cases, the flow pattern called *"Separation Region"* was observed around this area. However, it appears that in this case the interaction of the crossflow which is in the right direction with both the downward direction of the jet which is also deviated to the right in this case with the recirculation zone on the right hand side of the center rod creates a relatively large recirculation zone in that area. The presence of this additional recirculation zone along with the other two recirculation areas at each side of the center rod and other vortical structures that exist all over the measurement plane will help in enhancement of the mixing between the jets and the crossflow.

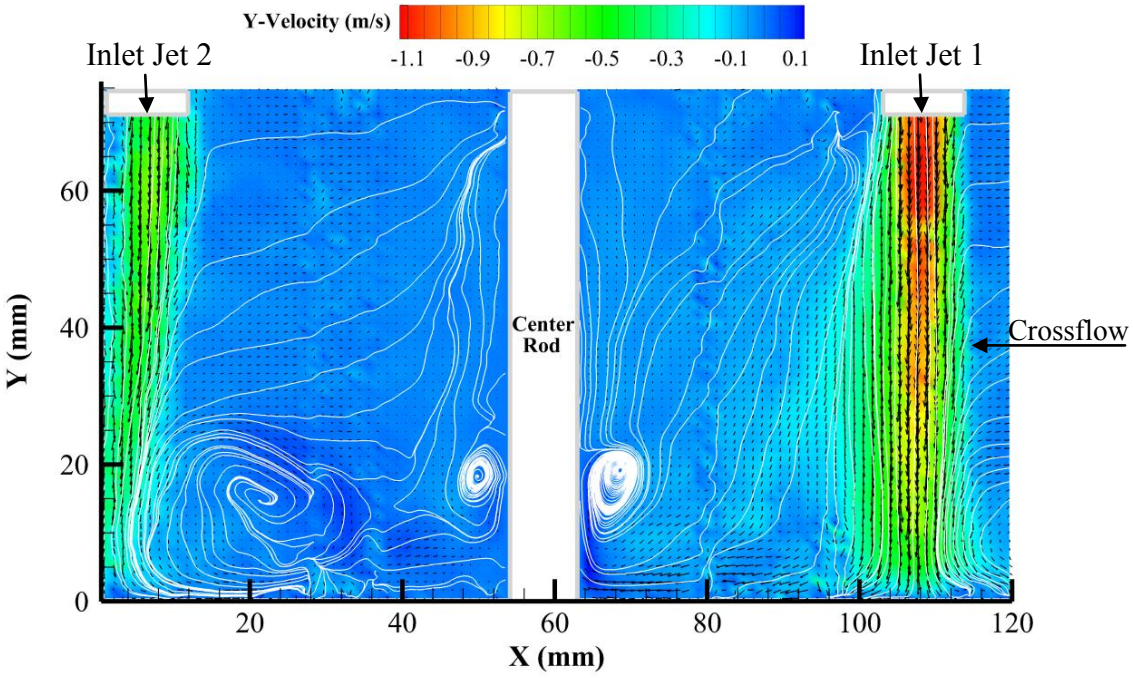

Figure II-10 Time-averaged velocity fields, the contour plot of the Y-velocity component and the streamlines along the vertical mid-plane for two isothermal inlet jets with different Reynolds numbers and with crossflow: $Re_{jet\ 1}$=11,160, Re $Re_{jet\ 2}$=6,700, and $Re_{crossflow}$=1,670.

II.3.2. Instantaneous Vorticity Fields

In this section, the instantaneous vorticity fields are presented for a few sample cases to indicate the presence of the vortical structures throughout the measurement field and to further clarify the connection between these vortex patterns and some of the phenomena observed in the time-averaged velocity fields.

II.3.2.1. Single Impinging Jet within the Mid-Plane

In Figure II-11, the instantaneous velocity vectors are presented with the vorticity fields for a single impinging jet with Reynolds numbers of 13,400 and 4,470. As shown in Figure II-11, in both cases, vortex structures with opposite directions are seen in the outer regions of the impinging jets. The opposite directions of the vortices are shown by positive and negative values in this figure. It should be noted that vortex structures have scarcely been identified in the center region of the jet. Expectedly, the magnitude of the vorticity is noticeably higher for the higher Reynolds number jet. The presence of the vortices in the outer regions of the jets explains the shift of the streamtraces toward the jet in Figure II-7. More simply, the jets entrain some of the channel flow while injecting into the channel. In Figure II-11 (a), the vorticity pattern in the opposite outer regions of the jet is more intense and exhibits symmetry. Alternatively, in Figure II-11(b), the vortex structures are more scattered and non-symmetrical.

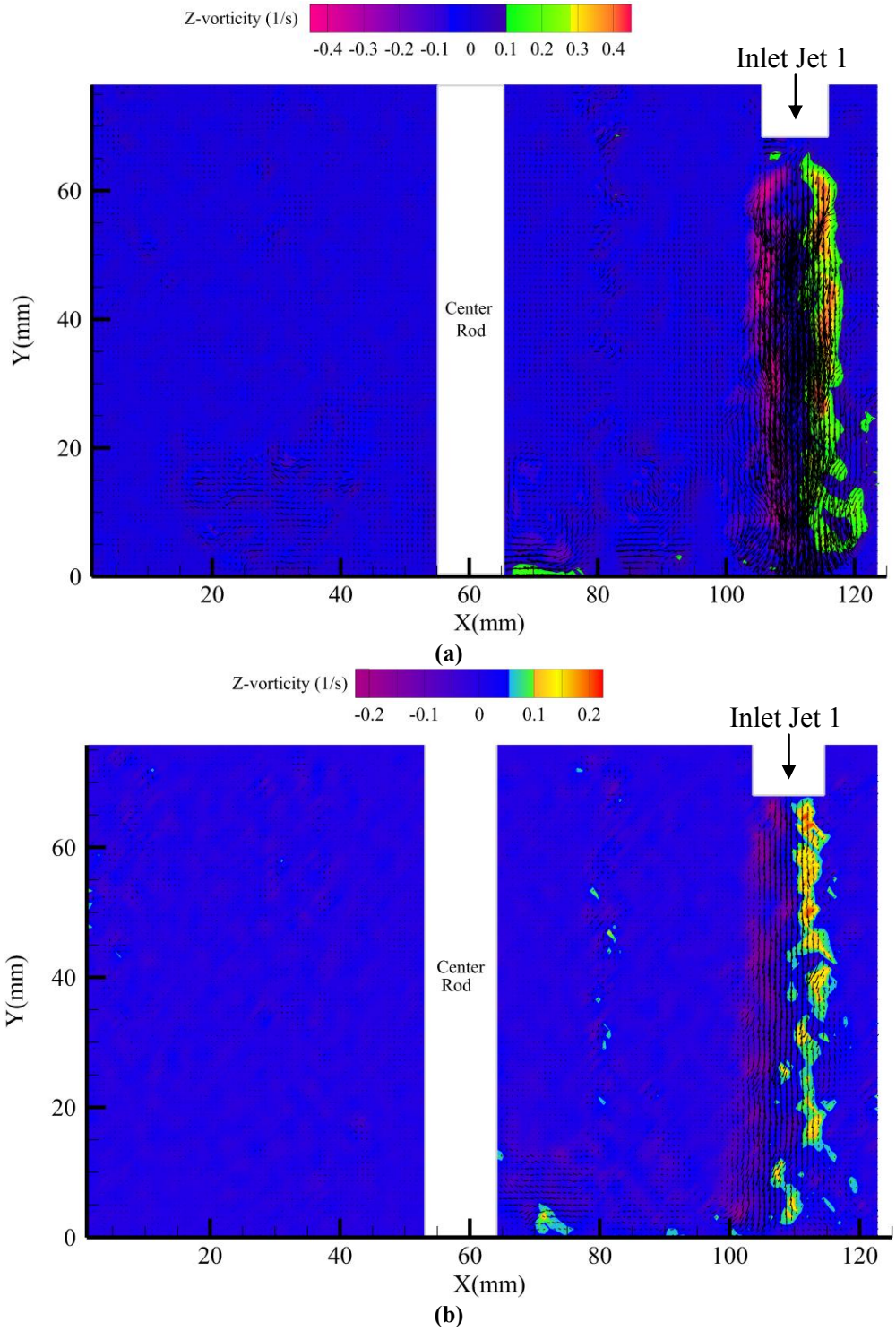

Figure II-11 Instantaneous velocity vectors overlaid on a contour map of Z-vorticity along the vertical mid-plane for a single isothermal inlet jet with (a) $Re_{jet\ 1}$=13,400, (b) $Re_{jet\ 1}$=4,470.

II.3.2.2. Dual Impinging Jets within the Mid-Plane

In Figure II-12, the instantaneous velocity vectors and the vorticity field are shown for the case of dual impinging jets each having a different Reynolds number. As seen in the Figure II-12, vortex structures with opposite directions are seen in the outer regions of each impinging jet. As mentioned before, the opposite directions of the vortices are shown by positive and negative values. Similar to the single jet cases, vortex structures have scarcely been identified in the center region of each jet. The magnitude of the vorticity is noticeably higher for the higher Reynolds number jet when compared to the jet with the lower Reynolds number. As before, the presence of the vortices in the outer regions of the jets validates the entrainment of channel flow indicated by the shifted streamtraces toward the jet in Figure II-9.

Additionally, the prediction made about the streamtraces on the right hand side of the higher Reynolds jet is confirmed by the vortex structures located on that side of the jet, such that the jet is pulling the channel flow towards itself. On the whole, it could be said that the jets entrain some of the channel flow while injecting into the channel. Also it is observed in Figure II-12 that the vorticity patterns in the opposite outer regions of the higher Reynolds jet portray symmetry, especially in the top part of the jet. On the other hand, the vortex structures are more spread out and non-symmetrical for the lower Reynolds number jet. Furthermore, a number of small vortex structures are observed on the left hand side of the lower Reynolds jet, which is closer to the channel outlet. These small vortices help to explain why the streamtraces in this region were shifted towards the left hand side of the picture in Figure II-9.

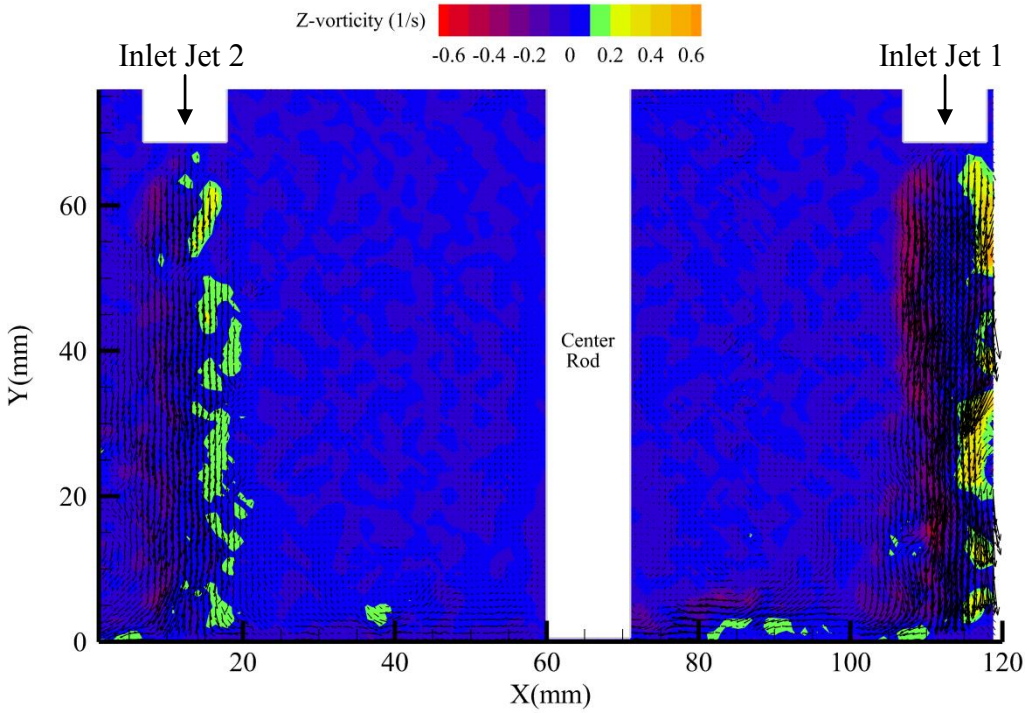

Figure II-12 Instantaneous velocity vectors overlaid on a contour map of Z-vorticity along the vertical mid-plane for two isothermal inlet jets with different Reynolds numbers: $Re_{jet\ 1}$=11,160 and $Re_{jet\ 2}$=6,250.

II.3.3. Velocity Line-Probes

To have a better understanding of the jet flow behavior and the velocity changes in the vertical direction, line-probes of the Y-velocity component and X-velocity component were obtained for three different heights of the channel's mid-plane.

II.3.3.1. Single Impinging Jet within the Mid-Plane

The Y-velocity and X-velocity line-probes for three different heights in the mid-plane of a channel with a single impinging jet are represented in Figure II-13 and Figure II-14, respectively. In each of the figures, the Y-velocity magnitude and X-velocity magnitude are normalized by the inlet jet's mean velocity obtained from flowmeter readings. Additionally, the horizontal distance is normalized by the inlet jet's inner diameter.

In Figure II-13, for both cases the highest measured velocity is happening at 40 mm above the bottom surface of the channel and a positive velocity is observed near the center rod at 20 mm above the bottom surface where the key recirculation zone is happening. In Figure II-13 (a), line-probes of Y= 40 mm and Y= 30 mm match well with each other in the region where the jet impinges and the line-probe of Y= 20 mm shows a maximum velocity at the center of the jet which is lower than the maximum velocity of the other two line-probes at the same region showing that the jet's maximum velocity decreases as it gets closer to the bottom surface of the channel. It is also seen that there is a minor fluctuation in the Y-velocity line-probes of Y= 30 mm and Y= 20 mm on the left hand side of the center rod in the region where one of the two recirculation zones

appearing on the left hand side of the center rod in Figure II-7 (a) were located. This is the recirculation zone located closer to the bottom surface of the channel and which covers an area between Y= 30 mm and Y= 20 mm. In Figure II-13 (b), line-probe of Y= 40 mm shows the highest maximum velocity at the center point of the impingement area among the three line-probes which are shown. On the whole, the maximum velocity at the center point of the impingement area decreases as the jet gets closer to the bottom surface of the channel.

Figure II-14 shows the line-probes of normalized X-velocity component for a single jet impinging into the mid-plane of the channel with two different Reynolds numbers. Both of the plots show that the magnitude of the X-velocity component is rather small compared to the jet's mean velocity and apparently compared to the magnitude of the Y-velocity component of that specific case. In Figure II-14 (a), the maximum magnitude of the X-velocity component, which is less than four percent of the inlet jet's mean velocity, is observed at Y= 40 mm. Furthermore, for the case of the lower Reynolds number (Figure II-14 (b)), it is seen that the maximum value of the X-velocity component happens at Y= 30 mm and is less than seven percent of the inlet jet's mean velocity. Consequently, the horizontal components of the velocities do not contribute significantly to the whole velocity field and thus will not be discussed further.

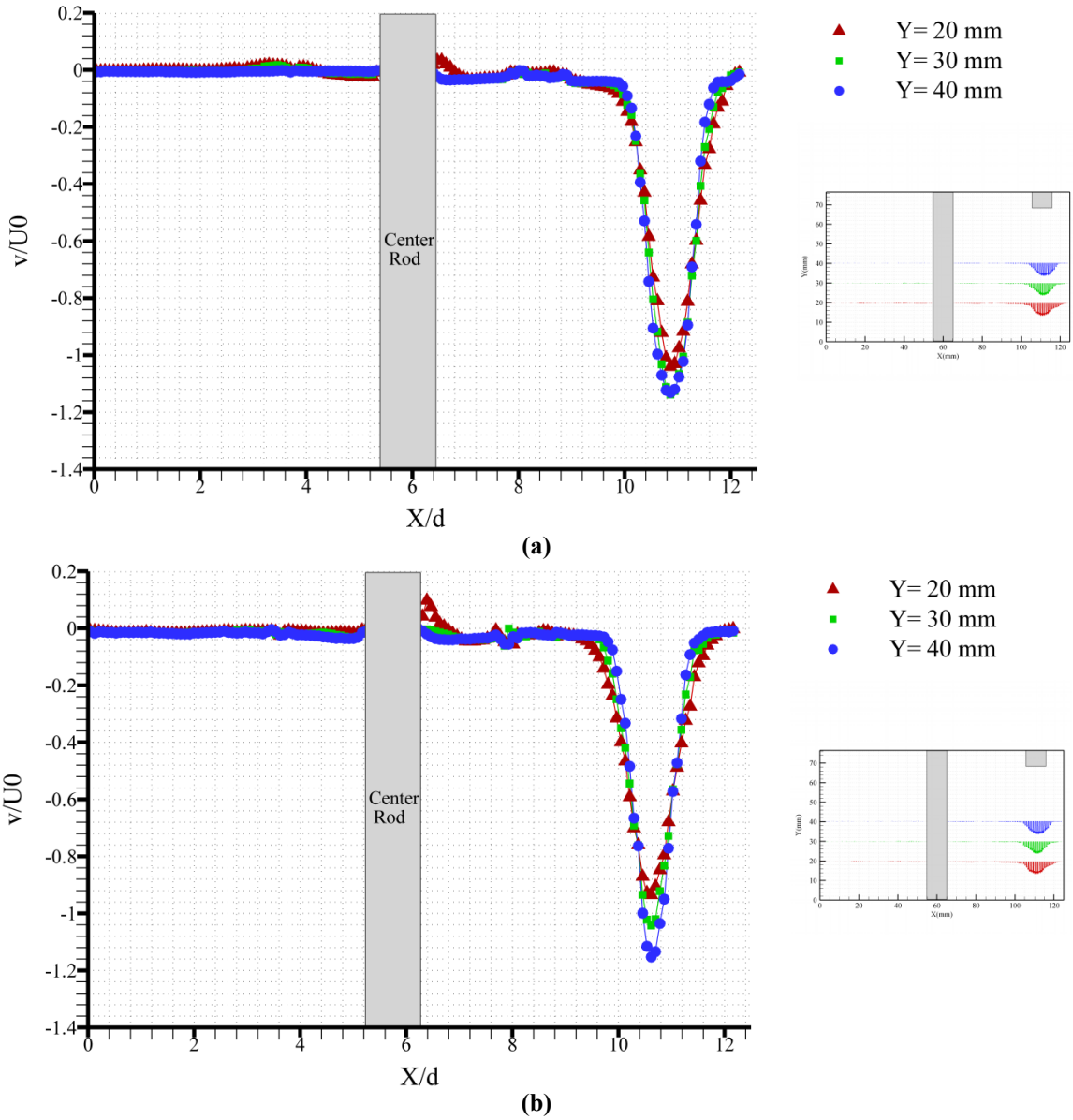

Figure II-13 Normalized Y-velocity component plot along a line-probe for different heights of the channel's mid-plane for a single isothermal inlet jet with (a) $Re_{jet\ 1}$=13,400, (b) $Re_{jet\ 1}$=4,470.

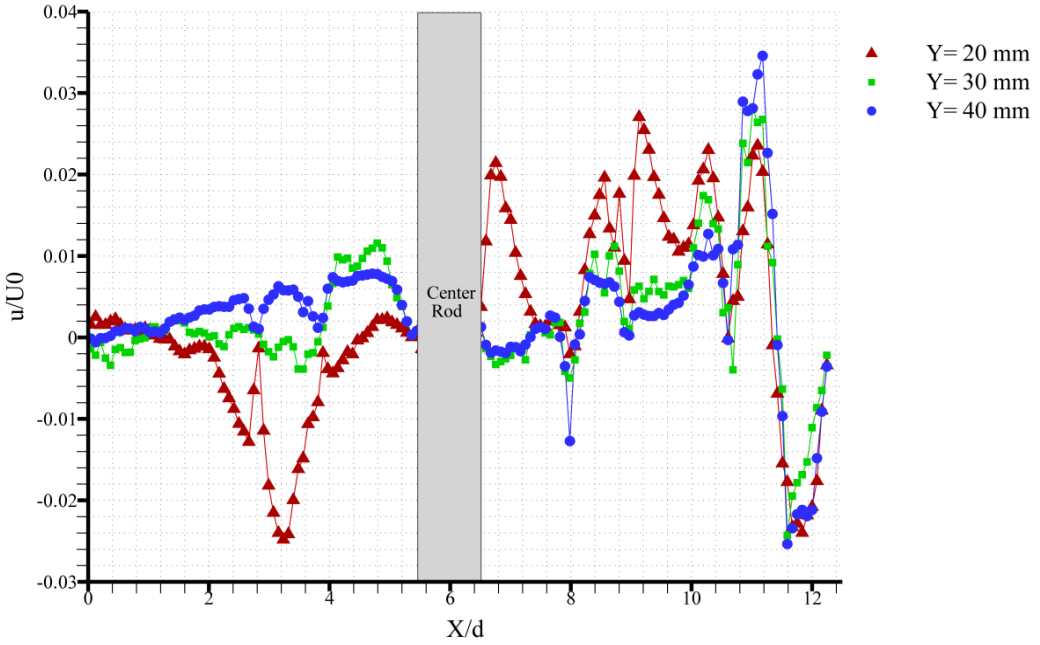

(a)

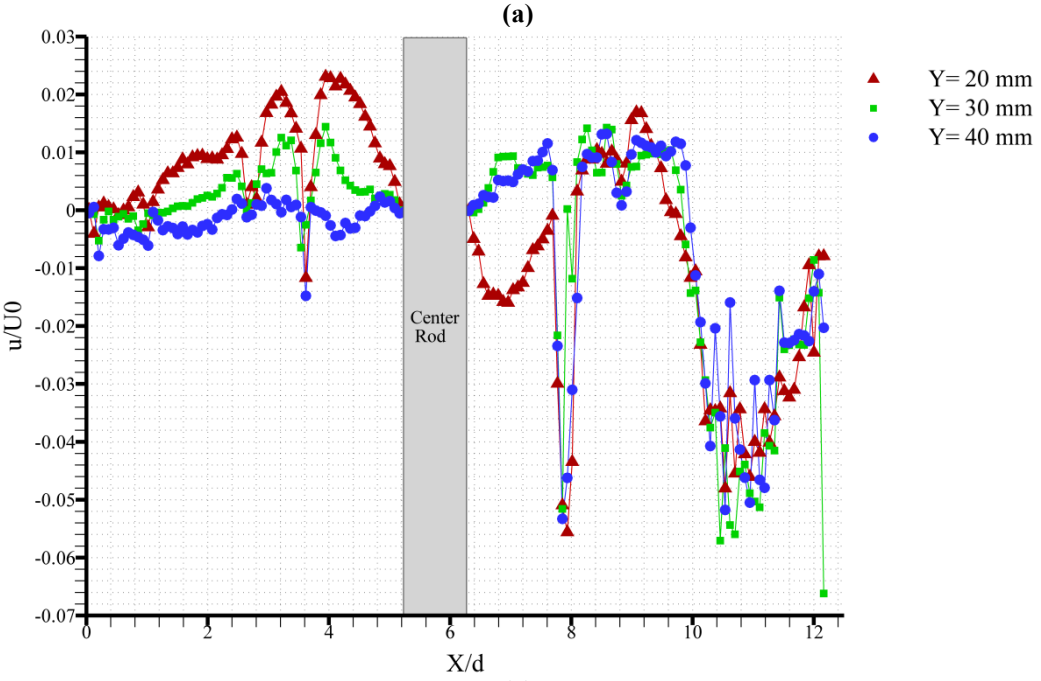

(b)

Figure II-14 Normalized X-velocity component plot along a line-probe for different heights of the channel's mid-plane for a single isothermal inlet jet with (a) $Re_{jet\ 1}$=13,400, (b) $Re_{jet\ 1}$=4,470.

II.3.3.2. Dual Impinging Jets within the Mid-Plane

The line-probes of the Y-velocity component and X-velocity component are taken for three difference heights of the channel's mid-plane to help provide a more quantitative understanding of the jet's velocity profile and its evolution. The Y-velocity and X-velocity components are shown in Figure II-15 and Figure II-16, respectively. Here also, the velocity components and horizontal distance are normalized according to the higher Reynolds number jet's mean velocity and the inlet jet's inner diameter, respectively.

In Figure II-15, both jets provide the highest measured velocity at 40 mm above the bottom surface of the channel. A positive velocity is also observed on both sides of the center rod at 20 mm above the bottom surface where the two recirculation zones appear in Figure II-9. As seen in Figure II-15, the line-probes of Y= 40 mm and Y= 30 mm for both of the jets match well with each other in the region where the jet impinges, while the line-probe of Y= 20 mm shows a slightly reduced maximum velocity at the center of the jet when compared to the other two line-probes at the same region. Thus, the jets' maximum velocity decrease as they get closer to the bottom surface of the channel. This difference between the maximum velocity of the line-probe at Y= 20 mm and the other two line-probes is more apparent for the case of the higher Reynolds jet.

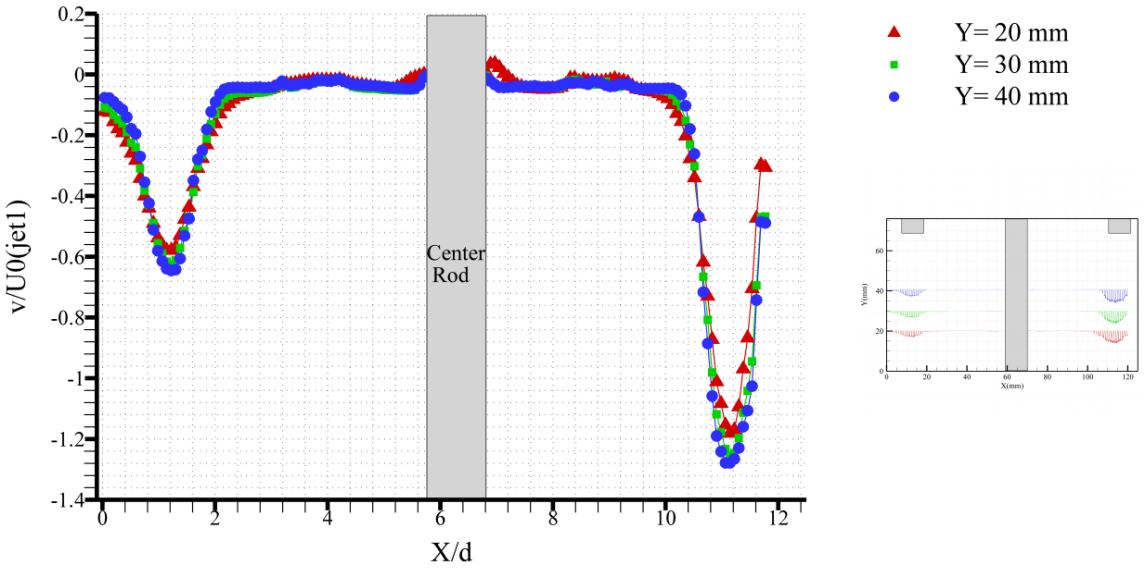

Figure II-15 Normalized Y-velocity component plot along a line-probe for different heights of the channel's mid-plane for two isothermal inlet jets with different Reynolds numbers: $Re_{jet\ 1}$=11,160 and $Re_{jet\ 2}$=6,250.

The normalized line-probes of the X-velocity component for dual impinging jets of different Reynolds numbers are presented in Figure II-16. All of the line-probes in this figure show that the magnitude of the X-velocity component is quite small compared to the higher Reynolds number jet's mean velocity. The maximum magnitude of the X-velocity component is less than four percent of the higher Reynolds jet's mean velocity and is located at Y= 40 mm. Therefore, the X-velocity component in this case similar to the X-velocity component in both of the single jet cases does not have a major role in determining the whole velocity field.

One interesting feature observed in Figure II-16 is the two small peaks on either side of the center rod at Y= 20 mm. The two peaks correspond well with the two recirculation zones seen in Figure II-9 at each side of the center rod. The reason why one

of the peaks has a positive value and the other one has a negative value is that the two recirculation zones of Figure II-9 have opposite directions.

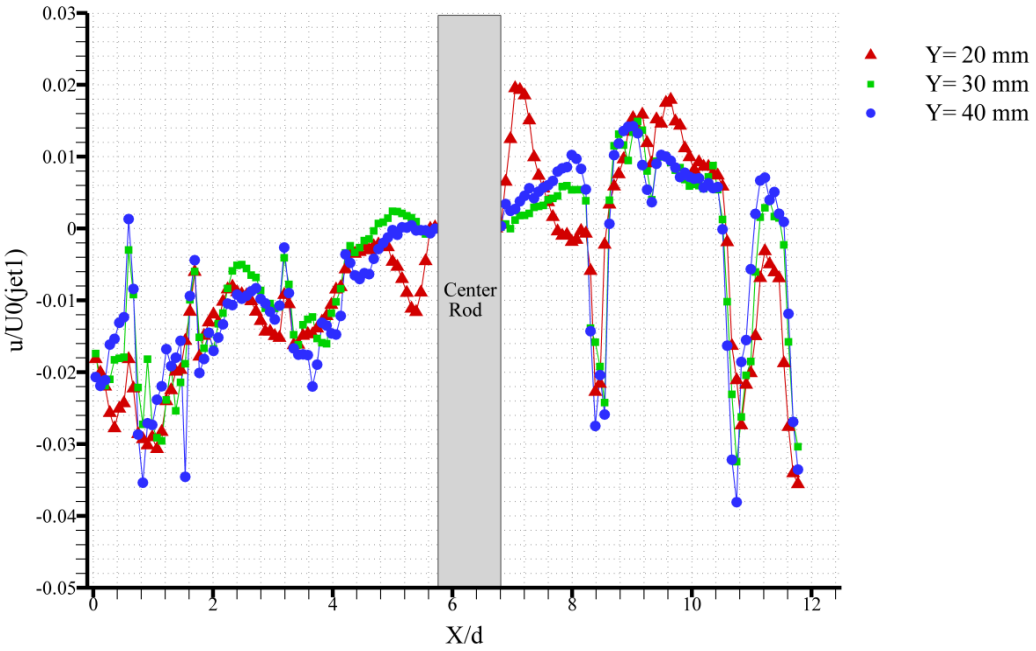

Figure II-16 Normalized X-velocity component plot along a line-probe for different heights of the channel's mid-plane for two isothermal inlet jets with different Reynolds numbers: $Re_{jet\ 1}$=11,160 and $Re_{jet\ 2}$=6,250.

II.3.4. Turbulence Intensity Line-Probes

The turbulence intensities play an important role in transferring momentum between the neighboring fluid layers; therefore, they enhance flow mixing. The turbulence intensities of Y-velocity and X-velocity components were studied along a line-probe for three different heights of the channel's mid-plane for both cases of single and dual impinging jets with variations of Reynolds number.

II.3.4.1. Single Impinging Jet within the Mid-Plane

The line-probes of the turbulence intensity of the Y and X-velocity components at three different heights of the channel's mid-plane for two different cases of single impinging jet are shown in Figure II-17 and Figure II-18, respectively.

Figure II-17 and Figure II-18 show similar trends; the highest values of turbulence intensities for both Y-velocity and X-velocity components appear within the region where the jet impinges. There are some other turbulence intensity peaks on both the right and left hand side of the center rod in all cases which correspond well with the recirculation zones and the vorticity patterns that appeared in Figure II-7 and Figure II-11. For the higher Reynolds number case, the maximum of turbulence intensity of the Y-velocity component observed in Figure II-17 (a) is almost double the maximum of turbulence intensity of the X-velocity component seen in Figure II-18 (a) which shows the higher contribution of the Y-velocity fluctuations in the flow field. On the other hand, the maximum turbulence intensity of Y-velocity component observed in Figure II-17 (b) is close to the maximum turbulence intensity of X-velocity component seen in Figure II-18 (b) which shows the fact that velocity fluctuations in both directions contribute to the flow field to the same extent.

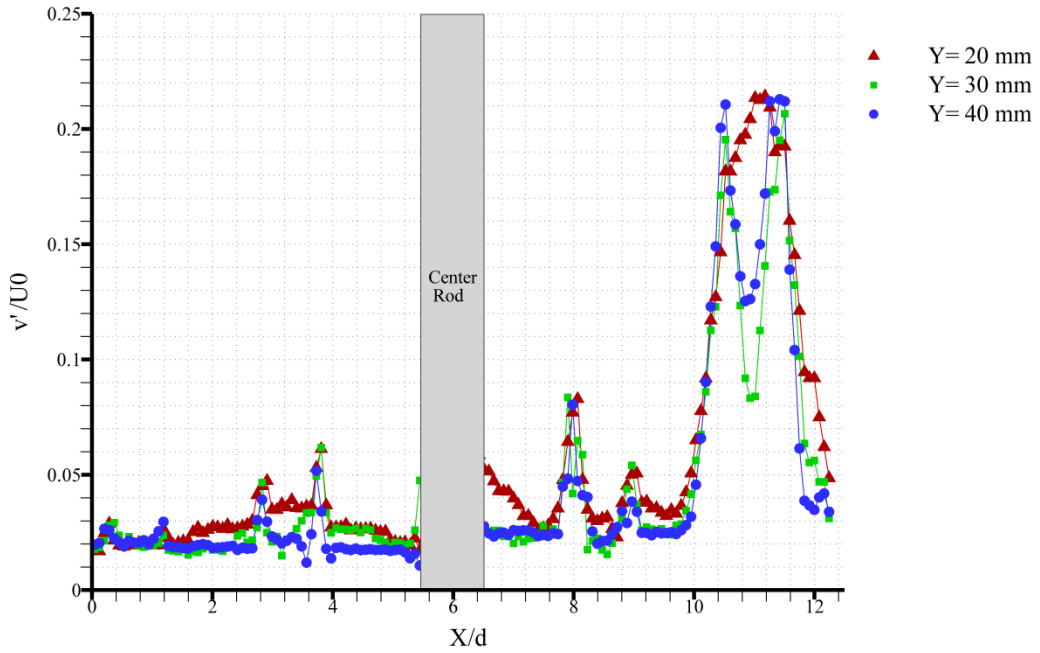

(a)

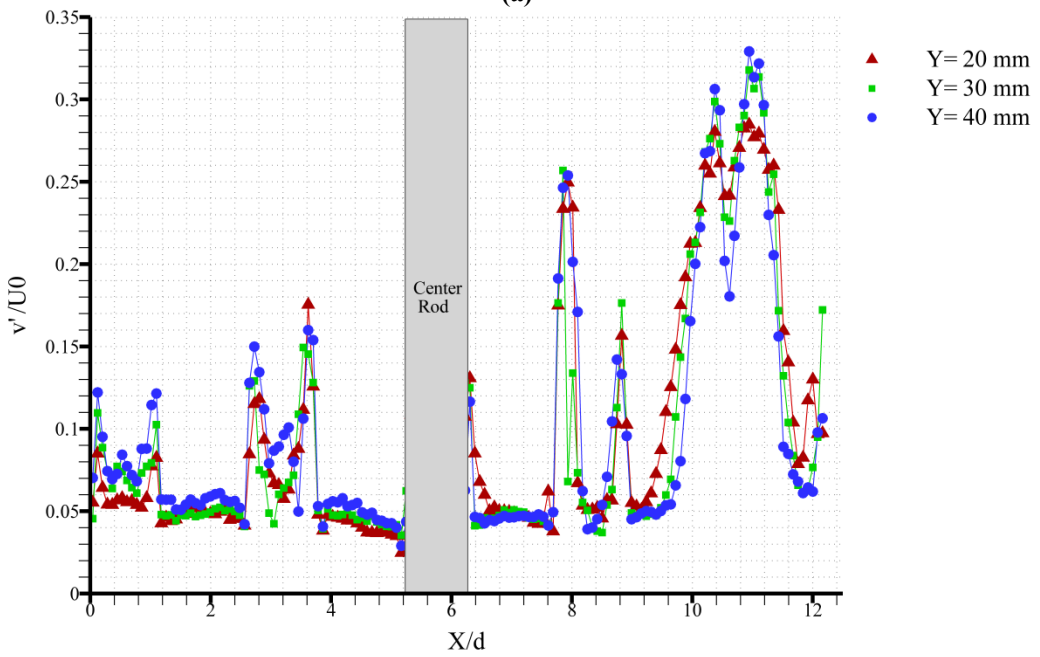

(b)

Figure II-17 Turbulence intensity of Y-velocity component plot along a line-probe for different heights of the channel's mid-plane for a single isothermal inlet jet with (a) $Re_{jet\ 1}$=13,400, (b) $Re_{jet\ 1}$=4,470.

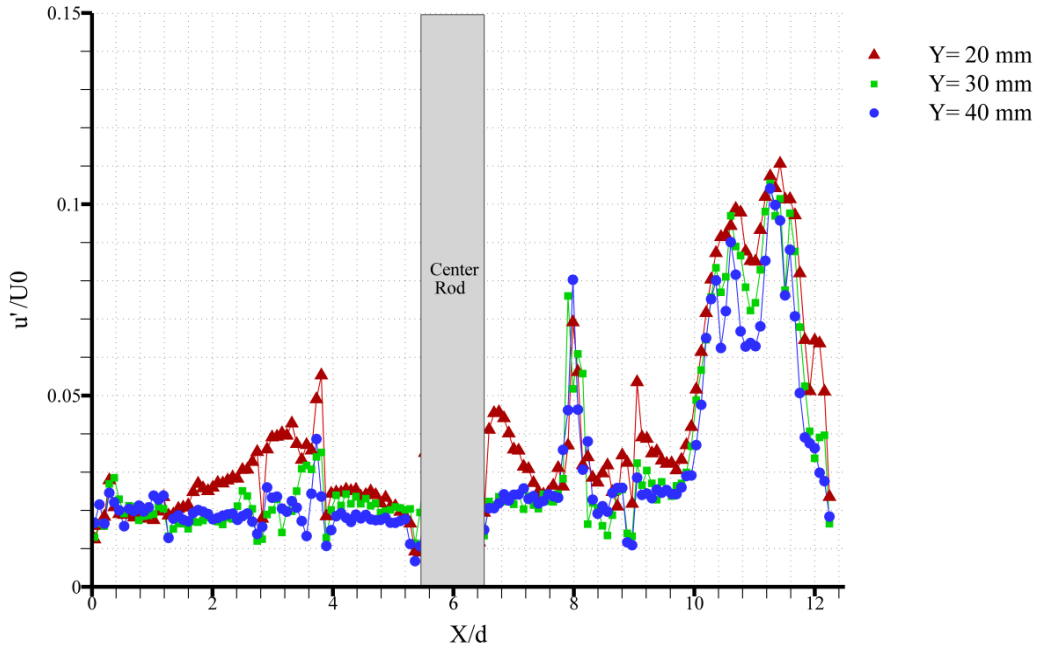

(a)

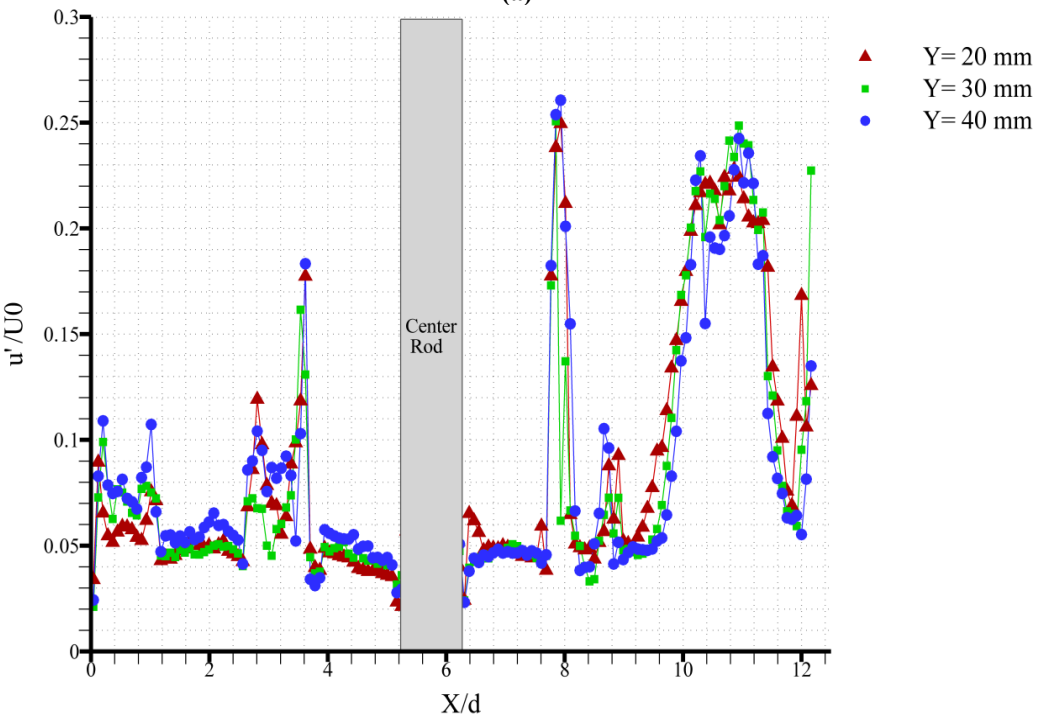

(b)

Figure II-18 Turbulence intensity of X-velocity component plot along a line-probe for different heights of the channel's mid-plane for a single isothermal inlet jet with (a) $Re_{jet\ 1}$=13,400, (b) $Re_{jet\ 1}$=4,470.

II.3.4.2. Dual Impinging Jets within the Mid-Plane

The turbulence intensities of Y-velocity and X-velocity components were also plotted along a line-probe for three different heights of the channel's mid-plane for two impinging jets with two different Reynolds numbers and the results are shown in Figure II-19 and Figure II-20, respectively. The camera view could not cover the whole region in the right hand side area of the first jet; therefore, a peculiarity is seen at the line-probes of the turbulence intensities of Y-velocity and X-velocity components in Figure II-19 and Figure II-20 in that region and a small section of the line-probe passing through the right hand side of the higher Reynolds number jet is missing.

Figure II-19 and Figure II-20 both show the highest values of the turbulence intensities of Y-velocity and X-velocity components appear within the region where the higher Reynolds jet impinges. Furthermore, there are some other turbulence intensity peaks on the right and left hand side of the center rod which corresponds with the recirculation zones and the vorticity patterns that were observed in Figure II-9 and Figure II-12. In both Figure II-19 and Figure II-20, the turbulence intensities of Y-velocity and X-velocity components drop abruptly at the center of each of the jets for all of the line-probes. It should be noted that for the higher Reynolds number jet, the maximum of the turbulence intensity of Y-velocity is significantly higher than the maximum of the turbulence intensity of X-velocity. While for the lower Reynolds number jet, the maximum of the turbulence intensities of Y-velocity and X-velocity are in the same order.

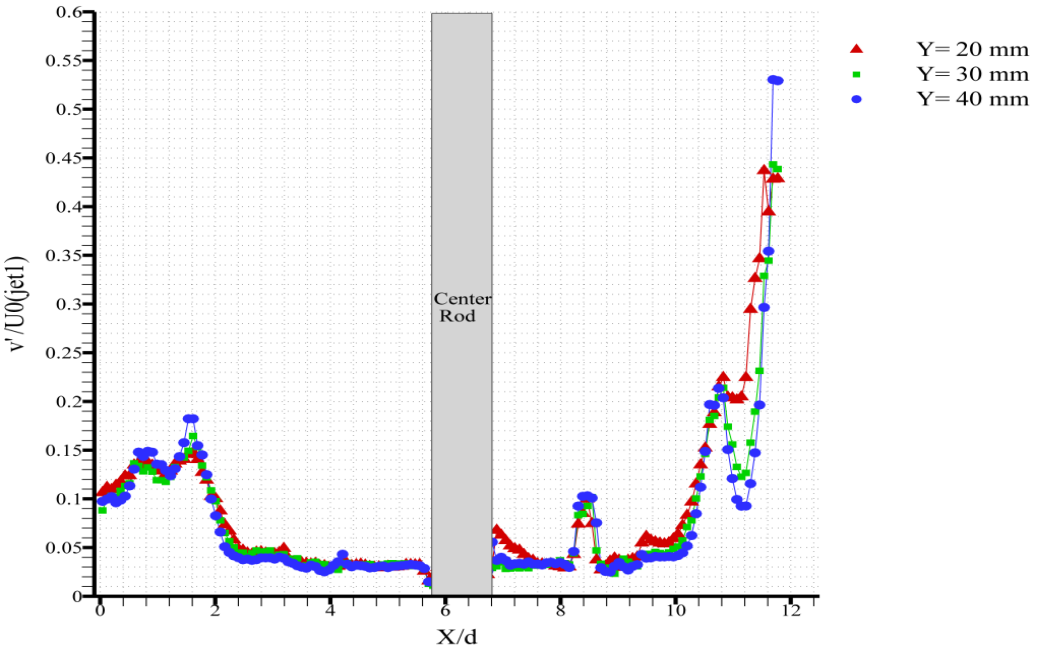

Figure II-19 Turbulence intensity of Y-velocity component along a line-probe for different heights of the channel's mid-plane for two isothermal inlet jets with different Reynolds numbers: $Re_{jet\ 1}$=11,160 and $Re_{jet\ 2}$=6,250.

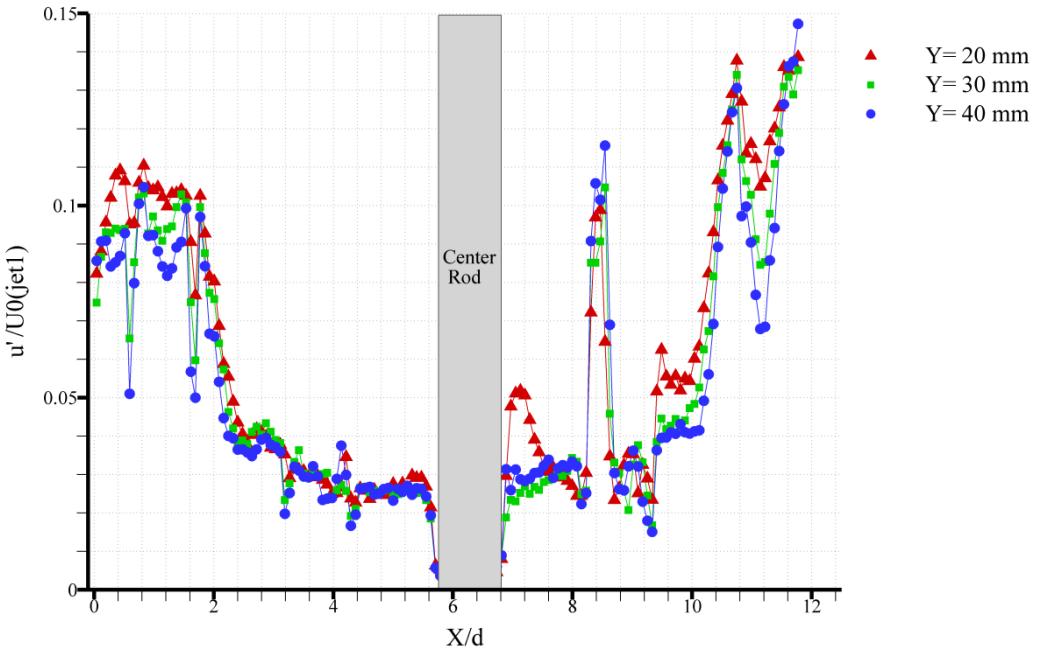

Figure II-20 Turbulence intensity of X-velocity component along a line-probe for different heights of the channel's mid-plane for two isothermal inlet jets with different Reynolds numbers: $Re_{jet\ 1}$=11,160 and $Re_{jet\ 2}$=6,250.

II.3.5. Reynolds Shear Stress Line-Probes

Distribution of Reynolds shear stresses along line-probes at three different height of the channel is obtained for different cases of single and dual impinging jets within the mid-plane of the measurement volume.

II.3.5.1. Single Impinging Jet within the Mid-Plane

Figure II-21 shows the distribution of the Reynolds stresses along a line-probe for three different heights of the channel's mid-plane for two cases of single impinging jets with different Reynolds numbers. As seen in Figure II-21, the jet has two peaks of similar magnitude in opposite directions for both Reynolds numbers. Another similarity between the cases is that the magnitude of Reynolds stresses goes to zero in the outer region and the center point of the impinging jets. All of these characteristics validate the definition of the Reynolds stresses for a standard turbulent jet. Also in both cases, far from the impinging area the Reynolds stresses are zero with some minor fluctuations due to the velocity fluctuations in those areas.

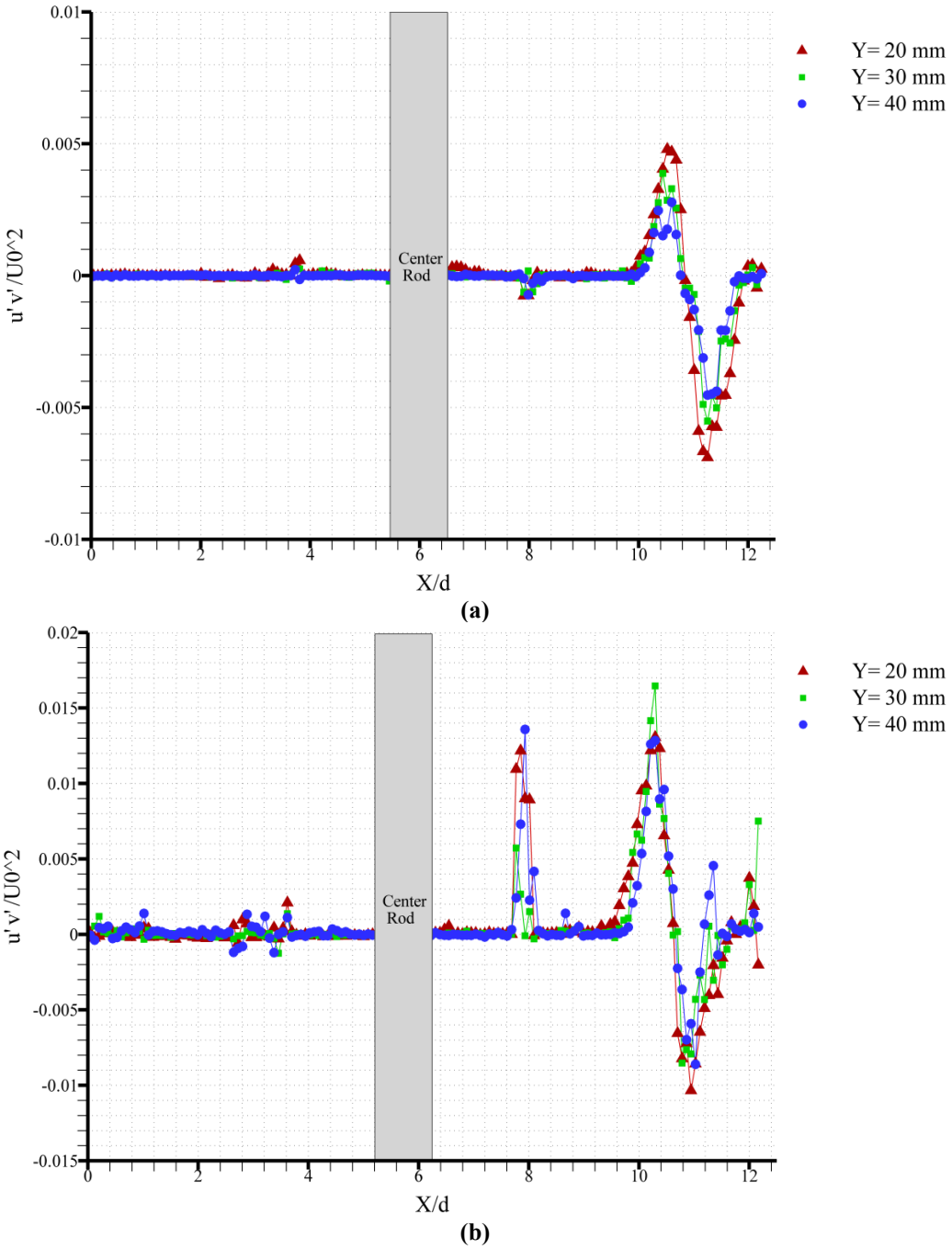

Figure II-21 Normalized Reynolds shear stresses plot along a line-probe for different heights of the channel's mid-plane for a single isothermal inlet jet with (a) $Re_{jet\ 1}$=13,400, (b) $Re_{jet\ 1}$=4,470.

II.3.5.2. Dual Impinging Jets within the Mid-Plane

Figure II-22 shows the distribution of the Reynolds shear stresses along a line-probe for three different heights of the channel's mid-plane for the case of dual impinging jets with different Reynolds numbers. The Reynolds shear stresses of both jets in Figure II-22 show the same characteristics as the Reynolds shear stresses of the impinging jets of each of the jets in Figure II-21. In this case also, the Reynolds shear stresses of both of the jets have two peaks with slightly different magnitude in opposite directions and the magnitude of Reynolds shear stresses goes to zero in the outer regions and the center point of each jet. The Reynolds shear stresses reduce to zero (with minor fluctuations) far from the impingement area for both jets. The minor fluctuations in the Reynolds shear stresses far from the jets could be due to the minor velocity fluctuations observed in those areas. However, the Reynolds shear stresses on the left hand side of the lower Reynolds number jet do not approach to zero which could be because of the fact that this inlet jet is located closer to the outlet of the channel leading to higher velocity fluctuations in that area.

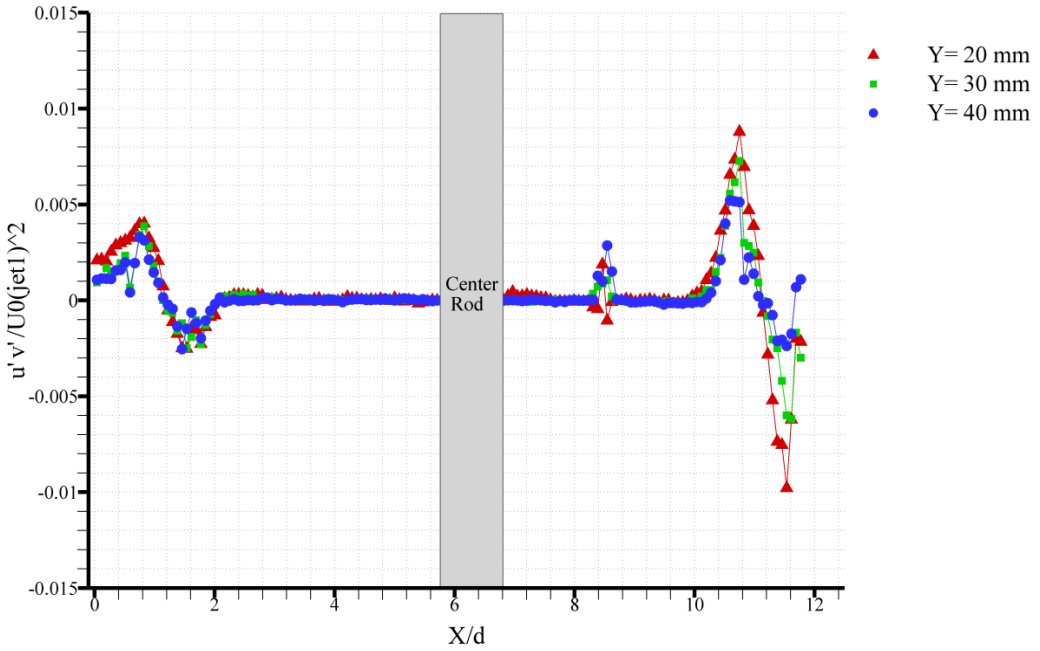

Figure II-22 Normalized Reynolds shear stresses plot along a line-probe for different heights of the channel's mid-plane for two isothermal inlet jets with different Reynolds numbers: $Re_{jet\ 1}$=11,160 and $Re_{jet\ 2}$=6,250.

II.3.6. Y-velocity Line-Probes within Different Measurement Planes

As mentioned previously, in order to visualize the flow behavior throughout the measurement volume, three discrete planes inside the interrogation volume were monitored for the different inlet jet conditions. However, in most cases so far the velocity fields and line-probes along the mid-plane have been presented. The reason to focus more on the data obtained from the mid-plane is that since the jet impingement occurs within the mid-plane of the channel, it is expected for most of the turbulence phenomena such as mixing, entrainment, and most of the coherent structures to happen within the mid-plane of the channel. In this section, to compare the flow field development in each of the measurement planes, Y-velocity line-probes at a certain

height of the channel are obtained for all three measurement planes and compared to each other.

II.3.6.1. Single Impinging Jet within the Mid-Plane

Figure II-23 compares the Y-velocity line-probes of those three different planes at a specific height of the channel (Y= 40 mm) for two cases of single impinging jets with different Reynolds numbers. In each of the plots, the Y-velocity magnitude is normalized by the inlet jet's mean velocity obtained from the readings of the flowmeter which is installed upstream of the inlet jet and the length and depth of the measurement volume are normalized by the inlet jet's inner diameter.

In both plots of Figure II-23, the Y-velocity line-probes in the back-plane and the front-plane of the measurement volume have much less fluctuation compared to the Y-velocity line-probe of the mid-plane where the jet is located. Furthermore, in both cases, the jet's Y-velocity profile has a parabolic shape with its maximum at the center of the region where the jet impinges. Apart from this region, the Y-velocity line-probe behaves similarly to the Y-velocity line-probes of the front-plane and the back-plane, where little fluctuation in its velocity occurs. The time-averaged velocity fields along the front-plane and back-plane of the measurement volume for cases shown in Figure II-23 can be found in Appendix B.

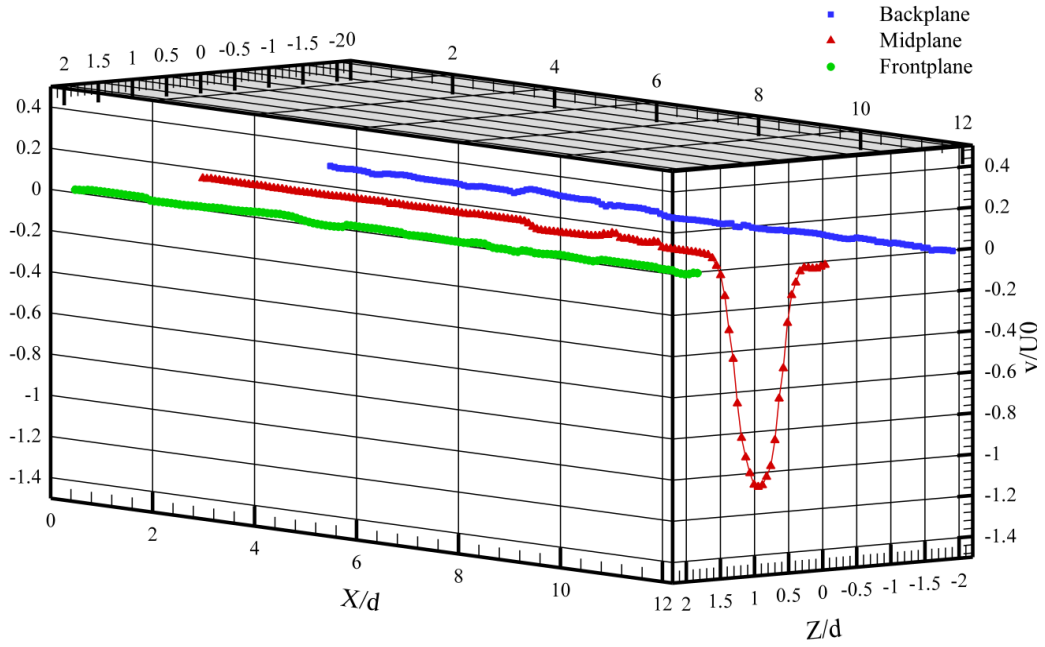

(a)

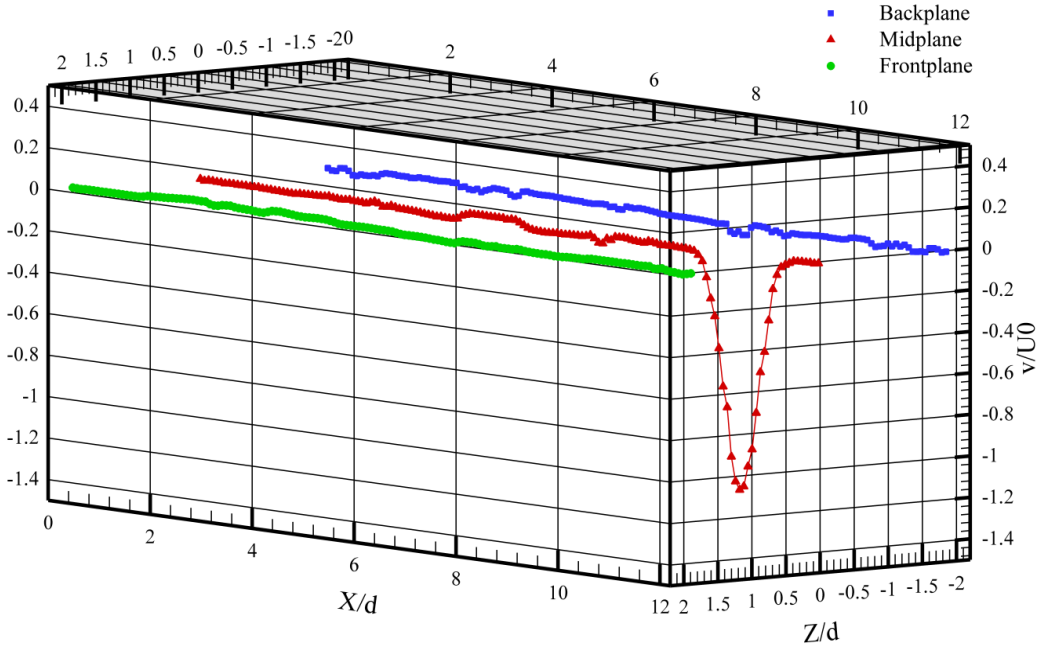

(b)

Figure II-23 Normalized Y-velocity component plots along a line-probe for a constant height of the channel (Y= 40 mm) for three different planes for a single isothermal inlet jet with (a) $Re_{jet\ 1}$=13,400, (b) $Re_{jet\ 1}$=4,470.

II.3.6.2. Dual Impinging Jets within the Mid-Plane

In this case also, to visualize the flow behavior within the measurement volume, data were taken for three discrete planes throughout the interrogation volume for different inlet jet's Reynolds numbers. Figure II-24 compares the Y-velocity line-probes of those three different planes at a specific height of the channel (Y= 40 mm) for two isothermal jets impinging into the channel's mid-plane with two different Reynolds numbers. Here again, the results are normalized in the same way as previously explained for Figure II-24.

Figure II-24 demonstrates that the Y-velocity line-probes in the back-plane and the front-plane of the measurement volume do not oscillate to the same extent as the Y-velocity line-probe of the mid-plane oscillates. In fact, for both of the jets, the jets' Y-velocity profiles have a parabolic shape with their maximum value at the center of the region where the jets impinge. Away from this region the Y-velocity line-probe behaves much more like the Y-velocity line-probes of the front-plane and the back-plane, lacking abrupt variations. These results strongly agree with the conclusion made about Figure II-23 for the two cases of a single isothermal jet with different Reynolds numbers. In this case, as well as the single inlet jet cases, the time-averaged velocity fields along the front-plane and back-plane of the measurement volume are presented in Appendix B.

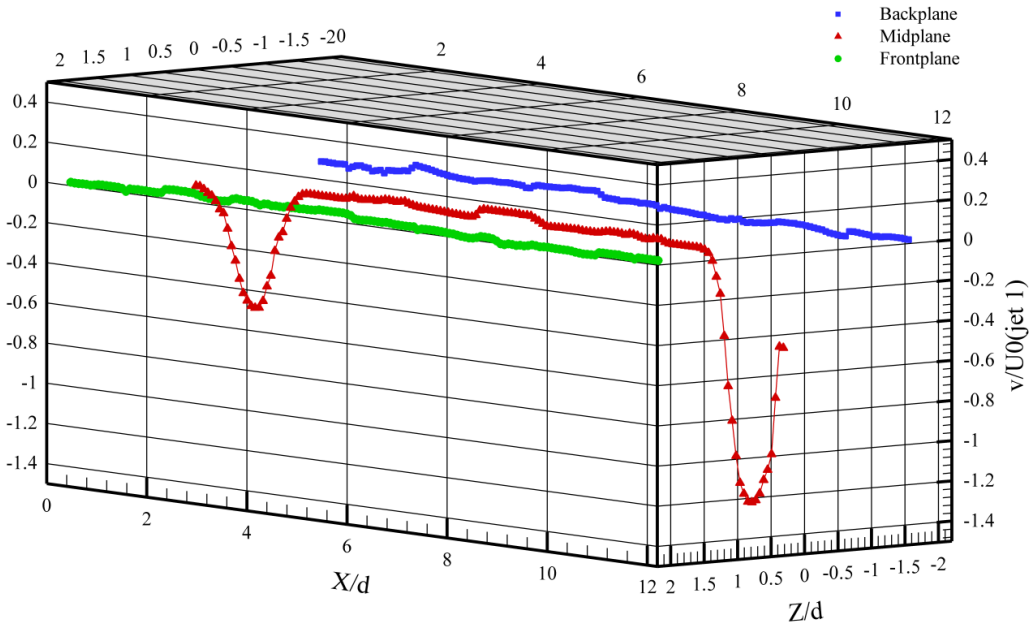

Figure II-24 Normalized Y-velocity component plot along a line-probe for a constant height of the channel (Y= 40 mm) for three different planes for two isothermal inlet jets with different Reynolds numbers: $Re_{jet\ 1}$=11,160 and $Re_{jet\ 2}$= 6,250.

II.3.7. POD Analysis of the Velocity Fields

In this investigation, POD analysis is carried out on the velocity fields obtain by PIV technique for different cases with single or dual impinging jets. Consequently, the energy distributions of the POD eigenmodes of the different cases, the POD reconstruction of the vorticity fields, and the temporal evolution of some of the first eigenmodes are obtained and represented.

II.3.7.1. Energies of the POD modes

In this section, the energy content of different POD modes is obtained for a few of the cases for which velocity fields were previously obtained through PIV analysis. As mentioned earlier, the energy content of each eigenmodes is represented by the value of its eigenvalue. It should be noted that the POD modes energy contents are calculated using the fluctuating part of the velocity (mean velocity is subtracted from the velocity value at each point in the flow field).

II.3.7.1.1. Single Impinging Jet within the Mid-Plane

The energy distributions among the eigenmodes and the cumulative sum of the energy with respect to the mode number are presented in different plots of Figure II-25. It can be clearly seen from the results that for both cases of a single impinging jet with two different Reynolds numbers, most of the flow energy is stored in the first few eigenmodes. It is also observed that with increasing the Reynolds number of the jet, more energy gets stored in the same number of eigenmodes which is in agreement with the results obtained by Kim *et al.* (2007). The first hundred modes for the case of the single impinging jet with $Re_{jet\ 1}$=13,400 contains 58.6% of the energy of the field while the same number of modes contain 29.9 % of the total kinetic energy of the field in case of the single impinging jet with $Re_{jet\ 1}$=4,470. This expresses the fact that the flow field can be better represented with fewer number of POD eigenmodes as the Reynolds number increases.

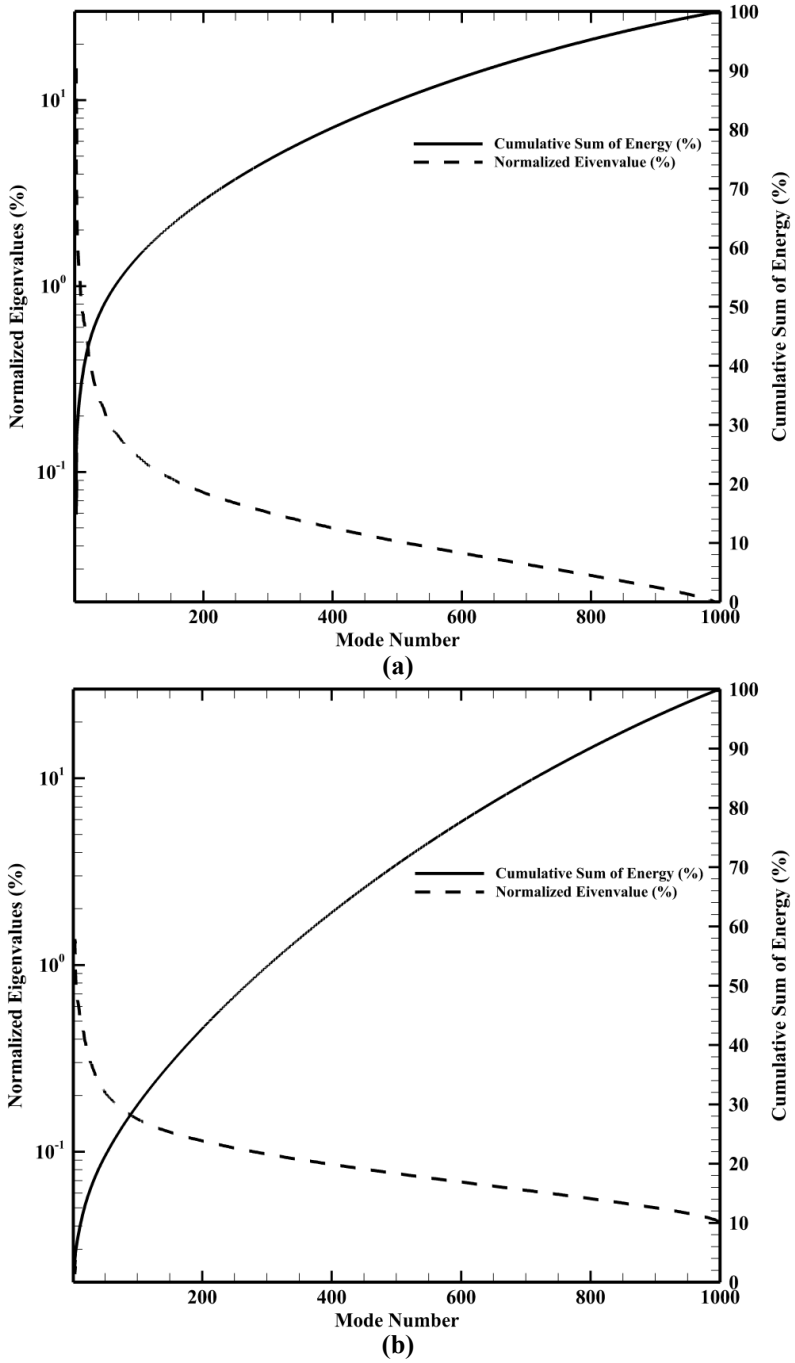

Figure II-25 Energy distribution of POD eigenmodes for a single isothermal inlet jet with (a) $Re_{jet\ 1}$=13,400, (b) $Re_{jet\ 1}$=4,470.

II.3.7.1.2. Dual Impinging Jets within the Mid-Plane

The energy distribution of POD eigenmodes for a case of dual impinging jets within the mid-plane of the test section are presented in Figure II-26. The results are in agreement with the findings of the previous section for cases of single impinging jets. It is seen from the figure that the first few eigenmodes contain most of the flow energy. In this case, 49.5% of the total kinetic energy of the flow field is stored in the first 100 POD modes.

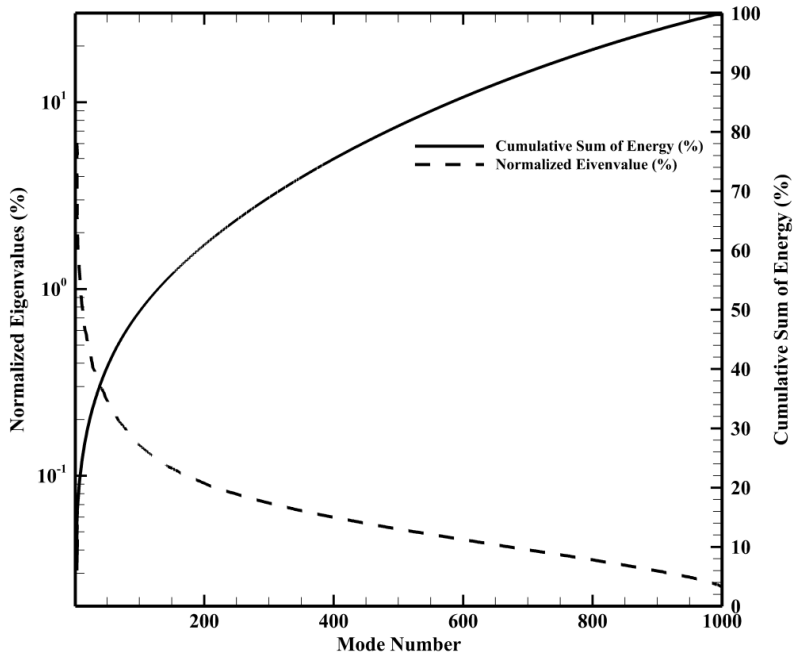

Figure II-26 Energy distribution of POD eigenmodes for dual isothermal inlet jets with $Re_{jet\ 1}$=11,160 and $Re_{jet\ 2}$= 6,250.

II.3.7.2. POD Mode Shapes and Their Temporal Evolution

In this section, the velocity fields and the contour plots of the velocity of the POD eigenmode as well as the time histories of the corresponding POD coefficients and the POD mode shapes are presented for the first five POD modes. POD mode shapes and the time evolution of the POD coefficients are obtained for cases of single and dual impinging jets and the results are shown in the following sections. It should be mentioned that the results presented in this section are acquired using the fluctuating part of the velocity. Moreover, in order to represent the time evolution of the POD modes, a non-dimensional form is defined for time using the measurement period (T= 5 sec), height of the channel, and inlet jet velocity in the single impinging jet case and the higher Reynolds' jet velocity in case of the dual impinging jets, specifically $t = \left(\frac{T \times U_0}{H} \right)$.

II.3.7.2.1. Single Impinging Jet within the Mid-Plane

The time evolution of the first five POD mode coefficients throughout the measurement period along with the corresponding POD mode shapes for two different cases of single impinging jet are presented.

The time histories of the POD coefficients for the first five modes presented in Figure II-27 which in fact represent the temporal variation of the POD mode amplitudes through the measurement period. However, several interesting points are observed in the plots of the first five mode shapes. A first look at the plots of all five mode shapes shows

that the main flow features captured by these modes are different parts of the jet and none of the other flow pattern that were previously observed in the time-averaged velocity and instantaneous vorticity fields represented in Figure II-7 (a) and Figure II-11 (a) are captured in these mode shape fields except for a small part of the main recirculation zone region in the fifth POD mode shape. This is an indication of the fact that in this case the high Reynolds number of the jet and its high energy content compared to the rest of the flow field makes it the dominant feature of the field which is captured by the most energetic modes. Therefore, higher number modes need to be investigated in order to see the behavior of the lower energy flow features.

A more detailed look at each individual mode shape indicates the contribution of each mode in different parts of the jet. The modal shape of the first POD eigenmode only captures the high velocity region at the top part of the jet exactly after the jet flow exits the jet exit plane. The second mode shape captures the top part of the jet with a lower velocity compared to the velocities seen in the first mode shape. Moreover, the middle part of the jet as well as a part of the bottom section of the jet is captured with this mode. It should be noted that in this plot, the middle section of the jet shows the high velocity core region of the jet. The third and fourth mode shapes major contributions are in illustrating the bottom part of the jet while the fifth mode represents the top half of the jet.

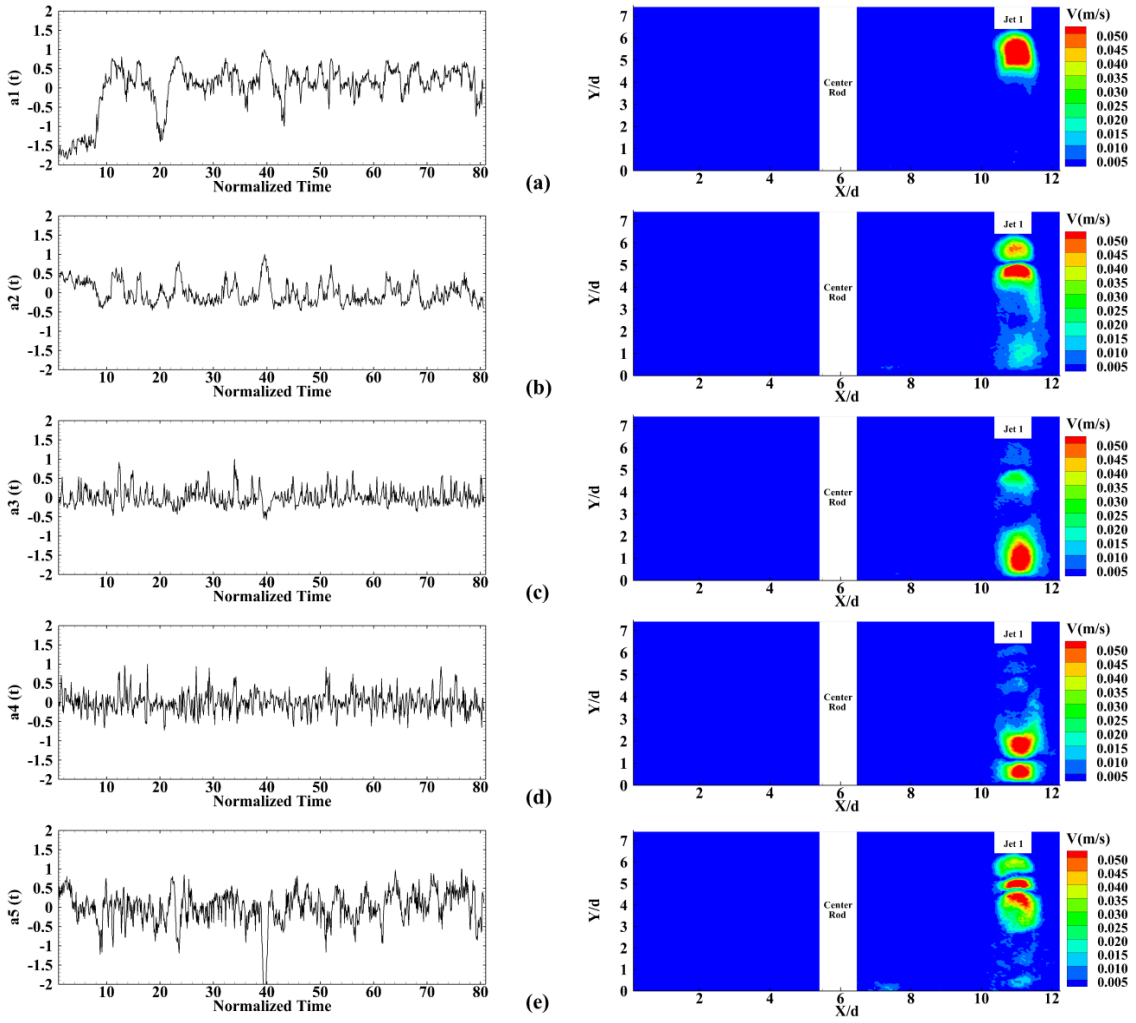

Figure II-27 Time evolution and the shape of the first five eigenmodes for single inlet jet with $Re_{jet\ 1}$=13,400 (a) Mode 1, (b) Mode 2, (c) Mode 3, (d) Mode 4, (e) Mode 5.

Figure II-28 represents the time histories of the POD coefficients of the first five modes along with the mode shapes of the corresponding modes for the case of a single impinging jet with a Reynolds number of 4,470 which is much lower than the Reynolds number of the jet studied in Figure II-27. The temporal evolution of the POD coefficients represents the variations in the amplitude of the POD mode shapes with time.

The mode shapes of the first five POD modes in this case are quite different from the mode shapes of the higher Reynolds jet represented in Figure II-27. In the POD mode shapes of Figure II-28, in addition to different parts of the jet, some parts of the recirculation area close to the center rod of the measurement plane are observed. Furthermore, the mode shapes represent different vortical structures within the jet impingement area which are in agreement with the findings of Figure II-11 (b) where the instantaneous z-vorticity field showed the presence of vortical structures with different directions within the jet region.

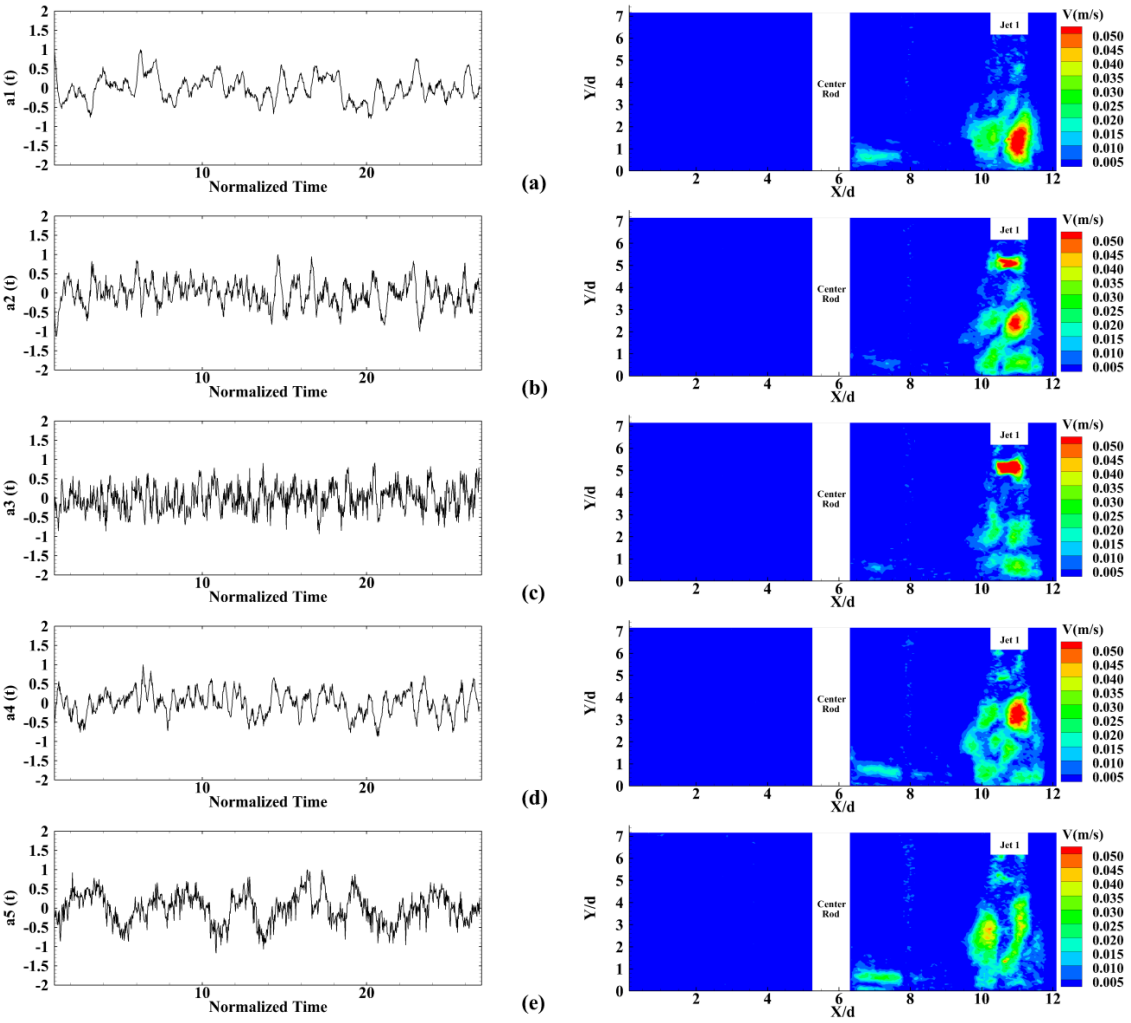

Figure II-28 Time evolution and the shape of the first five eigenmodes for single inlet jet with $Re_{jet\ 1}$=4,470 (a) Mode 1, (b) Mode 2, (c) Mode 3, (d) Mode 4, (e) Mode 5.

II.3.7.2.2. Dual Impinging Jets within the Mid-Plane

In this section, to represent the contribution of each POD mode to the whole velocity field, the temporal evolution of the POD coefficients and the mode shapes of the first five eigenmodes are obtained for a case of dual impinging jets within the mid-plane of the measurement volume and the results are shown in Figure II-29. The POD mode shapes of the case with dual impinging jets with two different Reynolds numbers confirm some of the conclusions made from the POD modes of the single impinging jet with $Re_{jet\ 1}$=13,400 (see Figure II-27). As seen in Figure II-29 (a) and (b), the higher Reynolds jet with a Reynolds number of 11,160 dominates the whole flow field, other flow features previously seen in Figure II-9 and Figure II-12, and even the second impinging jet which has a lower Reynolds number. In this case, the higher Reynolds jet's energy is much higher than the lower Reynolds jet; therefore, no significant part of the lower Reynolds jet is captured in the first tow mode shapes of the flow field. The top part of the lower Reynolds jet right after the jets exits the nozzle is captured in the third and fourth mode shapes due to the high velocity of its core region. In these mode shapes - i.e. the third and fourth POD modes-, the lower half of the higher Reynolds jet is captured along with some contributions of the top part of the jet. The mode shape of the fifth POD mode captures the top part of both jets and some smaller flow features in both jets impingement areas. Moreover, it is interestingly observed that a small part of the recirculation region on the higher Reynolds jet side is represented through the fifth POD mode; however, no parts of the recirculation zone on the lower Reynolds jet side is captured by this mode.

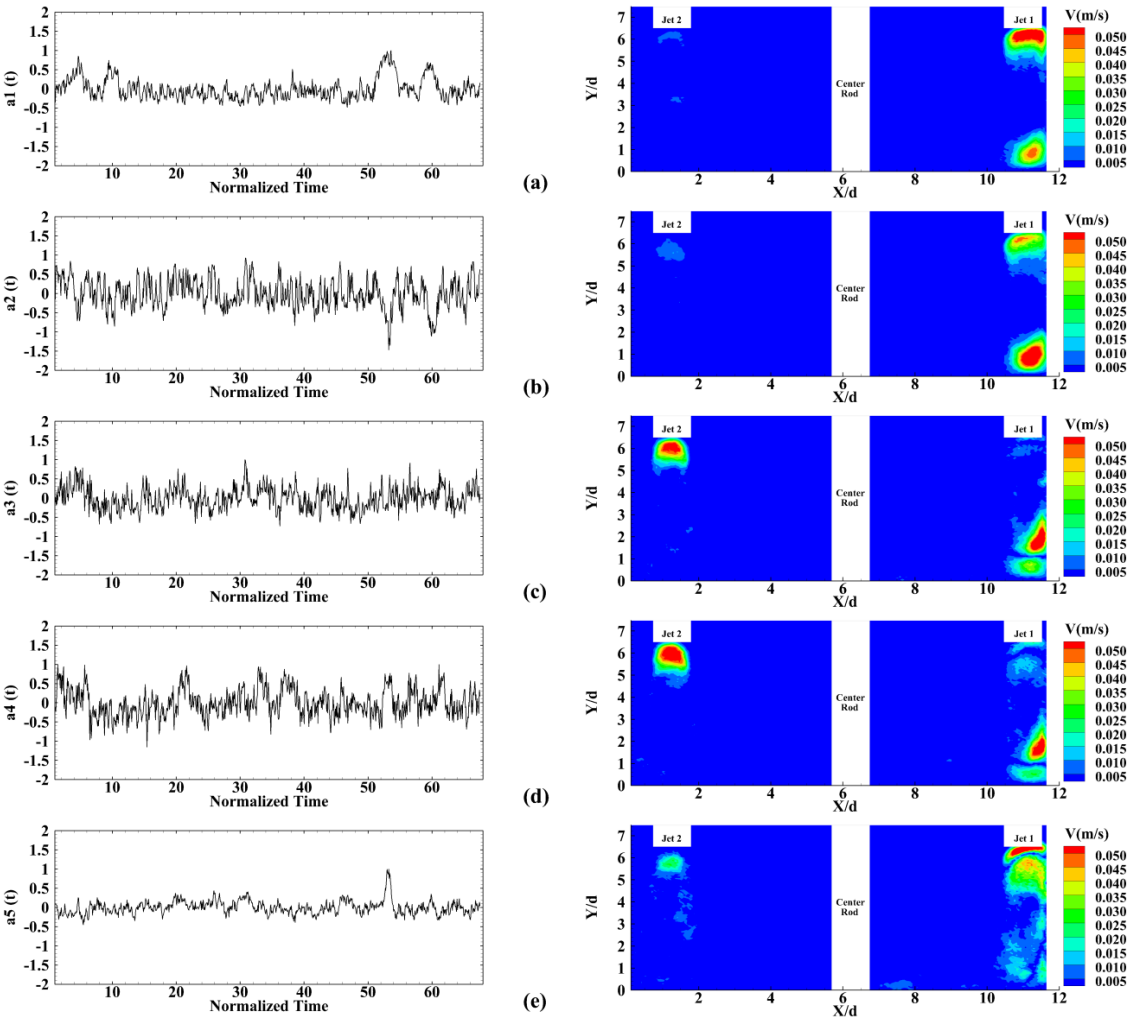

Figure II-29 Time evolution and the shape of the first five eigenmodes for dual inlet jets with $Re_{jet\ 1}$=11,160 and $Re_{jet\ 2}$= 6,250 (a) Mode 1, (b) Mode 2, (c) Mode 3, (d) Mode 4, (e) Mode 5.

II.3.7.3. POD Reconstructed Fields

As it was mentioned before, POD is a powerful tool which is used to create lower dimensional models of high dimensional systems. Moreover, POD technique provides a method to extract the large-scale coherent structures from complex flow fields by giving a cleaner view of these flow patterns; therefore, POD facilitates the study of the behavior of large-scale coherent structures that may be masked by the smaller structures within the flow field.

Here, to reconstruct the flow fields using POD technique the mean velocity which was previously eliminated from the velocity fields is added back to the field. Mean velocity is normally considered is the *Zeroth POD Mode.* The energy contribution of the mean velocity is represented in Table II-5. The energy content of the Zeroth POD Mode for the single impinging jets is consistent with the findings of section II.3.7.1.1 (see Figure II-25) which explained the fact that the higher Reynolds number of a jet leads into having a first POD mode with higher energy content. Here, 77.3% of the energy of the mean flow field is stored in the first mode for the case of single impinging jet with $Re_{jet\ 1}$=13,400 while for the lower Reynolds number jet the energy content of the first mode of the flow field decreases to 64.7% which is in agreement with the findings of Kim *et al.* (2007).

Case Study	Zeroth Mode Energy (%)	Cumulative Sum of Energy of the first 50 mode (%)
Single Jet, $Re_{jet\ 1}$=4,470	64.7	70.6
Single Jet, $Re_{jet\ 1}$=13,400	77.3	84.2
Dual Jets, $Re_{jet\ 1}$ =11,160 and $Re_{jet\ 2}$= 6,250	76.3	81.9

Table II-5 Energy content of the Zeroth POD mode and the cumulative sum of energies of the first 50 modes.

As it was mentioned before, the majority of the energy of the flow field is stored in the first few POD modes; therefore, POD reconstructed flow fields using these primary eigenmodes are expected to represent the spatial and temporal evolution of the dominant (most energetic) coherent structures in the flow field. In this investigation the first 50 modes are considered for reconstruction of the flow field using POD technique. It should be noted again that the mean flow is added to the fluctuating flow field for the reconstruction of the flow field.

II.3.7.3.1. Single Impinging Jet within the Mid-Plane

In this section, the instantaneous Z-vorticity fields obtained by PIV technique and their corresponding POD reconstructed fields are represented for two cases of single impinging jet with different Reynolds numbers. The results for each case are shown at three different time steps.

Figure II-30 shows the instantaneous and POD reconstructed vorticity fields for the case of single impinging jet with $Re_{jet\ 1}$=13,400. It is clearly seen that the instantaneous vorticity field is covered with smaller scale vortical patterns throughout the field while the POD reconstructed fields at each time step represent a cleaner view of the vorticity field by filtering the smaller scale coherent structure. In all three reconstructed fields, large vortical structures are observed in the outer layer of the jet. Moreover, the vorticity patterns seen on the opposite outer layers of the jet are almost symmetrical with different directions which are consistent with the findings of Figure II-11 (a). The presence of the large vortical structure in the shear layer of the jet at all three time steps confirm the jet entrainment phenomena and the presence of the Kelvin-Helmholtz instabilities at the shear layer of the jet. In this case, in all three time steps a part of the vortical structures occurring close to the bottom surface of the center rod is captured on the reconstructed fields.

Instantaneous and POD reconstructed vorticity fields for a single impinging jet with $Re_{jet\ 1}$=4,470 for three different time steps are represented in Figure II-31. A comparison between different plots of Figure II-30 and Figure II-31 reveals some interesting points. First, in this case it is seen that POD is successful in extracting the large-scale coherent structures from the flow field and representing the dominant flow features. The POD reconstructed fields emphasize on the larger vortical structures specifically in the jet shear layer by eliminating the small scale vorticity patterns from the flow field. This facilitates the understanding of some of the important phenomena such as the behavior of the jet in its shear layer and the entrainment process. However, in

this case, the coherent structures observed close to the center rod of the measurement plane are not fully captured in any of the three reconstructed fields. A different POD analysis approach may be needed for investigation of the evolution of those coherent structures occurring close to the center rod.

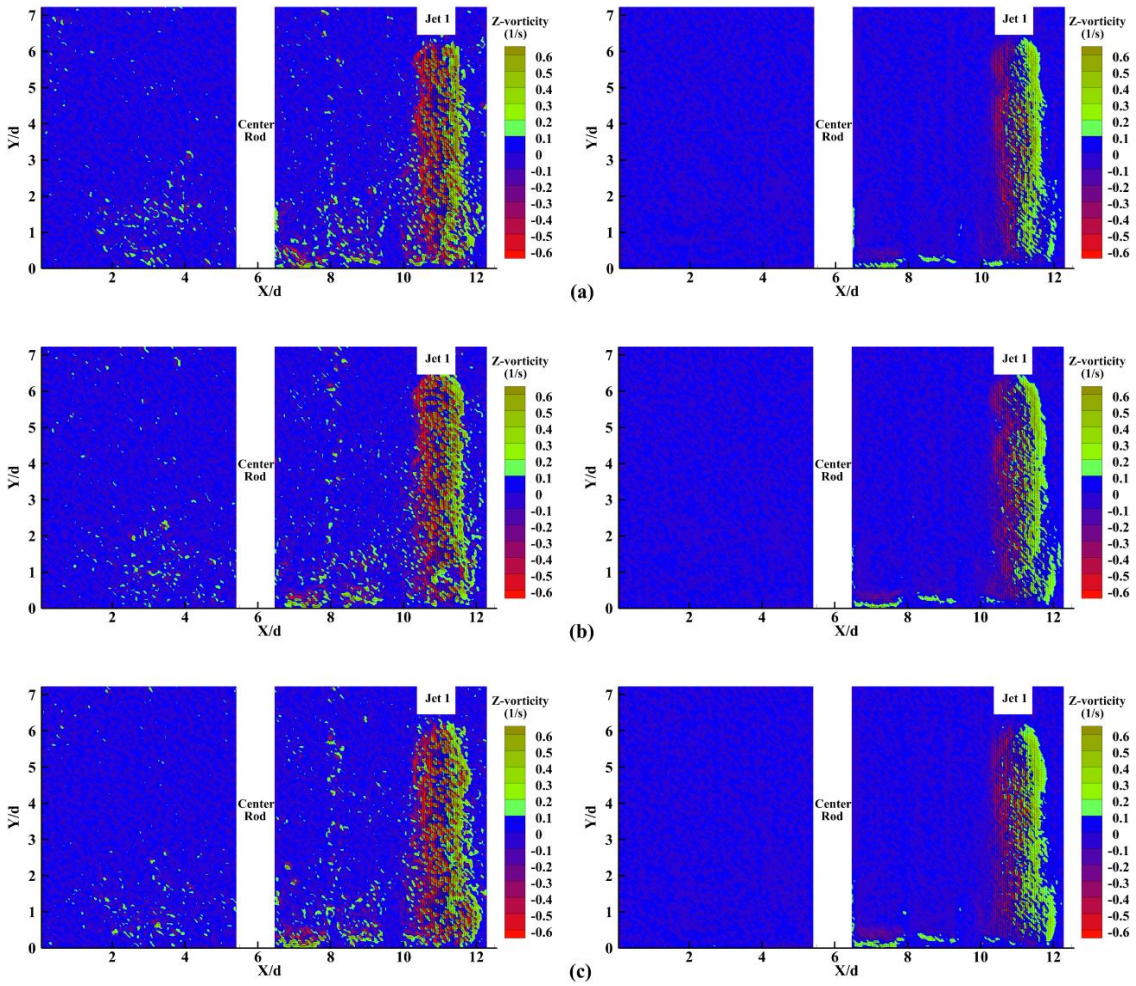

Figure II-30 Instantaneous and POD reconstructed velocity fields for single inlet jet with $Re_{jet\ 1}$=13,400 using the first 50 modes (a) t=0.05 sec, (b) t=0.15 sec, (c) t=0.25 sec.

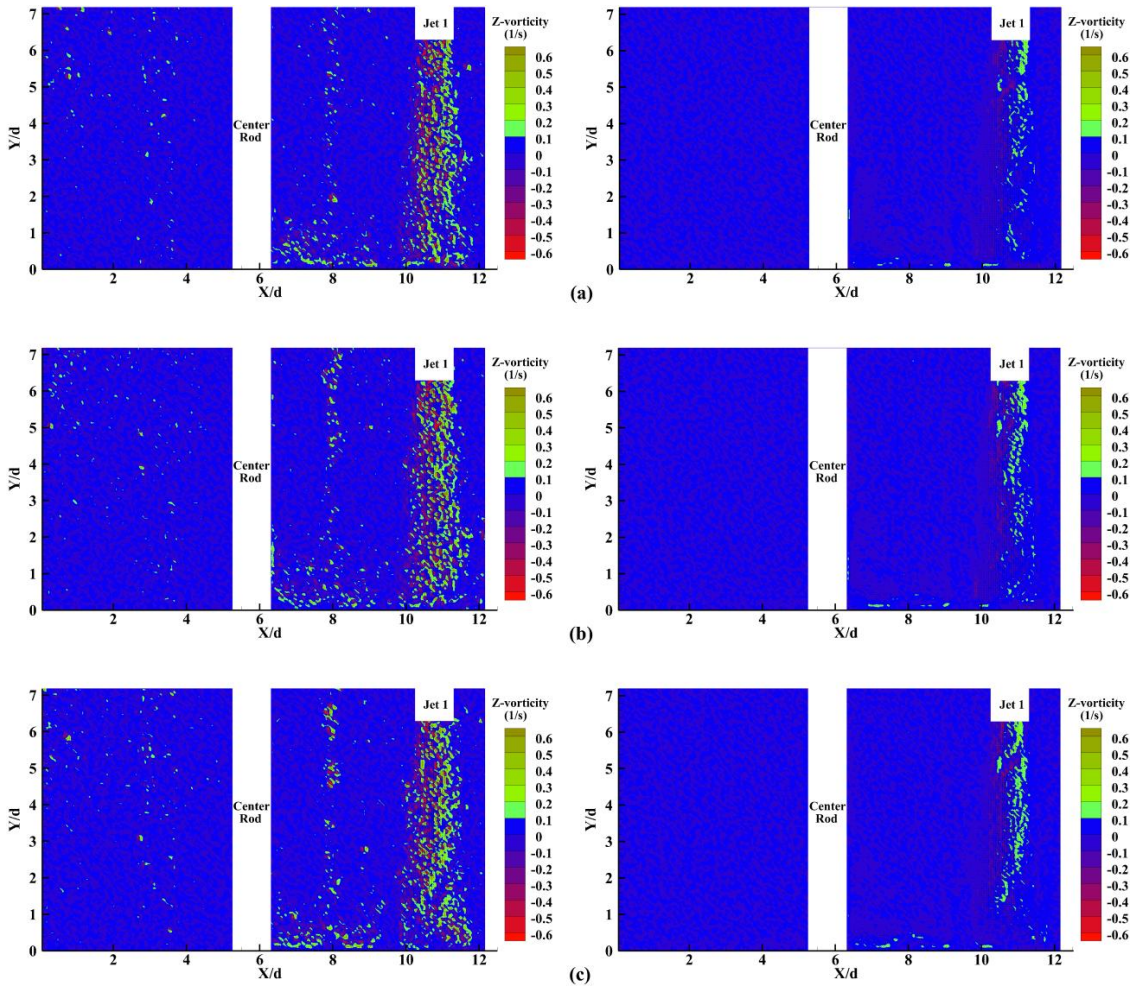

Figure II-31 Instantaneous and POD reconstructed velocity fields for single inlet jet with $Re_{jet\ 1}$=4,470 using the first 50 modes (a) t=0.05 sec, (b) t=0.15 sec, (c) t=0.25 sec.

II.3.7.3.2. Dual Impinging Jets within the Mid-Plane

In this section, the instantaneous vorticity fields of dual impinging jets for three time intervals along with their corresponding POD reconstructed field using the first 50 POD modes are represented in Figure II-32. This case is quite interesting since it represents two jets with two different Reynolds numbers and can be used to make a comparison on the performance of the POD routine in the reconstruction of each of the jets.

As observed in Figure II-32, the POD reconstructed vorticity fields represent the behavior of the jets at each time step more clearly by filtering the numerous smaller scale vorticity patterns present in the instantaneous vorticity fields. Both jets are very well captured by POD reconstruction. Moreover, as expected POD reconstruction provide a faithful image of the flow field apparent from the reconstruction of the jets with higher and lower Reynolds numbers with vorticity patterns with higher and lower magnitudes, respectively. In this case, as well as the cases of the single impinging jet the higher Reynolds number jet shows vorticity patterns with larger magnitudes and the vortical patterns in the opposite outer layers of the jet are more symmetrical compared to the lower Reynolds number jet. Furthermore, coherent structures close to the center rod are better represented on the higher Reynolds jet side; however, the vortical structures close to the center rod are not fully captured on either side of the center rod confirming the conclusion made in the previous section expressing the need for an improved POD technique to further investigate the evolution of the vortical structures close to the center rod.

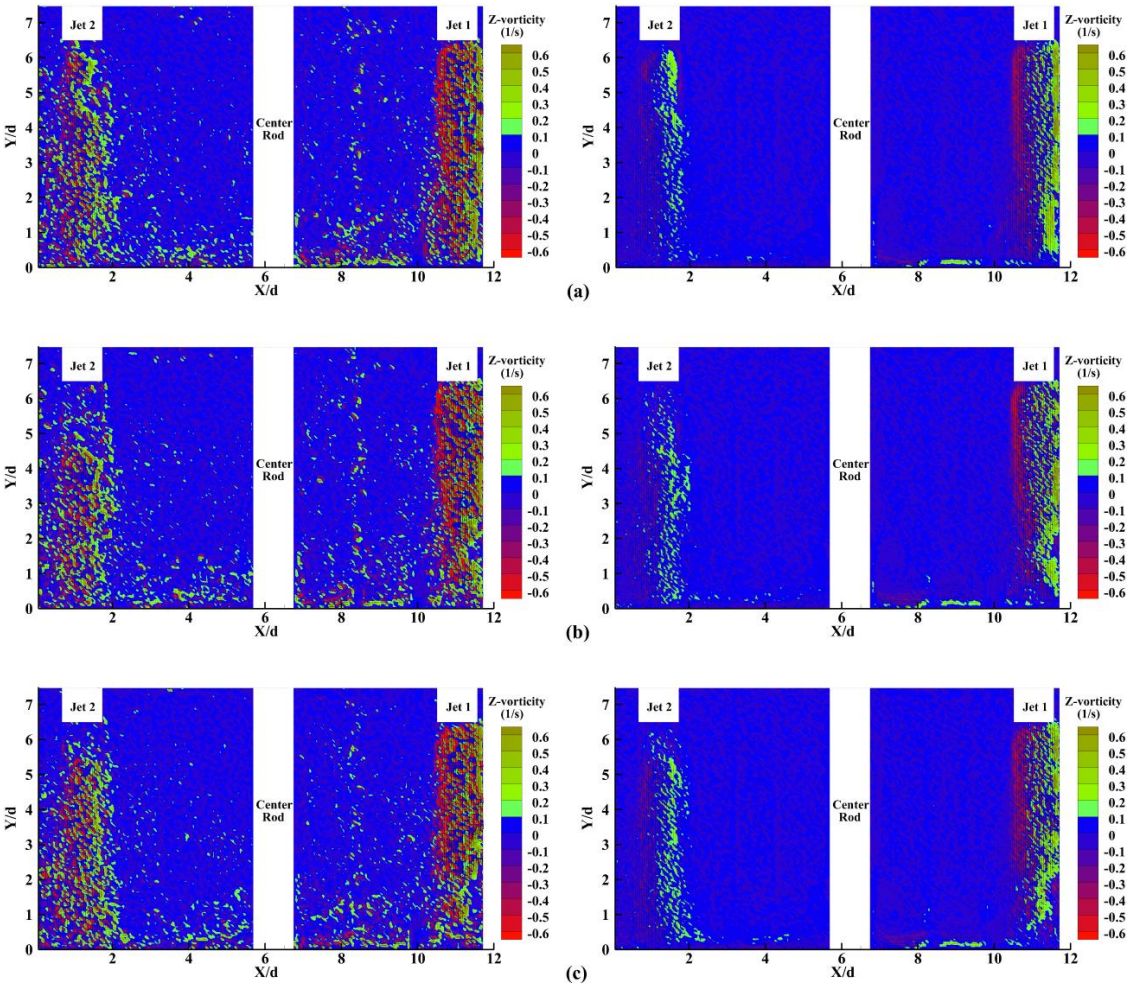

Figure II-32 Instantaneous and POD reconstructed velocity fields for dual inlet jets with $Re_{jet\ 1}$=11,160 and $Re_{jet\ 2}$= 6,250 using the first 50 modes (a) t=0.05 sec, (b) t=0.15 sec, (c) t=0.25 sec

II.3.8. POD Analysis of the Recirculation Area

As it was observed in the PIV velocity fields of all different cases, one common characteristic of all the velocity fields was the existence of a main recirculation zone and coherent structures close to bottom surface of the center rod on the jet impingement side. These vortical structures are believed to have a significant role on the enhancement of the mixing within the test section. Moreover, the presence of the coherent structures close to the rods which are representing the graphite support rods in the lower plenum of a VHTR may affect the structural integrity of the rods in long term by creating flow induced vibration on them. Also, the coherent structures existing in the vicinity of the bottom surface of the channel close to the center rod may interact with nuclear graphite comprising the bottom surface of the lower plenum and cause abrasions on the bottom surface by scouring it. Therefore, a comprehensive understanding of the behavior of this important flow feature as well as its temporal and spatial distribution is of great importance. However, as it was seen in the previous section, the spatial and temporal evolution of the key recirculation zone was not completely captured in the reconstructed vorticity fields using the first 50 POD modes. It was concluded that since this region is only a small part of the each velocity instantaneous field, it is expected to have much lower kinetic energy compared to the whole field. This could be the reason why the POD modes and the POD reconstructed fields using the first few POD modes are not able to thoroughly capture this flow feature.

In this section, a new approach is utilized for quantitative and qualitative investigation of the coherent structures occurring on the impingement side of the mid-

plane velocity fields close to the lower part of the center rod. The main objective of this approach is to comprehensively study the temporal and spatial distribution of the coherent structures happening in the vicinity of the bottom part of the center rod and the bottom surface of the channel (called *"Recirculation Area"* henceforth.) and compare their significance to the whole velocity field. For this purpose, a Snapshot POD technique has been utilized for both the whole field and the area of the coherent structure. Here, the same routine that was previously applied for the POD analysis of the whole field is utilized in which 1,000 successive frames evenly distributed over the measurement period are chosen out of the 5,000 PIV captured frames. Subsequently, the energy content of the coherent structures in the recirculation area is evaluated with respect to the whole field and the evolution of the coherent structure is investigated.

First, the boundaries of the *Recirculation Area* are obtained for each case by following the evolution of the coherent structures close to the center rod and the bottom surface of the channel through the instantaneous velocity fields obtained by PIV analysis. The *Recirculation Area* for different cases under investigation is marked in different plots of Figure II-33 by a solid red line. Subsequently, the kinetic energy content of this region is compared to the whole field to verify the assumption about the lower energy content of this recirculation with respect to the whole field. The results of this comparison are shown in Table II-6. The data presented in Table II-6 confirm the statement made about the energy of the recirculation area being much lower than the whole field. As seen in the table, the energy content of the *Recirculation Area* for different cases varies within a range of 0.17% to 2.82% of the energy content of the

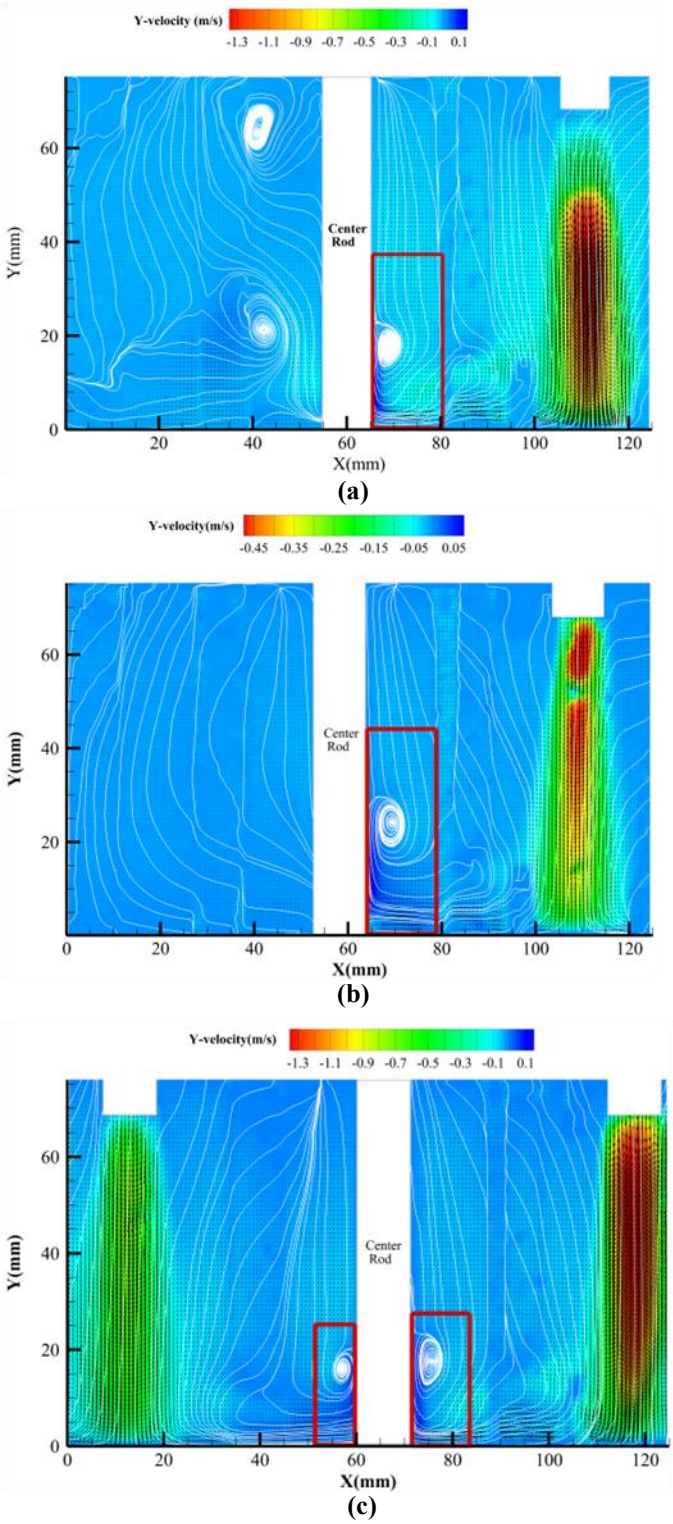

Figure II-33 Location and size of the *Recirculation Area* for different cases (a) $Re_{jet\ 1}$=13,400, (b) $Re_{jet\ 1}$=4,470, (c) $Re_{jet\ 1}$=11,160 and $Re_{jet\ 2}$= 6,250.

whole field. Therefore, to reasonably capture the relatively low energy coherent structures in the recirculation area with POD analysis, sufficient number of modes should be considered which may be larger than the number of modes needed to capture the behavior of the jet.

Case Study		$\left(\frac{E_{\text{Recirculation Area}}}{E_{\text{Whole Field}}}\right)\%$
Single Jet	$Re_{jet\ 1} = 4{,}470$	2.82
	$Re_{jet\ 1} = 13{,}400$	1.28
Dual Jets	$Re_{jet\ 1} = 11{,}160$	0.68
	$Re_{jet\ 2} = 6{,}250$	0.17

Table II-6 Comparison of the kinetic energy content of the *Recirculation Area* with the whole field.

One other solution for the detailed analysis of the *Recirculation Area* may be isolating this area from the flow field and applying POD technique to this smaller region; however, in this case no direct comparison can be made between the POD modes of the *Recirculation Area* and the whole field and each flow field is analyzed individually. This method may eventually clarify some of the features in the *Recirculation Area* which were not captured by the full-field POD reconstruction; however, the lack of direct correlation between the smaller region and the whole field makes it difficult to draw conclusions about the importance and interaction of the coherence structures in the *Recirculation Area* with respect to the whole field.

In this study, a *comparative POD* analysis method is proposed to comprehensively capture the evolution of coherent structures with lower energies with respect to the rest of the flow field. These smaller scale coherent structures may be important features of the flow and may have important roles with respect to other phenomena occurring in the flow field. The so called *Recirculation Area* in the case of the impinging jets within a rod bundle which is under investigation here is a good example of these smaller scale flow patterns having important roles in enhancing some of the important phenomena within the flow field such as the mixing phenomena or causing behavioral or structural change in other components in the flow field, for instance, possibility of creation of flow induced vibration on the center rod by the smaller-scale coherent structure present in the *Recirculation Area*.

The *comparative POD method* suggested in this study includes calculation of the energy of a specific flow feature (*Recirculation Area* in this investigation) with respect

to the whole field. Subsequently, the flow field is reconstructed using a certain number of POD modes which contain certain amount of energy of the flow field to capture the main flow features of the actual field and provide a faithful representation of the original field. The area of interest (*Recirculation Area*) is then separated from the reconstructed flow field and its energy content is compared with that of the original *Recirculation Area*. This comparison will demonstrate how well the *Recirculation Area* is reconstructed by the number of modes that were originally considered to reconstruct the flow field. Therefore, it can be concluded if a higher number of modes are required for representing a good reconstruction of the *Recirculation Area*.

II.3.8.1. Single Impinging Jet within the Mid-Plane

The results obtained by application of this *comparative POD* method are represented in Figure II-34 for the *Recirculation Area* located close to the center rod in the flow field of a single jet with $Re_{jet\ 1}$=13,400 impinging into a staggered rod bundle.

Figure II-34 provides a qualitative comparison between the *Recirculation Area* separated from the instantaneous vorticity field and its corresponding POD reconstructed fields using different number of eigenmodes. A magnified view of the *Recirculation Area* within the instantaneous Z-vorticity field of Figure II-30 (a) at time t= 0.05 sec is presented in Figure II-34. The Z-vorticity colormap is adjusted for this figure to better represent the details of the distribution of coherent structures in this region. As seen in this figure, several vortical structures with different magnitudes and directions exist in *Recirculation Area*. The details of the coherent structures present in this region were not

as obvious in the full-field plot (Figure II-30 (a)). As seen in Figure II-34 (a), vorticity patterns closer to the bottom surface of the *Recirculation Area* are of larger sizes and magnitudes compared to the ones happening close to the rod at higher Y/Ds. These larger size coherent structures were partially captured in the POD reconstructed instantaneous flow field represented in Figure II-30 (a). Figure II-34 (b) through (j) present the POD reconstructed *Recirculation Area* using different number of modes. It is clearly seen from these plots that the more number of the modes considered gives a better representation of the *Recirculation Are*; however, considering very large number of modes clearly contradicts the basic idea of the application of POD techniques which is extraction of the large-scale coherent structures from the flow field. As observed in Figure II-34, considering the first 50 modes for reconstruction of the *Recirculation Area* is not sufficient while the POD reconstruction of the whole field with the same number of modes was quite satisfactory. In the case of the *Recirculation Area*, it appears that at least the first 200 modes need to be taken to account for the reconstruction of this region for the reconstructed field to capture the vortical structures occurring in the vicinity of the center rod as well as the ones closer to the bottom surface.

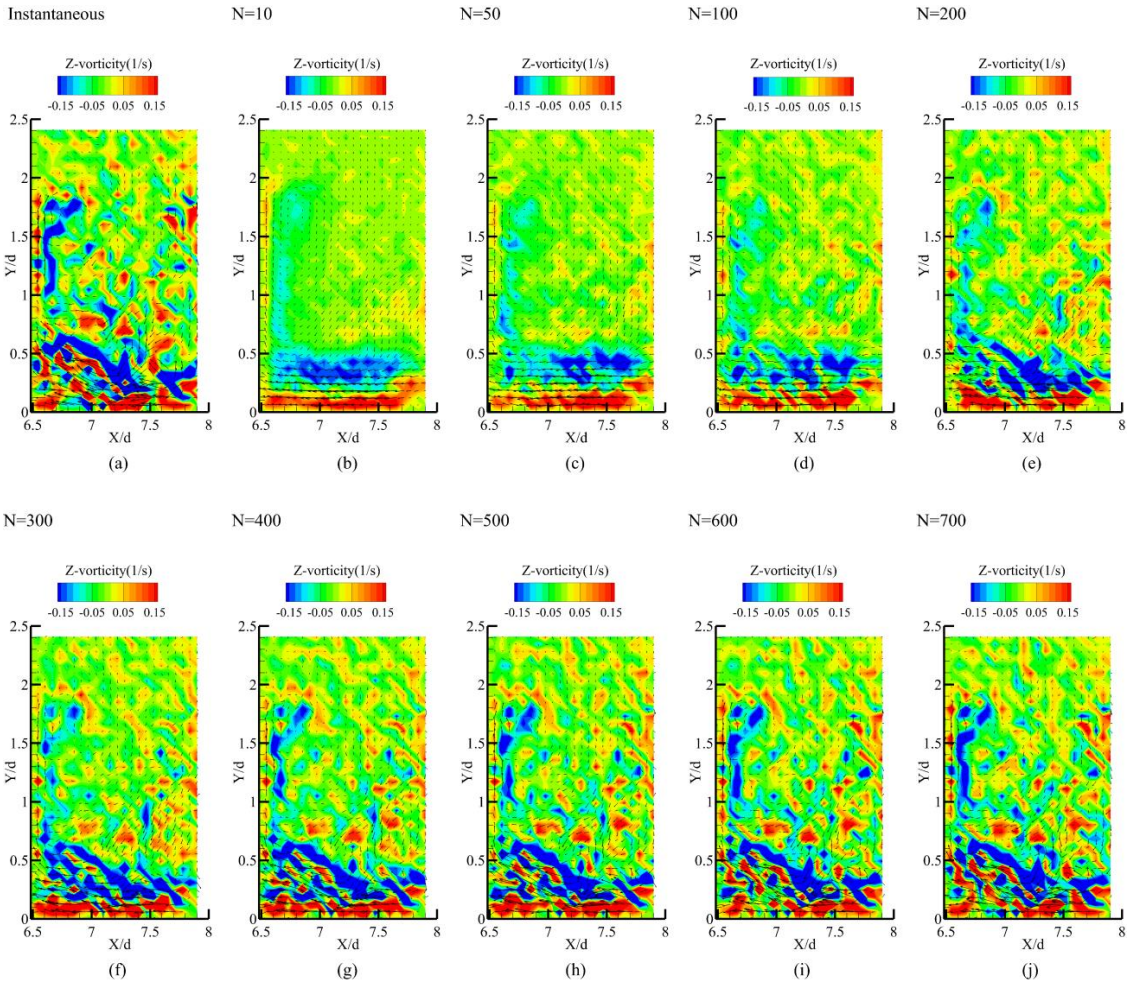

Figure II-34 *Recirculation Area* for the case of single impinging jet with $Re_{jet\ 1}$=13,400 (a) Instantaneous *Recirculation Area* at t=0.05 sec, (b)-(j) POD Reconstructed Recirculation Area with different number of modes (N: number of modes).

Figure II-35 represents the *Recirculation Area* separated from the instantaneous vorticitiy field and its corresponding POD reconstructed fields with different number of modes for a case of single impinging jet with a lower Reynolds number. A comparison between Figure II-35 and Figure II-34 clearly indicates that in the lower Reynolds jet case the size and magnitude of the vorticity patterns within the *Recirculation Area* are noticeably smaller than those observed in Figure II-34. This is an indication of how the jet's Reynolds number affect the flow structure close to the center rod as well as close to the bottom surface of the channel since the larger and stronger these coherent structures are the more they will affect the rod and the bottom surface of the channel. Another interesting point observed from Figure II-35 and the reconstruction of the coherent structures in this case is that it seems like more number of modes needs to be considered for a reliable reconstruction of the field compared to Figure II-34. Here, reconstructed field using 400 modes show a better representation of the original recirculation area. It is worth remembering that in the lower Reynolds number impinging case represented in Figure II-31 (a) reconstructed with the first 50 modes, a less significant trail of the coherent structures close to the center rod was observed compared to the reconstructed field of the higher Reynolds jet shown in Figure II-30 (a). The reason behind that became quite clear here by comparing the number of modes needed in the two cases to have an acceptable representation of the *Recirculation Area*.

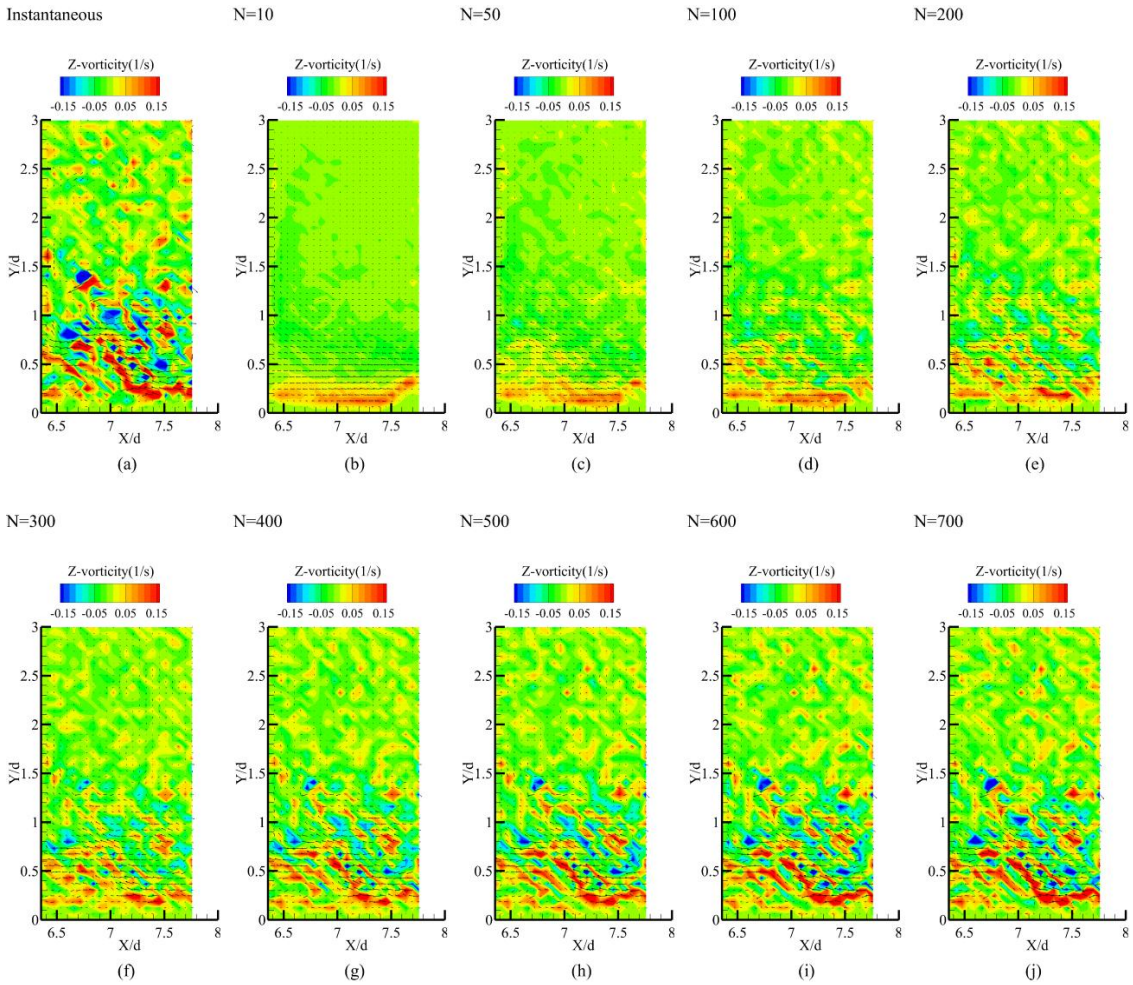

Figure II-35 *Recirculation Area* for the case of single impinging jet with $Re_{jet\ 1}$=4,470 (a) Instantaneous *Recirculation Area* at t=0.05 sec, (b)-(j) POD Reconstructed Recirculation Area with different number of modes (N: number of modes).

II.3.8.2. Dual Impinging Jets within the Mid-Plane

The instantaneous and the POD reconstructed plots for the two *Recirculation Areas* observed on each side of the center rod for the case of dual impinging jets with two different Reynolds numbers are separately presented in Figure II-36 and Figure II-37. The results shown in both figures confirm the observations made from Figure II-34 and Figure II-35. The Recirculation Area on the side with the higher Reynolds number jet has larger vortical structures with bigger magnitudes compared to the Recirculation Area on the lower Reynolds number jet which in turn confirms the fact that there exists an active interaction between the jet flow, the center rod, and bottom surface of the channel which might lead into having flow induced vibration on the rod or abrasions of the bottom surface of the channel.

Also, the number of modes needed for a reliable reconstruction of the *Recirculation Area* on the higher Reynolds jet side is approximately 200 modes while this number is increases to around 400 for the *Recirculation Area* on the lower Reynolds number jet side.

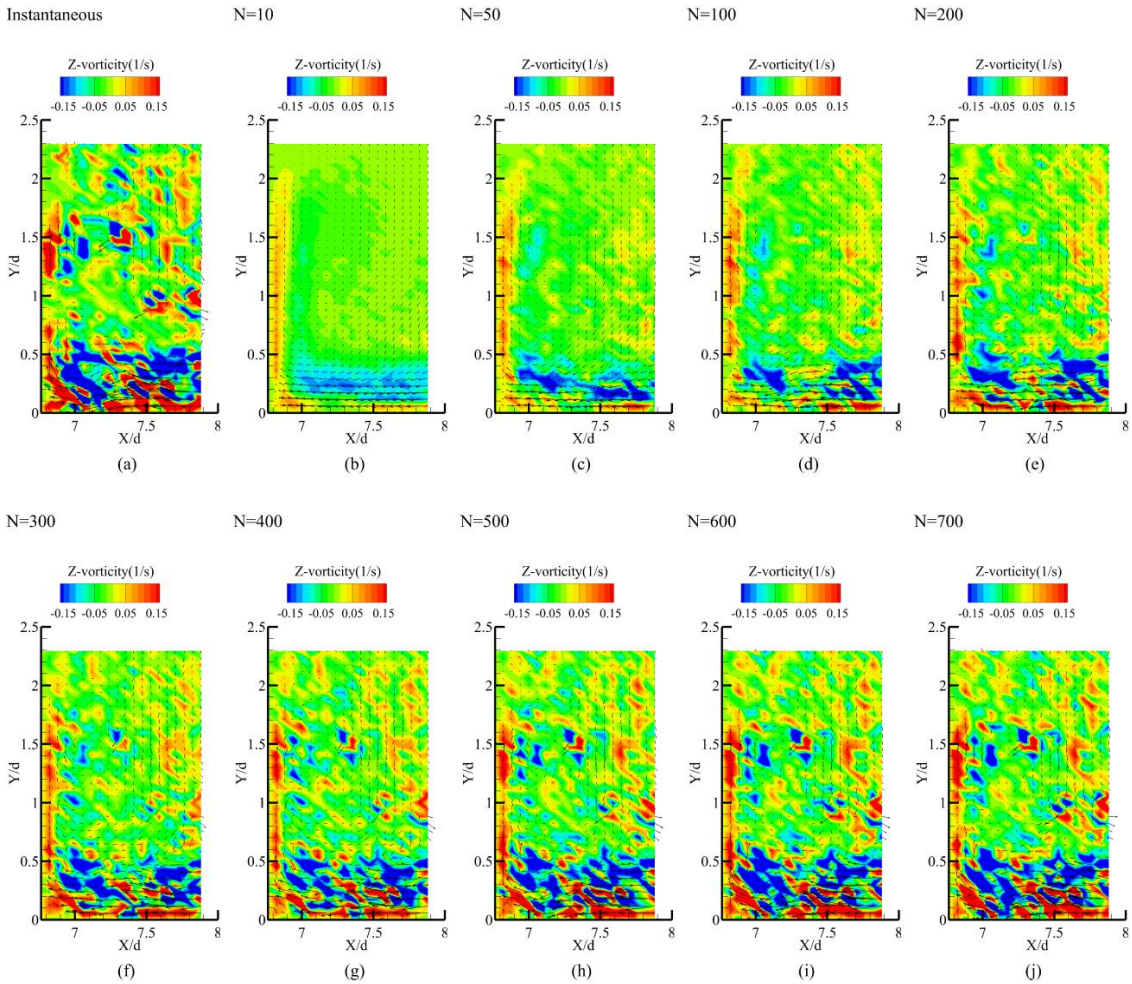

Figure II-36 *Recirculation Area* for the case of dual impinging jets on the higher Reynolds jet side ($Re_{jet\ 1}$=11,160) (a) Instantaneous *Recirculation Area* at t=0.05 sec, (b)-(j) POD Reconstructed Recirculation Area with different number of modes (N: number of modes).

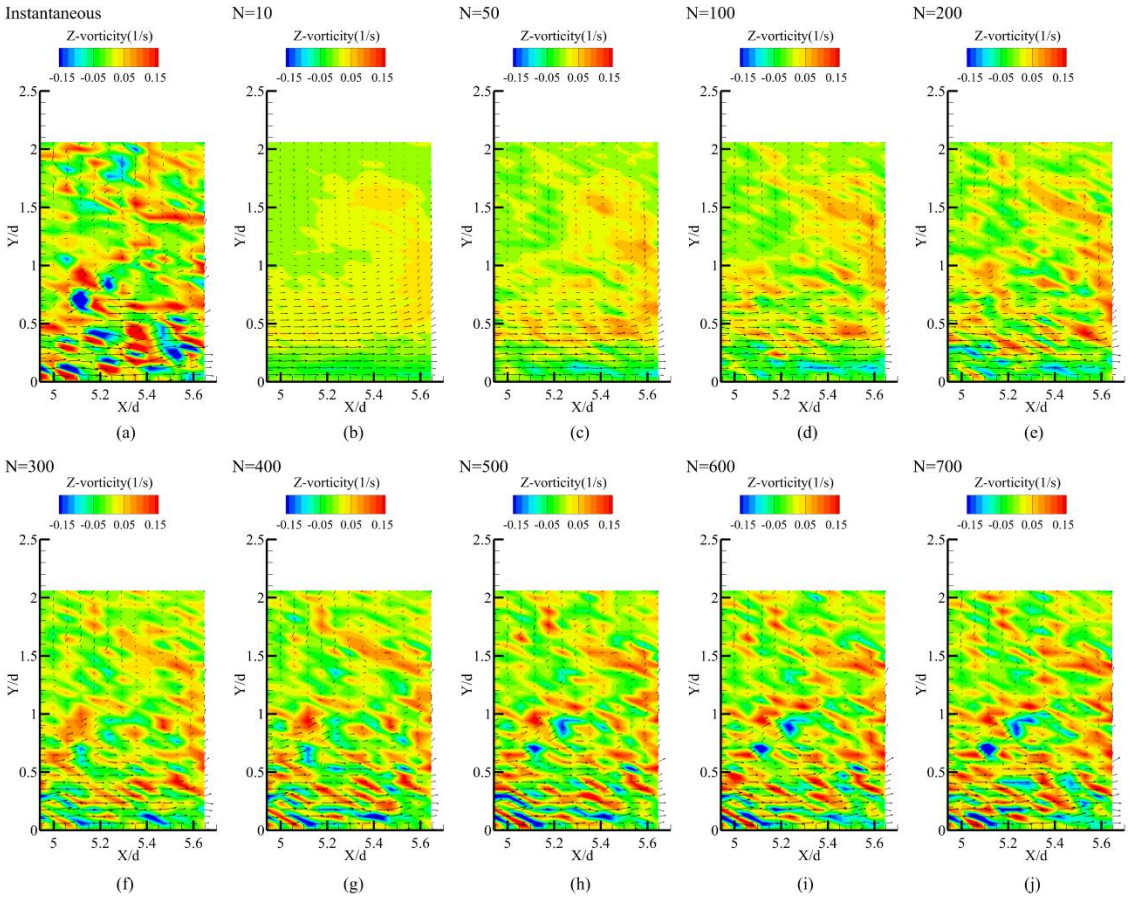

Figure II-37 *Recirculation Area* for the case of dual impinging jets on the higher Reynolds jet side ($Re_{jet\ 2}$= 6,250) (a) Instantaneous *Recirculation Area* at t=0.05 sec, (b)-(j) POD Reconstructed Recirculation Area with different number of modes (N: number of modes).

Table II-7 provides a quantitative comparison between the energy of the separated *Recirculation Area* from the instantaneous field and its corresponding POD reconstructed area by presenting the ratio of the energy content of the reconstructed *Recirculation Area* with certain number of modes to that of the original *Recirculation Area*.

Number of Modes	$\left(\frac{E_{\text{Reconstructed Recirculation Zone}}}{E_{\text{Recirculation Zone}}}\right)\%$			
	Single Jet		**Dual Jets**	
	$Re_{jet\ 1}$=4,470	$Re_{jet\ 1}$=13,400	$Re_{jet\ 1}$=11,160	$Re_{jet\ 2}$= 6,250
N=10	56.9	53.5	60.6	54.9
N=50	60.9	61.5	64.4	58.0
N=100	64.0	64.7	68.0	61.4
N=200	69.2	70.5	73.0	66.7
N=300	74.0	75.5	77.0	71.5
N=400	80.6	80.0	81.0	76.0
N=500	82.6	84.2	84.6	80.4
N=600	86.7	88.1	88.2	84.6
N=700	90.4	91.7	91.5	88.7

Table II-7 Relative energy of the POD reconstructed *Recirculation Area* using different number of modes compared to that of the original *Recirculation Area.*

One significant point observed in Table II-7 is that the ratio of the e energy content of the reconstructed *Recirculation Area* with 200 modes to that of the original *Recirculation Area* seems to be close for the two cases of single inlet jet with different Reynolds numbers. The energy ratio of the reconstructed to original is *Recirculation Area* is 69.2% for the case of reconstruction with 200 modes for the jet with a Reynolds number of 4,470 and this number only increases to a value of 70.5% for the higher Reynolds jet with a Reynolds number of 13,400. It is significant to notice that from the reconstructed *Recirculation Area* plots in Figure II-35, it seemed like more number of modes (approximately 400 modes) are needed for a better reconstruction of the *Recirculation Area*. However, the difference between the energy ratios of the reconstructed to original is *Recirculation Area* for the dual inlet jet case is much more significant which emphasizes on the fact that more number of modes are needed to reconstruct the lower energy content *Recirculation Area*. Therefore, both factors, i. e. the qualitative comparison between the coherent structures in the reconstructed *Recirculation Area* and in the original *Recirculation Area* as well as a quantitative comparison between the energy content of the reconstructed and original *Recirculation Area* while choosing the number of modes needed for the reconstruction of *Recirculation Area*.

II.4. Conclusion

In this investigation, the mixing of impinging jet flows of various Reynolds numbers into a rectangular channel containing a staggered rod bundle has been studied experimentally through the use of 2-D PIV and MIR techniques. The experiment included both single and dual jet flows over a Reynolds number range of 4,470 - 13,400, with data obtained for three separate planes within the interrogation volume. For each case, the time-averaged velocity fields and the instantaneous vorticity fields were obtained for the investigated flow conditions. Furthermore, the line-probes of different flow statistics were obtained for three different heights of the channel to study the jet flow evolution in the channel. The results show that using PIV techniques in a Matched Index of Refraction facility enabled the study of the flow field characteristics in regions within the rod bundle which are normally visually obstructed.

The time-averaged velocity fields of the mid-plane for the single jets identify the presence of one primary recirculation zone located close to the center rod on the impinging side. The size of this recirculation zone varies directly with the magnitude of the jets' Reynolds number. The time-averaged velocity field of the dual impinging jets confirms the presence of a key recirculation zone at each side of the center rod whose sizes changes proportionally with the jets' Reynolds numbers. The higher the Reynolds number of the jet is, the larger is the size of the major recirculation zone that forms near the adjacent rod. However, no such conclusion can be made about the location where the recirculation zone appears, it could only be said that the position in which the main

recirculation zone happens changes with the jets' Reynolds number, but no further conclusion can be made with the present data.

Studying the spatial distribution of vorticity confirms streamtrace observations where flow was shifted towards the jets due to strong vorticity structures found in the outer regions of each impinging jet. This verifies the fact that the jet entrains some of the channel flow in its outer regions. However, it is found that less mixing occurs in the center of the jets than in the outer regions. In addition to that, in all of the cases, several smaller vorticity patterns appear throughout the interrogation area.

Comparing the line-probes of the Y-velocity component and X-velocity components for different heights of the channel shows that the X-velocity component has a much less significant contribution towards the calculation of the mean velocity compared to Y-velocity component. Also, the line-probes of the Y-velocity component show that the jet's velocity - especially at its core - decreases as it gets closer to the channel's bottom surface.

By analyzing the line-probes of the turbulence intensities of Y-velocity and X-velocity components and the Reynolds shear stresses for different heights of the channel it was found for nearly all the cases that the highest values appear in the regions where the jet impinges. Particularly, for the higher Reynolds number jets, the maximum turbulence intensity of Y-velocity component is significantly higher than the maximum turbulence intensity of X-velocity component. While, for the lower Reynolds number jets, the values of maximum turbulence intensities of Y-velocity and X-velocity components are relatively close to each other.

The line-probes of the Y-velocity were taken at the same height for three different planes inside the rod bundle. They show that the major velocity fluctuations happen in the impinging plane for all cases. Otherwise, there only exist minor velocity fluctuations in the other two planes.

This study has indicated the presence of one key recirculation zone near to the closest rod to each jet. The combination of these recirculation zones along with the vorticity patterns at the outer regions of the jet, the smaller vortex structures found throughout the interrogation area, and the high values of turbulent intensities and Reynolds shear stresses in the jets' impinging area, all aid in the enhancement of mixing within the channel.

To obtain a better understanding of the behavior of the vortical structures present in the flow field and to extract the large-scale coherent structures from the velocity fields of the impinging jets within the rod bundle, the Snapshot POD technique was applied to the instantaneous PIV velocity fields. The results confirm that the majority of the energy of the flow field is stored in the first few primary eigenmodes; therefore, a lower-order model of the flow field can be reconstructed using these primary eigenmodes. Moreover, the increasing trend observed in the energy content of these primary modes with the increase in the Reynolds number for cases of single impinging jet compares well with the findings of the study done by Kim *et al.* (2007), even though the Reynolds number of the jets in this study are much higher than those in the investigation performed by Kim *et al.* (2007).

Subsequently, the mode shapes and amplitudes of the modes for the first five POD modes are obtained for two cases of single and dual impinging jets. It was observed that in the case of single impinging jet, the first few modes mainly capture different parts of the jet and other key flow features that were previously observed in the velocity fields are not fully captured with these modes. This led to the conclusion that the jet flow is the dominant feature of the whole field because of its high levels of kinetic energy compared to the other flow features within the velocity field. Therefore, the primary POD modes will mainly capture the high energy jet flow. This becomes even more interesting in the case of dual impinging jets with different Reynolds numbers. In this case, the first two modes only represent parts of the higher Reynolds jet. It is not until the third mode shape that a part of the lower Reynolds number jet is captured by the mode shapes.

The POD reconstructed vorticity fields using the first 50 modes offer a lower order model of the instantaneous vorticity fields. The reconstructed POD fields capture the large-scale vorticity patterns in the shear layer of the jets quite well; and present a clearer image of the large-scale coherent structures that may be covered by the presence of the smaller vertical structures within the instantaneous fields. However, the energy content of the main recirculation zone happening close to the center rod in the velocity fields are not fully captured in the POD reconstructed fields and this is consistent for cases with single and dual impinging jets with different Reynolds numbers.

A *comparative POD* analysis method was proposed here to further study the evolution of the coherent structure existing in the *Recirculation Area* close to the center

rod of the velocity field. As it was mentioned before, the importance of these set of coherent structures is due to their role in enhancement of mixing within the channel as well as their potential effect on the structural integrity of the center rod and the bottom surface of the channel through flow induced vibration and scouring processes, respectively. In this *comparative POD* method, the *Recirculation Area* is first separated from the flow field and its energy content is compared to that of the original flow field. It was observed that for all cases the energy content of the *Recirculation Area* was below 3% of the energy of the whole field. Therefore, it was concluded that to reasonably capture the evolution of the coherent structures in this *Recirculation Area* more number of modes need to be considered for POD reconstruction with respect to the number of modes which may be sufficient for reconstruction of the whole field or other high energy flow features e.g. jet flow. Consequently, the *Recirculation* Area was reconstructed with different number of modes and at each step its energy content was compared to that of the original area defined as *Recirculation Area*. It was observed that while the whole field may be well reconstructed using the first 50 POD modes, a higher number of modes are needed for a reasonable reconstruction of the coherent structures in the *Recirculation Area.* Moreover, to find the sufficient number of modes for faithful reconstruction of the *Recirculation Area*, a qualitative comparison between the coherent structures in the original and reconstructed *Recirculation Area* as well as a quantitative comparison between the energy content of the two regions is required.

The data presented in this study could serve as a benchmark for validation of the CFD codes used to simulate the lower plenum flows and their mixing. The complexity of

the behavior seen in these regions requires additional investigation to properly characterize the behavior of the thermal jets and their mixing properties.

CHAPTER III

EXPERIMENTAL STUDY OF BYPASS FLOW IN DIFFERENT NEAR WALL GAP GEOMETRIES OF A PEBBLE BED VHTR

III.1. Background

Characterization of the fluid flow behavior within packed beds is essential in a wide variety of engineering systems such as chemical engineering fluidized beds, packed bed nuclear reactors, oil recovery, and filtration systems. Fluid flow through porous media has been studied for decades in the field of chemical engineering and has recently received much attention in the field of nuclear engineering due to the extensive research being done on the pebble bed core VHTR concept as one of the main candidates for NGNP program. The core of a pebble bed VHTR is composed of spherical TRISO coated fuel particles which are randomly stacked in an annular bed. Characterization of the flow velocity within the packed beds are of great significance since heat, mass, and momentum transfer through the packed beds is quantitatively correlated to the coolant velocity profile within the bed. Therefore, the study of complex coolant flow behavior in gaps between the spherical fuel elements in the core of pebble bed VHTRs is highly important in the development of such reactors.

Research studies performed on the distribution of the fluid flow through packed beds indicated the complex nature of the flow passing through the gaps between the randomly stacked pebbles. Fluorescent PIV technique in conjunction with MIR was

applied by Northrup *et al.* (1991, 1993) to measure low flow velocities in the interstitial regions of a porous medium which resulted in making conclusions about the existence of intra-pore mixing within the porous medium. Hassan (2007) used Large Eddy Simulation (LES) technique to simulate the helium flow within a segment of pebble bed core where the coolant Reynolds number was 8×10^5. Also, an experimental facility representing the pebble bed core was used to measure the velocity in the fuel gaps. In this experiment Particle Tracking Velocimetry (PTV) and Matched Index of Refraction (MIR) techniques were used to measure the velocity in the mid-plane of the packed bed. Both LES results as well as the experimental results show very complex flow structures within the gaps between the fuel elements. Hassan & Dominguez-Ontiveros (2008) applied Particle Image Velocimetry (PIV) along with MIR technique to obtain the full-field velocity measurements in the interior region of a randomly packed bed. Vortical structures were identified in some of the pores between the spheres while there were some flows with preferential direction in some other pores. On the whole, it was observed that the flow in the pores is of a very complicated nature. Lee & Lee (2009) used PIV to visualize the flow within a scaled up test facility representing the core of a pebble bed high temperature gas cooled reactor. A Reynolds number of 2.1614×10^4 was chosen for this experiment to match the Reynolds number in the core of an actual pebble bed gas cooled reactor. The results show that the presence of stagnation points within the fuel gaps might lead to having hot spots on the surface of the fuel particles.

Moreover, previous experimental and numerical research studies performed on flow distribution within packed beds have indicated that velocity profiles within the bed

significantly changes in the vicinity of the packed bed wall reaching a maximum in the near wall region. This sharp peak in the flow velocity profile close to the packed bed wall is considered a form of *Bypass Flow* (also called *Flow Channeling*). *Bypass flow* has been observed in chemical packed beds with different sizes and shapes of the bed and also various sizes and shapes of the packing pellets. In an investigation done by Schwartz & Smith (1953), the air velocities measured by a hot wire anemometer above the packed bed for different pipe sizes and different pellet shapes and sizes illustrate a peak in the velocity at approximately one pellet diameter away from the wall. The results of HWA velocity measurements above a cylindrical packed bed with air passing through it done by Marivoet *et al.* (1974) indicates peaks in the radial mean velocity profile close to the container wall. Johnston *et al.* (1975) applied LDA technique along with MIR technique in a hexagonal packed bed facility to obtain the axial velocity of the fluid passing through the bed which showed large velocities in regions close to the wall. Velocity profiles of the air passing through a packed bed column obtained by Drahoš *et al.* (1982) at the exit plane of the bed using HWA technique indicated a well-pronounced maximum in the vicinity of the wall for sphere and cylindrical pellets. Vortmeyer & Schuster (1983) developed a method for calculation of the flow distribution within packed bed columns through which they obtained a sharp peak on the velocity profile near the wall. Another model for velocity distribution through packed beds was developed by White & Tien (1987). The predictions of this model was in good agreement with previous numerical results and the experimental velocity profiles obtained at the exit of the packed bed in showing the flow channeling phenomena close

to the packed bed wall. In an investigation done by Ziólkowska & Ziólkowski (1988), the radial profile of the flow inside a packed bed was determined through LDA experiments as well as calculated on the basis of the Dupuit-Drochheimer hypothesis for different pellet sizes. The air flow profiles obtained through both approaches verified the presence of a region of higher velocity close to the packed bed container wall. Moise & Tudose (1998) obtained the local velocities of air passing through long packed beds (L/D>1) for different pebble sizes and for different Reynolds numbers (Re=100-400). The velocity measurements in the bed were obtained by a thermo-anemometer passing through a free zone with a 20 mm height. The velocity distributions are shown to be strongly affected by the local porosity, pellet diameter, bed length and diameter, and the Reynolds number. The results confirm the existence of a region of higher velocity adjacent to the wall. The results of some other experimental studies on the flow distribution within the packed beds revealed a different flow pattern than the velocity profile obtained by the investigations that have been mentioned so far (i.e. presence of a sharp peak in the radial velocity profile close to the packed bed container wall). For instance, in a study done by Lerou & Froment (1977), the velocity profiles obtained by HWA technique downstream the packed bed for different air flowrates showed more than one peak. More interestingly the peak close to the wall was not necessarily the highest one. They emphasized on the fact that rearrangement of the structure of the packing significantly affected the velocity profile and in some cases resulted in obtaining the classical velocity profile with one sharp peak at the wall.

Many research studies have confirmed that the flow behavior and consequently heat, mass, and momentum transfer through packed beds are directly correlated to the porosity of the bed as well as the individual pore geometries. In fact, many studies have related the *Bypass Flow* phenomena to the increased porosity close to the solid wall of the packed bed. Therefore, a variety of theoretical, experimental and numerical techniques have been applied to calculate/measure the porosity profiles within packed beds. One of the early experimental porosity studies of the packed beds was done by Roblee *et al.* (1958) where the radial porosity variations within a cylindrical cardboard packed bed was measured for different cases with different types of packing (spheres, cylinders, etc.). The results confirmed that the packed bed wall has a significant effect on the porosity of the bed in areas close to the wall meaning that the bed porosity was much higher close to the container wall. Other studies such as the investigation done by Goodling *et al.* (1983) confirmed the results obtained by Roblee *et al.* (1958) showing a porosity value of one at the container wall which then oscillates around the mean porosity value with a decreasing amplitude. Fluid flow passes within the packed bed through the free gaps between the packing material meaning that the flow chooses the paths of least resistance between the pebbles to flow through the bed. Therefore, the sharp peak in the velocity profile of the fluid flow corresponds well to the maximum porosity value close to the packed bed wall.

In the present study, HWA technique will be applied to obtain high frequency velocity measurements in the gaps between the pebbles in areas close to the outer reflector wall of an annular packed bed for different Reynolds number of the flow

passing through the bed. Subsequently, time-averaged velocity fields for each point is calculated and the average velocity profiles of the flow within the near wall gaps are obtained for different Reynolds numbers. Moreover, the time histories of the velocities obtained at each measurement point and for different Reynolds numbers will be further analyzed utilizing Power Spectra Density (PSD) method to acquire a more in-depth insight of the turbulence characteristics of the flow within the near wall gaps of an annular packed bed.

III.2. Experimental Methodology

III.2.1. Experimental Set-up and Flow Configuration

Schematic of the test facility which is designed to model the core of an annular pebble bed VHTR in this investigation is presented in Figure III-1 (a). In addition to the schematic of the whole test facility, a picture of the test section modeling the annular packed bed along with pictures of a sample measurement point and the location of the HWA probe in the gap is shown in Figure III-1 (b). As seen in Figure III-1, the test facility used for this study is an annular bed containing spheres representing the spherical TRISO coated fuel elements. The outer cylinder is made of clear Acrylic with a height of 2.18 m and an outer diameter of 0.89 m. The radius of the annulus inside the cylinder is 0.27 m. The experimental setup is designed to accommodate both PIV and HWA measurement techniques. Therefore, as seen in Figure III-1 (b), two different types of spheres are used to stack the annular bed: 1- Black spheres made of plastic with a diameter of 0.03302 m used in the upper and lower sections of the bed, 2-Clear spheres

made of Acrylic with a diameter of 0.03175 m used in the middle section of the annular bed. The area packed with clear Acrylic spheres will be used for PIV measurements to provide optical access to regions inside the packed bed. The Acrylic spheres are chosen to have nearly the same size of the black plastic spheres to ensure an approximately uniform porosity throughout the bed. In this experiment, air is chosen as the working fluid instead of helium and it is passed through the bed using a high power blower. The velocity of air passing through the gaps between the pebbles is measured in certain locations of the bed using HWA technique. Four evenly spaced sets of holes (columns A to D, as shown in Figure III-1) are made through the circumference of the cylinder. Each set has ten equally spaced holes (0.17 m apart) along the cylinder height which could be used for air velocity measurements within the gaps close to the packed bed wall. Since the annular bed is randomly packed, it is expected to have holes which are blocked by the presence of the spheres; therefore, not every single hole could be used to take hot wire measurements.

In this study, two different near wall gaps with significantly different geometries at different heights and on different measurement columns of the bed are used for velocity measurements (gaps A4 and B6). Figure III-2, represents pictures of the two measurement gaps and the three dimensional reconstructions of the gap geometries. It can be visually seen from Figure III-2 that Gap B6 is much deeper than Gap A4.

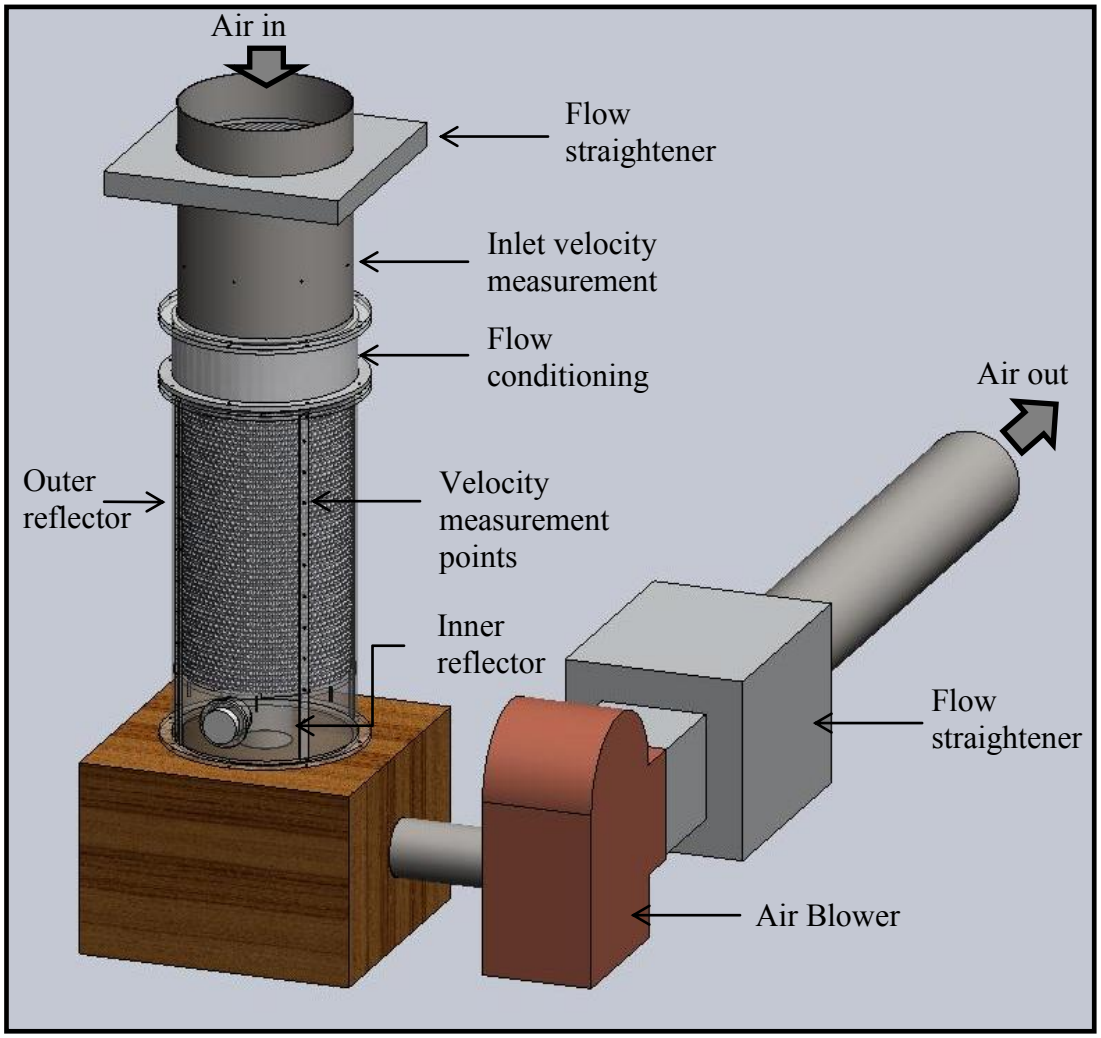

(a)

Figure III-1 (a) Schematic of the experimental facility representing an annular packed bed, (b) Picture of the model representing a packed bed and the measurement points.

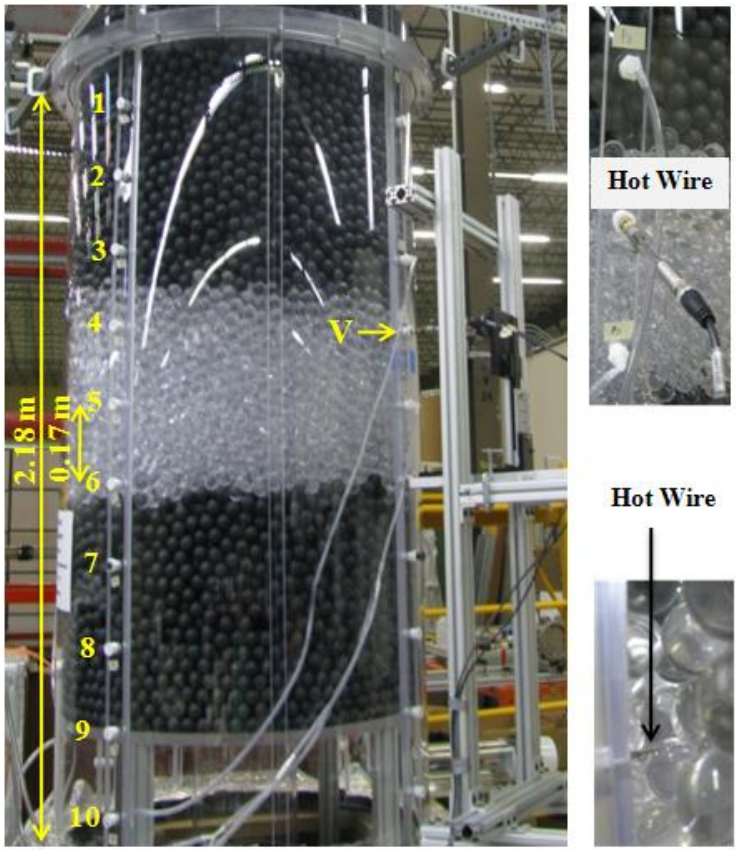

(b)

Figure III-1 Continued.

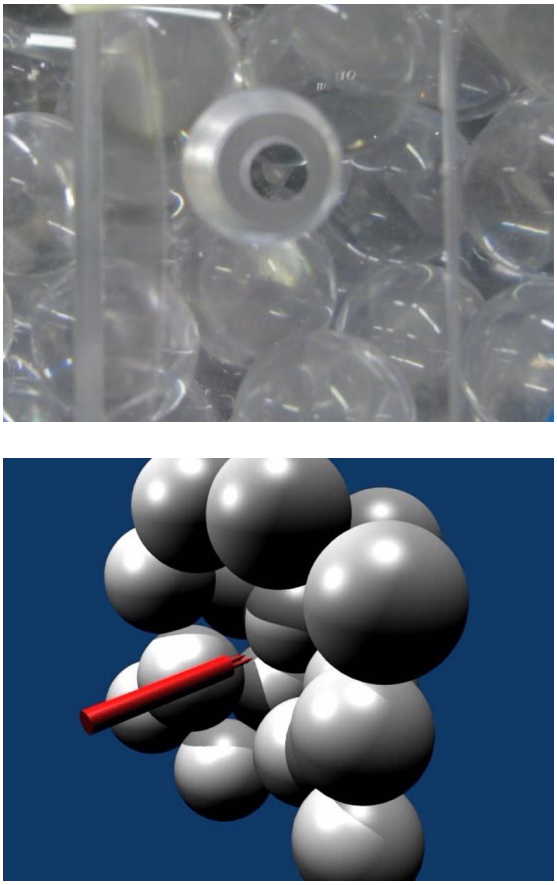

(a)

Figure III-2 Picture and three dimensional reconstruction of near wall gap geometry (a) Gap A4, (b) Gap B6.

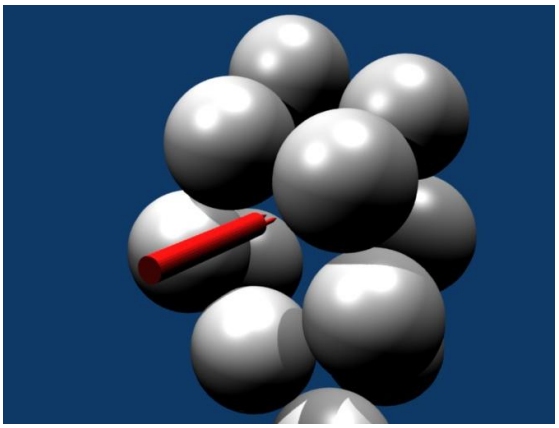

(b)
Figure III-2 Continued.

In order to obtain the velocity profile within each gap, the HWA probe is moved within the gap along a straight line in radial direction with very fine increments. For Gap A4, the measurement points have been chosen to be 0.5 mm apart (starting from 0.5 mm far from the outer cylinder wall) for the first 3mm of the depth of the gap and 1mm apart from 3mm up to the end of the gap resulting in having a total of 18 velocity measurement points along the radial direction within the gap (see Figure III-3 (a)). For Gap B6, the first 18 points are chosen in the same manner that measurement points within gap A4 were selected. However, since this gap is significantly deeper than gap A4, for the rest of the depth of the gap (starting from 15 mm from the outer cylinder wall) seven more points each being 5 mm apart are chosen for velocity measurements. Therefore, for this gap (B6) a total of 25 points are selected for velocity measurements within the depth of the gap in the radial direction (see Figure III-3 (b)). It should be noted that for both gaps, the last point for the velocity measurements is chosen in a way to be approximately 5 mm away from the sphere blocking the end of the gap.

At each measurement point within each gap, the velocity measurements have been acquired using HWA technique. To ensure a good accuracy for the velocity measurements at each point the measurements have been repeated three times and average values of those readings are recorded to acquire the velocity profiles within each gap. The velocity profiles in each gap have been obtained for five different air flowrates through the packed bed.

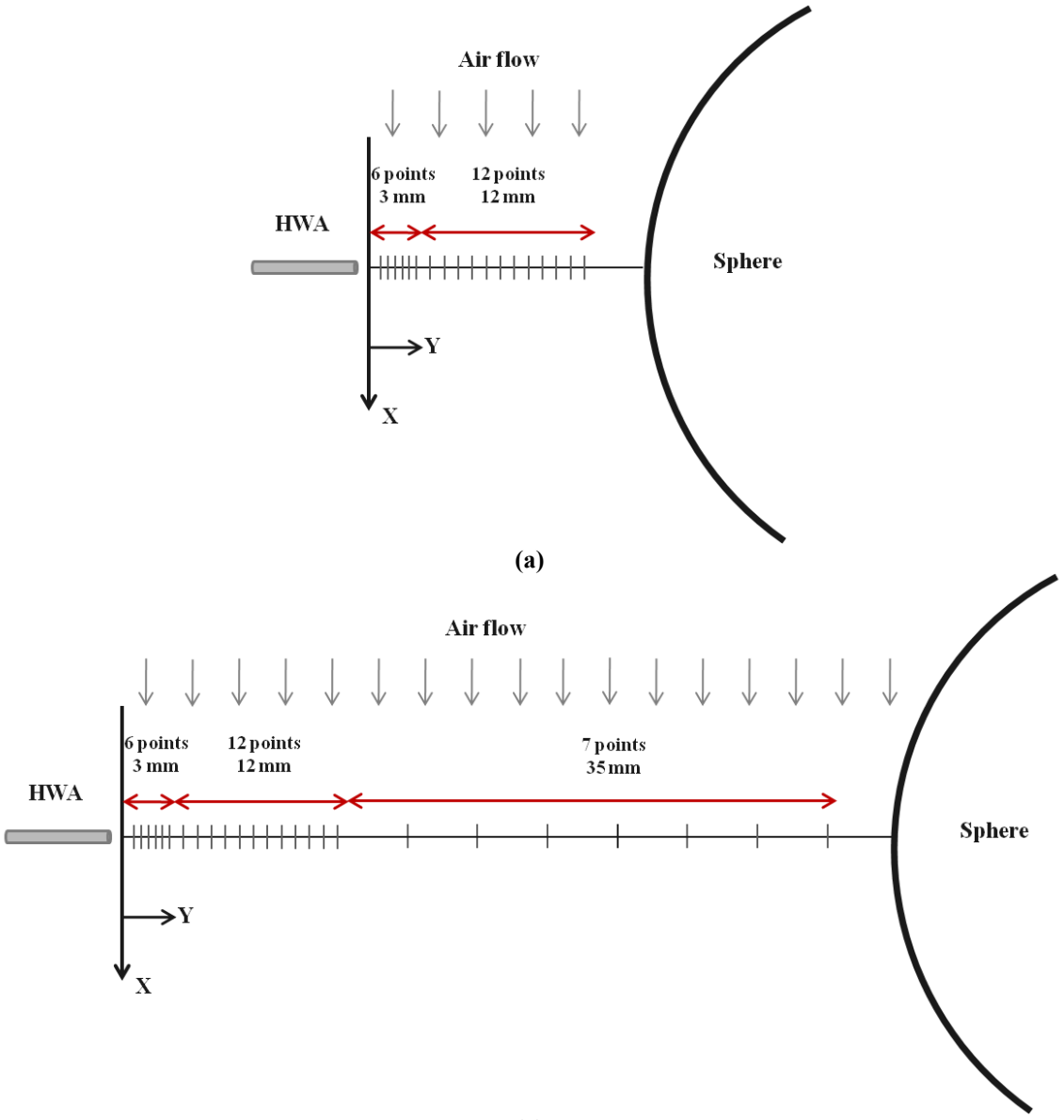

Figure III-3 Arrangement of the velocity measurement points within (a) Gap A4, (b) Gap B6.

To measure the air flowrate through the packed bed, the inlet, the outlet, and to calculate the Reynolds number of the air flow within the bed, a TSI portable air velocity meter with an of accuracy ±3% was used. The velocity of the air at the inlet of the bed is measured by inserting the velocity meter probe into the holes made on the upper cylindrical part of the bed (shown in Figure III-1 (a)). The air velocity is measured at the outlet of the bed using the same velocity meter probe to check and ensure that the air velocity flowrate through the bed is constant and there is no leakage in the system. At each flowrate, the inlet and outlet velocity of the air is measured at 10 different points along four different diameters of the circular inlet and outlet of the bed. Therefore, a total of 40 measurements are taken at the inlet and another 40 velocity measurements at the outlet for each flowrate and average of the 80 measured velocities are reported as the bed velocity. Once the bed velocity is acquired, a modified version of the Reynolds number for air passing through the porous media of the packed bed is calculated. Modified Reynolds number Re_m is defined as follows:

$$\mathrm{Re}_m = \frac{U_0 D}{\upsilon(1-\varepsilon)} \qquad \text{(III-1)}$$

where:

U_0: Bed Velocity,

D: Bed Diameter,

υ: Air Kinematic Viscosity

ε: Bed Porosity

The velocity profiles within the near wall gaps between the spherical particles used as packing for the bed are obtained for five different Reynolds numbers as indicated in Table III-1.

Bed Velocity (m/s)	Modified Re Number
0.6	2043
1.0	3354
1.4	4541
1.7	5735
2.0	6857

Table III-1 Air velocity and Reynolds number through the annular packed bed.

III.2.2. Hot Wire Anemometry (HWA) Technique

As it was mentioned before, in this investigation, HWA technique is applied to obtain velocity profiles of the coolant flow within the gaps between the pebbles in areas close to the outer reflector wall of a test section representing an annular packed bed. HWA technique takes advantage of a considerably high frequency response which is required for velocity measurements in turbulent flows. Moreover, this technique does not have the limitations of optical techniques such as PIV and PTV, e.g. laser light blockage by fuel particles, etc.; therefore, it can be used on the entire height of the annular bed regardless of the type of the spheres, i.e. clear Acrylic or black plastic.

III.2.2.1. Introduction to HWA Technique

Thermal anemometers are widely used in the experimental measurements of local flow velocity and temperature in turbulent flow fields. Thermal anemometers measure the local flow velocity based on the convective heat transfer from an electrically heated metallic sensor to the surrounding fluid. Different types of heated sensors are used for velocity measurements in different types of fluid, for instance, hot wire sensors are applied in clean air or any other gas flows and hot film sensors are applicable for both gas and liquid velocity measurements. The higher strength of the hot film sensors compared to hot wires makes them a better choice for flows with high velocity ranges, flows with contamination, and especially for the multi-sensor probes (X-probes or triple probes) where the rigidity of the sensor is of great importance. The sensors are normally made of tungsten or platinum alloys with diameters in the range of 2.5-7.5 μn and sensor length of 0.8-1.5 mm. Sensors with thicker diameters are used in high-speed flows or flows with some impurities in them in order to have a higher strength of the probe. The principles of Hot Wire Anemometry technique has been extensively explained in the literature (Brunn 1995, Jørgensen 2002). The principle equation governing the performance of a hot wire sensor is as follows:

$$I^2 R_W = h\, A (T_W - T_f) \qquad \text{(III-2)}$$

where:

I: Electric current passing through the wire,

R_W: Wire resistance,

h: Heat transfer coefficient of the wire

A: Projected surface area of the wire

T_W: Wire Temperature

T_f: Fluid Temperature

The type of the hot wire/film sensor for a certain experiment is chosen based on the specific application or type of measurement needed. For instance, single wire/film probes are used for high frequency single velocity component measurements, X-probes are applied in flows where two velocity components are needed to be measured simultaneously, and triple probes are utilized for simultaneous measurement of all three velocity components.

The hot wire anemometer systems are categorized into two groups based on the design of their internal electric circuit which in turn is selected with regards to the parameter that the system needs to measure. The two systems are called Constant Temperature Anemometry (CTA) and Constant Current Anemometry (CCA). The former is used for velocity measurements while the latter is used for temperature measurements. A CTA system is chosen for this experiment, since the air flow velocity is the parameter that needs to be measured.

III.2.2.2. HWA System

The hot wire system that is used in this experiment is a TSI IFA 300 unit. The unit can accommodate any of the cylindrical or non-cylindrical single wire or film probes as well as the X-probes. Consequently, the system is capable of measuring a single or two velocity components. The hot wire system used in this experiment has the

ability to measure samples with high frequencies which enables the system to resolve the smallest turbulence scales. In this investigation, an X-probe hot film anemometer is used to measure the two velocity components at a frequency of 20 KHz for a period of 26.214 sec. The hot wire probe needs to be first calibrated before being used for velocity measurements in the experiment. Table III-2 shows the characteristics of the HWA unit used in this experiment as well as the properties of the X-probe utilized for measurements.

HWA system	**TSI constant-temperature, model IFA 300**
X-probe	Standard TSI hot film, model 1240
Sensor length	1.02 mm
Sensor diameter	50.8 µm
Sensor material	Platinum
Calibration system	Round jet with 12.7mm diameter
Data acquisition /analysis software	THERMALPRO Software 5.0
Operating System	Windows XP
Sampling frequency	20 KHz
Sampling period	26.214 sec

Table III-2 Characteristics of the HWA system and the measurement conditions.

As it is mentioned in Table III-2, a TSI hot film X-probe model 1240 which is capable of simultaneously resolving tow velocity components. The probe consists of two

film sensors made of platinum which are oriented normal to each other and inclined with respect to the probe body axis by a ±45° angles. The detail characteristics of the X-probe and its orientation with respect to each velocity component while being used in the experiment are shown in Figure III-4.

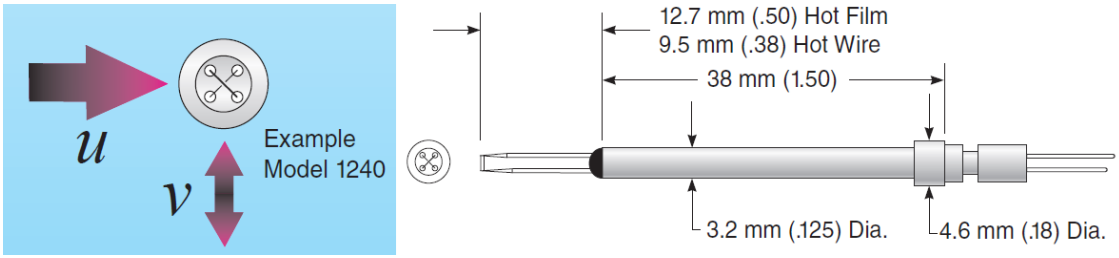

Figure III-4 Schematic of the X-probe used in this experiment and its orientation with respect to the flow (TSI1 2011).

III.2.2.3. HWA Probe Calibration

As mentioned before, a TSI Constant Temperature Anemometry (CTA) system coupled with a hot film X-probe is used in this investigation for air velocity measurements within the near wall gaps of an annular packed bed. The hot film X-probe needs to be calibrated before being used in the actual experiment. The calibration process establishes a relationship between the flow velocity and the measured voltages recorded by the HWA system. The facility used for calibration (called *"Calibrator"* henceforth) of the hot wire probes in this experiment is shown in Figure III-5. Clean pressurized air passes supplied from an air compressor is passed through a pressure regulating valve and then into the calibrator. Figure III-5 (b) shows the details of the components inside the calibrator which are: a quick disconnect fitting, a jet breakup plate, three wire mesh screens (40 mesh per inch screen), housing and the nozzle. The air enters the housing of the calibrator as a jet which will lose its structure after passing the jet breakup plate. The jet breakup plate generates large scale eddies which will be broken into slammer eddies after passing through the mesh screens. Furthermore, the mesh screens create a resistance against the flow which in turn creates a uniform flow profile downstream the last layer of screens. The flow exiting the nozzle of the calibration has a uniform velocity and a low turbulence intensity (approximately 2%). It should be mentioned that the air velocity passing through the calibrator should not exceed 100 (m/s).

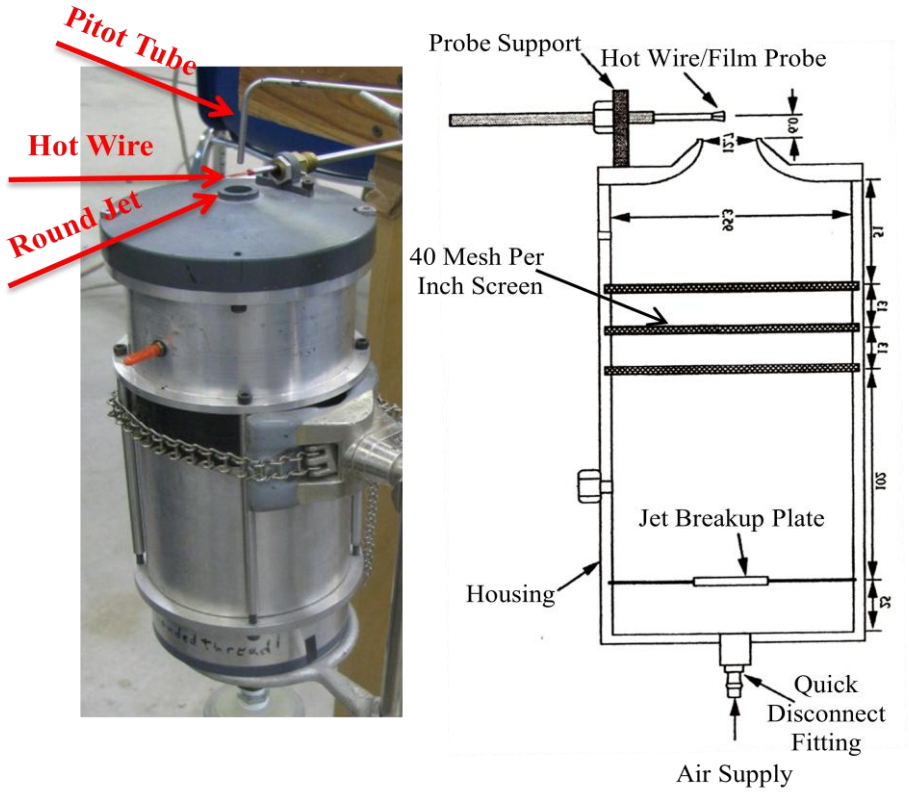

(a) **(b)**

Figure III-5 (a) Picture of the calibrator unit, (b) detailed schematic of the inside of the calibrator unit.

The following procedure is pursued in order to calibrate the hot film X-probe used for measurement of the air velocity profile in this experiment.

- Probe is placed in the potential core region of a round air jet with a diameter of 12.7 mm and with low turbulence intensity at a distance of approximately 6mm from the nozzle exit plane. The direction of the probe with respect to the flow needs to be exactly the same as the direction that it will have with respect to the flow in the actual experiment. In this experiment, the X-probe is positioned against the flow in a way that both sensors make a 45° angle with the flow exiting the nozzle.
- The velocity range chosen for calibration should cover the velocity range expected in the actual experiments. For this calibration process, measurement points are chosen in a velocity range of 0-38 (m/s). Such high velocities are needed for the calibration of the X-probe since very high velocities were observed in the near wall gaps for the highest air flowrates through the bed.
- Normally, 15 to 20 properly spaced velocity points are chosen in the velocity range to obtain the calibration curve. In the current calibration process, total of 76 appropriately spaced points are chosen within the aforementioned velocity range. Furthermore, to ensure obtaining a calibration curve with high accuracy (i.e. a better curve fit), the calibration points are closely spaced in the lower velocity range and more widely spaced in the higher velocity range.
- The air compressor is turned on and the air velocity exiting the nozzle of the calibrator is adjusted using the pressure regulating valve. The air jet velocity at the nozzle exit plane is set by increasing the pressure slowly until the desired differential

pressure (ΔP) is measured by the Pitot tube at the nozzle exit. This method is valid for the whole range of velocities that can be set through the calibrator. It should be noted that ΔP needs to be kept approximately constant while the measurements are being taken and it should not vary more than 3%.

- At each calibration point, the reading of the Pitot tube is used to calculate the velocity as follows:

$$U_{jet} = \left(\frac{2\,\Delta P}{\rho} \right)^{1/2} \qquad \text{(III-3)}$$

where:

U_{jet} : air jet velocity exiting the calibrator nozzle,

ΔP: differential pressure measured by the Pitot tube,

ρ: density of the air jet exiting the calibrator nozzle at the calibration temperature.

- The air jet temperature is monitored and recorded using a T-type thermocouple which is set downstream the jet exit plane and the recorded voltages are corrected to this temperature.

- After recording the voltage regarding all the velocity points, the THERMALPRO software is used to obtain the calibration curve which is normally a polynomial curve fit through the points (E, U_{jet}). This calibration function is used while converting the voltage data obtained in the actual experiment to velocity values.

- The polynomial or power law coefficients representing the calibration curve are given by the THERMALPRO software. The polynomial curve fit normally has the form of:

$$U_{jet} = K + AE + BE^2 + CE^3 + DE^4 \quad \text{(III-4)}$$

where:

E: Voltage,

U_{jet}: air jet velocity,

K, A, B, C, D: Polynomial coefficients

The power law curve fit is normally in the form of:

$$E^2 = A + BU_{jet}^{(1/n)} \quad \text{(III-5)}$$

where:

E: Voltage,

U_{jet}: air jet velocity,

A, B, n: Calibration coefficients

- The software also provides the mean square error which is a measure of how well the curve fits the calibration points.
- If the points on the curve are plotted correctly and show a smoothly increasing trend, then the calibration process is complete. However, if one or a few points on the calibration curve do not look good, it might be needed to repeat the calibration process.
- An additional type of calibration called *"directional calibration"* needs to be done for X-probes which provides directional sensitivity coefficient (*"yaw coefficient (k)"*) for each individual sensor. These coefficients are used to decompose the velocities obtained by each sensor into actual velocity components. In cases where maximum

accuracy is not needed, the default value for yaw coefficient which is provided by manufacturer can be used.

- The yaw calibration is performed by choosing 11 different angles between 25-75° with an angle increment of 6°. The angles are chosen in a manner that the middle angle is the "head –on" orientation which is the direction of the X-probe that was previously used during velocity calibration for which both sensors were positioned at a 45° angle with respect to the direction of the flow.
- A constant velocity of the air flow is required throughout the yaw calibration process. It is suggested to set the air jet velocity at a value close to 40% of the maximum velocity used in the calibration process. For yaw calibration of the X-probe in this experiment, air velocity is fixed at a value of 1.419E+01 (m/s).
- The THERMALPRO software calculates the yaw coefficient for each sensor once the voltage readings for all 11 angles are completed.
- In Figure III-6, the data points obtained through the calibration process are shown as black circles. The voltage vs. velocity plots in Figure III-6 show the calibration curve obtained for each individual sensor of the X-probe used in this experiment. The calibration curve is shown with the red line passing through the data points. Both calibration curves are in agreement with the expected operation of a hot film sensor for which the increase in the velocity of the air flow corresponds to an increased output voltage. Different calibration curve options were tested among which King's law curve fit provide a more accurate approximation of the data. The calibration equations obtained

for each sensor along with the mean square error of the calibration curve fitting as well as the yaw coefficient of each sensor are presented in Table III-3.

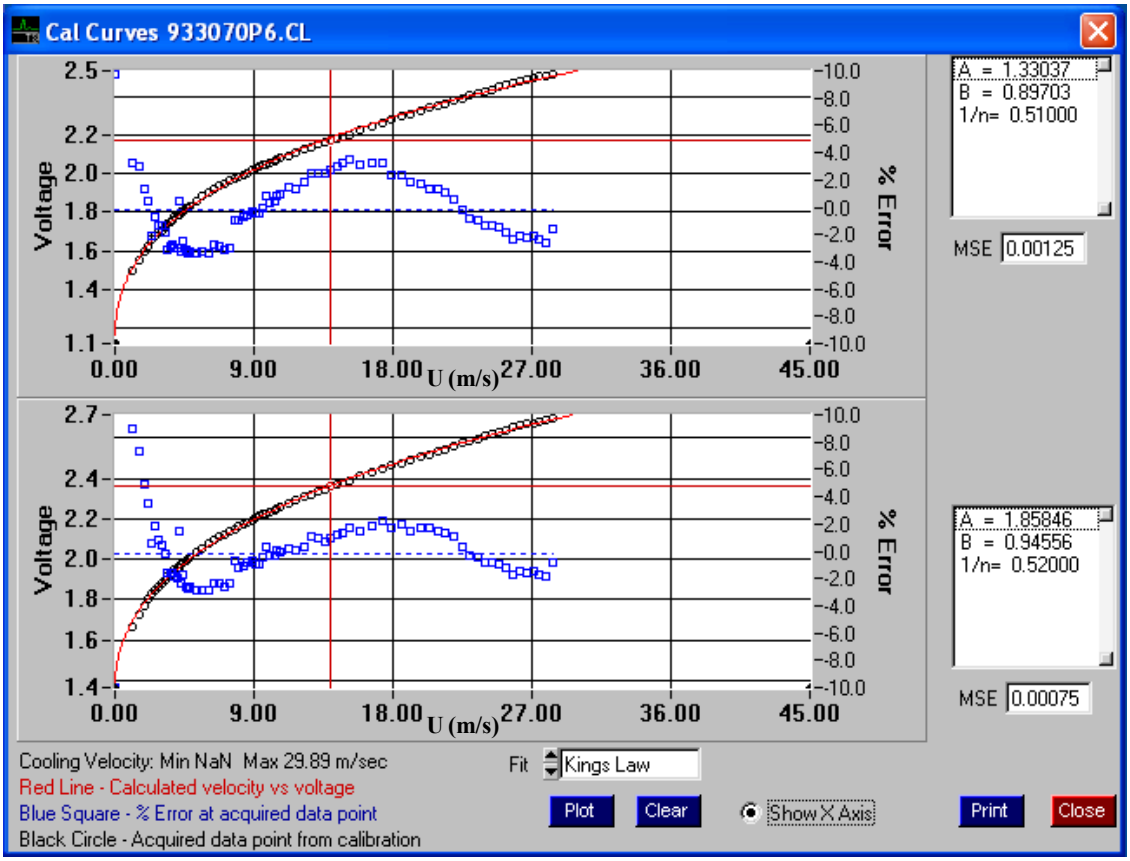

Figure III-6 Calibration curves obtained for each sensor of the X-probe used for velocity measurements (TSI2 2011).

	King's Law Calibration Equation	Mean Square Error	Yaw Coefficient
Sensor 1	$U_{jet}^2=1.33037E^{0.51}+0.89703$	0.00125	3.08491E-01
Sensor 2	$U_{jet}^2=1.85846E^{0.52}+0.94556$	0.00075	3.29428E-01

Table III-3 Calibration curve equations and their corresponding error for each sensor of the X-Probe.

III.2.2.4. HWA Data Acquisition and Analysis

As mentioned before, TSI THERMALPRO software is used for data acquisition and analysis of the data. Once the probe is calibrated, it can be used for velocity measurements in the experiment. The following steps were taken during the data acquisition and analysis using the hot film X-probe:

- The calibrated probe is placed in the experimental facility with the same direction with respect to the flow as it had in the calibration process (each sensor at a 45° angle with respect to the direction of the flow).
- The fluid flow temperature in the experiment will be measured using a thermocouple and corrections will be made through the software in case the fluid temperature is different from the calibration temperature.
- The atmospheric pressure is measured at the time of data collection and corrections will be made in case it is different from the pressure measured during the calibration of the probe.

- The sampling rate and the sampling period are set through the THERMALPRO software. In this case, as it was mentioned before, velocity data is taken at a sampling frequency of 20 KHz for a period of 26.214 sec.
- The acquired data can be displayed graphically immediately after acquisition. Plots of velocity vs. time and velocity vs. probability distribution are displayed by the software. Furthermore, the values of mean velocity, turbulence intensity, and temperature are also shown by the software.
- The acquired data will be saved in raw data files. The raw data filed containing the time histories of output voltage of each sensor through the measurement period need to be further analysis to obtain the time histories of the two velocity components.
- The post-analysis part of the THERMALPRO software allows for calculation and graphical display of velocity statistics and velocity time histories.

III.3. Results

As it was mentioned before, in this investigation, HWA technique is used to measure the air velocity profiles within two different near wall gaps in an annular packed bed. The time histories of the velocities at each measurement point are averaged over the data acquisition time and subsequently the axial and radial time-averaged velocity profiles are obtained within each gap. Moreover, the time histories of the velocity at each point within each gap are further analyzed using a PSD method to acquire a more in depth insight to the turbulent flow characteristics of the coolant flow

within each gap which is essential for accurate predictions of the helium coolant flow inside the core of a pebble bed VHTR.

III.3.1. Velocity Profiles within Near Wall Gaps

Time histories of the two velocity components, i.e. axial and radial components, are acquired using a hot film X-probe at several points within each measurement gap for five different Reynolds numbers. For each case, the time-averaged velocities at each point are normalized with the corresponding bed velocity and the radial distance is normalized with the sphere diameter.

III.3.1.1. Axial Velocity Profiles

Figure III-7 shows the time-averaged axial velocity profiles of the air flow along the radial direction within gaps A4 and B6 for five different Reynolds numbers. It is observed in Figure III-7 (a) that all five velocity profiles measured within gap A4 follow a similar pattern to a good extent. As seen in the Figure III-7 (a), for all the five different Reynolds numbers, the axial velocity increases from a low value close to the packed bed wall (no slip condition at the wall) to a maximum velocity which is approximately 6-7 times higher than the corresponding bed velocity. This sudden increase in the velocity close to the container wall of the packed bed is observed for all different Reynolds numbers around the radial distance of $Y/D \approx 0.05\text{-}0.25$. For $Y/D > 0.25$, all of the velocity profiles for all Reynolds numbers show a decreasing trend as the hot film probe gets closer to the end of the gap where one sphere is blocking the end of the gap. The

existence of this sharp peak in the axial velocity profile within gap A4 is in agreement with all the previous studies indicating the existence of *bypass flow* close to the container wall of packed beds (Schwartz & Smith 1953, Marivot *et al.* 1974, Johnston *et al.* 1975, Čermák *et al.* 1982, Vortmeyer &Schuster 1983, White & Tien 1987, Ziólkowska & Ziólkowski 1988, Moise &Tudose 1998).

The time-averaged axial velocity profiles within gap B6 presented in Figure III-7 (b) show a very different pattern than what was observed in Figure III-7 (a). In this case, two different peaks are observed in the axial velocity profiles for all Reynolds number cases. More interestingly, as seen in Figure III-7 (b), the second peak for the three cases with highest Reynolds numbers (Re_m = 4,542, 5,735, and 6,857) are significantly higher than the first peak happening closer to the wall. On the other hand, the profiles of the time-averaged axial velocity fields for the two lower Reynolds number cases (Re_m = 2,043 and 3,355) show a totally different behavior. For these two profiles, there are still two peaks in the time-averaged axial velocity profile; however, the peak closer to the wall is the peak with the largest magnitude. The observations made from time-averaged velocity profiles of gap B6 are quite similar to the results of the study done by Lerou & Froment (1977). In the experiment done by Lerou & Froment (1977), the axial velocity profiles were measured at the exit of the packed bed. There were more than one peak in the velocity profiles obtained at the exit of the packed bed and interestingly the peak closest to the wall was not always the largest one. In addition, they showed that the change in the arrangement of a few layers of the packing had a great influence on the velocity profile.

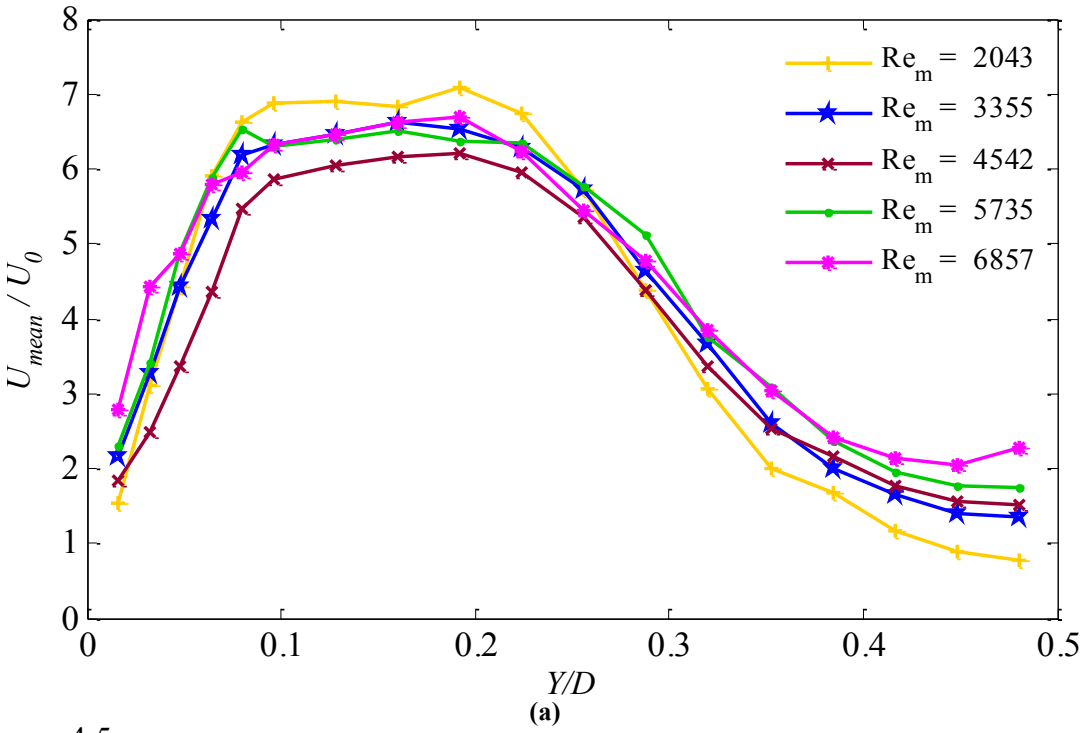

(a)

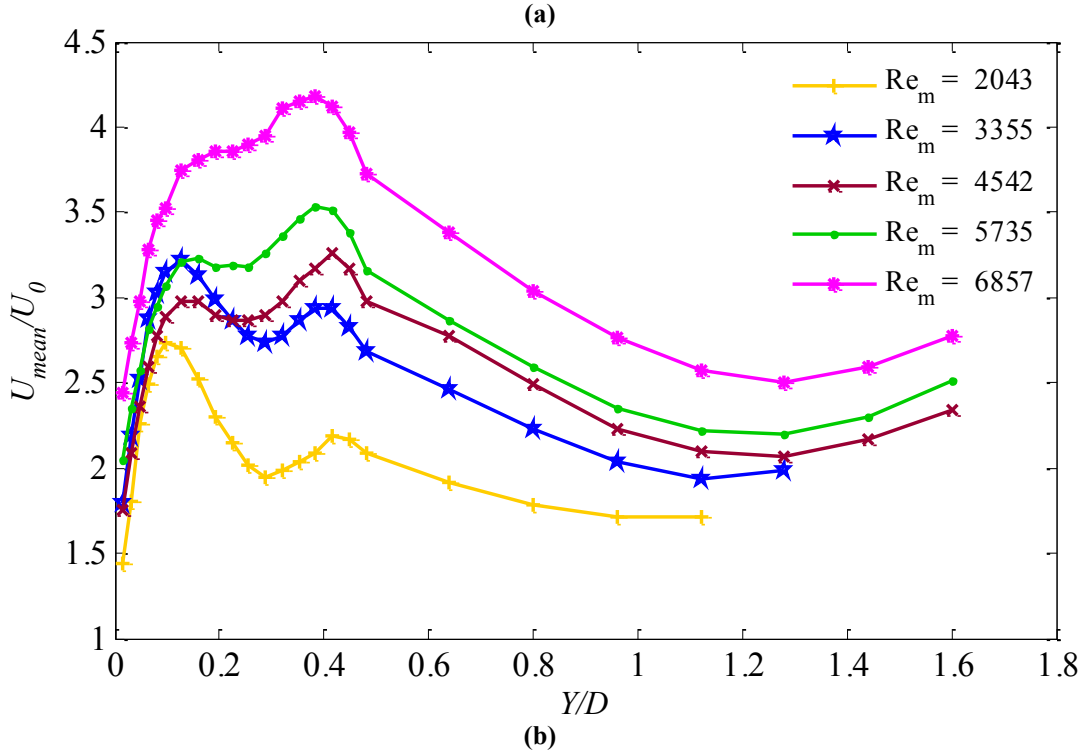

(b)

Figure III-7 Normalized time-averaged axial velocity profile within gap (a) A4, (b) B6.

III.3.1.2. Radial Velocity Profiles

The plots of time-averaged radial velocity profiles within both measurement gaps are shown in Figure III-8. The radial velocity profiles obtained for gap A4 presented in Figure III-8 (a) show a maximum value approximately around the same location where the peaks in the time-averaged axial velocity profiles (Figure III-7 (a)) were observed. There are two main differenced seen between the axial and radial velocity profiles of gap A4. First, the peaks in the radial velocity profile have much lower magnitudes than the peaks in the axial velocity profile which is anticipated since the main direction of the flow is in the axial direction. The magnitude of the peaks of the radial velocity profiles for all different Reynolds numbers is approximately 1.5-2 times more than the corresponding bed velocity. Secondly, the peaks in the radial velocity profiles of gap A4 are narrower compared to the peaks observed in the axial velocity profiles.

Figure III-8 (b), represents the time-averaged radial velocity profiles within gap B6 for five different Reynolds numbers. There are some similarities and differences between the radial and axial velocity profiles within gap B6. First, similar to the axial velocity profiles of gap B6, there are two peaks in the time-averaged radial velocity profiles. However in this case, only for the two highest Reynolds number cases, the second velocity peak (the one farther from the packed bed wall) has a larger magnitude than the peak that is closest to the wall. In this case, for the three lowest Reynolds number cases, the closest peak to the wall is the one with higher magnitude. In all five different cases, the radial velocity profile decreases after the second peak as the probe approaches the sphere, which is blocking the end of the measurement gap.

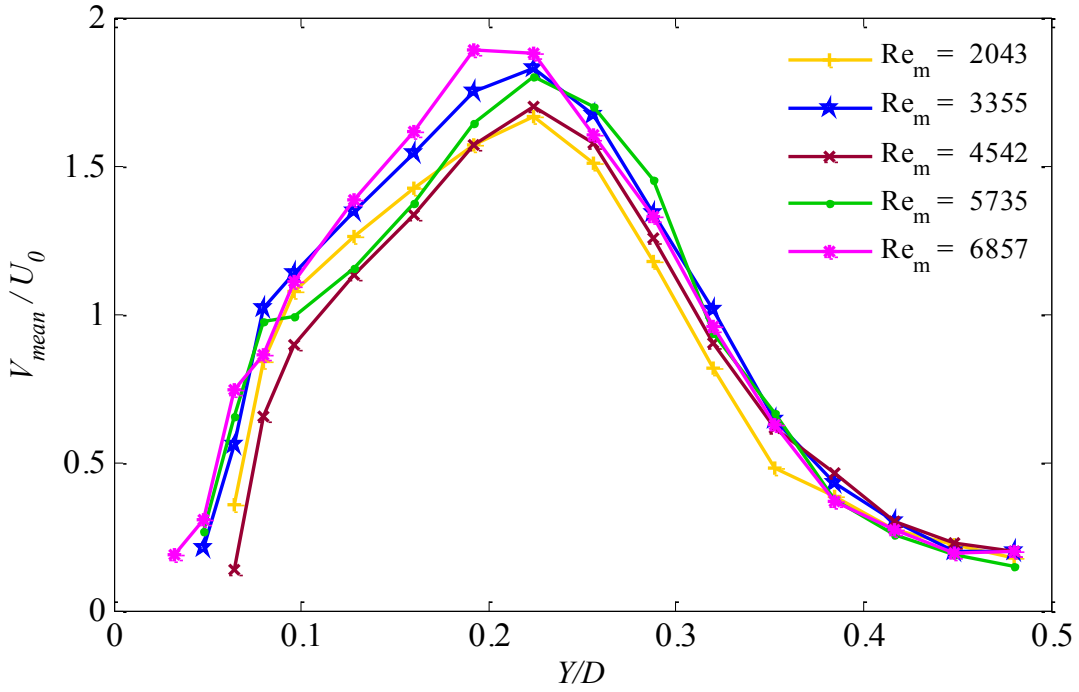

(a)

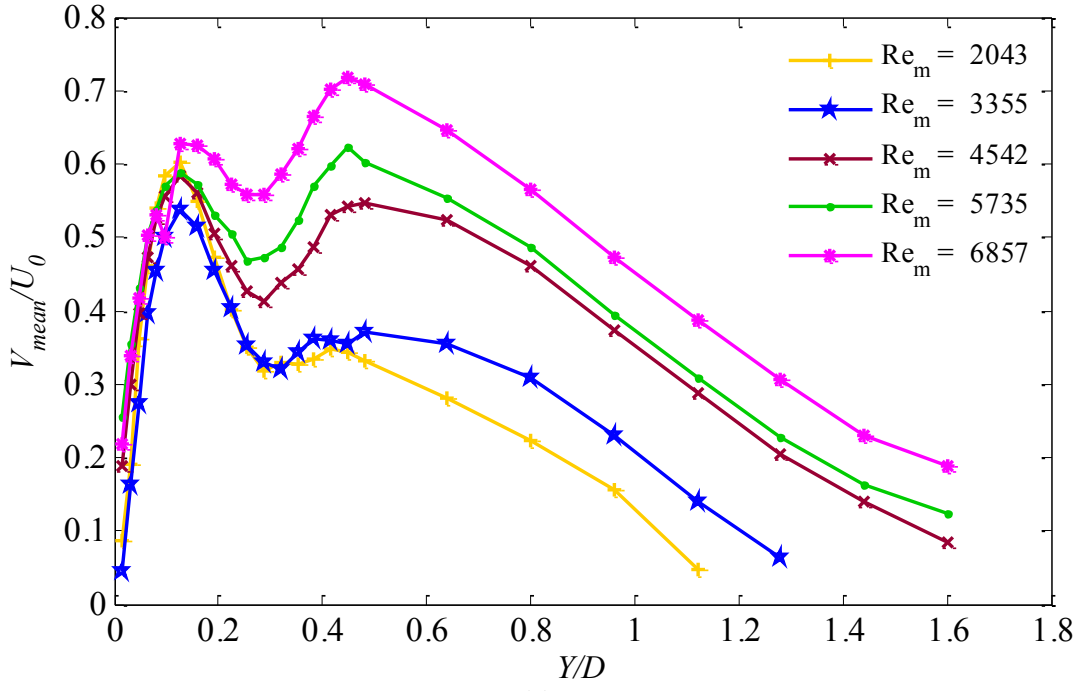

(b)

Figure III-8 Normalized time-averaged radial velocity profile within gap (a) A4, (b) B6.

It should be noted that, the magnitude of the radial velocity peaks are much smaller than those observed in the axial velocity profiles.

III.3.2. Power Spectra Density (PSD) Analysis

To have a more comprehensive understanding of the energy distribution of the axial and radial velocity at different points and at different Reynolds numbers of the flow, the power spectral density analysis is performed on the time histories of the axial and radial velocities for different measurement points for both gaps A4 and B6. The PSD analysis have been performed in two different ways: 1- at a constant Reynolds number of the flow for different spatial locations within the gap, 2- at a specific point with varied Reynolds numbers. This method helps in separately identifying the effect of the distance of the point from the wall as well as influence of the Reynolds number on the distribution of the energy among eddies of different sizes. In all the power spectrum plots obtained for gaps A4 and B6, the black solid line represents the equivalent slope of the inertial sub-range in the wavenumber domain for the classical Kolmogrov power spectrum for the frequency domain (Tennekes & Lumely 1972). The inertial sub-range is the section of the energy cascade where energy transfers from production (low frequency section, large eddies) to dissipation (high frequency section, smaller eddies) in homogenous turbulent flows. Here it is important to notice the advantage of HWA technique in taking samples with considerably high frequencies helps in resolve all parts of the energy cascade, especially in the dissipation range.

III.3.2.1. Spectral Analysis of Velocity Points

In this section, five different points are chosen along the velocity measurements within each gap and the axial and radial energy spectrum for each point is obtained at three different Reynolds numbers.

Figure III-9, Figure III-10, and Figure III-11 present the result of the PSD analysis for five different points within gap A4 for three different Reynolds numbers. These five points are particularly chosen: 1- close to the container wall to study the effect of the solid boundary on the spectrum, 2- at the left side of the axial velocity peak, 3- the center of axial velocity peak, 4- at the right side of the axial velocity peak, 5- close to the end of the gap to study the effect of the sphere at the end of the gap. It should be noted that the energy spectrum of radial velocity of the point that is closest to the wall is not shown in the plots since the velocities at that point have such low values that the spectrum was not considered reliable.

The temporal energy spectra presented in Figure III-9 to Figure III-11 show a high spatial dependency. This effect is more clearly seen in the case of the axial energy spectra compared to the radial energy spectra. It is also observed that the change in the radial location of the points affect both high frequency and low frequency parts of the spectrum. Moreover, the slope of the spectra in the inertial sub-range, particularly for the axial power spectra, varies with changes in the radial location of the points to values smaller or larger than the predicted value for a classical spectrum shown by the black solid line. It can be concluded that the rate of energy transfer from the large eddies in the low frequency region of the spectra to the smaller eddies in the high frequency section of

the spectra is highly sensitive to the location of the points within the measurement gap. In addition, for all three Reynolds number cases, power spectra of the radial velocity component show a significant variation when approaching the solid boundary i.e. the sphere at the end of the gap.

The result of the PSD analysis for five different points within gap B6 for three different Reynolds numbers are presented in Figure III-12, Figure III-13, and Figure III-14. These five points are specifically chosen: 1- close to the container wall to study the effect of the solid boundary on the spectrum, 2- at the center of the first axial velocity peak, 3- the trough observed between the two axial velocity peaks, 4- at the center of the second axial velocity peak, 5- close to the end of the gap to study the effect of the sphere at the end of the gap. It should be noted that the energy spectrum of radial velocity of the point that is closest to the wall is not shown in the plots since the velocities at that point have such low values that the spectrum was not considered reliable.

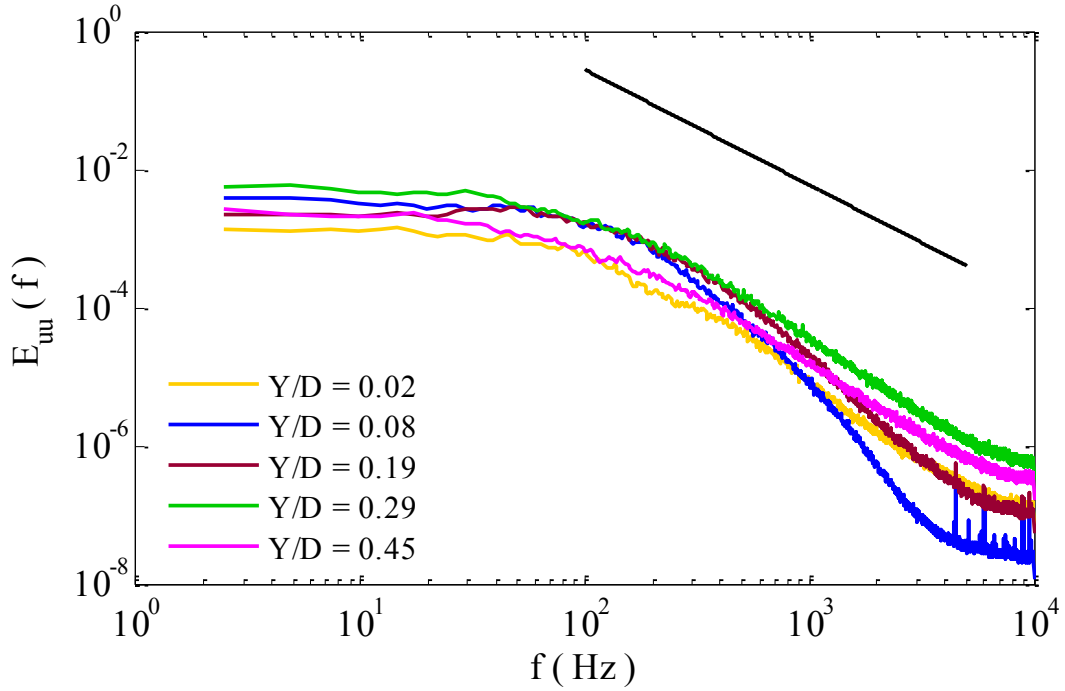

(a)

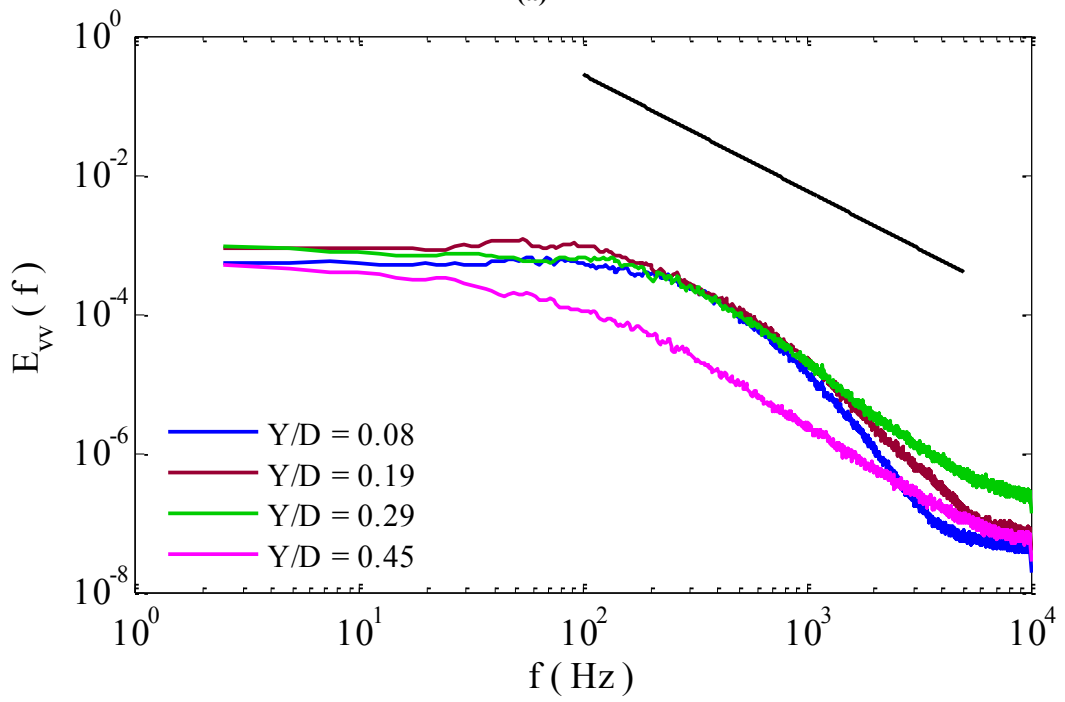

(b)

Figure III-9 Power spectra density for points within gap A4 at Re_m= 2,043 obtained by the time histories of (a) axial velocity, (b) radial velocity.

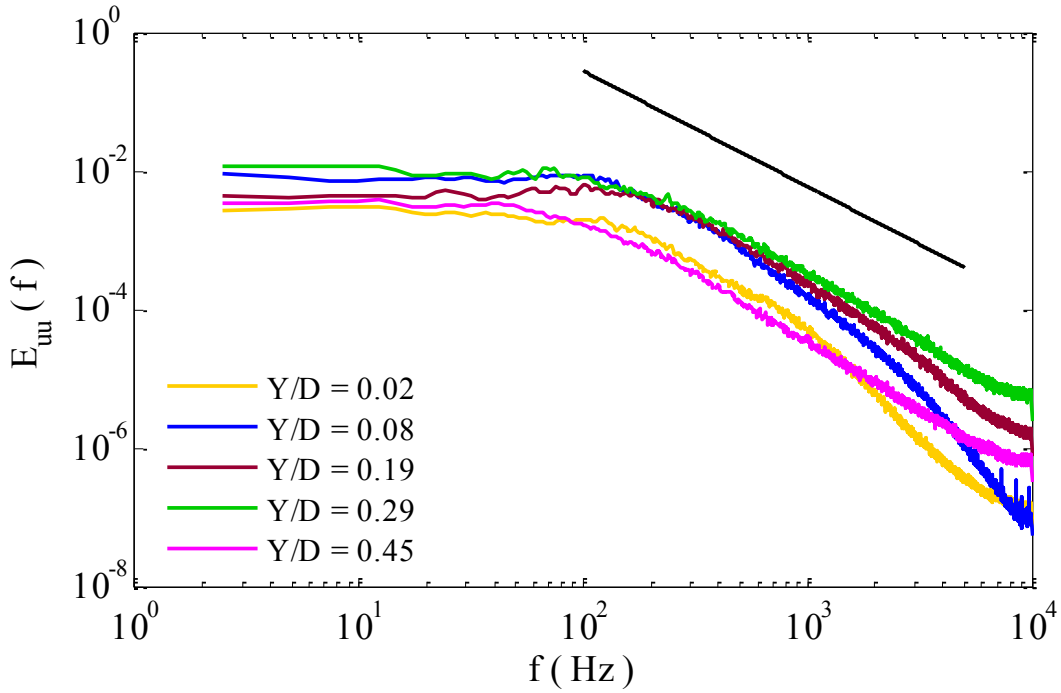

(a)

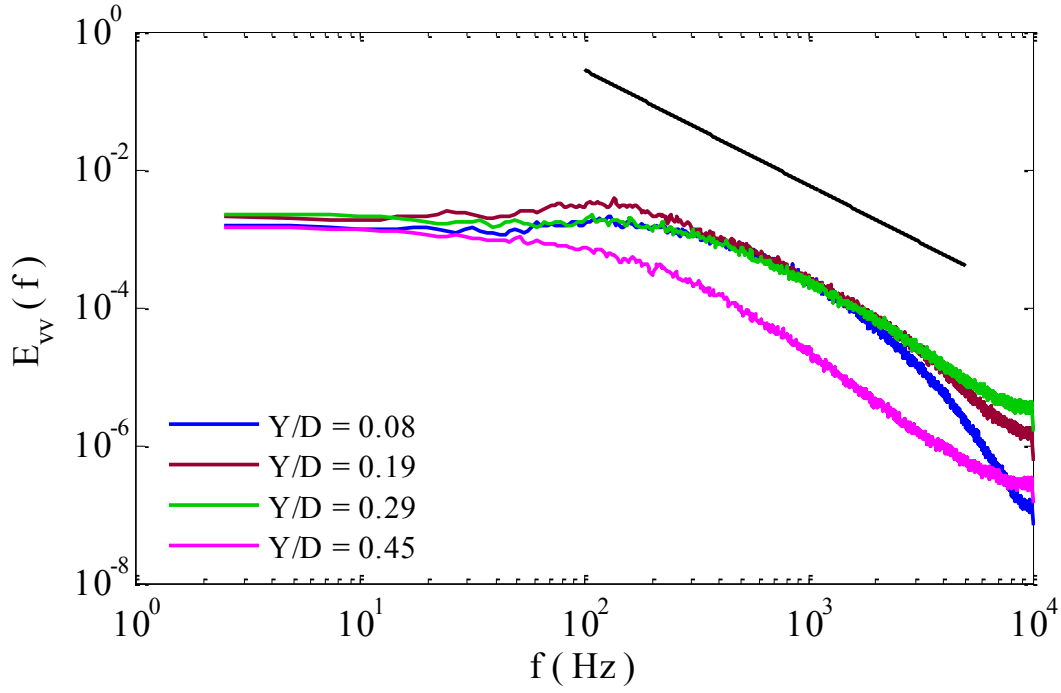

(b)

Figure III-10 Power spectra density for points within gap A4 at Re_m= 4,541 obtained by the time histories of (a) axial velocity, (b) radial velocity.

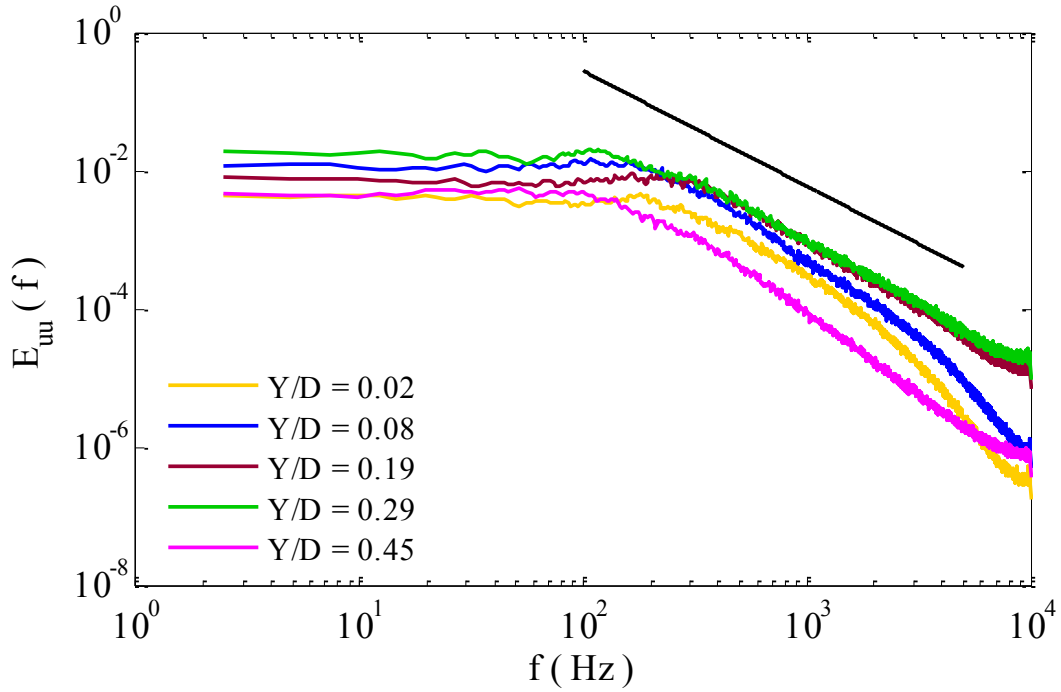

(a)

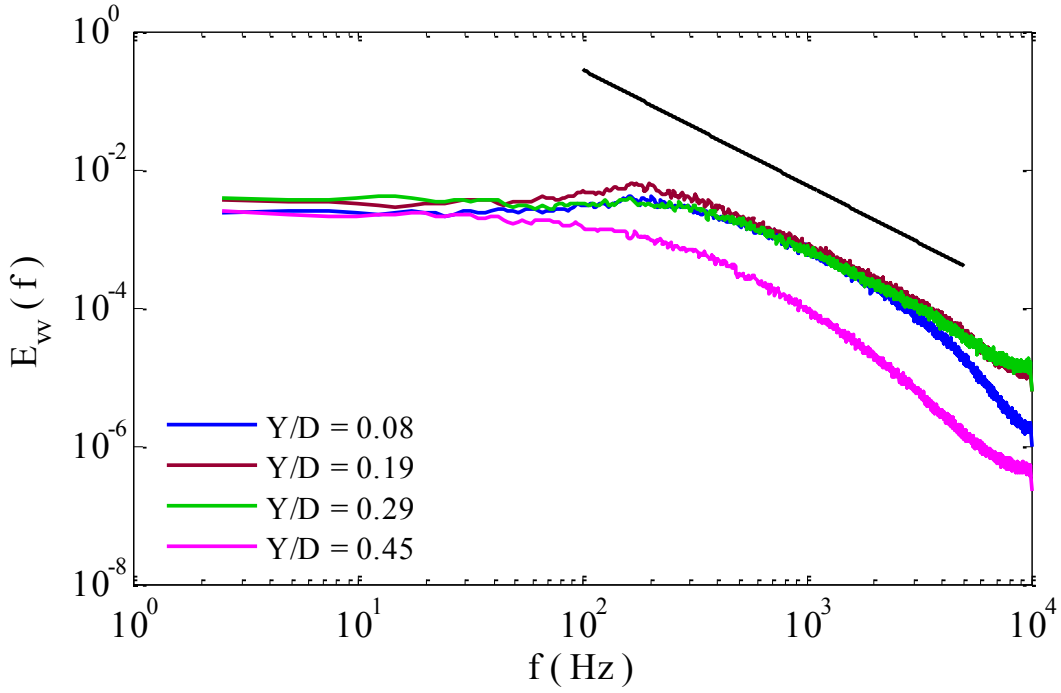

(b)

Figure III-11 Power spectra density for points within gap A4 at Re_m= 6,857 obtained by the time histories of (a) axial velocity, (b) radial velocity.

The temporal distribution of the energy spectra presented in Figure III-12 to Figure III-14 show less sensitivity to the radial position compared to the results presented in Figure III-9 to Figure III-11. The power spectra of both axial and radial velocities obtained for the three points in the middle of the gap approximately follow the same slope in the inertial sub-range and in some cases overlap. This effect is more pronounced in the case of power spectra of the radial velocity for the three middle points shown in (Figure III-12 (b), Figure III-13 (b) and Figure III-14 (b)). The slope of the energy cascade especially in the case of the temporal spectrum of the axial velocity follows the predicted slope of the inertial sub-range by Kolmogrov. Moreover, the effect of the solid boundary on the power spectra of both axial and radial velocities is clearly seen in all the distributions shown in Figure III-12 to Figure III-14. In case of the power spectra of the axial velocity, it is observed that the effect of the container wall of the packed bed is more pronounced on the power spectra than that of the sphere at the end of the gap.

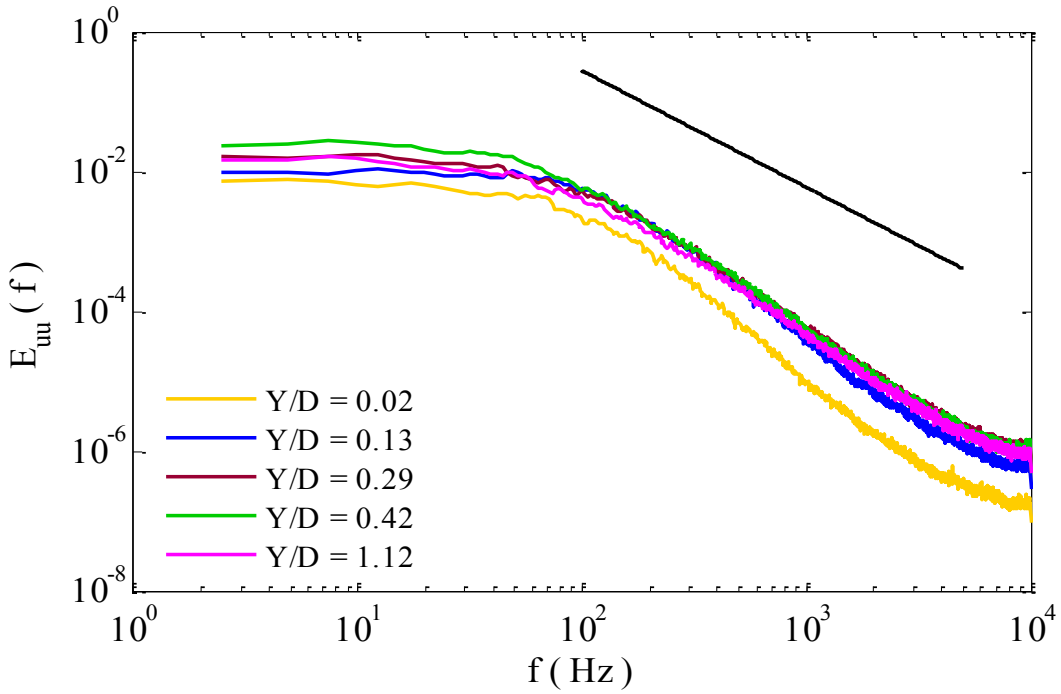

(a)

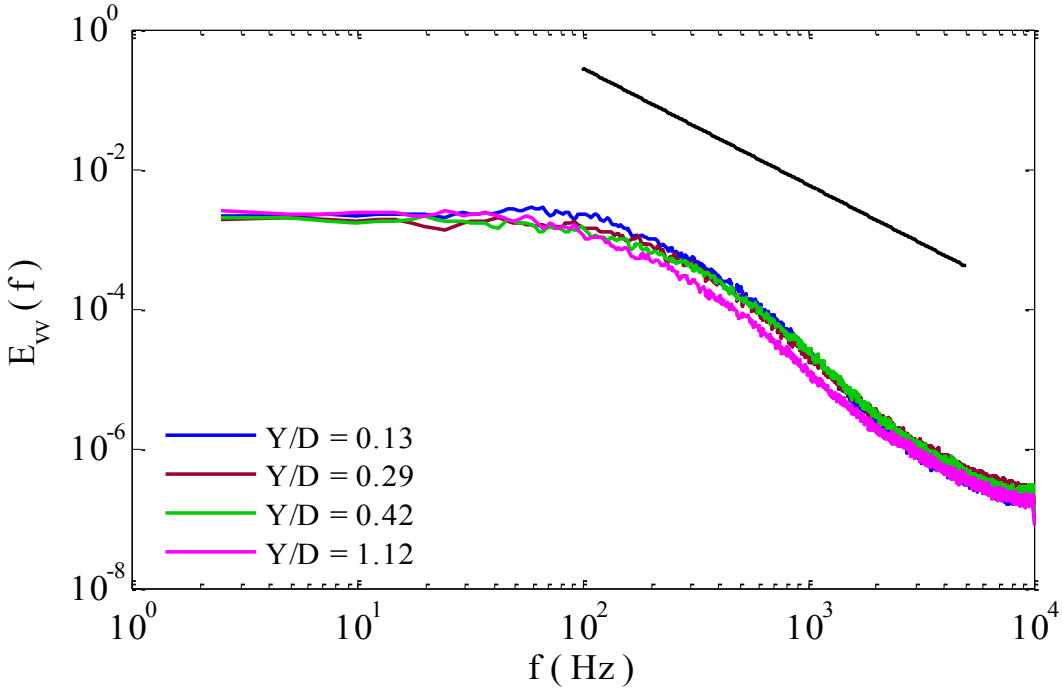

(b)

Figure III-12 Power spectra density for points within gap B6 at Re_m= 2,043 obtained by the time histories of (a) axial velocity, (b) radial velocity.

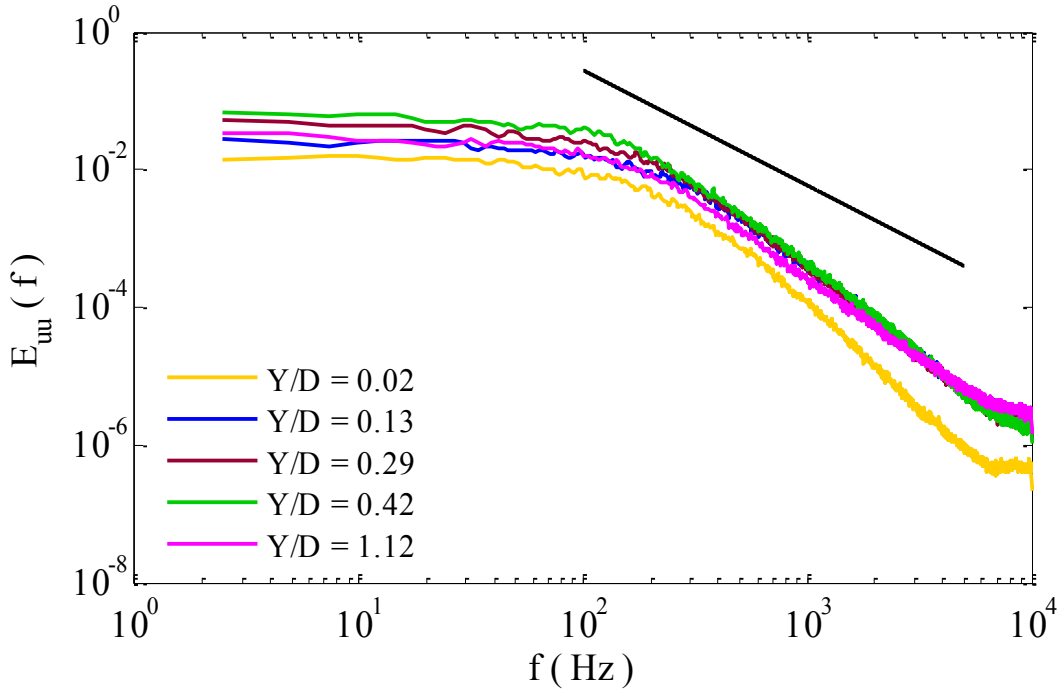

(a)

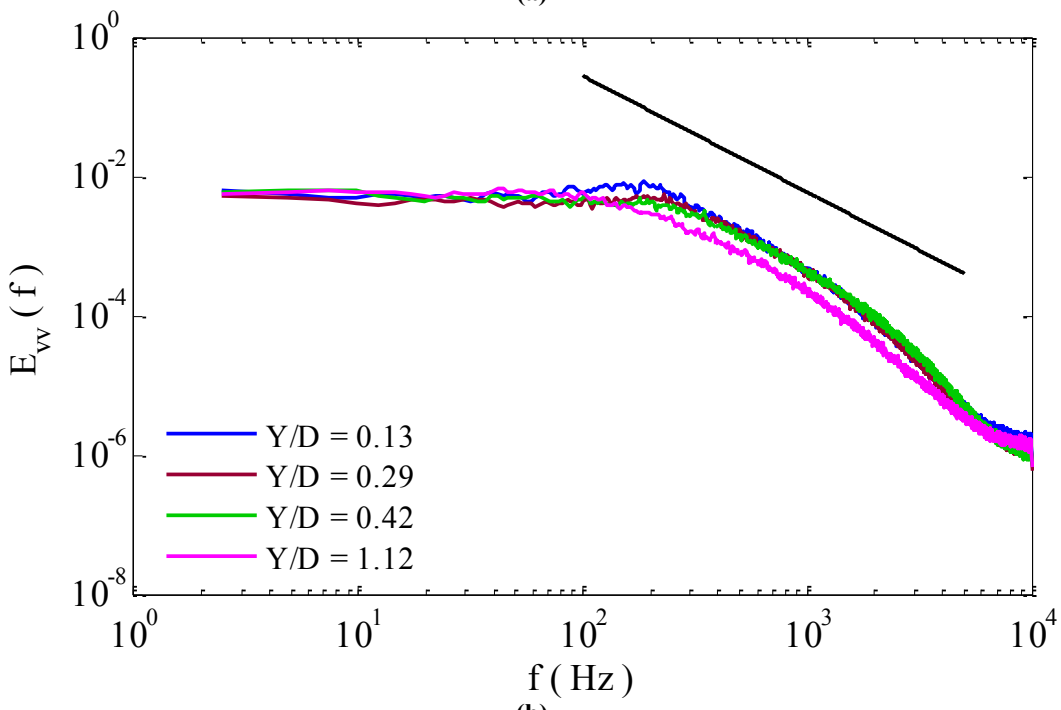

(b)

Figure III-13 Power spectra density for points within gap B6 at Re_m= 4,541 obtained by the time histories of (a) axial velocity, (b) radial velocity.

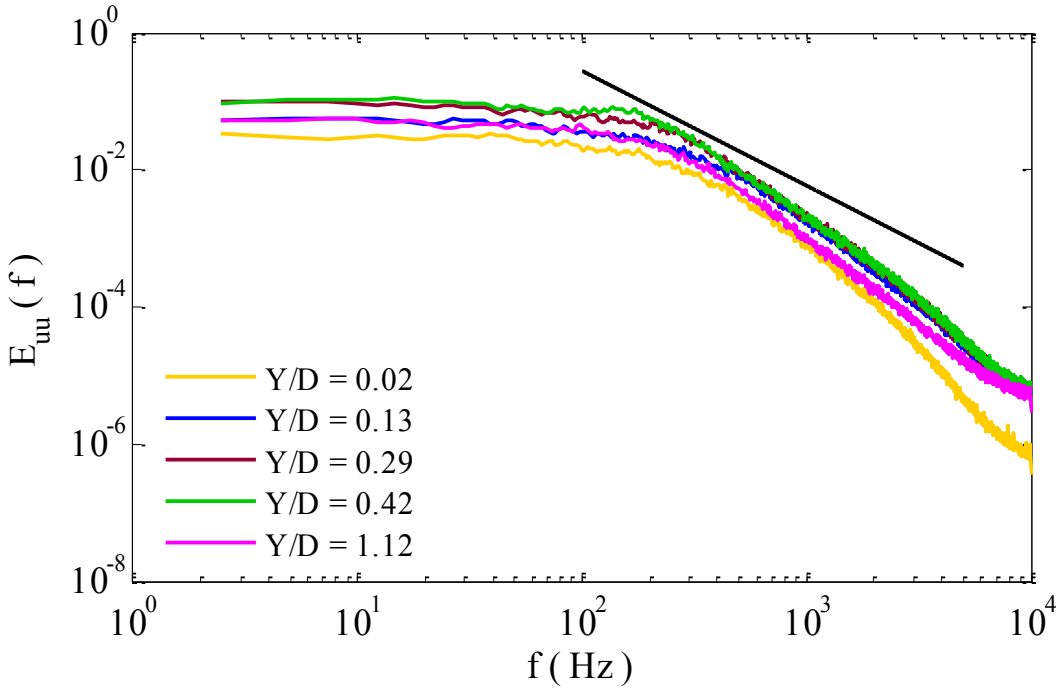

(a)

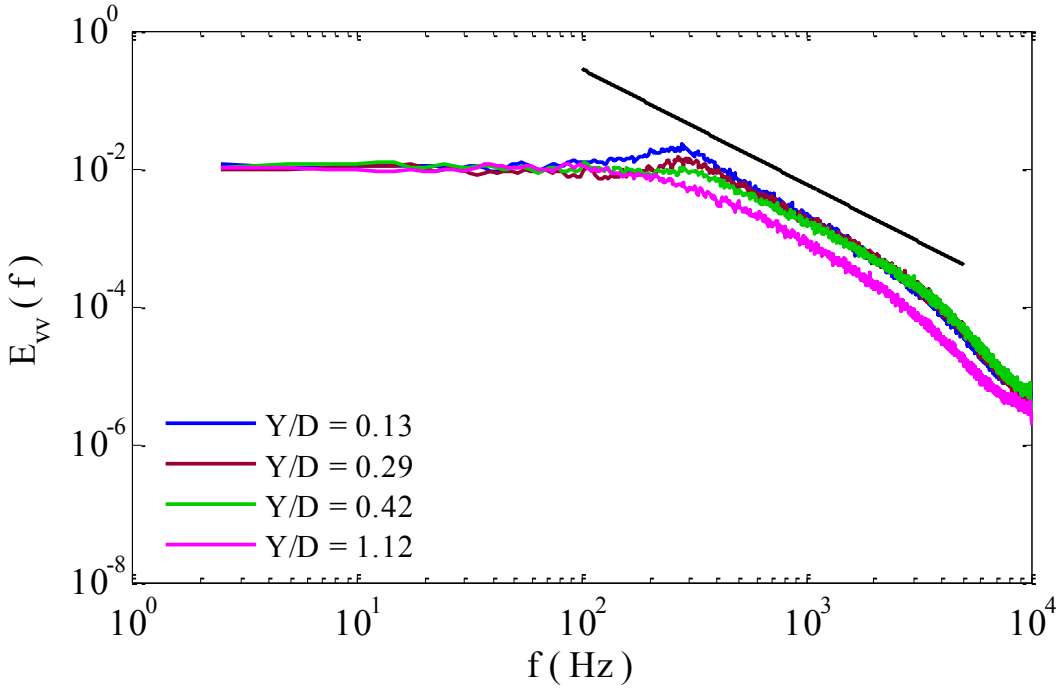

(b)

Figure III-14 Power spectra density for points within gap B6 at Re_m= 6,857 obtained by the time histories of (a) axial velocity, (b) radial velocity.

III.3.2.2. Spectral Analysis at the Peak Point of Time-Averaged Axial Velocity Profiles for Different Reynolds Numbers

In this section, to investigate the effect of the Reynolds number on the behavior of the power spectra, the spectra is obtained for specific points within the gaps for all five different Reynolds numbers.

Figure III-15 shows the power spectra of the axial and radial velocities for the point at the peak of the time-averaged velocity profile (Y/D= 0.19) within gap A4 for five different Reynolds numbers. The significant point here is the exchange in the transfer of energy from low frequency section of the spectra to the high frequency part as the Reynolds number increases. As seen in the distributions, the energy spectrum of the lower Reynolds number cases begins with a higher energy content at the lower frequency part while the energy content drops quickly for the lower Reynolds cases and is lower than that of the higher Reynolds cases in the higher frequency range. This trend is clearly observed in both power spectra of axial and radial velocity in Figure III-15.

To obtain a more clear understanding of the effect of Reynolds number on the evolution of the power spectra within gap B6, two points at the center of the two axial velocity peaks (Y/D = 0.13 and Y/D = 0.42) are estimated and shown in Figure III-16 and Figure III-17, respectively. The results of the power spectra analysis for both axial and radial velocity components indicate the same trend of energy transfer from lower frequency section to higher frequency section of the spectra as the Reynolds number increases.

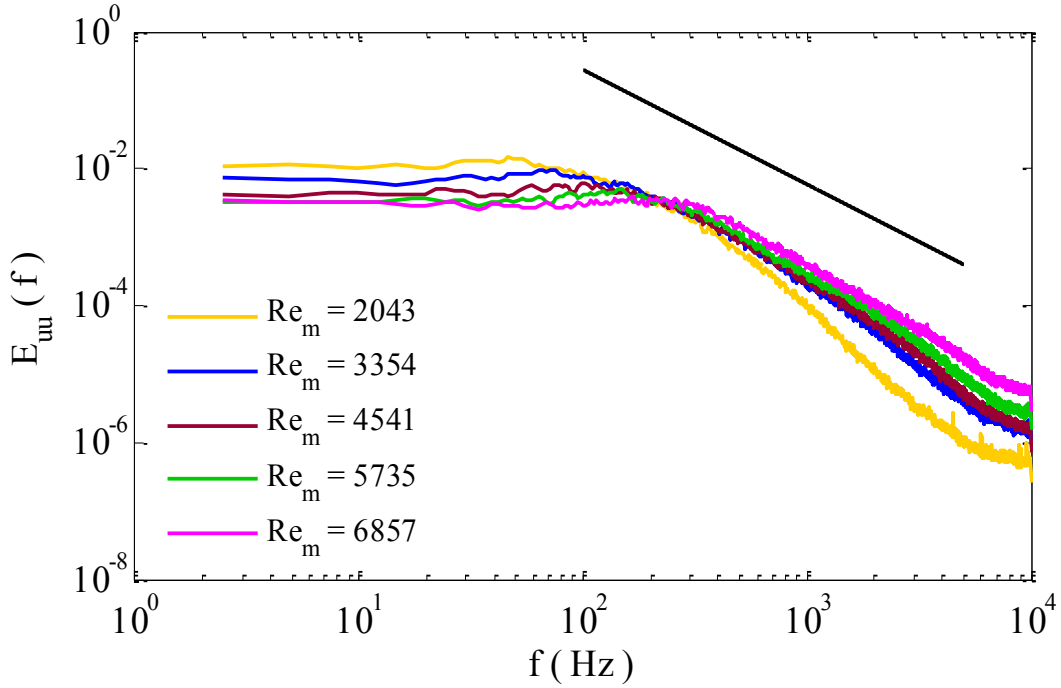

(a)

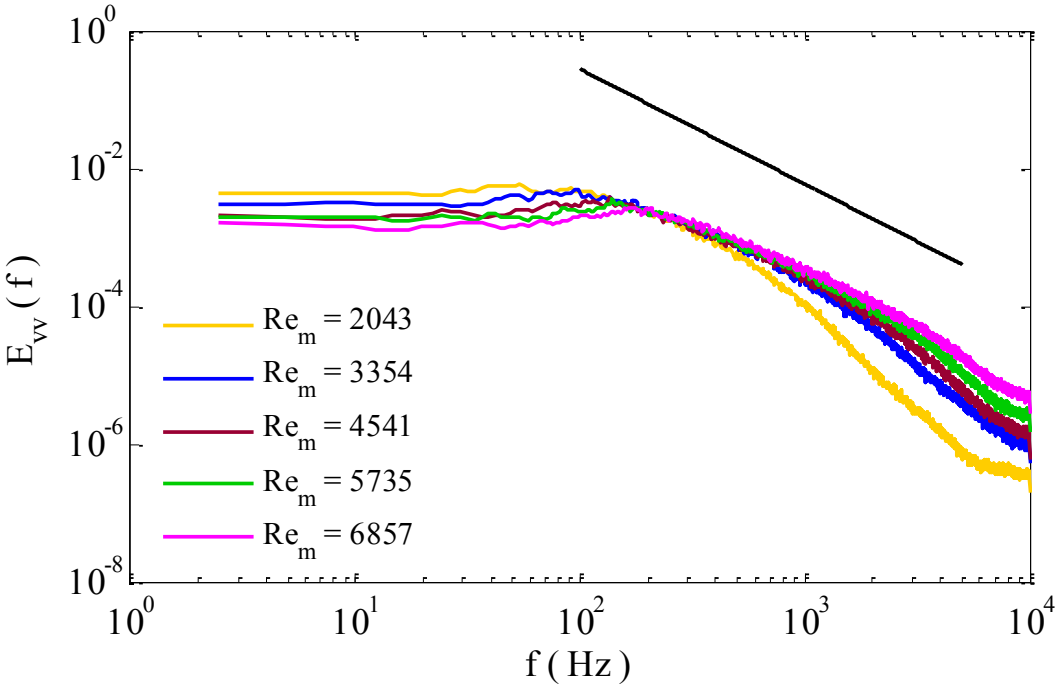

(b)

Figure III-15 Power spectra density at the peak of the time-averaged axial velocity of gap A4 (Y/D= 0.19) obtained by the time histories of (a) axial velocity, (b) radial velocity.

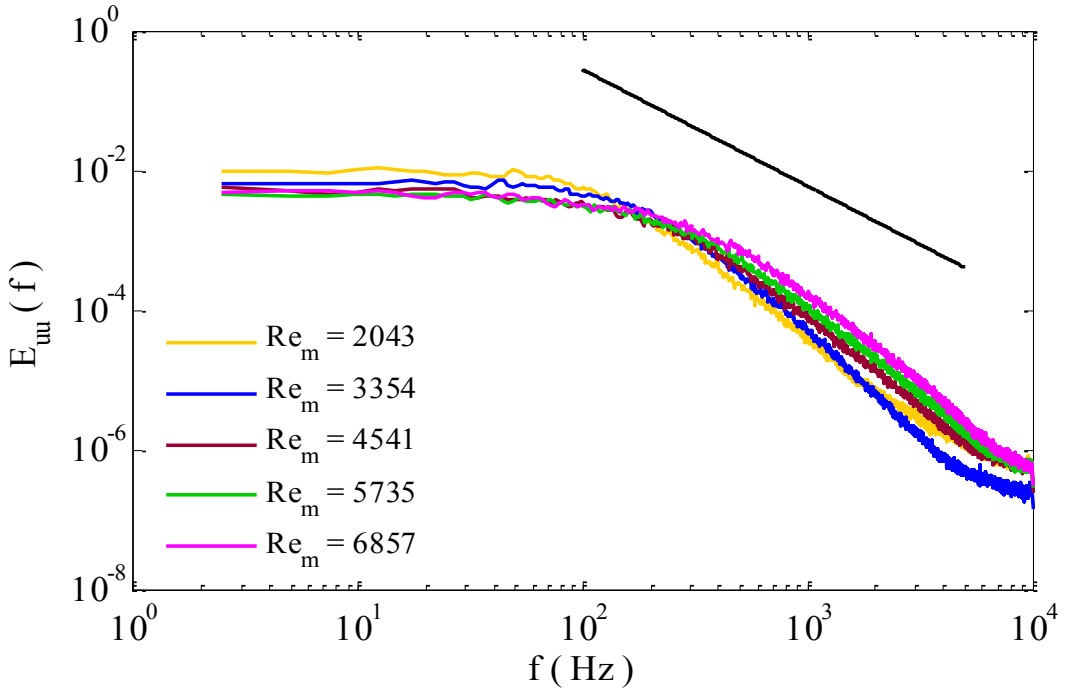

(a)

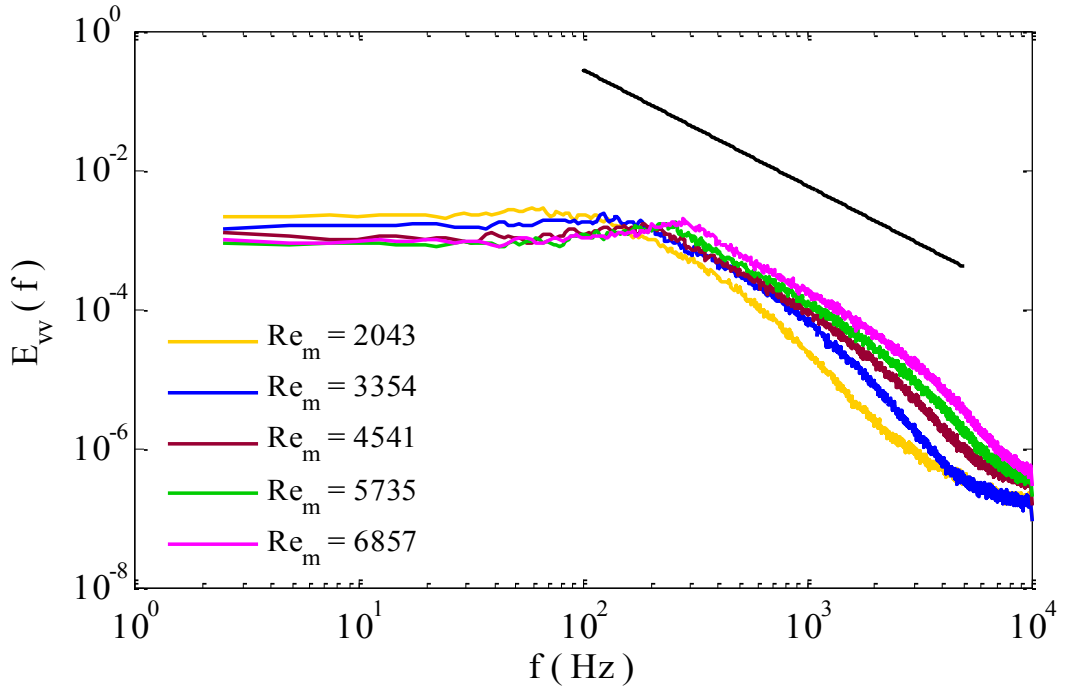

(b)

Figure III-16 Power spectra density at the first peak of the time-averaged axial velocity of gap B6 (Y/D= 0.13) obtained by the time histories of (a) axial velocity, (b) radial velocity.

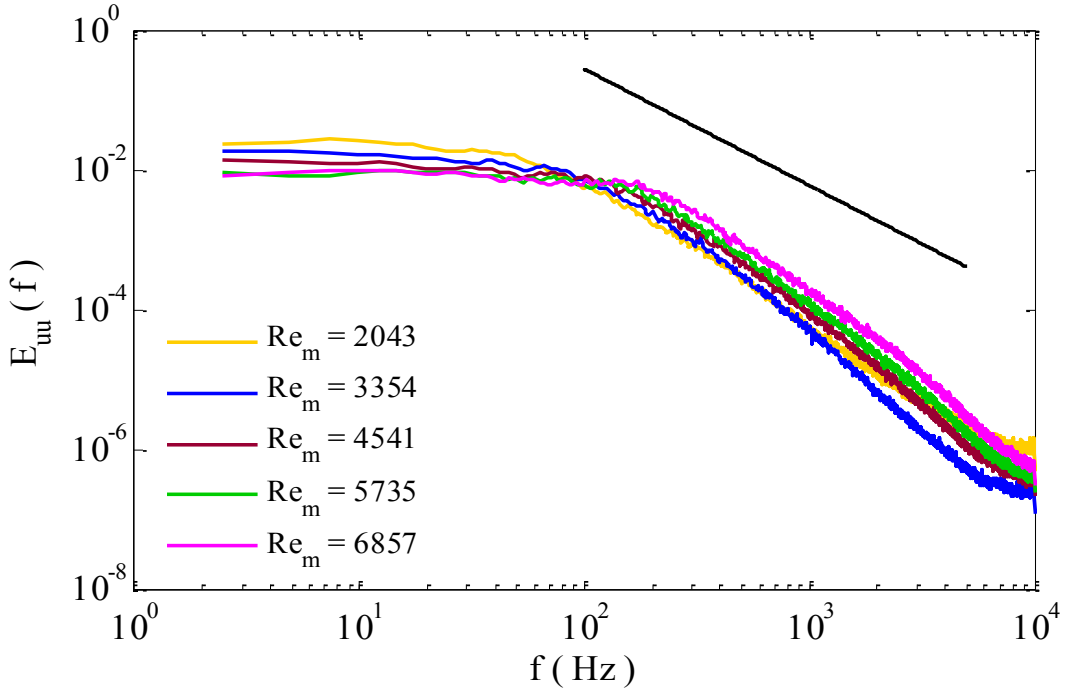

(a)

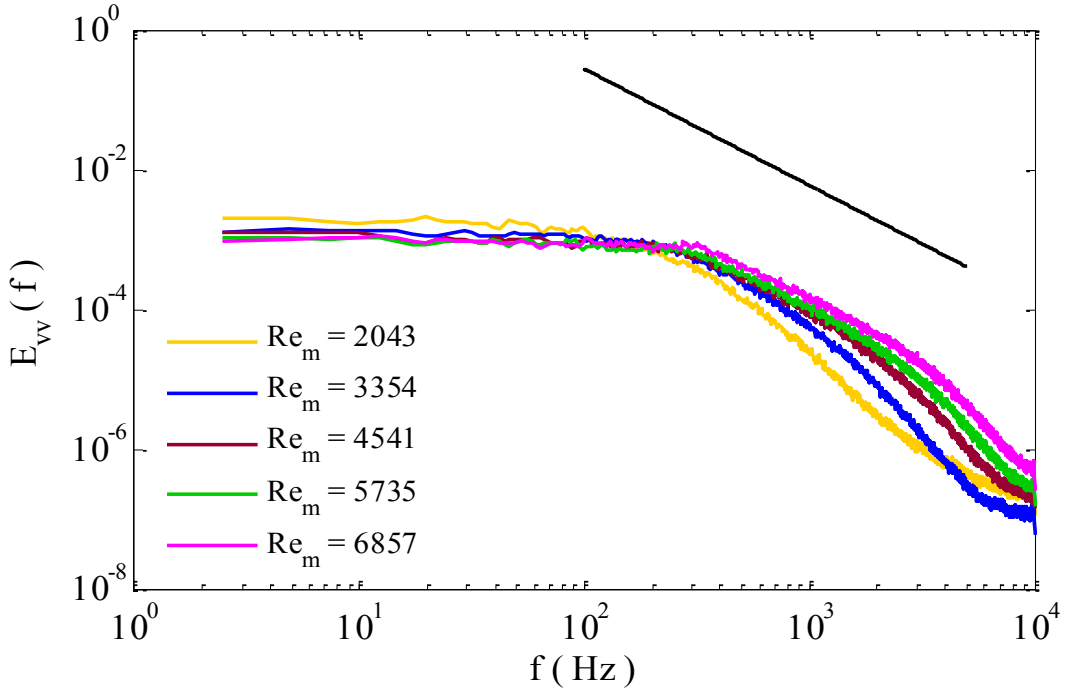

(b)

Figure III-17 Power spectra density at the second peak of the time-averaged axial velocity of gap B6 (Y/D= 0.42) obtained by the time histories of (a) axial velocity, (b) radial velocity.

III.4. Conclusion

Characterization of complex coolant flow behavior in gaps between the spherical fuel elements in the core of pebble bed VHTRs is highly important in the design and development of such reactors. In this study, a Hot Wire Anemometry system coupled with a hot film X-probe is utilized to measure the two components of the coolant velocity within the near wall gaps of a pebble bed VHTR. For this purpose, two different gaps with extremely different geometries and at different heights and radial position of the bed were chosen for velocity measurements. The results of hot wire velocity measurements for five different Reynolds numbers of the air passing through the bed compares well with the results from previous studies confirming the presence of an annular region of a higher velocity close to the outer reflector wall (*bypass flow*). The results indicate the presence of *bypass flow* in both time-averaged axial and radial velocity profiles obtained by HWA technique. Moreover, the results show a strong dependence of the velocity profiles and the characteristics of the *bypass flow* to the gap geometry. In one geometry (gap A4), the classical behavior of *bypass flow* with one sharp peak in the velocity profile close to the packed bed wall was clearly observed while in the other gap, two peaks were identified in both axial and radial velocity profiles. In the second gap, the peak close to the wall was not always the highest one.

The effect of Reynolds number on the velocity profile was found to be quite consistent for one of the gap geometries (gap A4) while for the second gap the magnitude of the two peaks changed with the change in Reynolds number. Specifically for the second gap, for the higher Reynolds numbers, the peak closest to the wall was the

lower peak and for the lower Reynolds numbers, the peak closest to the wall was the higher peak. It can be concluded that the gap geometry and Reynolds number of the flow simultaneously affect the velocity profile of the coolant through the gap. Further measurements in different gaps with different geometries and different Reynolds number of the flow are required in order to categorize the effect of each of these parameters on the velocity profiles of fluid passing through the gap.

The high frequency time histories of the velocities obtained at each point were further analyzed using power spectra method. The results of the power spectra density for specific points chosen within each gap reveal that the spatial variation within the gap highly affects the shape of the power spectra and the slope of the energy cascade. Moreover, the effect of the solid boundary i.e. packed bed wall and the sphere at the end of the gap was found to be significant on the power spectra. In addition, the effect of the Reynolds number on the evolution of the power spectra at specific points within each gap was investigated. The results show that as the Reynolds number increases, from the slope of energy transfer from the lower frequency part of the spectrum to the higher frequency part decreases resulting into a milder slope for the energy cascade in the inertial sub-range.

The results of this experimental study could provide as a benchmark for validation of the numerical models attempting at modeling the flow behavior within porous media and specifically for development of models to predict the helium coolant flow behavior within the core of a pebble bed VHTR.

CHAPTER IV

SUMMARY

In this dissertation, turbulent flow behavior within two experimental models with highly complex geometries was studied with the application of appropriate experimental turbulent flow measurement techniques. The first experimental study involves the investigation of coolant flow behavior within the lower plenum of a prismatic core VHTR. In the second experimental investigation, coolant flow behavior and bypass flow phenomenon within the near wall gaps of a pebble bed VHTR were studied. A summary of the problem under study in each case, the experimental techniques applied in each experiment, and the results and findings of each investigation is presented in the following sections.

IV.1. Experimental Study of the Coolant Flow Behavior within the Lower Plenum of a Prismatic Core VHTR

This experimental investigation aims at modeling the helium coolant flow behavior within the lower plenum of a prismatic core VHTR. The experimental test section representing the geometry of the lower plenum consisted of a rectangular channel with a length of 1016 mm and a square cross section of 76.2×76.2 mm^2. Inside the channel a rod bundle including 29 tubes with an outside diameter of 10.67 mm and an inside diameter of 10.16 mm were set in a staggered configuration modeling the configuration of graphite support rods within the lower plenum. Two circular inlet jets

with dimensions similar to that of the tubes used in the rod bundle were entering the channel top wall in areas within the rod bundle. The two jets were representing the helium coolant jets impinging into the lower plenum environment. The channel has a single inlet and a single outlet modeling different crossflow velocities within the lower plenum and the single outlet of the lower plenum, respectively. In this experiment water was used as the working fluid and various cases with different numbers of the jets and different Reynolds numbers of the jets with or without crossflow were studied.

A 2-D Dynamic PIV technique was applied to obtain the velocity fields within the rod bundle. To provide the complete visual access to areas inside the rod bundle which is required for the PIV method, MIR technique was used in the selection of the material for the tubes representing the graphite support rods. For this purpose, FEP tubes were selected to be used both for the rod bundle and the inlet jets. Moreover, to ensure a uniform refractive index within the test section the FEP tubes used in the rod bundle were filled with water.

In this investigation, for each case study, velocity fields of three different vertical planes within the rod bundle were obtained applying PIV technique (image acquisition frequency of 1,000 fps and image acquisition period of five seconds). Different sources that may affect the accuracy of the PIV measurements and analysis were considered and error analysis was performed on the PIV analysis software as well as on the adequacy of the number of images obtained by PIV for each case. Both procedures showed a high level of accuracy for the PIV acquired data.

The time-averaged velocity fields of the mid-plane for cases with single or dual impinging jets identified a key recirculation zone close to the bottom part of the adjacent rod of the inlet jets on the impingement side. Interestingly, these recirculation zones exist even in the presence of a crossflow. These key flow features along with the other vertical patterns observed within the instantaneous vorticity fields could contribute to the enhancement of mixing within the lower plenum environment. Moreover, the coherent structures observed close to the bottom part of the neighboring rod of inlet jets (representing the graphite support rods within the lower plenum) could potentially affect the structural integrity of the rods and the bottom surface of the actual model in long term.

To further study the behavior of the coherent structures within the flow field, a Snapshot POD method was applied to the PIV velocity fields. POD analysis helps in extracting the large-scale coherent structures from the flow field and in reconstructing lower-order models of the highly complex flow fields. The results of the POD analysis confirm that the first few POD modes (also called the primary POD modes) contain the majority of the energy of the flow field. Hence, lower order models of the flow fields can be reconstructed by only applying these primary modes which will represent the flow features with the highest energy content. In this study, the mode shapes of the first five POD modes for all cases are mainly representing the jet flow which confirms that the jet is the dominant feature of the flow field. Therefore to capture the lower energy but highly important flow features of the flow field (i.e. the coherent structures close to

the bottom part of the adjacent rod of the inlet jet, called "*Recirculation Area*") through POD analysis, a different approach needs to be adopted.

In this investigation, a *Comparative POD* analysis technique is suggested to study the behavior of the coherent structures existing within the *Recirculation Area*. In this technique, first the *Recirculation Area* is separated from the flow field and its energy content is compared to that of the whole field. The results showed that for all cases, the energy content of the *Recirculation Area* is lower than 3% of the energy content of the whole field. Consequently, a higher number of POD modes is required to be considered for a reasonable reconstruction of the coherent structures within the *Recirculation Area* compared to the number of modes required for the reconstruction of the whole field or the higher energy content flow features (e.g. jets). Therefore, the flow field was reconstructed using different number of POD modes, the *Recirculation Area* was separated from the reconstructed field, and its energy was compared to the original *Recirculation Area*. The results confirm that a higher number of modes is needed for a faithful reconstruction of the vortical structures within the *Recirculation Area*. Furthermore, a qualitative comparison between the coherent structures within the reconstructed *Recirculation Area* and the original *Recirculation Area* as well as the quantitative comparison between the energy content of the two regions would help in obtaining the sufficient number of modes for a reasonable reconstruction of the *Recirculation Area*.

The data acquired through this experimental study could be applied as a benchmark for validation of the existing CFD codes and also for development of new

models predicting the behavior of helium coolant flow within the lower plenum of a prismatic VHTR under normal operation as well as accident scenarios.

IV.2. Experimental Study of Bypass Flow in Different near wall Gap Geometries of a Pebble Bed VHTR

The main objective of this experimental study is characterization of the coolant flow behavior and specifically the *bypass flow* phenomenon within gaps between the spherical fuel elements in areas close to the outer reflector wall of an annular pebble bed VHTR. The test section modeling the core of an annular packed bed which was used in this experiment was an annular bed filled with spheres representing the spherical fuel particles in the core of an actual pebble bed VHTR. The outer cylinder has a height of 2.18 m and an outer diameter of 0.89 m while the radius of the inner annulus is 0.27 m. Two different types of spheres are used to fill the annular bed: 1- Black spheres with a 0.03302 m diameter used in the upper and lower sections of the bed and, 2- Clear acrylic spheres with a 0.03175 m diameter used in the middle section of the bed. The two types of spheres are chosen to have nearly identical sizes to ensure a uniform porosity throughout the bed. Air is used as working fluid in this experiment and it is passed through the bed using a high power blower. In this experiment, a high frequency HWA system is applied to obtain the velocity profiles within the near wall gaps of the annular packed bed. Four evenly spaced columns (columns A to D) each containing ten evenly spaced holes were considered on the circumference of the packed bed to provide access

to the near wall gaps in order to carry out the velocity measurements using the HWA probe.

For this experimental study, two different near wall gaps on different measurement column at different heights of the channel (gaps A4 and B6) which have significantly different geometries were considered for velocity measurements. To obtain the velocity profile within each gap, the HWA probe was moved along a straight line in radial direction within the gap in very fine increment. An X-probe hot film anemometer is used in this set of experiments to obtain both axial and radial components of the velocity at each measurement point. The X-probe records the velocity data at a frequency of 20 KHz for a period of 26.214 seconds. To ensure a high level of accuracy for velocity measurements at each point within each gap, the velocity measurements have been repeated three times and an average value of those measurements is recorded as the average velocity at each point. For each near wall gap geometry, the velocity profiles within the gaps were obtained for five different Reynolds numbers of air passing through the packed bed.

Both axial and radial time-averaged velocity profiles obtained in the two near wall gaps for all five different Reynolds numbers show a sharp peak in the velocity (*bypass flow*) close to the outer cylinder wall representing the outer reflector in the actual pebble bed VHTR. Furthermore, it was observed that the gap geometry has a major influence on the shape of the velocity profiles and the characteristics of the *bypass flow* within each gap. For instance, both axial and radial velocity profiles within gap A4

showed a sharp peak close to the outer cylinder wall while the axial and radial velocity profiles within gap B6 represented two separate peaks with two different magnitudes.

The effect of the Reynolds number on the velocity profiles within each gap was found to be changing from one gap geometry to the other. In gap A4, the shape of both axial and radial velocity profiles and the location of the bypass flow peak were quite similar for all different Reynolds numbers. On the other hand, in gap B6, variations in the Reynolds number resulted in the changes in the shape of the velocity profiles (i.e. for the higher Reynolds numbers the peak closest to the outer cylinder wall had a higher magnitude compared to the second peak observed in the velocity profile while this peak had a lower magnitude for the lower Reynolds numbers).

To further study the turbulent flow behavior of the coolant flow within the near wall gaps of a pebble bed VHTR, the time-histories of the velocities at each measurement point within both gaps were analyzed applying power spectra density technique. It was observed that spatial variation within each gap significantly affects the power spectrum as well as the slope of the energy cascade. Moreover, investigations carried out on the effect of variations in the Reynolds number on the power spectra at specific points within each gap showed that the increase in the Reynolds number results in having a milder slope of the energy cascade in the inertial sub-range.

The result of this investigation could be applied in developing an experimental database for validation of CFD codes modeling the flow behavior within porous media particularly for validation of the numerical models used for prediction of the helium coolant flow behavior within the core of pebble bed VHTRs.

REFERENCES

ABDEL-FATTAH, A. 2007 Numerical and experimental study of turbulent impinging twin-jet flow. *Experimental Thermal and Fluid Science* **31**, 1061-1072.

ADRIAN, R. J. 1984 Scattering particle characteristics and their effect on pulsed laser measurements of fluid flow: speckle velocimetry vs particle image velocimetry. *Applied Optics* **23**, 1690-1691.

ADRIAN, R. J. 1991 Particle-imaging techniques for experimental fluid mechanics. *Annu. Rev. Fluid Mech* **23**, 261-304.

ADRIAN, R. J. 2005 Twenty years of particle image velocimetry. *Experiments in Fluids* **39**, 159-169.

ADRIAN, R. J., Christensen, K. T. & Liu, Z. -C. 2000 Analysis and interpretation of instantaneous turbulent velocity fields. *Experiments in Fluids* **29**, 275-290.

ALEKSEENKO, S. V., BILSKY, A. V., DULIN, V. M. & MARKOVICH, D. M. 2007 Experimental study of an impinging jet with different swirl rates. *International Journal of Heat and Fluid Flow* **28**, 1340-1359.

AMINI, N., DOMINGUEZ-ONTIVEROS, E. E., ESTERADA-PERAZ, C. E., FORTENBERRY, S. D. & HASSAN, Y. A. 2008 PIV Measurements of jet flow mixing in the vicinity of rod bundles using matched-index of refraction. In *Proceedings of the 16th International Conference on Nuclear Engineering (ICONE-16)*. Orlando, FL, 1–5.

AMINI, N. & HASSAN, Y. A. 2009 Measurements of jet flows impinging into a channel containing a rod bundle using dynamic PIV. *International Journal of Heat and Mass Transfer* **52,** 5479-5495.

ASHTON, H. M. & GUGGENHEIM, E. A. 1956 A new method for determining the second virial coefficient of a gas, In *Proceedeings of Physical Society* **B 69**, 693-694.

AZIZ, A. R. A. & WONG, K. F. V. 2003 Velocity measurements across fluid-porous medium interface using particle image velocimetry. *International Jounral of Modelling and Simulation* **23,** 1-8.

BAILEY, B. C. & YODA, M. 2003 An aqueous low-viscosity density- and refractive index-matched suspension system. *Experiments in Fluids* **35,** 1-3.

BERKOOZ, G., HOLMES, P. & LUMLEY, J. L. 1993 The proper orthogonal decomposition in the analysis of turbulent flows. *Annual Reviews of Fluid Mechanics* **25**, 539-575.

BERNERO, S. & FIEDLER, H. E. 2000 Application of particle image velocimetry and proper orthogonal decomposition to the study of a jet in a counterflow. *Experiments in Fluids* **29**, 274-281.

BEYSENS, D. & CALMETTES, P. 1977 Temperature dependence of the refractive indices of liquids: Deviation from Lorentz-Lorenz formula. *The Journal of Chemical Physics* **66**, 766-771.

BI, W., SUGII, Y., OKAMOTO, K. & MADARAME, H. 2003 Time-resoleved proper orthogonal decomposition of the near-field flow of a round jet measured by

dynamic particle image velocimetry. *Measurement Science and Technology* **14**, L1-L5.

BRUUN, H. H. 1995 Hot-Wire Anemometry Principles and Signal Analysis, Oxford University Press.

BUDWIG, R. 1994 Refractive index matching methods for liquid flow investigations. *Experiments in Fluids* **17**, 350-355.

CARIOU, J. M., DUGAS, J., MARTIN, L. & MICHEL, P. 1986 Refractive-index variations with temperature of PMMA and polycarbonate. *Applied Optics* **3,** 334-336.

CHANG, S. K., MOON, S. K., BAEK, W. P. & CHOI, Y. D. 2007 Phenomenological investigations on the turbulent flow structures in a rod bundle with mixing devices. *Nuclear Engineering and Design* **238,** 600-609.

CHEN, R. C. & FAN, L. S. 1992 Particle image velocimetry for characterizing the flow structure in three-dimensional gas-liquid-solid fluidized beds. *Chemical Engineering Science* **47,** 3615-3622.

CITRINITI, J. H. & GEORGE, W. K. 2000 Reconstruction of the global velocity field in the axisymmetric mixing layer utilizing the proper orthogonal decomposition. *Journal of Fluid Mechanics* **41,** 137-166.

COOPER, D., JACKSON, D. C., LAUNDER, B. E. & LIAO, G. X. 1993 Impinging jet studies for turbulence model assessment-I. Flow-field experiments. *Int. J. Heat Mass Transfer* **36,** 2675-2684.

DONALDSON, C. DUP. & SNEDEKER, R. S. 1971 A study of free jet impingement. Part 1: Mean properties of free and impinging jets. *Journal of Fluid Mechanics* **45**, 281-319.

DONALDSON, C. DUP., SNEDEKER, R. S. & MARGOLIS, D. P. 1971 A study of free jet impingement. Part 2: Free jet turbulent structure and impingement heat transfer. *Journal of Fluid Mechanics* **45,** 477-512.

DRAHOS, J., CERMAK, J., ZILOKOWSKA, I. & ZIKOKOWSKI, D. 1982 Statistical analysis of local gas velocities at the exit from a packed bed. *The Chemical Engineering Journal* **24,** 71-80.

DUDLEY, T., BOUWER, W., DE VILLIERS, P. & WANG, Z. 2008 The thermal-hydraulic model for the pebble bed modular reactor (PBMR) plant operator training simulator system. *Nuclear Engineering and Design* **238,** 3102-3113.

DYBBS, A. & EDWARDS, R. V. 1984 An index matched flow system for measurements of flow in complex geometries. In *Proceedings of the International Symposium on the Application of Anemometry to Fluid Mechanics.* Lisbon, Portugal, 171-184.

EGELHOFF, C. J., BUDWIG, R. S. , ELGER, D. F., KHRAISHI, T. A. & JOHANSEN, K. H. 1999 Model studies of the flow in abdominal aortic aneurysms during resting and exercise conditions. *Journal of Biomechanics* **32**, 1319-1329.

ESTRADA-PEREZ, C. 2004 Analysis, comparison and modification of various particle image velocimetry (PTV) algorithms. M. S. Thesis, Texas A&M University, College Station.

ESTRADA-PEREZ, C. & HASSAN, Y.A. 2010 PTV experiments of subcooled boiling flow through a vertical rectangular channel. *International Journal of Multiphase Flow* **36**, 691-706.

GLADSTONE, J. H. & DALE, T. P. 1863 Researches on the Refraction, Dispersion, and Sensitiveness of Liquids. *Proceedings of the Royal Society of London.*

GLAUSER, M. N., LEIB, S. J. & GEORGE, W. K. 1987 Coherent structures in the axisymmetric turbulent jet mixing layer. *Turbulent Shear Flows* **5,** 134-145.

GOHARZADEH, A., KHALILI, A. & JØRGENSEN, B. B. 2005 Transition layer thickness at a fluid-porous interface. *Physics of Fluids* **17**, 057102-1:10.

GOODLING, J. S., VACHON, R. I., STELPFLUG, W. S. & YING, S. J. 1983 Radial porosity distribution in cylindrical bes packed with spheres. *Powder Technology* **35,** 23-29.

GORDEYEV, S. V. & THOMAS, F. O. 2002 Coherent structures in the turbulent planar jet. Part 2. Structural topology via POD egienmode projection. *Journal of Fluid Mechanics* **460,** 349-380.

GT-MHR 2001 http://gt-mhr.ga.com/.

GUIDECHEM 2011 http://www.guidechem.com/products/10035-04-8.html.

HAAM, S. J. & BRODKEY, R. S. 2000 Motions of dispersed beads obtained by particle tracking velocimetry measurements Part II. *Internation Journal of Multiphase Flow* **26**, 1419-1438.

HAAM, S. J., BRODKEY, R. S., FORT, I., KLABOCH, L., PLACNIK, M. & VANECEK, V. 2000 Laser Doppler anemometry measurements in an index of

refraction matched column in the presence of dispersed beads Part I. *International Journal of Multiphase Flow* **26**, 1401-1418.

HANNOUN, I. A., FERNANDO, H. J. S. & LIST, E. J. 1988 Turbulence structure near a sharp density interface. *Journal of Fluid Mechanics* **189,** 189-209.

HARVEY, A. H., GALLAGHER, J. S. & LEVELET SENGERS, J. M. H. 1998 Revised formulation for the refractive index of water and steam as a function of wavelenth, temperatuer and density. *J. Phys. Chem. Ref. Data* **27**, 761-774.

HASSAN, Y. A. 2007 Large eddy simulation in pebble bed gas cooled core reactors. *Nuclear Engineering and Design* **238,** 530-537.

HASSAN, Y. A., BLANCHAT, T. K. & SEELEY JR., C. H. 1992 PIV flow visualization using particle tracking techniques. *Meas. Sci. Technol.* **3**, 633-642.

HASSAN, Y. A. & DOMINGUEZ-ONTIVEROS, E. E. 2008 Flow visualization in a pebble bed reactor experiment using PIV and refractive index matching techniques. *Nuclear Engineering and Design* **238,** 3080-3085.

HECHT, E. 2002 *Optics. 4th Ed*. Addison-Wesley.

HOLMES, P., LUMELY, J. L., & BERKOOZ, G. 1996 *Turbulence, coherent structures, dynamical systems and symmetry*, Cambridge University Press.

HOOPER, J. D. & REHME, K. 1984 Large-scale structural effects in developed turbulent flow through closely-spaced rod arrays. *Journal of Fluid Mechanics* **145**, 305-337.

HOOPER, J. D. & WOOD, D. H. 1984 Fully developed rod bundle flow over a large range of Reynolds number. *Nuclear Engineering and Design* **83**, 31-46.

HUANG, A. Y, L. & HUANG, M. Y. F. 2008 Optical measurements of pore geometry and fluid velocity in a bed of irregularly packed spheres. *Experiments in Fluids* **4**5, 309-321.

HUSSAIN, A. K. M. F. 1983 Coherent structures-reality and myth. *Physics of Fluids* **10,** 2816-2850.

JOHNSTON, W., DYBBS, A. & EDWARDS, R. 1975 Measurement of fluid velocity inside porous meida with a laser anemometer. *The Physics of Fluids* **18,** 913-914.

JØRGENSEN, F. E. 2002 How to measure turbulence with hot-wire anemometers - a practical guide. Dantec Dynamics, Skovlunde, Denmark.

KIM, K. C, MIN, Y. U., OH, S. J., AN, N. H., SEOUDI, B., CHUN, H. H. & LEE, I. 2007 Time-resoleved PIV investigation on the unsteadiness of a low Reynolds number confined impinging jet. *Journal of Visualization* **10**, 367-379.

KOSTER, A., MATXNER, H. D. & NICHOLASI, D. R. 2003 PBMR design for future. *Nuclear Engineering and Design* **222**, 231-245.

LANDRETH, C. C. & ADRIAN, R. J. 1990 Impingement of a low Reynolds number turbulent circular jet onto a flat plate at normal incidence. *Experiments in Fluids* **9,** 74-84.

LEE, J. Y. & LEE, S. Y. 2009 Flow visualization in the scaled up pebble bed of high temperature gas-gooled reactor using particle imave velocimetry method. *Journal of Engineering for Gas Turbines and Power* **131,** 064502-1-064502-4.

LEROU, J. J. & FROMENT, G. F. 1977 Velocity, temperature and conversion profiles in fixed bed catalytic reactors. *Chemical Engineering Science* **32,** 853-861.

LORENZ, L. & LORENTZ, M. A. 1880 Theory of electrons. The London, Edinburgh and Dublin Philosophical Magazine and Journal of Science 11:70.

LOWE, M. L. & KUTT, P. H. 1992 Refraction through cylindrical tubes. *Experiments in Fluids* **13,** 315-320.

LUMLEY, J. L. 1967 The structure of inhomogeneous turbulent flows . In *Atmospheric Turbulence and Radio Wave Propagation*, Moscow, Nauka, 166-178.

MACDONALD, P. E., STERBENTZ, J. W., SANT, R. L. , BAYLESS, P. D., SCHULTZ, R. R., GOUGAR, H. D., MOORE, R. L., OUGOUAG, A. M. & TERRY, W. K. 2003 NGNP point design results of the initial neutronics and thermal hydraulic assessment during FY-03. Idaho Engineering and Environmental Laboratory, Idaho Falls, Idaho.

MARIVOET, J., TEODORIOU, P. & WAJC, S. J. 1974 Porosity, velocity and temperature profiles in cylindrical packed beds. *Chemical Engineering Science* **29,** 1836-1840.

MAUREL, S., BORÉE, J. & LUMLEY, J. L. 2001 Extended Proper Orthogonal Decomposition: Application to Jet/Vortex Interaction. *Flow, Turbulence and Combustion* **67**, 125-136.

MCCREERY, G. E. & CONDIE, K. G. 2006 Experimental modeling of VHTR plenum flows during normal operation and pressurized conduction cooldown. Idaho National Laboratory, Idaho Falls, Idaho.

MCDOUGALL, T.J. 1979 On the elimination of refractive index variations in turbulent density-stratified liquid flows. *Journal of Fluid Mechanics* **93**, 83-96.

MCELIGOT, G. E. & MCCREERY, D. M. 2004 Scaling studies and conceptual experiment designs for NGNP CFD assessment. Idaho National Engineering and Environmental Laboratory Bechtel BWXT, Idaho Falls, Idaho.

MERZARI, E. & NINOKATA, H. 2009 Proper orthogonal decomposition of the flow in a tight lattice rod bundle. In *Proceedings of 13th Nuclear Reactor Thermal Hydraulics (NURETH-13).* Kanazawa City, Japan.

MEYER, K. E., PEDERSEN, J. M. & ÖZCAN, O. 2007 A turbulent jet in crossflow analysed with proper orthogonal decomposition. *Journal of Fluid Mechanics* **583,** 199-227.

MI, J., NOBES, D. S. & NATHAN, G. J. 2001 Influence of jet exit conditions on the passive scalar field of an axisymmetric free jet. *Journal of Fluid Mechanics* **432,** 91-125.

MILLER, P., DANIELSON, K., MOODY, G., SLIFKA, A., DREXLER, E. & HERTZBERG, J. 2006 Matching index of refraction using a diethyl phthalate/ethanol solution for in vitro cardiovascular models. *Experiments in Fluids* **41,** 375-381.

MOISE, A. & TUDOSE, R. Z. 1998 Air isothermal flow through packed bes. *Experimental thermal and fluid science* **18,** 134-141.

NARROW, T. L., YODA, M. & ABDEL-KHALIK, S. I. 2000 A simple model for the refractive index of sodium iodide aqueous solutions. *Experiments in Fluids* **28,** 282-283.

NGUYEN, T. T., BIADILLAH, Y., MONGRAIN, R., BRUNETTE, J., TARDIF, J. C. & BERTRAND, O. F. 2004 A method for matching the refractive index and kinematic viscosity of a blood analog for flow visualization in hydraulic cardiovascular models. *Journal of Biomechanical Engineering* **126,** 529-535.

NISHINO, K., SAMADA, M., KASUYA, K. & TORII, K. 1996 Turbulence statistics in the stagnation region of an axisymmetric impinging jet flow. *International Journal of Heat and Fluid Flow* **17,** 193-201.

NIST Chemistry WebBook 2011 http://webbook.nist.gov/cgi/fluid.cgi?Action=Load&ID=C7732185&Type=IsoBar&Digits=5&P=1&THigh=30&TLow=20&TInc=5&RefState=DEF&TUnit=C&PUnit=atm&DUnit=mol%2Fl&HUnit=kJ%2Fmol&WUnit=m%2Fs&VisUnit=uPa*s&STUnit=N%2Fm.

NORTHRUP, M. A., KULP, T. J. & ANGEL, S. M. 1991 Fluorescent particle image velocimetry: application to flow measurement in refractive index-matched porous media. *Applied Optics* **30,** 3034-3040.

NORTHRUP, M.A., KULP, T. J. & ANGEL, S. M. 1993 Direct measurement of interstitial velocity field variations in porous medium using fluorescent-particle image velocimetry. *Chemical Engineering Science* **48,** 13-21.

PATTE-ROULAND, B., LALIZEL, G., MOREAU, J. & ROULAND, E. 2001 Flow analysis of an annular jet by particle image Velocimetry and proper orthogonal decomposition. *Measurement Science and Technology* **12,** 1404-1412.

PEURRUNG, L. M., RASHIDI, M. & KULP, T. J. 1995 Measurement of porous medium velocity fields and their volumetric averaging charachteristics using particle tracking velocimetry. *Chemical Engineering Science* **50,** 2243-2253.

PICKERING, C. J. D. & HALLIWELL, N. 1984 LSP and PIV: photographic film noise. *Applied Optics* **23,** 2961-2969.

PIV CHALLENGE 2011 http://piv.vsj.or.jp/piv/image3d/image301.html.

POPE, S. B. 2000 *Turbulent Flows.* Cambridge University Press.

RAFFEL, M., WILLERT, C. E. & KOMPENHANS, J. 1998 *Particle Image Velocimetry- A Practical Guide.* Springer-Verlag, Berlin, Heidelberg, Germany.

RASHIDI, M., PERURRUNG, L., TOMPSON, A. F. B. & KULP, T. J. 1996 Experimental analysis of pore-scale flow and transport in porous media. *Advances in Water Resources* **19,** 163-180.

REHME, K. 1987 The structure of turbulent flow through rod bundles. *Nuclear Engineering and Design* **99,** 141-154.

RENKSIZBULUT, K. & HADALLER, G. I. 1986 An experimental study of turbulent flow through a square_array rod bundle. *Nuclear Engineering and Design* **91,** 41-55.

ROBLEE, L. H. S., BAIRD, R. M. & TIERNEY, J. W. 1958 Radial proosity variations in packed beds, *A.I.Ch.E. Journal*, 460-464.

SAKAKIBARA, J., HISHIDA, K. & MAEDA, M. 1997 Vortex structure and heat transfer in the stagnation region of an impinging plane jet (simultaneous measurements of velocity and temperature fields by digital particle image

velocimetry and laser-induced fluorescence). *Int. J. Heat Mass Transfer* **40,** 3163-3176.

SALEH, S., THOVERT, J. F. & ADLER, P. M. 1992 Measurement of two-dimendional velocity fields in porous media by partice image displacement velocimetry. *Experiment in Fluids* **12,** 210-212.

SANADA, Y., OKAMOTO, K. & TODA, Y. 2005 Flow field visulization inside the head of gravity currents using refractive index matching technique. In *Proceedings of The 2nd Joint Japan/Korea Workshop on Marine Environmental Engineerin.* Kyushu University, Japan.

SCHIEBENER, P., STRUAB, J., LEVELT SENGERS, J. M. H. & GALLAGHER, J. S. 1990 Refractive index of water and steam as functions of wavelength, temperature and density. *J. Phys. Chem. Ref. Data* **19,** 677-717.

SCHMIDT, F. W., KULAKOWSKI, B. & WANG, D. F. 1984 Evaluation of the effect of variable refraction index on the path of a laser beam. *Experiments in Fluids* **2,** 153-158.

SCHULTZ, R. R., NIGG, D. W., OUGOUAG, A. M., TERRY, W. K., WOLF, J. R., GOUGAR, H. D., JOHNSEN, G. W., MCELIGOT, D. M., MCCREERY, G. E., JOHNSON, R. W., STERBENTZ, J. W., MACDONALD, P. E. , TAIWO, T. A., WEI, T. Y. C., YANG W. S., VILIM R. B. , POINTER W. D. & KHALIL, H.S. 2004 Next generation nuclear plant-design methods development and validation research and development program plan. Idaho National Engineering and Environmental Laboratory, Idaho Falls, Idaho.

SCHWARTZ, C. E. & SMITH, J. M. 1953 Flow distribution in packed beds. *Industrial and Engineering Chemistry* **45**, 1209-1218.

SCIENCELAB1 2011 http://www.sciencelab.com/msds.php?msdsId=9923637.

SCIENCELAB2 2011 http://www.sciencelab.com/msds.php?msdsId=9927152.

SINGH, S. 2002 Refractive index measurements and its applications. *Physica Scripta* **65**, 167-180.

SIROVICH, L. 1985 Turbulence and the dynamic of coherent structures Part I: Coherent structures. *Quarterly of Applied Mathematics* **XLV**, 561-571.

SMITH III, L. D., CONNER, M. E. , LIU, B., DZODZO, M. B., PARAMANOV, D. V. , BEASLEY, D. E., LANGFORD, H. M. & HOLLOWAY, M. V. 2002 Benchmarking computational fluid dynamics for application to PWR fuel. In *Proceedings of the 10th International Conference on Nuclear Engineering.* Arlington, VA, 823-830.

STANISLAS, M., OKAMOTO, K. , KÄHLER, C. J. , WESTERWEEL, J. & SCARANO F. 2008 Main results of the third international PIV challenge. *Experiments in Fluids* **45,** 27-71.

STEPHENSON, J. L. & STEWART, W. W. 1986 Optical measurments of porosity and fluid motion in packed beds. *Chemical Engineering Science* **41,** 2161-2170.

STÖHR, M., ROTH, K. & JAHNE, B. 2003 Measurement of 3D pore-scale flow in index-matched porous media. *Experiments in Fluids* **35,** 159-166.

STOOTS, C., BECKER, S., CONDIE, K., DURST, F. & MCELIGOT, D. 2001 A large-scale matched index of refraction flow facility for LDA studies around complex geometries. *Experiments in Fluids* **30,** 391-398.

SULLIVAN, P. & POLLARD, A. 1996 Coherent structures identification from the analysis of hot-wire data. *Measurement, Science and Technology* **7**, 1498-1516.

TAVOULARIS, S. 2005 *Measurements in Fluid Mechanics.* Cambridge University Press.

TENNEKES, H. & LUMELY, J. L. 1972 *A first course in turbulence*, MIT Press.

THORMÄHLEN, I., STRAUB, J. & GRIGULL, U. 1985 Refractive index of water and its dependence on wavelength, temperature, and density. *Journal of Physical and Chemical Reference Data* **14,** 933-945.

TRUPP, A. C. & AZAD, R. S. 1975 The structure of turbulent flow in triangular array rod bundles. *Nuclear Engineering and Design* **32,** 47-84.

TSI1 2011 http://www.tsi.com/uploadedFiles/Product_Information/Literature/Catalogs/Hotwire_Catalog_2980465.pdf.

TSI2 2011 http://www.tsi.com/en-1033/products/3734/thermal_anemometry_system/3744/thermalpro%E2%84%A2_software.aspx.

U.S. Department of Energy 2011 http://nuclear.energy.gov/genIV/neGenIV4.html.

UZOL, O., CHOW, Y. C., KATZ, J. & MENEVEAU, C. 2001 Unobstructed PIV measurements within an axial turbo-pump using liquid and blades with matched refractive indices. In *Proceedings of 4th International Symposium on Particle Image Velocimetry*. Göttingen, Germany.

VEE GEE 2011 http://veegee.thomasnet.com/Asset/VEE-GEE-Model-C10-Refractometer.pdf.

VELASCO, F. J. S., LO´PEZ DEL PRA´, C. & HERRANZ, L. E. 2007 Expansion of a radial jet from a guillotine tube breach in a shell-and-tube heat exchanger. *Experimental Thermal and Fluid Science* **32,** 947-961.

VORTMEYER, D. & SCHUSTER, J. 1983 Evaluation of steady flow profiles in rectangular and circular packed beds by a variational method. *Chemical Engineering Science* **38**, 1691-1699.

WAXLER, R. M., HOROWITZ, D. & FELDMAN, A. 1979 Optical and physical parameters of Plexiglas 55 and Lexan. *Applied Optics* **18,** 101-104.

WEAST, R. C. 1976-1977 *Handbook of Chemistry and Physics* 57th Edition, CRC Press.

WHITE, S. M. & TIEN, C. L. 1987 Analysis of flow channeling near the wall in packed beds. *Warme-und Stoffubertrangung* **21,** 291-296.

YARLAGADDA, A. P. & YOGANATHAN, A. P. 1989 Exeperimental Studies of model porous media fluid dynamics. *Experiments in Fluids* **8,** 59-71.

ZIOLKOWSKA, I. & ZIOLKOWSKI, D. 1988 Fluid flow inside packed beds. *Chem. Eng. Proccess.* **23**, 137-164.

APPENDIX A

As mentioned in Chapter II, optical distortions caused by non-uniformities of the refractive index within the measurement volume is a major impediment for all laser diagnostic imaging techniques applied in experimental fluid dynamic studies. An effective solution for this problem is obtained through matching the refractive index of the working fluid to that of the test section walls and interfaces. The experimental set-ups designed to be used along with laser imaging techniques are typically constructed of transparent solid materials.

This investigation is mainly focused on finding working fluids with refractive indices matched with those of fused quartz and acrylic which are commonly used for construction of test sections in fluid dynamics experiments (see section II.2.2.2 for more details). Consequently, different types of aqueous salt solutions with different salt concentrations as well as various organic fluids are studied for refractive index matching with acrylic and fused quartz. One aqueous $CaCl_2.2H_2O$ solution and two organic fluids, Dibutyl Phthalate and P-Cymene, are suggested for refractive index matching with fused quartz and acrylic, respectively. Moreover, the temperature dependence of the refractive indices of these fluids is investigated and the *Thermooptic Constant* is calculated for each fluid. Finally, the fluid viscosity for different shear rates is measured as a function of temperature and is applied to characterize the physical behavior of the proposed fluids.

A.1. Experimental Methodology

A.1.1. Refractive Index Measurements

In this investigation, a VEE GEE ABBE Refractometer is utilized to measure the refractive index of different liquid samples (see Figure A-1). This refractometer works based on the optical refraction critical angle detection technique and has a measuring range of 1.3-1.7, a resolution of 0.0005n (25%), and an accuracy of ±0.0003n (±0.15%). The refractometer has two circulating nozzles for the primary prism and two more for the secondary prism through which it could be connected to a circulating bath to precisely control the prism/sample temperature. The prism is made of optical glass and its temperature is shown on an external glass thermometer which has a range of 0-70°C. Distilled water is used for calibration of the refractometer since its refractive index is well-known. A small sample of the liquid is placed directly on the measuring prism, the eyepiece section and the base prism are then locked together to ensure good contact between the sample and the measuring prism, the shadow-line is matched with the center of a crosshair seen through the eyepiece of the refractometer using a control knob. The refractive index is read where the vertical line on the scale bar is matched with the center of the crosshair.

In this study, for all refractive index measurements, the ambient temperature was recorded as 23°C. Moreover, in order to control the temperature of the prism, the refractometer was connected to a NESLAB RTE-221 Refrigerated Bath/Circulator with a temperature range of -23°C to +100°C (with a temperature stability of ±0.01°C) and water running though it as the working fluid. To obtain more accurate values for the

refractive index, a minimum of two readings was performed at each prism temperature while measuring the refractive index of each individual material. The average values of those two readings are reported here as the refractive index.

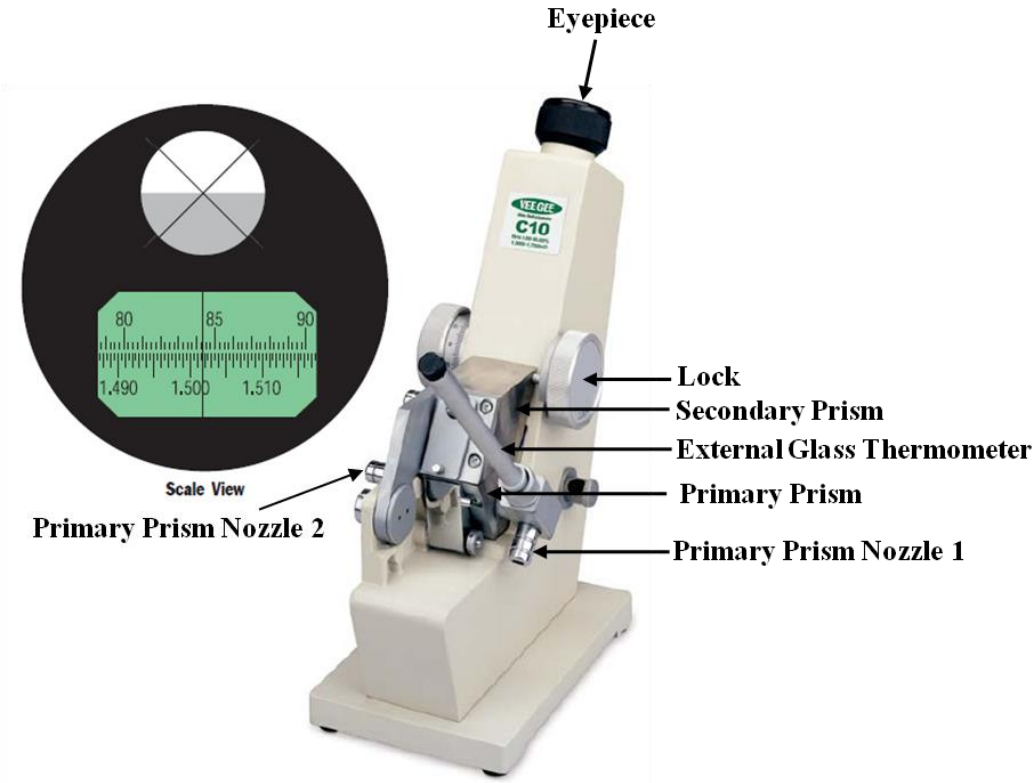

Figure A-1 Picture of the VEE GEE ABBE Refractometer (VEE GEE 2011).

A.1.2 Viscosity Measurements

Viscosity is one of the most important physical characteristics of any fluid that needs to be fully known in fluid flow experiments to obtain the parameters characterizing the experiment such as dimensionless numbers (e.g. Reynolds number, Prandtl Number, Nusselt number, etc.). In this investigation, a Physica MCR 300 Modular Compact Rheometer manufactured by Anton Paar is used for viscosity measurements. The rheometer is equipped with a "Cone-Plate" type probe (Anton Paar, model: CP50-1, diameter: 49.95 mm, angle: 0.987). In order to control the temperature of the samples while measuring their viscosity, the rheometer is connected to a Brinkmann Lauda RE-106 Refrigerated Bath with an operating temperature range of -30°C to +120°C (with a control accuracy of ±0.02°C) and water running through it as the working fluid. Viscosity measurements for each sample are done under different shear rates and different temperatures. It should be noted that for all viscosity measurements the ambient temperature was recorded as 23°C. Furthermore, viscosity measurement for each substance at any temperature increment was done two times and an average value of the two readings is reported.

A.2. Results

A.2.1. Refractive Index Matching

The main focus here is to study a wide variety of fluids and to obtain practical fluids that have refractive indices matching with those of fused quartz and acrylic. For this purpose, two categories of fluids are considered: (a) aqueous salt solutions, and (b) organic fluids.

A.2.1.1. Refractive index matching using aqueous salt solutions

As mentioned earlier, water is considered to be a robust candidate for working fluid in many fluid flow experiments. However, water has a much lower refractive index (n_{water} = 1.33) than refractive indices of both acrylic and fused quartz. One solution to increase the refractive index of water is to add salts with high refractive indices to water which will lead into having a solution with a higher refractive index than that of water and possibly matching the refractive indices of fused quartz and acrylic. The main issue here is finding the appropriate type of salt and the right concentration of salt for the aqueous solution. Therefore, several types of salt have been considered in this study which are listed in Table A-1. In this table, some of the important chemical and optical characteristics of the studied materials, i.e. refractive index, specific gravity, and their solubility in water are summarized.

Inorganic Compound	Refractive Index	Specific Gravity	Solubility (in grams per 100 cc)	
			Cold water	Hot water
Calcium Chloride (anhydrous) ($CaCl_2$)	1.52	2.15	74.5	159
Calcium Chloride (dehydrate) ($CaCl_2.2H_2O$)	1.531††	0.835	97.7	326
Calcium Chloride (hexahydrate) ($CaCl_2 .6H_2O$)	1.417,1.393†††	1.71	279	536
Potassium Chloride (KCl)	1.49	1.984	34.7	56.7`
Sodium Chloride (NaCl)	1.5442	2.165	35.7	39.12
Sodium Iodide (NaI)	1.7745	3.667	184	302

Table A-1 Physical properties of different types of salts†.

†Ref: Weast (1976-1977)

†† Ref: Guidechem (2011)

††† For different crystalline forms: Ref: Weast (1976-1977)

The first salt that is discussed here is NaI which has the highest refractive index among all the studied salts. Additionally, NaI has excellent solubility in water. As mentioned by Uzol *et al.* (2001) a 62%-64% aqueous solution of NaI (by weight) would have a refractive index of 1.49-1.5 which matches the refractive index of acrylic. Therefore, a less concentration of NaI in water would provide a solution with a refractive index matched with that of fused quartz. Although NaI aqueous solution seems to be an appropriate candidate for working fluid in facilities constructed with both acrylic and fused quartz, there are some major issues with this solution that limit its application: (a) NaI is relatively expensive compared to the other types of salt mentioned in Table A-1, (b) More importantly, as pointed out by Uzol *et al.* (2001), small amount of I_3^- ions form in the solution when the aqueous NaI solution is exposed to light and oxygen. I_3^- ions absorb the light in some sections of the visible range including the green light which can lead into attenuation of the laser sheet passing through the test facility where the optical

measurements are performed. This causes difficulties in acquisition of PIV images in the regions where the laser light is attenuated. Uzol *et al.* (2005) suggested keeping the NaI solution under vacuum condition and away from light sources as much as possible. However, the suggestions made by Uzol *et al.* (2005) are not applicable in case of experiments where the facility is not entirely closed or in cases where it is not possible to keep the test section in darkness. Considering the mentioned difficulties, NaI aqueous solution does not seem to be a practical option for MIR purposes in this investigation.

The second salt that will be discussed here is NaCl. As indicated in Table A-1, NaCl has the second highest refractive index among all other types of salts; however, its low solubility in water makes it impossible for its aqueous salt solution to reach refractive indices as high as fused quartz or acrylic (see solution 1 in Table A-2). As it is seen in the table a saturated aqueous solution of NaCl has a refractive index of 1.38 which is much lower than the refractive indices of both fused quartz and acrylic. Therefore, another approach has been followed in which a combination of different types of salt is utilized to achieve a higher refractive index for the solution. This approach has been chosen since it gives the possibility of using those types of salts with highest refractive index and lower solubility (e.g. NaCl) along with salts having lower refractive indices than NaCl but higher solubilities in water (e.g. $CaCl_2$). It should be mentioned that careful measures have been taken while solving different types of salt in water not to add all different types of salts to water at once and add each of them separately at a different stage after making sure that the previous salt is entirely solved. This method

Solution	Material	Concentration (by weight)%	Refractive index
1	NaCl	26.310	1.3800
	H_2O	73.690	
2	$CaCl_2.6H_2O$	32.354	1.3800
	KCL	4.339	
	NaCl	0.152	
	H_2O	63.155	
3	$CaCl_2.6H_2O$	46.653	1.3935
	KCL	0.218	
	H_2O	53.129	
4	$CaCl_2.2H_2O$	32.354	1.4040
	KCL	4.339	
	NaCl	0.152	
	H_2O	63.155	
5	$CaCl_2.6H_2O$	54.862	1.4070
	NaCl	0.535	
	H_2O	44.603	
6	$CaCl_2.6H_2O$	51.230	1.4120
	KCL	6.870	
	NaCl	0. 240	
	H_2O	41.660	
7	$CaCl_2.2H_2O$	45.756	1.4285
	NaCl	2.136	
	H_2O	52.108	
8	$CaCl_2.2H_2O$	47.620	1.4340
	NaCl	4.760	
	H_2O	47.160	
9	$CaCl_2.2H_2O$	55.007	1.4430
	NaCl	0.257	
	H_2O	44.736	
10	$CaCl_2.2H_2O$	55.015	1.4450
	NaCl	0.257	
	H_2O	44.728	

Table A-2 Refractive index of a number of aqueous salt solutions at room temperature.

ensures that different salts do not interfere with each other and do not prevent other salts from being solved. The refractive indices of different solutions that were tested are shown in Table A-2. As seen in the table, the refractive index of the solution with the highest refractive index obtained by this approach (solution 10, n=1.445) is still significantly lower than the refractive indices of either fused quartz or acrylic.

Therefore, it is concluded that the studied approach is not appropriate for this particular purpose.

As indicated in Table A-1, all types of $CaCl_2$ take advantage of having high solubilities in water as well as relatively high refractive indices. Moreover, all types of $CaCl_2$ are reasonably priced and are appropriate for application in large volume experiments. Efforts are made here to obtain aqueous $CaCl_2$ solutions with refractive indices close to those of fused quartz and acrylic. The results of the refractive index measurements of aqueous $CaCl_2$ solutions with different types and various concentrations of $CaCl_2$ are listed in Table A-3. It should be noted that none of the three types of $CaCl_2$ aqueous solutions that have been tested in this investigation shows any significant chemical or physical changes while exposed to either oxygen or light. All the above mentioned characteristics make $CaCl_2$ aqueous solutions good candidate working fluids for a wide variety of fluid flow experiments.

$CaCl_2$ (anhydrous) has a granular form and releases noticeable amount of heat while being dissolved in water (exothermic reaction). As mentioned in Table A-3, the $CaCl_2$ solution becomes opaque at a 23% concentration by weight; therefore, additional experiments will not be done on $CaCl_2$ since optical clarity of the fluid is the main factor for the laser diagnostic techniques. $CaCl_2.6H_2O$ (hexahydrate) has the highest solubility in cold water among all other types of $CaCl_2$ which is an advantage since high concentrations of salt in water is required to achieve the necessary refractive index. Therefore, solutions with different concentrations of $CaCl_2.6H_2O$ were made and their refractive indices were measured. As seen in Table A-3, an aqueous solution of

$CaCl_2.6H_2O$ with 75% concentration by weight which is slightly higher than maximum soluble amount of $CaCl_2.6H_2O$ in cold water (according to Table A-1), has a refractive index which is still much lower than that of either fused quartz or acrylic. Hence, $CaCl_2.6H_2O$ solutions will not be further tested for MIR purposes.

	Refractive index (n)							
	Concentration (by weight)%							
	9%	13%	23%	37.5%	49%	50%	63%	75%
$CaCl_2$	1.354	1.364	1.389 (opaque)	-	-	-	-	-
$CaCl_2.2H_2O$	1.3485	-	1.376	1.405	1.43	-	1.458	-
$CaCl_2.6H_2O$	-	-	-	1.381	-	1.3975	-	1.434

Table A-3 Refractive index of aqueous Calcium Chloride solutions at room temperature.

It can be seen in Table A-1 that $CaCl_2.2H_2O$ has a relatively high solubility in cold and hot water (≈ 49% by weight in cold water and ≈ 77% by weight in hot water) as well as a noticeably high refractive index. The results of refractive index measurement of aqueous $CaCl_2.2H_2O$ solution with different concentration are shown in Table A-3. The refractive index of a 49% (by weight) aqueous $CaCl_2.2H_2O$ solution in cold water was measured at 1.43 which was still lower than even the refractive index of fused quartz. In this case, attempts were made to make solutions with higher concentrations of $CaCl_2.2H_2O$ with the help of heating up the solution by indirectly exposing it to a heat source. It should be mentioned that $CaCl_2.2H_2O$ was gradually added to the solution to make sure that at each step, the added $CaCl_2.2H_2O$ is completely dissolved. This

procedure was done multiple times, and the refractive indices of the solutions were measured until an aqueous $CaCl_2.2H_2O$ solution with 63% concentration by weight showed a refractive index of 1.458 which is identical to that of fused quartz. This solution remained at the liquid phase even when the heat source was removed and even after days of remaining at room temperature. However, it was observed that the solution crystallizes if it is rapidly cooled down or is kept at very low temperatures. This solution is considered a reasonable candidate for fluid dynamics experiments in which the facility is made of fused quartz. Since this solution is a water-based salt solution, it is expected to have similar characteristics to that of water. The refractive index and viscosity variations of this solution with respect to temperature will be further investigated in the following sections. It should be noted that a much higher concentration of $CaCl_2.2H_2O$ in water is needed for the solution to reach to the refractive index of acrylic. Considering that the existing solution is nearly a fully saturated solution, application of $CaCl_2.2H_2O$ solution for refractive index matching with acrylic is not practical.

A.2.1.2. Refractive index matching using organic fluids

In this investigation, organic fluids are studied as alternatives to water based solutions to find a working fluid with a refractive index closely matched with that of fused quartz and acrylic. Organic fluids normally have a higher refractive index than water. Some of the organic compounds which were found to have refractive indices close to refractive indices of fused quartz and acrylic were tested and their refractive indices were measured using the ABBE Refractometer. A list of the organic compounds

that have been investigated is shown in Table A-4. In this table, some important physical properties of these organic compounds e.g. viscosity, specific gravity, and flash point are also provided. P-Cymene and Dibutyl Phthalate have refractive indices which are closely matched to that of acrylic. The physical characteristics of P-Cymene (viscosity and specific gravity) make it a good candidate to be used in MIR facilities where acrylic is used for the construction of the test section. The only issue that needs to be considered while working with P-Cymene is its low Flash Point (47.222°C for a close loop (ScienceLab1 2011) which is an important factor in experiments where the working fluid needs to be heated more than 47.222°C. Dibutyl Phthalate, on the other hand, has a relatively high flash point (157°C for a close loop (ScienceLab2 2011); therefore, it may be a better choice for heated flow experiments. However, the higher viscosity of Dibutyl Phthalate needs to be considered while selecting the hydraulic pump in fluid flow experiments. Both P-Cymene and Dibutyl Phthalate are listed as materials with type 2 health hazard in the Material Safety Data Sheet (MSDS) charts. Therefore, both materials should be applied carefully and personal protection equipments such as splash goggles, gloves, and respirator masks need to be worn while working with these two substances. The MSDS charts provide more detailed information regarding the health hazards and personal protection for these materials.

Fluid	Refractive Index† (n)	Viscosity†† (Pa.s)	Specific Gravity††	Flash Point†† (°C)
Ethanol	1.362	-	0.79	14
P-Cymene	1.4905	0.876×10^{-3}	0.861	47.222
Dibutyl Phthalate	1.4905	13.329×10^{-3}	1.043	157
Diethyl Phthalate	1.5040	12×10^{-3}	1.118	156

Table A-4 Refractive index of some organic fluids.

† The refractive indices of all organic compounds except for Ethanol are measured in this study.

†† Viscosity, Specific Gravity, and Flash Point of all the material as well as the refractive index of Ethanol are taken from Hassan & Dominguez-Ontiveros (2008)

As suggested by Nguyen *et al.* (2004) and Miller *et al.* (2006), another option to make a solution with a refractive index matched with fused quartz or acrylic is to dilute the higher refractive index organic fluids with lower refractive index ones (in case they are soluble in each other). In this case, refractive index of the mixture of the two fluids can be calculates as (Budwig 1994 and Nguyen *et al.* 2004):

$$n_{mixture} = n_1 p + n_2 (1 - p) \tag{A-1}$$

where n is the refractive index and p is the relative volume percentage. As it is shown in Table A-4, Diethyl Phthalate has a refractive index of 1.504 which is higher than that of both acrylic and fused quartz. Therefore, as suggested by Nguyen *et al.* (2004) and Miller *et al.* (2006), diluted solutions of Diethyl Phthalate with Ethanol (with different concentrations) would have refractive indices close to acrylic or fused quartz. Based on Eq. A-1, a Diethyl Phthalate/Ethanol solution of 90% Diethyl Phthalate to 10% Ethanol would have a refractive index of 1.49 at room temperature. This is confirmed in the current study by measuring the refractive index of the mixture with the refractometer.

There are two main issues with this mixture: 1- Ethanol is in fact a solvent for acrylic; therefore, it reacts with acrylic and affects the optical clarity of acrylic after sometime. 2- Ethanol is volatile; therefore, the solution should be kept in a perfectly sealed container to maintain the ethanol content of the mixture and prevent changes in the refractive index of the solution over time. This is even more critical in case a solution of Diethyl Phthalate and Ethanol is made to match the refractive index of fused quartz since a higher percentage of Ethanol (≈ 32% by volume) is needed. Hence, this solution will not be further pursued as a candidate working fluid for MIR facilities.

A.2.2. Refractive Index Variations with Temperature

As indicated in the previous section, three different fluids are chosen among which one has a refractive index matched with fused quartz, aqueous $CaCl_2$.$2H_2O$ solution (63% by weight), and the other two possess refractive indices closely matched with refractive index of acrylic, P-Cymene and Dibutyl Phthalate.

To have a more comprehensive understanding of the optical characteristics of the solutions chosen for refractive index matching, the dependency of the refractive index of all three solutions on temperature is measured using the ABBE refractometer which is connected to a water bath for temperature control of the prism and the sample. The results of refractive index measurements as a function of temperature for all three solutions are shown in Figure A-2. To provide a basis for comparison, the temperature dependence of the refractive index of water as a reference fluid is also measured and shown in Figure A-2. The "*Thermooptic Constant (dn/dT)*" which represents the

temperature dependence of the refractive index of each fluid is obtained from the slope of the linear regression lines for each data set shown in Figure A-2. As mentioned in the methodology section, the external glass thermometer which indicates the prism/sample temperature has a range of 0-70°C; therefore, all refractive index measurements have been acquired in this range. It should be mentioned that since water is used as the working fluid in the thermal bath controlling the temperature of the refractometer prism, the lowest temperature chosen for the measurements is set at 6°C to avoid approaching the freezing point of water. Moreover, the refractive index measurements are presented in the range of 26-70°C in case of the $CaCl_2$.$2H_2O$ solution and within the range of 6-65.5° for P-Cymene. It should also be noted that Error *Bars* shown in Figure A-2 are hardly seen due to their small value.

As seen in Figure A-2, the refractive index of all the materials under investigation decreases with the increase in the temperature. Figure A-2 shows that the refractive index of water does not drastically change with temperature increase and the *Thermooptic Constant* in this case is estimated as $\left({}^{dn}/_{dT}\right) = -1 \times 10^{-4}$ which is in agreement with the value obtained by Stöhr *et al.* (2003) $\left({}^{dn}/_{dT}\right) = -0.99 \times 10^{-4}$. As expected, the refractive index of the aqueous $CaCl_2$.$2H_2O$ solution shows a relatively similar behavior to that of water with a *Thermooptic Constant* of -0.2×10^{-4} . This is a significant advantage of aqueous salt solutions for applications in MIR facilities specifically in those where sharp temperature gradients exist or where the working fluid needs to be heated.

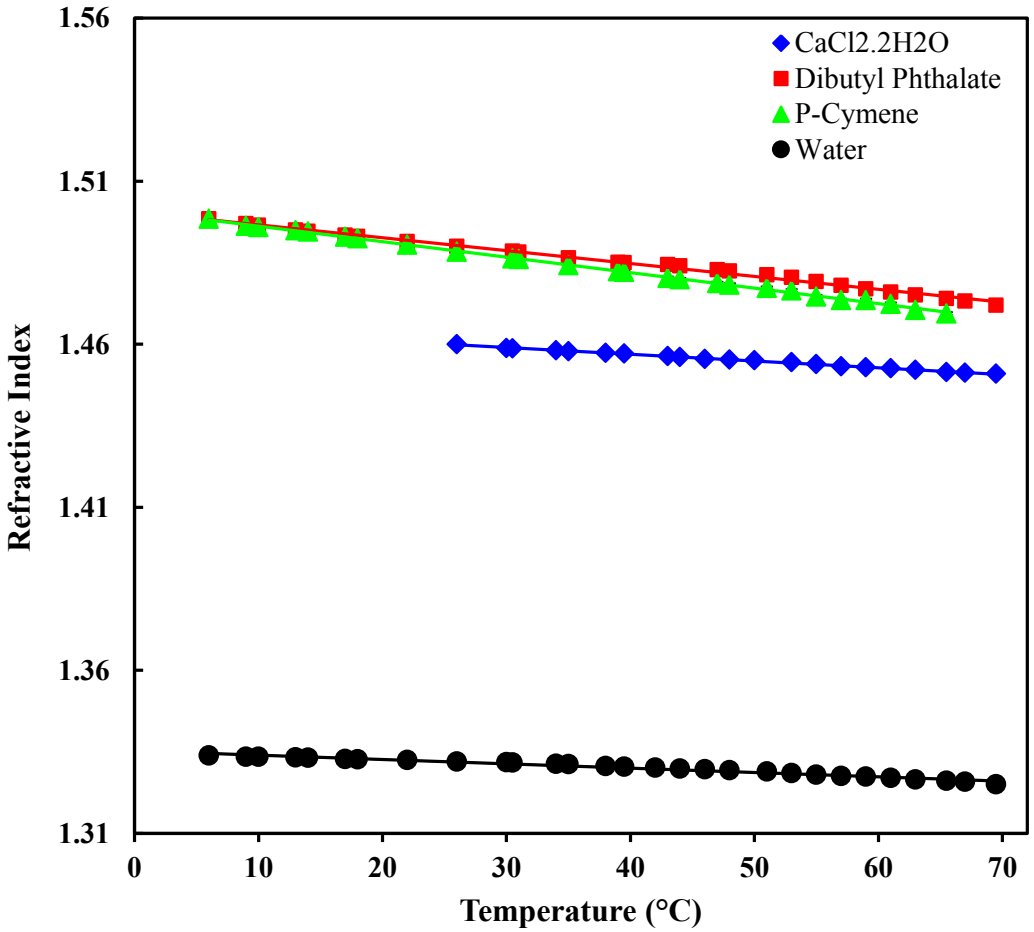

Figure A-2 Temperature dependence of the refractive index of fluids suggested for MIR technique.

As observed in Figure A-2, the refractive indices of P-Cymene and Dibutyl Phthalate rapidly decrease with the temperature increase. The line for P-Cymene shows a steeper decaying slope than that of Dibutyl Phthalate. The *Thermooptic Constant* is acquired as -4×10^{-4} and -5×10^{-4} for Dibutyl Phthalate and P-Cymene, respectively. The relatively large decrease in the refractive indices of Dibutyl Phthalate and P-Cymene (going from 1.499 at 6°C down to 1.472 at 70°C for Dibutyl Phthalate and decreasing from 1.499 at 6°C to 1.469 at 66°C for P-Cymene) needs to be considered while working with any of these two fluids in heated fluid flow experiments.

It should be noted that for both fluids at higher temperatures (higher than 48°C for Dibutyl Phthalate and higher than 35°C for P-Cymene) the refractive indices of both fluids are below the acceptable range for refractive index matching purposes.

A.2.3. Viscosity Variations with Temperature

Another important factor that needs to be considered while selecting fluids for MIR technique for fluid flow experiments is the viscosity of the fluid and the temperature dependence of the viscosity of that specific fluid. Therefore, viscosity measurements have been performed for each of the three candidate working fluids at different temperatures and under different shear rates and the results are presented in Figures A-3-5. Viscosity measurements have been performed in the practical range of 5-80°C. As an exception, in case of the aqueous $CaCl_2$ $.2H_2O$ solution, the lowest temperature is chosen to be 25°C in order to keep the solutions from crystallization. Furthermore, the highest temperature for P-Cymene viscosity measurements is set at 60°C not to largely pass the flash point of P-Cymene.

Figure A-3 represents the results of viscosity measurements of the aqueous $CaCl_2$ $.2H_2O$ solution with a refractive index matched with that of fused quartz. As seen in the figure, viscosity profiles of $CaCl_2$ $.2H_2O$ solution show a similar trend under different shear rates for temperatures lower than 65°C. In the temperature range of 25-60°C, viscosity of the solution decreases with increasing the temperature; however, the solutions shows a totally different behavior for temperatures higher than 60°C. For the temperature range of 60-80°C, viscosity values obtained under most shear rates show an

increasing trend while the temperature increases. Moreover, for temperatures higher than 60°C, the viscosity values acquired under different shear rates do not follow a similar pattern. Therefore, in case of using aqueous $CaCl_2$.$2H_2O$ solution for MIR purposes, it is suggested to use the solution in temperatures below 60°C for which the viscous behavior of the solution is predictable and follows a certain trend. It is worth mentioning that this solution has a higher viscosity than water. Water has viscosity of 0.00089008 Pa.s at a temperature of 25°C and a pressure of 1 atm (NIST Chemistry WebBook 2011).

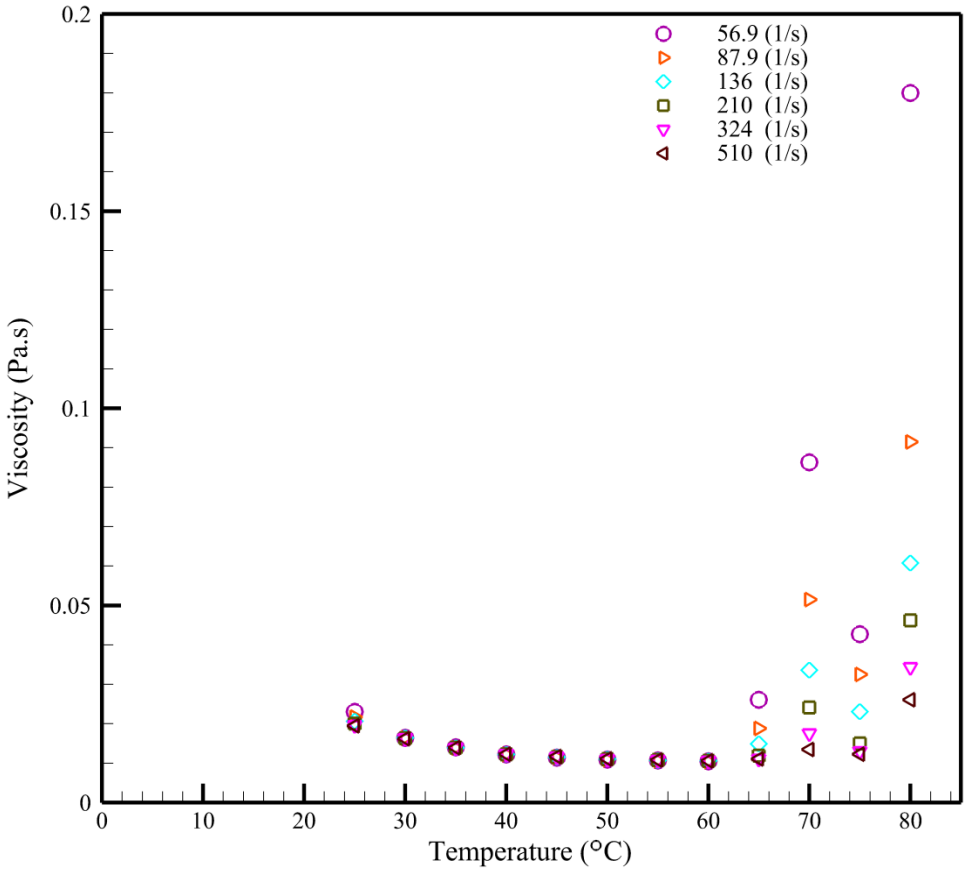

Figure A-3 Temperature dependence of the dynamic viscosity of aqueous $CaCl_2.2H_2O$ solution under different shear rates.

The results of viscosity measurements for Dibutyl Phthalate in the temperature range of 5-80°C are shown in Figure A-4. As observed in this figure, viscosity of Dibutyl Phthalate decreases with temperature increase for all applied shear rates. Moreover, the viscosity profile of Dibutyl Phthalate under all shear rates follows a similar pattern and the data points at each temperature with different shear rates are almost identical.

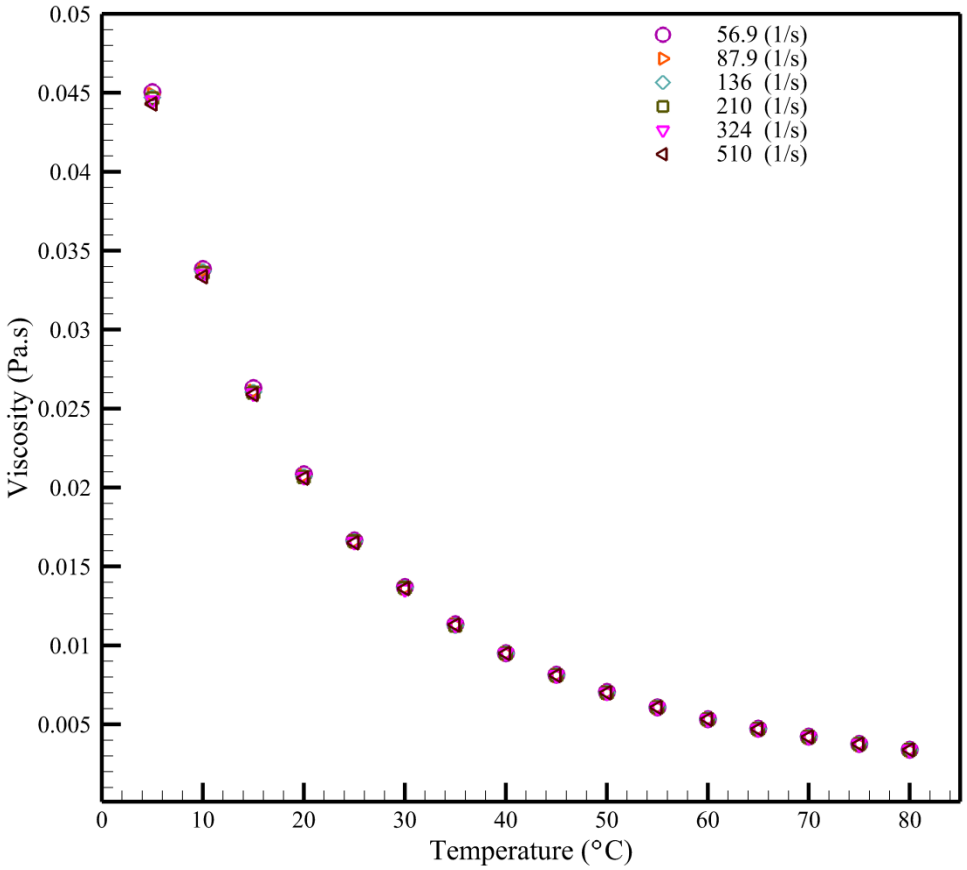

Figure A-4 Temperature dependence of the dynamic viscosity of Dibutyl Phthalate under different shear rates.

Figure A-5 represents the results acquired for the viscosity variations of P-Cymene under temperature variations and different shear rates. It is observed from the figure that for most shear rates -except for some temperatures at the shear rate of 56.9(1/s)- the viscosity data points at each temperature match up pretty well.

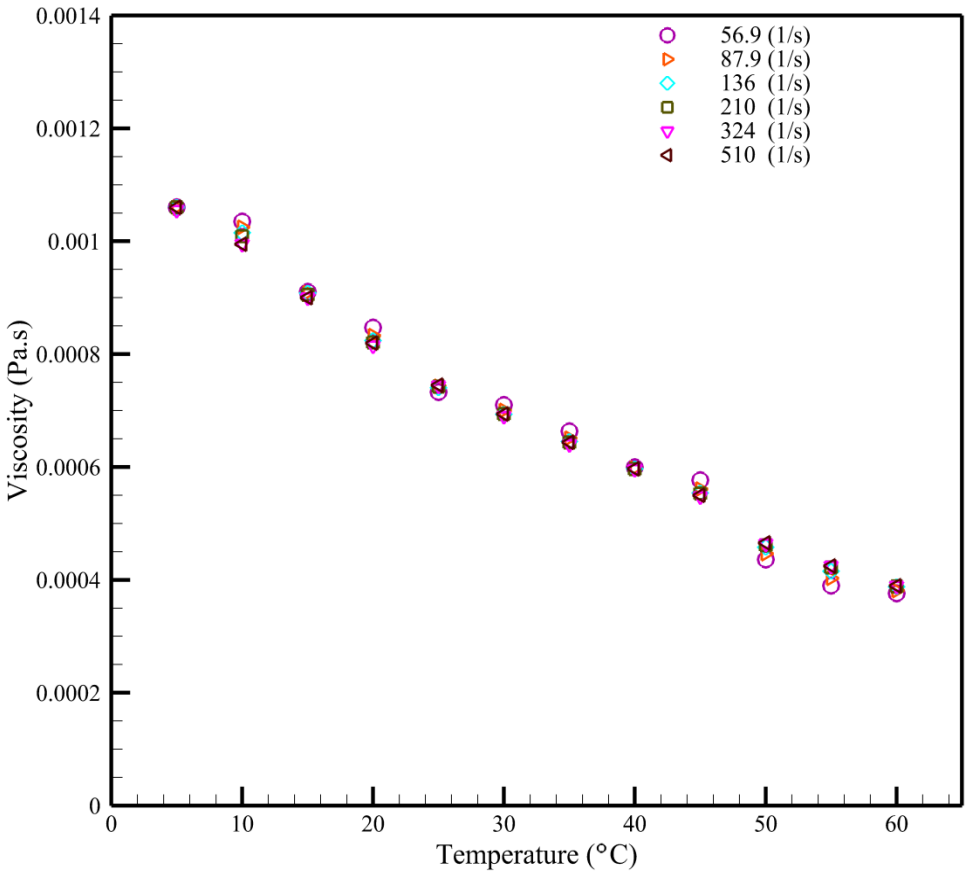

Figure A-5 Temperature dependence of the dynamic viscosity of P-Cymene under different shear rates.

A.3. Conclusion

Optical distortions caused either by the refraction of the laser light passing through the test section walls/interfaces or by the non-uniformities in the refractive index in the measurement volumes is a main issue for the optical imaging techniques. Matched Index of Refraction technique - which involves matching the refractive indices of the transparent materials utilized in the construction of the test section and the working fluid- helps in eliminating the image distortion problem. Another major factor that needs to be considered while choosing a working fluid is the viscosity of the candidate fluid.

In this investigation, several aqueous salt solutions and organic fluids have been studied for their refractive index and viscosity characteristics to find appropriate working fluids for transparent MIR facilities constructed with either fused quartz or acrylic.

An aqueous $CaCl_2.2H_2O$ solution with a concentration of 63% by weight of $CaCl_2.2H_2O$ in water provides a solution with a refractive index matched with that of fused quartz. The temperature dependence of the refractive index and viscosity of this solution is further studied. Similar to water, the refractive index profile of the $CaCl_2.2H_2O$ solution shows a low *Thermooptic Constant*. It has been observed that the $CaCl_2.2H_2O$ solution crystalizes under lower temperatures and has unpredictable viscosity behavior for temperatures higher than 60°C; therefore, it is suggested that this solution is more applicable in a temperature range of 20-60°C.

Two different organic fluids (Dibutyl Phthalate and P-Cymene) were proposed for refractive index matching with acrylic. The refractive indices of these fluids indicate a decaying trend with the increase in temperature which is more sensible in case of P-

Cymene. Both Dibutyl Phthalate and P-Cymene have predictable viscosity profiles with a decreasing trend with respect to temperature. Dibutyl Phthalate has a higher viscosity (16.583×10^{-3} (Pa.s) at 25°C) compared to P-Cymene (0.741×10^{-3} (Pa.s) at 25°C). Moreover, Dibutyl Phthalate has a higher flash point (157°C) than P-Cymene (47.222°C). Regarding the results of this study, it can be concluded that Dibutyl Phthalate is the preferable working fluid in heated fluid flow experiments while P-Cymene is more suitable for isothermal experimental fluid dynamic studies.

APPENDIX B

The time-averaged velocity fields along the vertical front-plane and back-plane of the measurement volume for the cases presented in Figure II-23 and Figure II-24 in Chapter II are presented in this Appendix. As observed from Figures B-1, B-2, and B-3, the velocity values within the back-plane and front-plane for each case are much smaller compared to those of the time-averaged velocity fields along their corresponding mid-planes. This was somewhat expected since the mid-plane is the plane into which the jets inject. However, despite the relatively low velocities observed in the front-planes and back-planes, the key flow feature, the recirculation zone, which was observed close to the center rod of the mid-plane for all cases, is also observed in these planes. In cases with single impinging jets, the recirculation zones are observed close to the first two rods from the left-hand side of the field which are closer to location of the impinging jet in the mid-plane. In case of two impinging jets, the recirculation zone appears in the vicinity of all three rods within back-plane and front-plane. These flow features appearing close to the rods needs to be considered in the design process of the graphite support rods present in the lower plenum of a prismatic core VHTR.

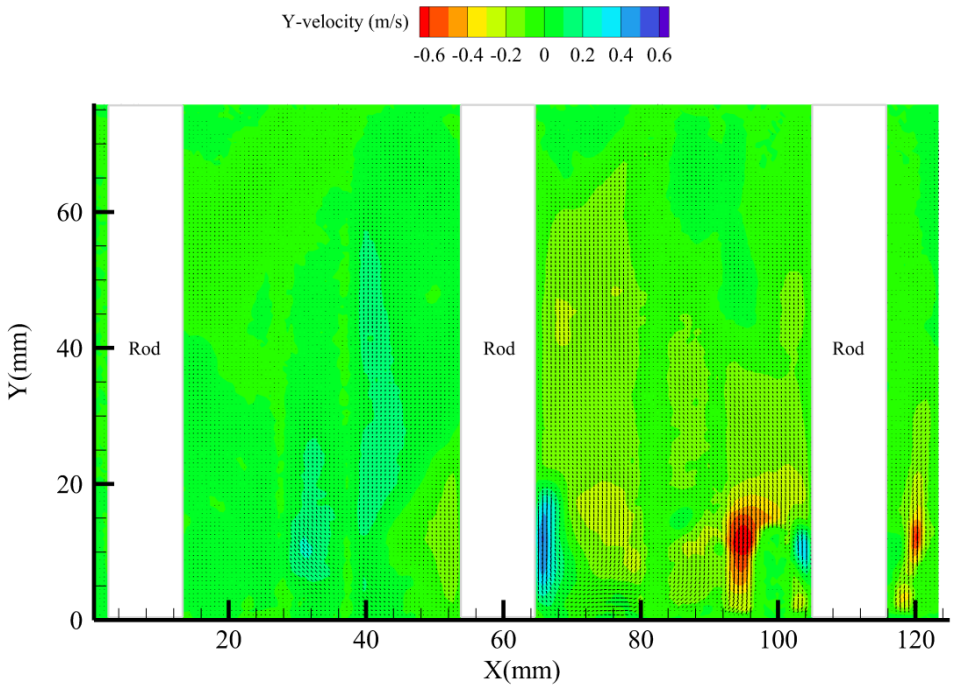

(a)

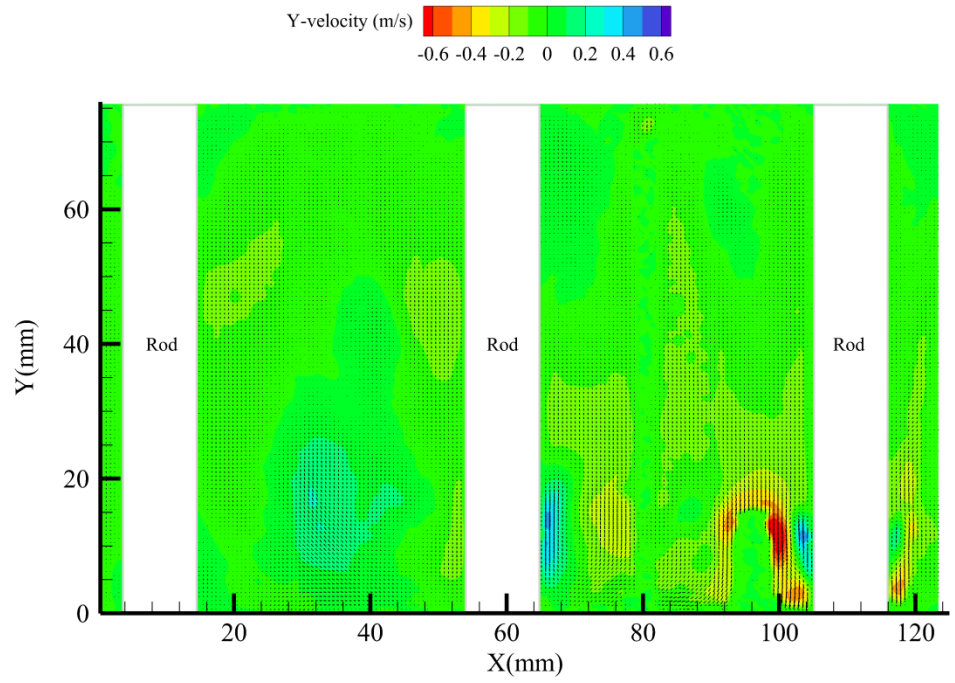

(b)

Figure B-1 Time-averaged velocity field, the contour plot of the Y-velocity component for a single isothermal inlet jet with $Re_{jet\ 1}$=13,400 (a) along the vertical back-plane, (b) along the vertical front-plane.

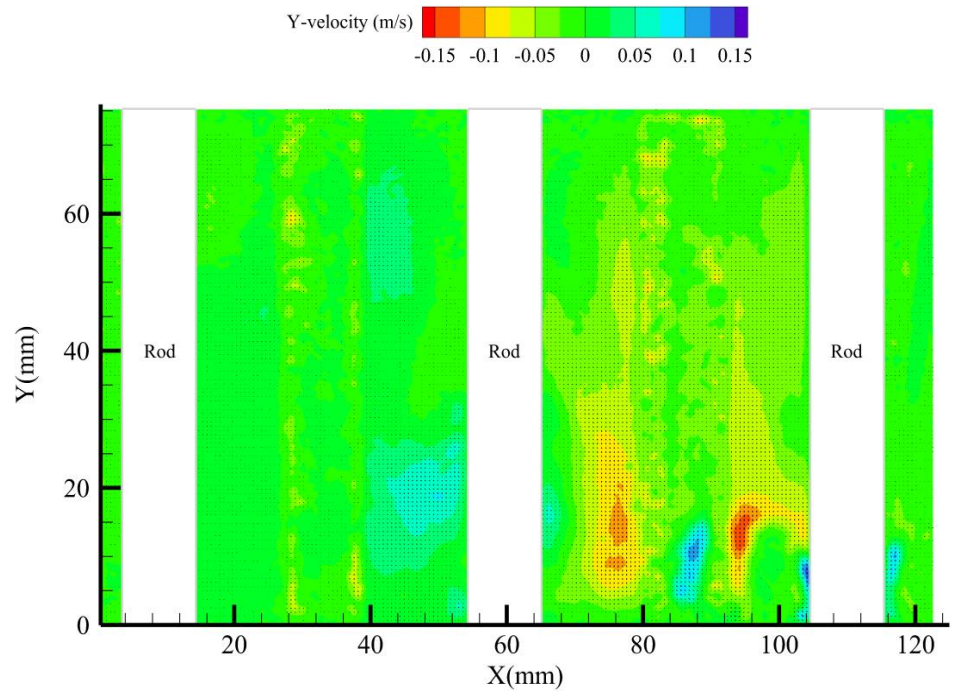

(a)

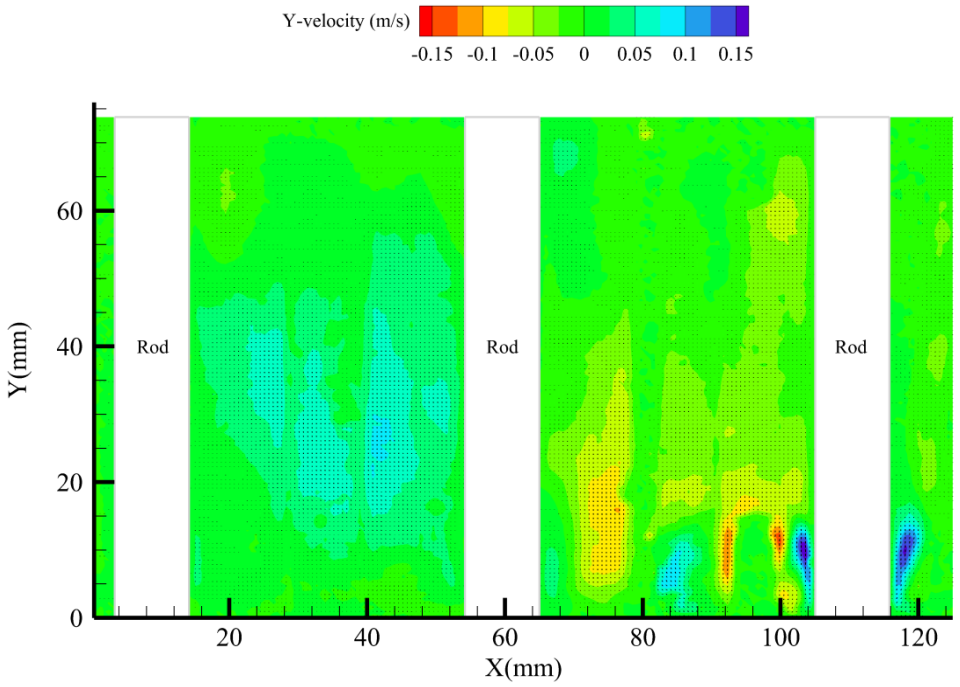

(b)

Figure B-2 Time-averaged velocity field, the contour plot of the Y-velocity component for a single isothermal inlet jet with $Re_{jet\ 1}$=4,470 (a) along the vertical back-plane, (b) along the vertical front-plane.

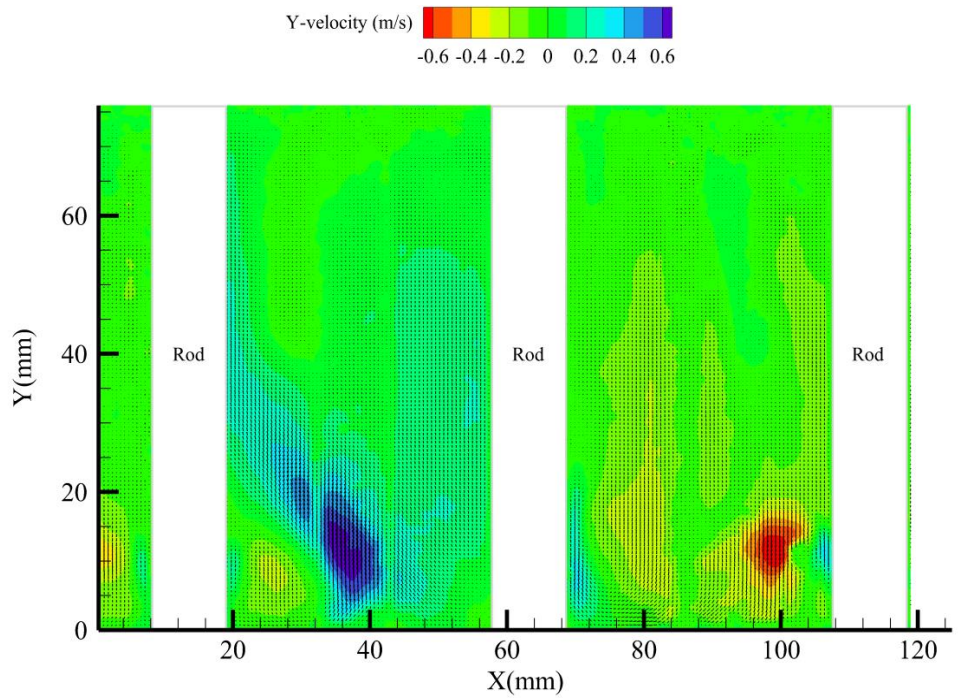

(a)

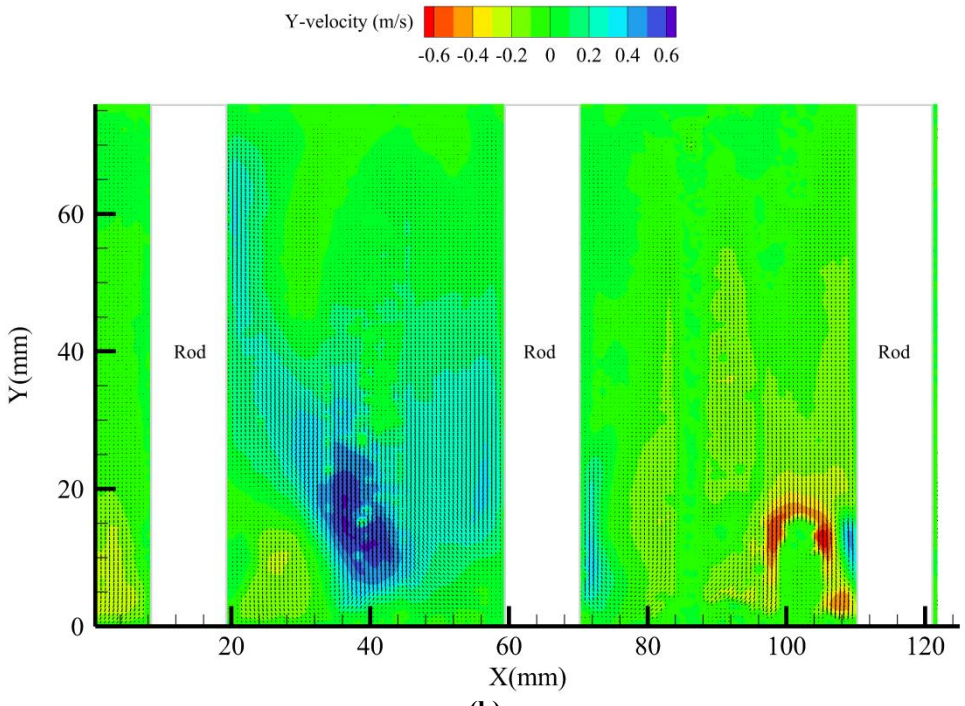

(b)

Figure B-3 Time-averaged velocity field, the contour plot of the Y-velocity component for two isothermal inlet jets with different Reynolds numbers $Re_{jet\ 1}$=11,160 and $Re_{jet\ 2}$=6,250 (a) along the vertical back-plane, (b) along the vertical front-plane.

VITA

Noushin Amini received her Bachelor of Science in applied physics-nuclear from Amirkabir University of Technology (Tehran Polytechnic), Tehran, Iran in January 2002. She got her Master of Science in nuclear engineering from Shahid Beheshti University, Tehran, Iran in August 2006. Afterwards, she began her PhD studies at Texas A&M University majoring in mechanical engineering and graduated with her PhD in December 2011. Her research interests include turbulent flow analysis and coherent structures identification in flows with highly complex geometries, single and multi-phase flow, heat transfer, and measurement techniques applied in experimental fluid dynamics studies. She plans to pursue a career in engineering research and education.

Miss Amini may be reached at 337 Zachary Engineering Center, Texas A&M University, 3133 TAMU, College Station, TX 77843-3133. Her email address is noushin.amini@gmail.com.